

# Germanium, Tin and (Zinc) Gallium Oxide for Advanced Micro- and Optoelectronics: Insights into the Surface Electronic Structure with Photoemission Techniques

Von der Fakultät 1 - MINT - Mathematik, Informatik, Physik,  
Elektro- und Informationstechnik  
der Brandenburgischen Technischen Universität Cottbus–Senftenberg  
genehmigte Dissertation  
zur Erlangung des akademischen Grades eines

Doktor der Naturwissenschaften  
(Dr. rer. nat.)

von

**Felix Reichmann**  
geboren am 08.11.1990 in Berlin

Vorsitzende/r: Prof. Dr. rer. nat. habil. Götz Seibold  
Gutachter/in: Prof. Dr. rer. nat. habil. Inga Anita Fischer  
Gutachter/in: Prof. Dr. rer. nat. habil. Christian Wenger  
Gutachter/in: Prof. Dr. rer. nat. habil. Jan Ingo Flege  
Gutachter/in: Prof. Dr. Giovanni Capellini  
Tag der mündlichen Prüfung: 02.12.2022



# Erklärung zur selbstständigen Anfertigung der Dissertation

Ich, **Felix Reichmann**, erkläre, dass ich die bei der Fakultät MINT - Mathematik, Informatik, Physik, Elektro- und Informationstechnik der Brandenburgischen Technischen Universität Cottbus-Senftenberg zur Eröffnung des Promotionsverfahrens vorgelegte Dissertation mit dem Titel

**Germanium, Tin and (Zinc) Gallium Oxide for Advanced Micro- and Optoelectronics: Insights into the Surface Electronic Structure with Photoemission Techniques**

unter der Betreuung von **Prof. Dr. Inga A. Fischer** selbstständig und ohne sonstige Hilfe erstellt, andere als die angegebenen Quellen und Hilfsmittel nicht benutzt und die den benutzten Quellen wörtlich oder inhaltlich entnommenen Stellen als solche kenntlich gemacht habe.

- 1) Ich habe die Dissertation in dieser oder ähnlicher Form weder früher noch gleichzeitig in einem anderen Prüfungsverfahren als Prüfungsleistung vorgelegt.
- 2) Teile der Dissertation entstammen bereits veröffentlichten Arbeiten. Sie sind entsprechend gekennzeichnet und mein Eigenanteil als Autor oder Co-Autor zutreffend kenntlich gemacht.
- 3) Ich habe den angestrebten Doktorgrad noch nicht erworben und bin nicht in einem früheren Promotionsverfahren für den angestrebten Doktorgrad endgültig gescheitert.
- 4) Die Veröffentlichung der Dissertation verletzt keine bestehenden Schutzrechte Dritter. Die Rahmenpromotionsordnung der BTU Cottbus-Senftenberg ist mir bekannt, insbesondere habe ich die Bedeutung von § 18 der Promotionsordnung der Fakultät MINT (Ungültigkeit der Promotion und Entzug des Doktorgrades) zur Kenntnis genommen.

**Ort, Datum, Unterschrift**



# Acknowledgements

I want to thank **Prof. Dr. Christian Wenger** for the unique opportunity to work at “IHP – Leibnizinstitut für Innovative Mikroelektronik”. Being part of the “Materials Research” department always felt like a great honor to me and I cannot thank him enough for this.

I want to thank **Prof. Dr. Inga A. Fischer** for the support and the scientific discussions we had.

**Prof. Dr. Giovanni Capellini** supervised me throughout my research on Germanium and Tin. I am beyond thankful for the support I received and the scientific discussions we had.

**Dr. Wolfgang M. Klesse** was always available for all sorts of question, especially when I learned how to work in surface science cluster at the beginning of my PhD.

Thanks to the experience of **Dr. Mattia Mulazzi**, I was able to improve my knowledge and skills on photoelectron spectroscopy. I deeply appreciate the time we spend in the laboratory and on scientific discussions.

I want to thank **Dr. Emilio Scalise** the theory support on the Ge-Sn material systems. His first-principle calculations, especially on the Ge(001) surface, allowed for a deeper understanding of my experimental results. Equally valuable to me were the scientific discussions we had together with **Prof. Dr. Francesco Montalenti**.

**Dr. Jaroslaw Dabrowski** was available for any scientific questions I had. His calculations on the electronic band structure of  $\text{ZnGa}_2\text{O}_4$  were important to verify my experimental observations on the material.

I appreciate the collaboration with **Dr. Zbigniew Galazka**, who kindly provided me the  $\text{ZnGa}_2\text{O}_4$  (100) samples for my investigations. Furthermore, I would like to thank him for the invitation to the SPIE Photonics West.

**Dr. Yuji Yamamoto** offered me to join his visit in Japan and allowed me to investigate his Ge/SiGe quantum wells by XPS. I want to thank him for his trust in my capabilities and the great time we had.

I want to thank my fellow PhD-students for their support and the overall great time we had. **Andreas P. Becker** and **Emily V. S. Hofmann** worked together with me at the surface science cluster and performed the scanning tunneling microscopy measurements on my Germanium and Tin samples. My office neighbor **Henriette Tetzner** was always up for all sorts of discussions, despite working on a completely different topic. Finally, I want to thank **Agnieszka A. Corley-Wiciak** for the support on my  $\text{ZnGa}_2\text{O}_4$  samples, doing the actual AFM characterization.

Additionally, I would like to thank everyone else in the Materials Research department for the extremely kind and supportive atmosphere.

To all of my family members and friends: Thank you for the support and the distraction in my free time.

Finally, I want to thank my wife for understanding what all of this meant to me and supporting me wherever she could.

# Abstract

Historically, Ge is one of the oldest materials in the semiconductor industry and its (001) surface has been the subject of extensive investigations by photoelectron spectroscopy. I am going to challenge the predominant attribution of a semi-conducting nature of the Ge(001) surface in this thesis. My investigations reveal the presence of a Ge(001) surface state above the Fermi-level, occupied at room temperature. Employing time- and temperature-dependent angle-resolved photoelectron spectroscopy, I will demonstrate that the presence of this surface state is evidence for the conducting nature of the surface at room temperature.

Sparked by the remarkable properties of the GeSn-alloy and a trend towards Ge-Sn-related multi-quantum well fabrication, I investigate the surface electronic structure of Ge(001) after adsorption and incorporation of Sn. With an in-depth analysis of surface core-level shifts, I will extend the growth model of the Sn wetting layer formation by also detailing structural changes in the subsurface region. At the same time, the modifications of the electronic structure will be detailed, observing the removal of the Ge(001) surface states, the creation of a new, Sn-related surface state and the initial stages of the Schottky barrier formation.

$\beta$ -Ga<sub>2</sub>O<sub>3</sub> is a transparent semi-conducting oxide that has sparked a lot of interest over the last decade, because it offers an ultra-wide band gap and high break down voltage. However, due to its monoclinic crystal structure, device fabrication is rather challenging and researchers are already looking into alternative materials. One of these candidates is  $\epsilon$ -Ga<sub>2</sub>O<sub>3</sub> and this work presents a combined study by photoelectron spectroscopy and *ab initio* calculations of its electronic structure. (Hard) X-rays reveal the impact of photoelectron recoil and the absence of a band bending to the surface, while the dispersion of experimentally determined valence states compares favorably with the calculations based on hybrid density-functional theory.

Another alternative to  $\beta$ -Ga<sub>2</sub>O<sub>3</sub> could be ZnGa<sub>2</sub>O<sub>4</sub> and I will present an investigation on the electronic structure of its (100) surface. Due to the novelty of ZnGa<sub>2</sub>O<sub>4</sub> single-crystals, I am first going to explore the preparation of a clean and well-ordered surface by standard *in-situ* sputtering and annealing. I will show that already low annealing temperatures induce Zn-deficiency, leading to non-stoichiometric surfaces, further exacerbated by sputtering. By changing the sputtering parameters and the annealing conditions, the preparation of a surface with sufficient quality for subsequent investigations will be demonstrated. The results by photoemission techniques compare favorably with the expectations from theory and allowing the first fundamental insights into the surface electronic structure.





# Zusammenfassung

Ge ist eines der ältesten Materialien in der Geschichte der Halbleiter-Industrie und die Ge(001) Oberfläche wurde bereits umfassend durch Photoelektronenspektroskopie untersucht. Die dominierende Zuschreibung einer halbleitenden Eigenschaft der Oberfläche werde ich in dieser Dissertation anfechten. Meine Untersuchungen zeigen einen Ge(001) Oberflächenzustand oberhalb des Fermi-Niveaus, der bei Raumtemperatur besetzt ist. Durch zeit- und temperaturabhängige, winkelaufgelöste Photoelektronenspektroskopie werde ich zeigen, dass die Beobachtung dieses Zustands der Beweis für die leitende Eigenschaft der Oberfläche, bei Raumtemperatur, ist.

Inspiziert von den außergewöhnlichen Eigenschaften der GeSn-Legierung und einem Trend hin zu Ge-Sn-basierten Multi-Quantentopfstrukturen, werde ich die Modifizierung der Ge(001) Oberflächenbandstruktur nach Adsorption von Sn untersuchen. Mit einer detaillierten Analyse von Energie-Niveau-Verschiebungen, der inneren Elektronen der Oberflächenatome, werde ich das Modell des Sn-Wachstums auf der Ge (001) Oberfläche, um die darunter liegenden Schichten erweitern. Gleichzeitig werden Änderungen in der elektronischen Struktur gemessen. So kann die Entfernung von Ge(001) Oberflächenzuständen, die Entstehung eines neuen, Sn-basierten Oberflächenzustands und die ersten Stufen der Formation der Schottky-Barriere beobachtet werden.

$\beta$ -Ga<sub>2</sub>O<sub>3</sub> ist ein transparentes halbleitendes Oxid, welches im vergangenen Jahrzehnt dank seiner extrem breiten Bandlücke und hohen Durchbruchspannung großes Interesse geweckt hat. Jedoch ist die Herstellung von Bauteilen aufgrund der monoklinischen Kristallstruktur eine Herausforderung und Wissenschaftler suchen bereits nach alternativen Materialien. Ein möglicher Kandidat ist  $\epsilon$ -Ga<sub>2</sub>O<sub>3</sub> und in dieser Arbeit wird dessen elektronische Bandstruktur mit einer Kombination aus Photoelektronenspektroskopie und *ab initio* Berechnungen untersucht. (Harte) Röntgenstrahlung erlaubt die Beobachtung von Rückstoßeffekten der Photoelektronen und die Abwesenheit von Bandverbiegungen, während die Dispersionen der experimentell gemessenen Valenzbandzustände Berechnungen mit hybrid-density-functional-Theorie bestätigen.

Eine andere Alternative zu  $\beta$ -Ga<sub>2</sub>O<sub>3</sub> könnte ZnGa<sub>2</sub>O<sub>4</sub> sein und ich werde eine Untersuchung der elektronischen Struktur, der (100)-Oberfläche präsentieren. Aufgrund die Neuartigkeit von ZnGa<sub>2</sub>O<sub>4</sub>-Einkristallen werde ich zuerst die Vorbereitung einer sauberen und kristallinen Oberfläche mittels *in-situ* Sputtern und Heizen untersuchen. Ich werde zeigen, dass es selbst bei niedrigen Heiztemperaturen zu Zn-Mangel in der Oberfläche kommt, welcher sich durch Sputtern verschlimmert. Durch das ändern der Sputterparameter und der Bedingungen beim Heizen, werde ich eine Oberfläche mit hinreichender Qualität für eine weitergehende Charakterisierung der elektronischen Struktur demonstrieren. Die Ergebnisse aus der Photoelektronenspektroskopie passen zu theoretischen Berechnungen der Bandstruktur und liefern somit die ersten Einsichten in die elektronische Struktur der Oberfläche.



# Scientific Visibility

## Publications in Peer-Reviewed Journals (part of this Thesis)

**F. Reichmann**, A. P. Becker, E. V. S. Hofmann, N. J. Curson, W. M. Klesse and G. Capellini, “Modifications of the Ge(001) Subsurface Electronic Structure after Adsorption of Sn”, Applied Surface Science 599 (2022) 153884.

**F. Reichmann**, E. Scalise, A. P. Becker, E. V. S. Hofmann, J. Dabrowski, F. Montalenti, L. Miglio, M. Mulazzi, W. M. Klesse and G. Capellini, “New insights into the electronic states of the Ge(001) surface by joint angle-resolved photoelectron spectroscopy and first-principle calculation investigation”, Applied Surface Science, 571 (2022) 151264.

**F. Reichmann**, J. Dabrowski, A. P. Becker, W. M. Klesse, K. Irmscher, R. Schewski, Z. Galazka and M. Mulazzi, “Experimental and Theoretical Investigation of the Surface Electronic Structure of ZnGa<sub>2</sub>O<sub>4</sub>(100) Single-Crystals”, Physica Status Solidi B: Basic Solid State Physics, 259 (2021) 2100452.

M. Mulazzi, **F. Reichmann**, A. P. Becker, W. M. Klesse, P. Alippi, V. Fiorentini, A. Parisini, M. Bosi and R. Fornari, “The electronic structure of  $\epsilon$ -Ga<sub>2</sub>O<sub>3</sub>”, APL Materials, 7 (2019) 022522.

## Publications in Peer-Reviewed Journals (*not* part of this Thesis)

Y. Yamamoto, O. Skibitzki, M. A. Schubert, M. Scuderi, **F. Reichmann**, M. H. Zöllner, M. De Seta, G. Capellini and B. Tillack, “Ge/SiGe multiple quantum well fabrication by reduced-pressure chemical vapor deposition”, Japanese Journal of Applied Physics, 59 (2020) SGGK10.

## First Author Conference Contributions

(Award-winning poster) “The Electronic Structure of the Sn/Ge(001) Interface Studied by Angle-Resolved Photoelectron Spectroscopy and First-Principle Calculations”, Interdisciplinary Surface Science Conference (ISSC 2021), April 2021, Online

(Talk) “New Insights on the Electronic Structure of Ge(001) and the Modification upon Adsorption of Sn”, E-MRS Fall Meeting 2021, February 2021, Online

(Talk) “Investigation of the Surface Electronic Structure of Bulk ZnGa<sub>2</sub>O<sub>4</sub>”, SPIE Photonics West, March 2020, San Francisco, USA

(Talk) “The Electronic Band Structure of the Sn/Ge(001) Interface Studied by Angle-Resolved Photoelectron Spectroscopy”, 8th International Symposium on Control of Semiconductor Interfaces (ISCSI 2019), November 2019, Sendai, Japan

(Talk) “The Electronic Structure of the Sn/Ge(001) Heterointerface”, E-MRS Fall Meeting 2019, September 2019, Warsaw, Poland

(Talk) “Angle-Resolved Photoelectron Spectroscopy (ARPES) on Transparent Conducting Oxides (TCOs)”, GraFOx Summer School on Oxide Semiconductors for Smart Electronic Devices (2019), Menaggio, Italy

# Contents

<b>Acknowledgements</b>	<b>3</b>
<b>Abstract</b>	<b>5</b>
<b>Zusammenfassung</b>	<b>7</b>
<b>Scientific Visibility</b>	<b>9</b>
<b>1 Aim and Structure of this Thesis</b>	<b>13</b>
<b>2 The Electronic Band Structure of Crystals and Surfaces</b>	<b>15</b>
2.1 Nearly Free Electron Model . . . . .	15
2.2 Electronic States at the Crystal Surface . . . . .	17
<b>3 Photoelectron Spectroscopy</b>	<b>21</b>
3.1 Theoretical Description . . . . .	21
3.2 Experimental Setup for Photoelectron Spectroscopy . . . . .	28
3.3 Binding Energy Referencing and Energy Resolution . . . . .	31
3.4 Angle-Resolved Photoelectron Spectroscopy . . . . .	33
3.5 X-Ray Photoelectron Spectroscopy . . . . .	35
<b>4 Surface Structure Characterization</b>	<b>41</b>
4.1 Low-Energy Electron Diffraction . . . . .	41
4.2 Scanning Tunneling Microscopy . . . . .	45
<b>5 New Insights into the Electronic States of the Ge(001) Surface by Joint Angle-Resolved Photoelectron Spectroscopy and First-Principle Calculation Investigation</b>	<b>49</b>
<b>6 Modification of the Ge(001) Subsurface Electronic Structure after Adsorption of Sn</b>	<b>63</b>
<b>7 The electronic structure of <math>\epsilon</math>-Ga<sub>2</sub>O<sub>3</sub></b>	<b>79</b>
<b>8 Experimental and Theoretical Investigation of the Surface Electronic Structure of ZnGa<sub>2</sub>O<sub>4</sub>(100) Single-Crystals</b>	<b>89</b>
<b>Thesis Conclusion</b>	<b>104</b>
<b>References</b>	<b>107</b>



# Chapter 1

## Aim and Structure of this Thesis

Over several decades, photoemission techniques have established themselves as powerhouses in materials research and surface science, because they can directly probe the electronic structure at surfaces and interfaces. The aim of this thesis is to use photoemission techniques on material systems for advanced micro- and optoelectronics, leading to a deeper understanding of their electronic structure, which will help the ongoing research activities. The subjects of investigation in this thesis are:

- 1) the Ge(001) surface (**chapter 5**),
- 2) the Ge(001) surface after adsorption of Sn (**chapter 6**),
- 3) the surface of  $\epsilon$ -Ga<sub>2</sub>O<sub>3</sub> grown on (0001) sapphire (**chapter 7**) and
- 4) the ZnGa<sub>2</sub>O<sub>4</sub> (100) surface (**chapter 8**).

Before delving into the results, **chapter 2 - 4** will provide the necessary physical background to understand the results.

The concept of electronic bands will be reviewed in **chapter 2**. Based on the nearly free electron model, a description of electronic bands in a crystal and the effect of a surface onto the electronic states will be given.

**Chapter 3** is devoted to photoelectron spectroscopy. A general theoretical description based on the three-step model, followed by a description of the experimental setup at IHP, the binding energy referencing and the determination of the energy resolution will be given. Experimental considerations for angle-resolved and X-ray photoelectron spectroscopy will close this chapter.

In **chapter 4**, the basic knowledge to interpret low-energy electron diffraction and scanning tunneling microscopy data will be provided.

The electronic structure of the pristine Ge(001) surface will be investigated in **chapter 5**. First, an overview will summarize the controversy regarding the conducting/semi-conducting nature of the surface in the existing literature. Afterwards, the electronic structure probed by time- and temperature-dependent angle-resolved photoelectron spectroscopy will be explored; with the goal to eradicate the existing controversy in the literature and the experimental findings will be compared to first-principle calculations.

Modifications of the Ge(001) electronic structure after adsorption and incorporation of Sn will be investigated in **chapter 6**. The importance of such an investigation for the ongoing activities on the Ge-Sn material system will be outlined and the adsorption behavior of Sn on Ge(001) will

be referenced. The modifications of the electronic structure after adsorption of Sn at room temperature and post-growth annealing will be detailed, providing critical insights into the structural impact of Sn at the subsurface region and the Schottky barrier formation at the interface.

Following the investigation of the Ge(001) surface and the modification upon adsorption and incorporation of Sn, the next chapters will be devoted to the electronic structure of transparent semi-conducting oxides. In particular, I will focus on materials that may be alternative candidates to  $\beta$ -Ga<sub>2</sub>O<sub>3</sub> for future high-power electronics and deep-UV photonics.

A combined theoretical and experimental investigation of the electronic structure of  $\epsilon$ -Ga<sub>2</sub>O<sub>3</sub> is presented in **chapter 7**. An overview about the current status in the literature is followed by an investigation of the electronic structure with X-ray photoelectron spectroscopy, by comparing excitation energies of 1486.6 eV and 2984.3 eV. Using angle-resolved photoelectron spectroscopy, the dispersion of valence band states is probed and compared to *ab initio* calculations.

**Chapter 8** will detail the electronic structure of the ZnGa<sub>2</sub>O<sub>4</sub> (100) surface with a heavy emphasis on the surface preparation. To start this chapter, a literature overview about the research activities on ZnGa<sub>2</sub>O<sub>4</sub> will be given, finding that the surface preparation of ZnGa<sub>2</sub>O<sub>4</sub> crystals is elusive. Thus, I will explore *in-situ* preparation in ultra-high vacuum conditions and oxygen atmosphere. Since a near stoichiometric surface was prepared in oxygen atmosphere, the electronic structure of such surface will be investigated by X-ray photoelectron spectroscopy, followed by an investigation of the valence band structure. Finally, experimental results will be compared to density functional theory.

The final **chapter** of this thesis will give an overall conclusion and perspective of the work presented here.



## Chapter 2

# The Electronic Band Structure of Crystals and Surfaces

The electronic band structure is an important concept in solid-state physics to describe and understand fundamental electronic and optical properties of materials. The spatially close packing of atoms in a crystal results in an overlap of the discrete atomic energy levels and a continuous range of allowed energy levels forms the so-called electronic bands. Band gaps are ranges of energy that are not covered by the electronic bands.

Section 2.1 will describe the formation of bands and band gaps inside a crystal with a periodic potential. Section 2.2 will address the effect of a surface onto the electronic states. More in-depth theoretical descriptions of the electronic band structure can be found elsewhere [1, 2, 3].

### 2.1 Nearly Free Electron Model

The nearly free electron (NFE) model serves as a good approximation to understand the concept of electronic bands. A starting point for the quantum mechanical description of an electron in a crystal is the Schrödinger equation [1, 2]. For a single electron, the time-independent form reads

$$\left[ \frac{-\hbar^2}{2m_e} \frac{\delta^2}{\delta r^2} + U(\mathbf{r}) \right] \psi(\mathbf{r}) = E\psi(\mathbf{r}), \quad (2.1)$$

where  $\hbar$  is the reduced Planck's constant,  $m_e$  is the electron mass,  $\psi(\mathbf{r})$  is the wave function,  $\mathbf{r}$  is a spatial vector,  $E$  is the energy of the system and  $U(\mathbf{r})$  is the crystal potential. The exact form of  $U(\mathbf{r})$  is usually unknown, however, one can assume the same periodicity as the lattice [1, 2], so that

$$U(\mathbf{r}) = U(\mathbf{r} + \mathbf{r}_n). \quad (2.2)$$

$\mathbf{r}_n$  represents an arbitrary translation vector of the crystal lattice. According to the Bloch's theorem, the solution of equation (2.1) can be written as

$$\psi_{\mathbf{k}}(\mathbf{r}) = u_{\mathbf{k}}(\mathbf{r}) \cdot e^{i \cdot \mathbf{k} \cdot \mathbf{r}}. \quad (2.3)$$

These are the Bloch waves and  $\mathbf{k}$  is the wave vector, which also acts as an index to label the different solutions. The wave vector is required to be a real number, because an imaginary  $\mathbf{k}$  would not allow to normalize the wave function [1, 2]. This will become particularly important in section 2.2, when the surface is introduced.  $u_{\mathbf{k}}(\mathbf{r}) = u_{\mathbf{k}}(\mathbf{r} + \mathbf{r}_n)$  is the modulation function, which

has the same periodicity as the crystal lattice.

An important property of the Bloch waves is that

$$\psi_{\mathbf{k}}(\mathbf{r}) = \psi_{\mathbf{k}+\mathbf{G}}(\mathbf{r}). \quad (2.4)$$

Here,  $\mathbf{G}$  is the reciprocal lattice vector. With equation (2.1), the relation (2.4) implies that

$$E(\mathbf{k}) = E(\mathbf{k} + \mathbf{G}). \quad (2.5)$$

Therefore, the energy eigenvalues are a periodic function of the wave vectors  $\mathbf{k}$  [1, 2].

Figure 2.1 a) illustrates the concept of electronic bands for a vanishing small periodic potential  $U(\mathbf{r})$ . The band structure becomes a mere free electron parabola with

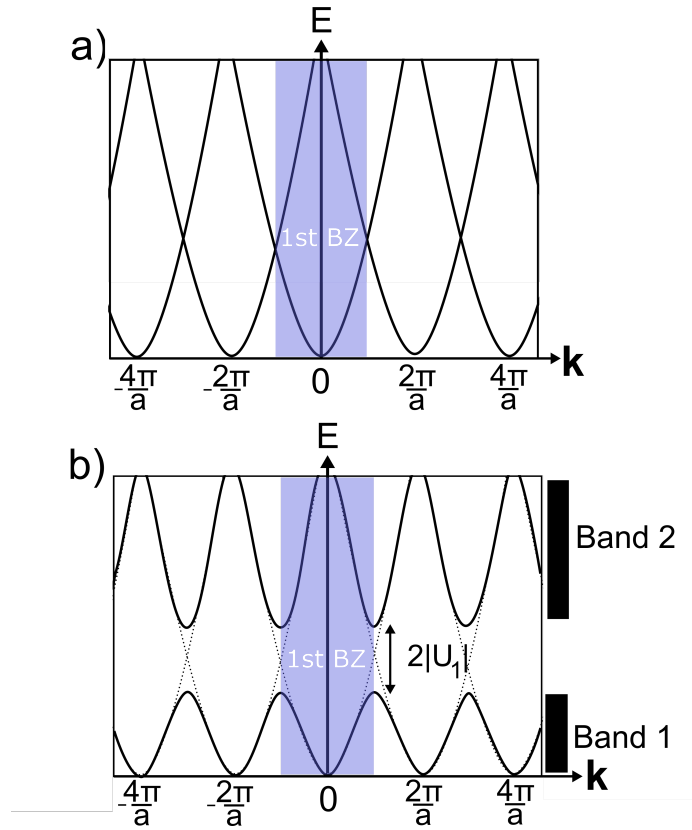


**Figure 2.1:** a) Electronic band structure of a nearly free electron in a periodic crystal with a vanishing small crystal potential  $U(\mathbf{r})$ . The first Brillouin zone (1st BZ) is indicated. b) Electronic band structure of a nearly free electron in a periodic after increasing the crystal potential to a finite value. Gaps open at the zone boundary of the first Brillouin zone and the magnitude of the gap is equal to two times the first coefficient  $U_1$  of the Fourier series that describes  $U(\mathbf{r})$ . After ref. [2].

$$E(\mathbf{k}) = \left[ \frac{\hbar \cdot |\mathbf{k}|^2}{2m_e} \right], \quad (2.6)$$

centered around  $\mathbf{k} = 0$ . To fulfil the requirement of periodicity in (2.5), the parabola is repeated every  $\frac{2\pi}{a}$ , i.e. the one-dimensional periodicity of the reciprocal lattice vector  $\mathbf{G}$ . As a result, it is generally sufficient to restrict the treatment of wave functions and energies to the first Brillouin zone, since both are periodic with  $\mathbf{G}$  [1, 2]. The band structure shown in Figure 2.1 a) changes its

appearance if  $U(\mathbf{r})$  increases from near 0 to a finite value. The crystal potential can be described by the Fourier series

$$U(\mathbf{r}) = \sum_{\mathbf{G}} U_{\mathbf{G}} \cdot e^{i \cdot \mathbf{k} \cdot \mathbf{r}}, \quad (2.7)$$

with the Fourier coefficient  $U_{\mathbf{G}}$ . If the first coefficient is non-zero, band gaps will open at the degeneracies of the zone boundary at  $\pm \frac{\pi}{a}$ , and the magnitude of the gap is two times the first coefficient of (2.7), i.e.  $2|U_1|$  [1, 2]. The band gap opening is illustrated in Figure 2.1 b). If the potential is further increased, also the second coefficient  $U_2$  is non-zero and another gap will open at the degeneracy of  $\mathbf{k} = 0$ . A more detailed description of the opening of gaps will be provided when the surface electronic states are discussed.

Overall, the NFE model provides an intuitive understanding of electronic bands and opening of gaps, which can be used to qualitatively describe electrical and optical properties of metals and semiconductors. Furthermore, the opening of gaps presents an important condition for the presence of surface states.

## 2.2 Electronic States at the Crystal Surface

The eigenstates inside a crystal were described in section 2.1 by Bloch waves that stretch infinitely in all directions, given an infinite crystal of perfect periodicity. Clearly, this cannot be the case anymore at the surface, where the crystal periodicity is broken.

To understand the influence of a surface on the bulk electronic states, a good starting point is to assume a free electron and two semi-infinite spaces, as illustrated in Figure 2.2: the bulk crystal ( $0 \leq z < \infty$ ) and the vacuum ( $-\infty < z < 0$ ), separated by a step-like potential  $U_0$  at the surface  $z = 0$  [1]. The electron resides in the bulk and can be described by a one-dimensional, time-independent Schrödinger equation

$$\left[ -\frac{\hbar^2}{2m_e} \frac{\delta^2}{\delta z^2} + U(z) \right] \psi_i(z) = E \psi_i(z). \quad (2.8)$$

The wave function solving the Schrödinger equation can be written as a superposition of left- and

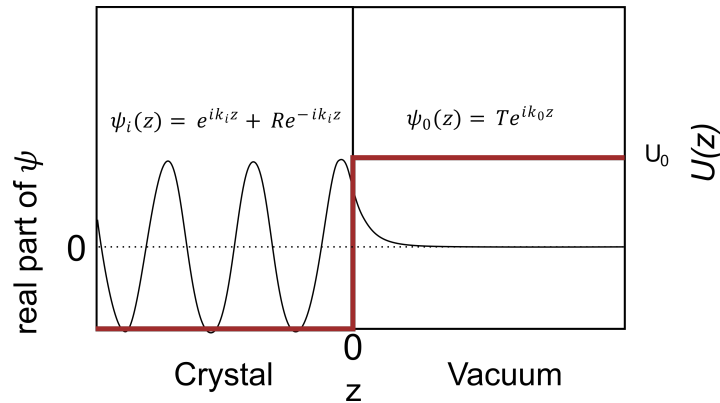


**Figure 2.2:** Illustration of a free electron wave function in a semi-infinite crystal. Vacuum and crystal are separated by a step-like potential of magnitude  $U_0$ . Inside the crystal, the electron is characterized by a left- and right-going plane wave  $\psi_i(z)$  with a real wave vector. In vacuum, it is described by the decaying wave function  $\psi_0(z)$  with an imaginary wave vector. Both wave functions are matched at the boundary  $z = 0$ , i. e. the surface. After ref. [1].

right-going plane wave [1]

$$\psi_i(z) = e^{i \cdot k_i \cdot z} + R \cdot e^{-i \cdot k_i \cdot z} \quad (2.9)$$

with

$$k_i = \sqrt{\frac{2m_e \cdot E}{\hbar^2}}, \quad (2.10)$$

which is, a real number. On the right-hand side in Figure 2.2, the wave function is written as

$$\psi_0(z) = T \cdot e^{i \cdot k_0 \cdot z} \quad (2.11)$$

with

$$k_0 = \sqrt{\frac{2m_e(E - U_0)}{\hbar^2}}, \quad (2.12)$$

which is an imaginary number ( $E < U_0$ ). The next step is to match the solutions at the boundary, such that their value and first-derivative are equal for  $z = 0$  [1, 3]. In principle, it can always be done by adjusting  $R$  and  $T$  and the result is a plane wave inside the crystal with tail outside the crystal [1].

After treating bulk states in the free electron model, the next step is to formulate the problem for the actual Bloch waves. The translation symmetry is broken in perpendicular direction ( $k_z$  or  $k_\perp$ ), while it is conserved parallel to the surface ( $k_\parallel$ ) and thus, the Bloch waves become two-dimensional [1, 3]. In perpendicular direction, the situation is comparable to the free electron: The Bloch wave is a plane wave that needs to be matched with a wave function decaying into vacuum, as shown in Figure 2.3. Notably, this features an imaginary wave vector on the vacuum

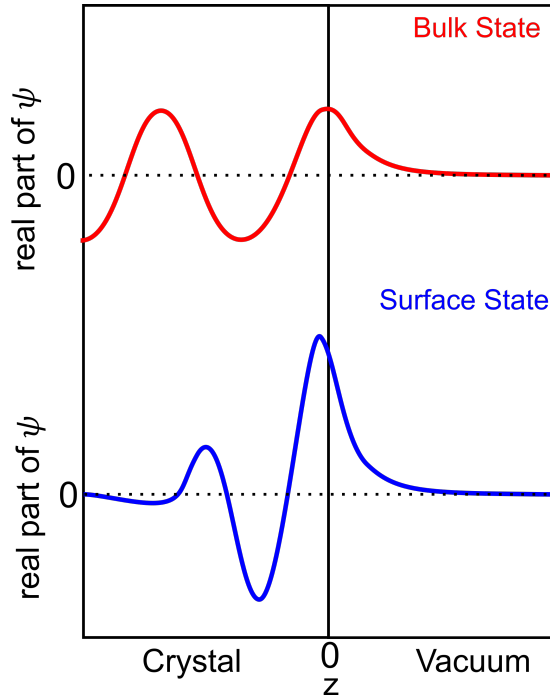


**Figure 2.3:** Illustration of bulk and surface electronic states in a crystal. In both cases, the wave function decays exponentially into the vacuum. The wave function of the surface state also decays into the crystal. After ref. [1].

side. For the infinite crystal, an imaginary wave vector needs to be discarded as unphysical, since the wave function (2.9) diverges when  $z \rightarrow \infty$ . However, in case of the semi-infinite crystal an imaginary wave vector becomes physical meaningful (equation (2.11)). Therefore, an interesting

consequence of the surface seems to be that solutions of the Schrödinger equation are no more restricted to a real wave vector. In fact, it is possible to obtain solutions that decay not only in vacuum, but also inside the crystal (Figure 2.3) [1, 3]. In describing the problem, one starts with a non-constant lattice periodic function with only two Fourier components  $+g$  and  $-g$  ( $g$  being the one-dimensional reciprocal vector) [1]. Inserting into (2.8) gives

$$\left[ -\frac{\hbar^2}{2m_e} \frac{\delta^2}{\delta z^2} + U(e^{i \cdot g \cdot z} + e^{-i \cdot g \cdot z}) \right] \psi_i(z) = E\psi_i(z) \quad (2.13)$$

and the solution is a Bloch wave

$$\psi_k(z) = \sum_g c_{k-g}(r) \cdot e^{i \cdot (k-g) \cdot z}. \quad (2.14)$$

The next step is to construct a trial wave function of in- and out-going wave in similar fashion as for the free electron (equation (2.9)). The region of interest is close to the Brillouin zone boundaries ( $\pm \frac{\pi}{a}$ ) and with  $k - g \approx -\frac{\pi}{a}$  one obtains

$$\psi(z) = I \cdot e^{i \cdot k \cdot z} + R \cdot e^{-i \cdot (k-g) \cdot z} \quad (2.15)$$

for the wave function. Inserting into (2.8), followed by some additional calculations and  $k = \frac{g}{2}$  one obtains [1]

$$E = \frac{\hbar^2}{2m_e} \frac{g^2}{2} \pm U. \quad (2.16)$$

Equation (2.16) explains the band gap opening at the Brillouin zone boundaries. One can see that the first term is just the free electron dispersion, while the second term opens the gap, with a total width of  $|2U|$  [1]. This is the setup for the description of surface states and the next step is to formulate the actual wave functions. Inserting (2.15) into (2.8) again (this time without  $k = \frac{g}{2}$ ) one obtains

$$E = \frac{\hbar^2}{2m_e} \left( \frac{g^2}{2} + q^2 \pm \sqrt{g^2 q^2 + V^2} \right) \quad (2.17)$$

for the energy dispersion, with the two abbreviations  $q = \frac{k-g}{2}$  and  $V = \frac{2m_e}{\hbar^2} \cdot U$ . Introducing the complex wave vector  $q = q' + iq''$ , the question is, if there is a solution to the Schrödinger equation that leads to real energy eigenvalues (equation (2.17)). With the wave function

$$\psi_i(z) = e^{-q'' \cdot z} \left( I \cdot e^{-i(q' + \frac{g}{2})z} + R \cdot e^{-i(q' - \frac{g}{2})z} \right) \quad (2.18)$$

such solutions can be obtained for  $q = 0 + iq''$  and as long as the square root in (2.17) remains positive (i.e.  $V^2 > g^2 q^2$ ) [1]. The wave function decays into the Bulk for  $z \rightarrow \infty$ , as required, but still diverges for  $z \rightarrow -\infty$ . Therefore, it needs to be matched with a wave function like (2.11), which decays into the vacuum. This can be done for at least one value of  $q''$  by adjusting the complex amplitudes  $I$  and  $R$  and the result is shown in Figure 2.3 [1]. Thus, it is possible to find “new” electronic states at a crystal surface that exist in the forbidden gaps and are named surface states. When the valence band structure of a material is probed by ARPES, it will be important to identify and distinguish the respective states in order to understand the fundamental electronic structure. The details of this will be explained in the following chapter 3.



## Chapter 3

# Photoelectron Spectroscopy

Photoelectron spectroscopy (PES) is a collective term for techniques that can directly probe the occupied electronic states of a material, and thus, will be the main characterization techniques in this thesis. This chapter will provide the most important fundamentals to the reader, which is referred to ref. [3] for a more detailed description.

Section 3.1 will focus on the theoretical fundamentals. Section 3.2 tackles the experimental setup, with the general requirements and the specifications at IHP. Section 3.3 will target the binding energy referencing and the energy resolution, while section 3.4 provides some additional details on angle-resolved photoelectron spectroscopy (ARPES). In the final section 3.5, I will explain the most important aspects of X-ray photoelectron spectroscopy (XPS).

### 3.1 Theoretical Description

PES utilizes the photoelectric effect to probe the electronic structure of solids. A sample is irradiated with photons and the kinetic energy  $E_{kin}$  of photoelectrons, that have been ejected from the sample, are measured. Using the fundamental energy conservation law of the photoemission process [3]

$$E_{kin} = h\nu - \Phi_s - E_{bin}, \quad (3.1)$$

where  $h\nu$  is the photon energy and  $\Phi_s$  is the sample work function, one can then obtain the binding energy  $E_{bin}$  that the electron had in its initial state. Equation (3.1) means that not any light will suffice: The energy of an incoming photon has to be high enough for the electrons to overcome an additional energy barrier (work function  $\Phi_s$ ) before they can leave the sample. After the electrons have left the sample, they are counted by an analyzer system (more details in section 3.2), which gives rise to a spectroscopic signal of the form  $I(E_{kin})$ . The situation is illustrated in Figure 3.1: In the initial state picture, electrons fill up energy levels with a certain binding energy and density of states (DOS). One may now expect a proportional intensity distribution of sharp lines for the core-level electrons and overlapping bands for the valence band structure in PES (“ideal” PES spectrum) [1]

$$I(E_{kin}) = DOS(h\nu - \Phi_s - E_{bin}). \quad (3.2)$$

However, the real spectrum is much more complicated as shown on the right-hand side of Figure 3.1 (“real” PES spectrum). The graph shows the XPS signal of a Ge(001) sample and the spectrum not only exhibits lines for the core-level electrons, but also lines that originate from initial and final state effects. A large, step-like background (BG) is visible, caused by electrons that have

been inelastically scattered. Additionally, the ‘‘DOS-assumption’’ fails to explain the dependence of the photoemission intensity on the photon energy. To describe the underlying fundamentals

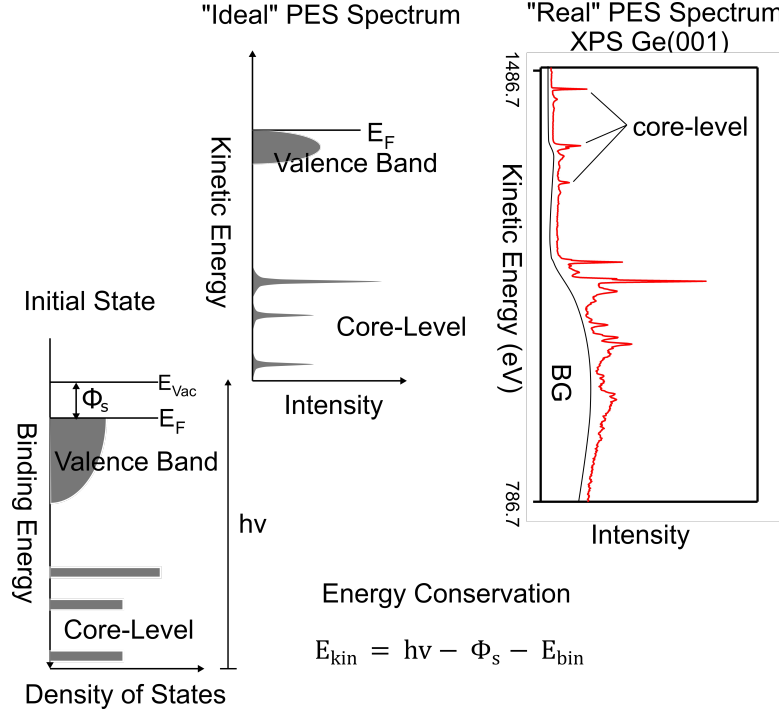


**Figure 3.1:** Schematic representation of the energy conservation in the photoemission process. In the initial state, electrons have energy levels given by their respective binding energies and occupied according to the density of states. Core-levels are discrete energy levels, while the valence band is more like a sea of bands. In the ‘‘ideal’’ image of the photoemission spectra, the photoemission intensity correlates directly to the density of states, with sharp peaks corresponding to the core-level peaks and an energy-broad feature corresponding to the valence states. In reality, the spectra are much more complex due to the many body processes involved, as can be seen in the XPS spectrum of a Ge(001) sample. The spectrum shows additional peaks that are not denoted as core-levels and a step like background (BG) is visible. After ref. [3].

of the photoemission process, the three-step model shown in Figure 3.2 is widely used [1, 3, 4]. In the first step of this model, the photon excites an electron from its initial state into the final state. Second, the photoelectron travels through the crystal to the surface, where it escapes from the crystal in the third and final step. This approach of describing the photoemission process is somewhat artificial, as, in reality, the process is actually more of a one-step process. Nevertheless, the phenomenological approach has proven to be accurate enough and serves up to date as a convenient, qualitative description of the process. I will now explain in the following how these individual steps contribute to the final intensity observed in the PES spectrum.

### Step 1: Excitation of the Photoelectron

The first parameter that changes the measured photoemission intensity from the expected DOS is the photoionization cross-section, i.e. the probability of an electron to be excited by a photon. Starting with Fermi’s golden rule, the transition probability between initial  $\psi_i$  and final  $\psi_f$  state (Bloch waves) is given by [3]

$$w_{f,i} \propto |\langle \psi_f | \mathbf{H}' | \psi_i \rangle|^2 \delta(E_f - E_i - hv). \quad (3.3)$$

The delta function  $\delta(E_f - E_i - hv)$  ensures the energy conservation inside the crystal, i.e. the final state energy of the photoelectron  $E_f$  must be higher than the initial state energy  $E_i$ .  $\langle \psi_f | \mathbf{H}' | \psi_i \rangle$  is the transition matrix element that represents an overlap integral of the form  $\int \psi_f(\mathbf{r}) \mathbf{H}'(\mathbf{r}) \psi_i(\mathbf{r}) d\mathbf{r}$ .



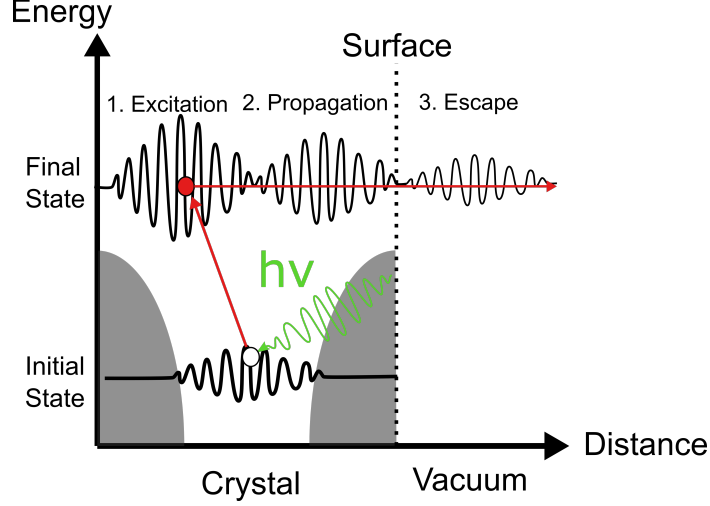


**Figure 3.2:** Schematic of the three-step model describing the photoemission process. The first step is the excitation of the electron from the initial state into the final state. In the second step, the electron propagates through the crystal before escaping from the crystal in the third and final step. After ref. [3].

The operator  $\mathbf{H}'$  describes the irradiation with light as a small perturbation. Thus, the momentum operator  $\mathbf{p}$  in the Hamiltonian of an unperturbed system  $\mathbf{H}_0$  is replaced by  $\mathbf{p} - e\mathbf{A}$ , where  $\mathbf{A}$  is the vector potential of the photon field and  $e$  is the electron charge. One then obtains for the interaction operator

$$\mathbf{H}' = \frac{e}{2m_e \cdot c} (\mathbf{A} \cdot \mathbf{p} + \mathbf{p} \cdot \mathbf{A}) - e\varphi + \frac{e^2}{2m_e} (\mathbf{A} \cdot \mathbf{A}), \quad (3.4)$$

where  $\varphi$  is the scalar potential and  $c$  is the constant of light. For weak radiation fields (typically the case, except for laser sources) the last two terms can be removed. With  $\mathbf{p} = i\hbar\nabla$ , equation (3.4) gives

$$\mathbf{H}' = \frac{e}{2m_e \cdot c} (2 \cdot \mathbf{A} \cdot \mathbf{p} + i\hbar(\nabla\mathbf{A})) = \frac{e}{2m_e \cdot c} \mathbf{A} \cdot \mathbf{p} \quad (3.5)$$

which is referred to as the dipole approximation, because  $\mathbf{A}$  is assumed to be constant (i.e. the wavelength is large compared to the atomic dimensions) and thus,  $\nabla\mathbf{A} = 0$  [1, 3, 4]. The transition probability can be written as

$$w_{f,i} \propto |\langle \psi_f | \mathbf{A} \cdot \mathbf{p} | \psi_i \rangle|^2 \delta(E_f - E_i - hv). \quad (3.6)$$

For the experiment, this means that the transition matrix element  $\langle \psi_f | \mathbf{A} \cdot \mathbf{p} | \psi_i \rangle$  causes the photoemission intensity to change with excitation energy, which can then result in photoemission intensities that do not reflect the DOS. As an example, one can consider the case of a harmonic oscillator (although a  $\frac{1}{r}$  potential is shown) illustrated in Figure 3.3 [3]: A low-energy initial state will only have low momentum dependence. According to the transition matrix element, the overlap between initial and final state is now calculated by applying the momentum operator  $\mathbf{p}$  on the initial state wave. The overlap will be largest if the final state has also a low momentum dependence, which means that the excitation energy has to be low. Vice versa, high energy initial states with large momentum dependence will have a high transition probability with increasing excitation energy. In fact, this is the reason why it is much easier to detect oxygen contamination compared to carbon contamination when probing the respective 1s core-level with XPS (assuming the same quantity is present) [1]. The higher binding energies in O (atomic number 8,  $\approx 530$  eV binding energy) compared to C (atomic number 6,  $\approx 285$  eV binding energy) mean that the final

state energy is lower in O than in C, when the same excitation energy is used. This means lower momentum dependence of the O 1s final state compared to the C 1s final state, resulting in a larger matrix element for oxygen.

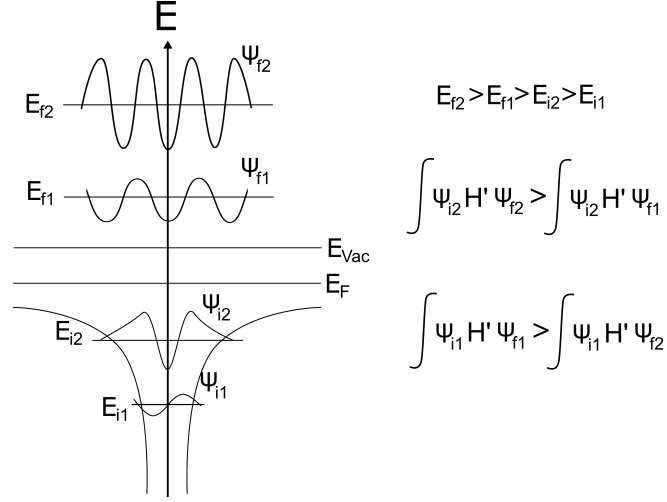


**Figure 3.3:** Comparison of the transition matrix element between different initial and final state energies. A high-energy final state  $\psi_{f2}$  has a large momentum dependence, leading to rapid oscillation. The low-energy final state  $\psi_{f1}$  has lower momentum dependence and slower oscillation. If the initial state  $\psi_{i2}$  is excited into the high-energy final state  $\psi_{f2}$ , the overlap will be larger compared to excitation in the low-energy final state  $\psi_{f1}$ . Thus, a high-energy initial state "prefers" a high-energy excitation energy. Vice versa, the low-energy initial state  $\psi_{i1}$  has a larger overlap with a low-energy final state  $\psi_{f1}$  compared to a high-energy final state  $\psi_{f2}$ , thus "preferring" low excitation energies. After ref. [3].

## Step 2: Propagation to the Surface

Upon reaching a final state, the electron is free to move through the solid and eventually reach the surface. On its path to the surface, an electron will see an ocean of charges and potentials; hence, some electrons will undergo inelastic scattering contributing to the PES spectra as the background signal observed in Figure 3.1. The question is now: how long is the average distance (the so-called inelastic mean free path (IMFP)  $\lambda$ ) that an electron can travel without losing the carried information [3]?

An experimental approach to obtain the value of the IMFP is the over layer method: A substrate photoemission signal is probed as the function of an increasing over layer thickness. As the over layer thickness increases, the inelastic scattering of photoelectrons from the substrate enhances and the photoemission signal decays at an exponential rate, given by [5]

$$I(L) = I_0 e^{-\frac{L}{\lambda(E) \cdot \cos(\alpha)}}. \quad (3.7)$$

Here,  $L$  is the overlayer thickness,  $I_0$  is the intensity without damping. Following this method, many experimentally values have been reported for classes of materials. Seah and Dench [6] derived the relation

$$\lambda = \frac{A}{E_{kin}^2} + B \sqrt{E_{kin}} \quad (3.8)$$

from the experimentally reported values. The fitting parameters  $A$  and  $B$  are material parameters. Figure 3.4 shows the IMFP as a function of the electron kinetic energy according to equation (3.8) and using the fitting parameters for elements and inorganic compounds. The qualitative behavior is the same: at low kinetic energies, the IMFP is large, reaching a minimum in the region of 20 eV – 80 eV. Typical laboratory ARPES and UPS experiments employ He I (21.2 eV) and He II (40.8

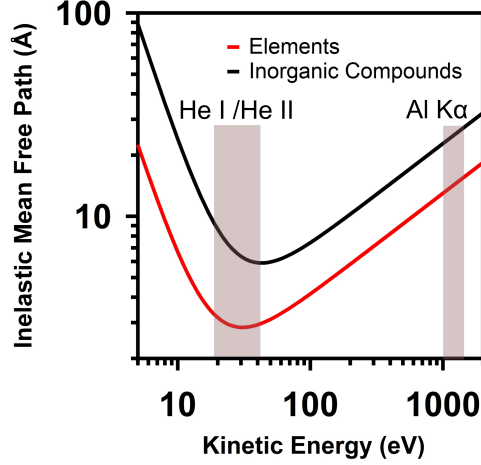


**Figure 3.4:** Inelastic mean free path (IMFP) as a function of kinetic energy for elements (red) and inorganic compounds (black). The curves represent fits after Seah and Dench [6]. A minimum is reached between 20 eV and 80 eV of electron kinetic energy. The marked areas indicate the expected maximum IMFP for excitation energies used in this work (He I, He II and Al K $\alpha$ ).

eV) excitation energies, meaning they usually provide the maximum surface sensitivity. The IMFP for these energies ranges from 3 Å - 10 Å. With increasing energy, the IMFP becomes larger. For example, XPS experiments employing Al K $\alpha$  (1486.7 eV) will have an IMFP ranging from 15 Å - 30 Å.

A more theoretical approach to determine the IMFP was reported by Tanuma et al. with the TPP-2M formalism [7]:

$$\lambda_{TPP-2M}(E_{kin}) = \frac{E_{kin}}{E_P^2 \left[ \beta \cdot \ln(\gamma E_{kin}) - \frac{c}{E_{kin}} + \frac{D}{E_{kin}^2} \right]}, \quad (3.9)$$

with the parameters being

$$\beta = -0.1 + \frac{0.944}{(E_P^2 + E_G^2)^2} + 0.069\rho^{0.1}, \quad (3.9a)$$

$$\gamma = 0.191\rho^{-0.5}, \quad (3.9b)$$

$$C = 1.97 - 0.91 \cdot U, \quad (3.9c)$$

$$D = 53.4 - 20.8 \cdot U, \quad (3.9 d)$$

and

$$U = \frac{N_{VB}}{M}. \quad (3.9 e)$$

Here,  $E_P$  is the plasmon energy,  $E_G$  is the band gap,  $M$  is the molecular weight,  $N_{VB}$  is the number of valence electrons. Inserting these values will then allow to calculate the IMFP for energies between 50 eV and 2000 eV.

While the IMFP is the reason that one is limited to the very surface of a sample with PES it also has useful implications. For example, the information depth corresponds to [5, 8]

$$d = 3 \cdot \lambda \cdot \cos(\alpha), \quad (3.10)$$

in which  $\alpha$  is the emission angle with respect to the surface normal. Rotating a sample by 60° will decrease the information depth by 50 %, drastically enhancing the surface sensitivity. This can

allow for a non-destructive depth profiling, enabling the investigation of depth-depended changes in the chemical composition and/or the presence/absence of a band bending in a sample.

The IMFP is one of the factors that sets the need for ultra-high vacuum conditions in the PES experiment. Particles and molecules in the chamber will eventually lead to inelastic scattering of the electron on its way to the analyzer and information about the initial state will be lost. Additionally, adsorbates may deposit on the surface, changing the IMFP and also the chemical environment. The rate of impinging molecules on the sample surface is given by [1]

$$R = \frac{P}{\sqrt{2\pi M k_B T}}, \quad (3.11)$$

where  $P$  is the chamber pressure,  $M$  is the molecule mass,  $k_B$  is the Boltzmann constant and  $T$  is the temperature. At room temperature and a pressure of  $10^{-6}$  mbar (high-vacuum) the impinging rate of oxygen is  $2.7 \cdot 10^{14} \text{ cm}^{-2} \text{ s}^{-1}$  [1]. Considering a typical atomic density of  $10^{15} \text{ cm}^{-2}$  at a surface, the entire surface is covered by a monolayer of rest gas molecules within seconds. The detection limit of PES experiments is typically given as 0.01 ML and experiments may take at least one hour. Thus, if the coverage of rest gas contamination has to stay below 1 % for several hours, the pressure needs to be in the order of  $10^{-9} - 10^{-10}$  mbar.

### Step 3: Escape from the Surface

The last step of the photoemission process is the escape of the electron from the surface. Figure 3.5

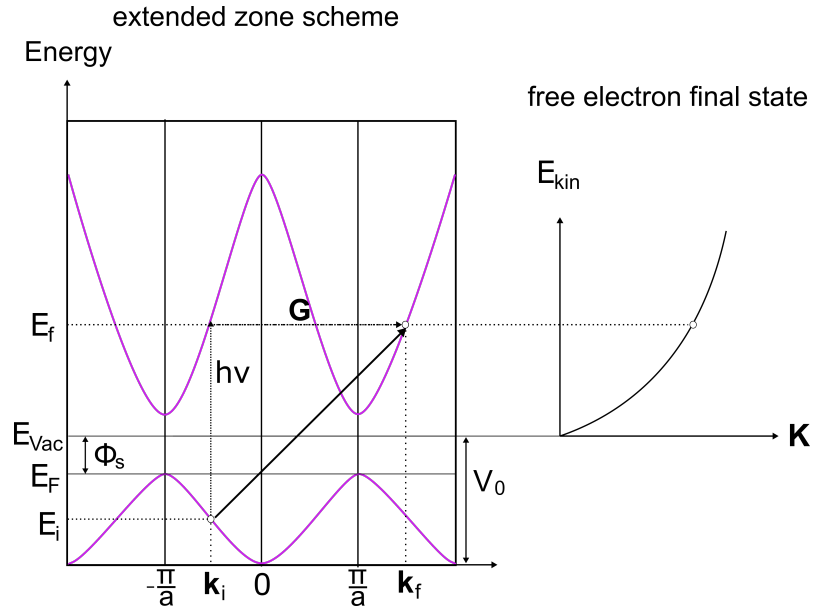


**Figure 3.5:** Kinematics of the photoemission process in the extended zone scheme of a periodic potential. Energy and momentum conservation between the initial and final state inside the periodic potential are indicated arrows. The final state energy dispersion  $E_f(\mathbf{k}_f)$  inside the crystal can be approximated by a free electron parabola outside the crystal  $E_{kin}(\mathbf{K})$ . After ref. [9].

illustrates the kinematics of the photoemission process from a periodic potential in the extended zone scheme. Energy conservation requires that the final state energy inside the crystal is higher than the initial state energy [3]. Furthermore, it is assumed that the final state energy dispersion inside the crystal  $E_f(\mathbf{k}_f)$  can be approximated by a free electron parabola  $E_{kin}(\mathbf{K})$  outside the crystal [3, 9]. Note that the wave vectors  $\mathbf{k}$  are just measures for the electron momentum, which is given by  $\mathbf{p} = \hbar\mathbf{k}$ . Figure 3.5 indicates that the electron requires momentum in order to transition from initial to final state. The difference between initial state momentum  $\mathbf{k}_i$  and final

state momentum  $\mathbf{k}_f$  is provided by the crystal lattice ( $\mathbf{G}$  is the reciprocal lattice vector). The conservation of electron momentum inside the crystal is then

$$\mathbf{k}_f = \mathbf{k}_i + \mathbf{G}, \quad (3.12)$$

and the reason why photoemission cannot take place in a constant potential. The general kine-

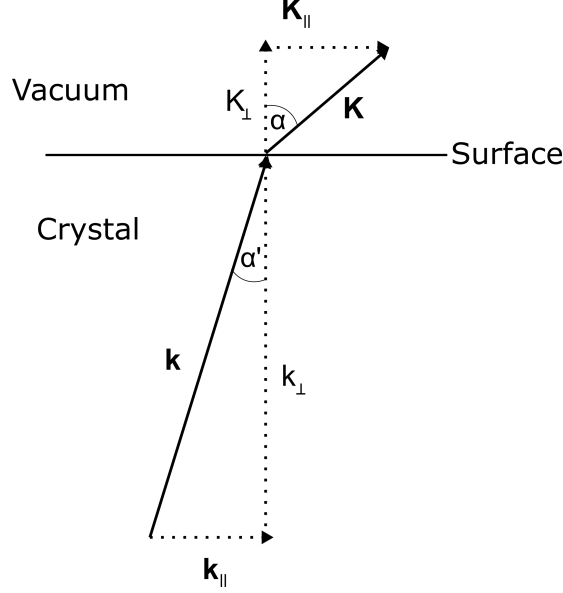


**Figure 3.6:** Illustration of the  $k$ -conservation of a photoelectron leaving the crystal. Only the  $k$ -component parallel to the surface is conserved. After ref. [3].

matics in Figure 3.5 demand

$$E_f(\mathbf{k}_f) = E_{kin}(\mathbf{K}) + V_0, \quad (3.13)$$

where,  $V_0$  is the inner potential of a material. The momentum conservation inside the crystal can be simplified by the using the reduced zone scheme (backfolding into the first Brillouin zone)

$$\mathbf{k} = \mathbf{k}_f = \mathbf{k}_i, \quad (3.14)$$

Using the free electron parabola approximation equation (3.13) becomes

$$E_{kin}(\mathbf{K}) = \frac{\hbar^2 \mathbf{K}^2}{2m_e} - V_0 = \frac{\hbar^2 \mathbf{k}^2}{2m_e} - V_0. \quad (3.15)$$

At the surface the periodic potential ends, resulting in a potential step from crystal to vacuum (section 2.2). The electron leaving the solid will then be elastically scattered and diffracted, meaning that it will change trajectory, as illustrated in Figure 3.6. The result is conservation of the  $k$ -component parallel to the surface but not of the  $k$ -component perpendicular to the surface. Using momentum conservation and the geometry of Figure 3.6 [1, 3, 4], equation (3.15) changes into

$$K_{\parallel} = k_{\parallel} = \sqrt{\frac{2m_e}{\hbar^2} E_{kin} \sin(\alpha)} \quad (3.16)$$

and

$$k_{\perp} = \sqrt{\frac{2m_e}{\hbar^2} (E_{kin} \cos^2(\alpha) + V_0)}. \quad (3.17)$$

In ARPES experiments, this means that one can measure the intensity as a function of the kinetic energy and emission angle to obtain an energy dispersion related to  $\mathbf{k}_{\parallel}$ . The perpendicular component  $\mathbf{k}_{\perp}$  requires knowledge about the inner potential  $V_0$  and a more sophisticated setup, e.g. tunable light sources, which is usually the case only at synchrotron facilities. In general, this will mean that laboratory setups are limited to the study of  $E(\mathbf{k}_{\parallel})$ .

### 3.2 Experimental Setup for Photoelectron Spectroscopy

At IHP, the PES setup is part of a larger surface science cluster, shown in Figure 3.7. The system operates under ultra-high vacuum (UHV) conditions at a base pressure between  $8 \cdot 10^{-11}$  mbar to  $5 \cdot 10^{-10}$  mbar. Samples are loaded into the load lock and can be sputtered and annealed in the preparation chamber I. Annealing can be done by focusing an electron beam on the backside or by resistive heating. Preparation chamber II is directly connected with preparation chamber I and contains a low-energy electron diffraction system (ErLEED 150) as well as MBE sources for the growth of Ge and Sn. Adjacent chambers to preparation chamber II are the CVD chamber, optimized for the growth of graphene, and the analysis chambers for scanning tunneling microscopy (STM) or PES. For details on ultra-high vacuum systems, the reader is referred to ref. [1]. Details on a general PES spectrometer design and the functionality of individual components can be found in ref. [8].

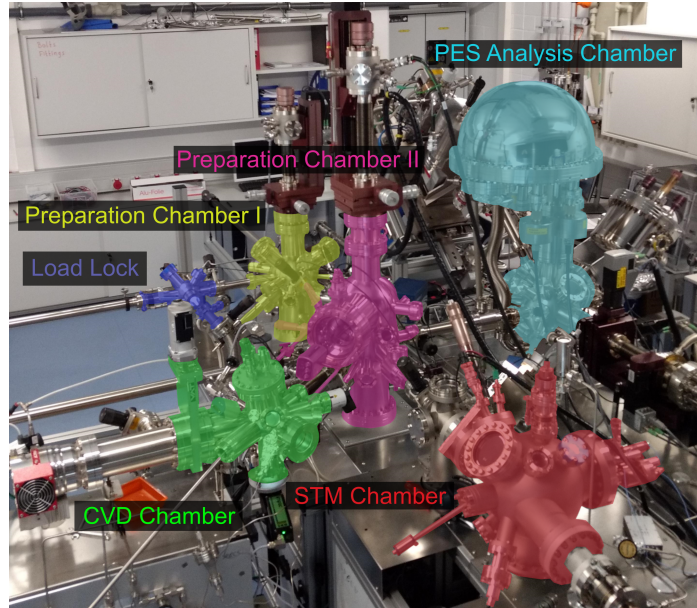


**Figure 3.7:** The surface science cluster at IHP. Samples can be introduced into the system via the load lock. Surface preparation like degas, sputtering and annealing can be done in preparation chamber I. Preparation chamber II features MBE sources for the growth of Ge and Sn, as well as a LEED optics. Adjacent to preparation chamber II are the CVD chamber for the growth of graphene and the two analysis chambers for sample characterization by STM and PES.

Two photon sources are attached to the analysis chamber. These photon sources have additional monochromators that narrow the energy range. This is achieved by focusing the beam and removing other characteristic lines, as well as the braking radiation background. The result is a better energy resolution and the removal of satellite peaks in the spectra at the expense of intensity by a few orders of magnitude. The available photon sources at the surface science cluster for XPS are monochromated Al  $K\alpha$  (1486.7 eV) and monochromated Ag  $L\alpha$  (2986.4 eV). A dual anode

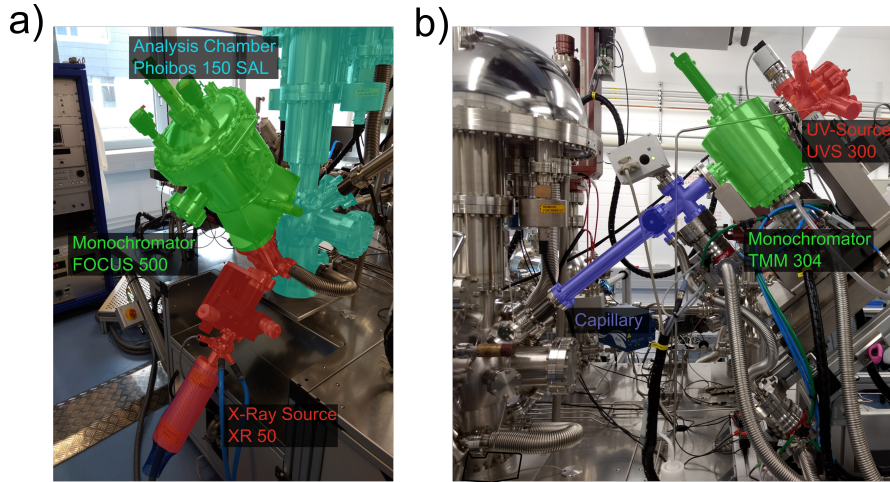


**Figure 3.8:** *a) Components for the generation of monochromated X-rays. The X-ray source (XR 50) operates with a dual anode, that allows the emission of Al  $K\alpha$  (1486.7 eV) and Ag  $L\alpha$  (2986.4 eV). Passing through the FOCUS 500, the X-rays are monochromated before reaching the chamber, improving the energy resolution. b) Components for the generation of He I (21.2) and He II (40.8) UV-radiation. The He discharge lamp UVS 300 generates a He plasma. Photons generated by the He-plasma have to pass the TMM 304 monochromator, selecting between the He I and He II lines. The capillary guides the photons into the analysis chamber.*

X-ray source (XR 50) produces the X-ray beams (Figure 3.8 a)). Before reaching the chamber, the X-ray beams pass the monochromator FOCUS 500. The mirror plate of the FOCUS 500 is made of a Quartz (1010) crystal and can be adjusted for each of the two excitation energies to fulfil Bragg's law, resulting in monochromated radiation. The irradiated area is  $3.5 \times 1 \text{ mm}^2$  on the sample, but the focus mode of the anode allows to narrow the probed area down to  $3.5 \times 0.2 \text{ mm}^2$ . This is achieved by focusing the electron beam with electron lenses onto a smaller area on the anode. Additionally, the focus mode improves the energy resolution by about 0.1 eV. For UPS and ARPES experiments, photons are generated in a He discharge lamp UVS 300, shown in Figure 3.8 b). The UV light emitted by the He plasma is transmitted into the chamber of the monochromator (TMM 304) comprising a plane grating and a toroidal mirror. Incoming light is dispersed by the grating before being focused with the mirror. Two cassettes are used, each with an optimized set of grating and mirror for the energies of He I (21.2 eV) and He II (40.8 eV). The monochromated light passes into the analysis chamber through a capillary, with a spot size of 0.7 mm in diameter to reach the sample surface.

Irradiation of the sample leads to emission of photoelectrons in all directions from the surface. An electron lens apparatus collects the photoelectrons before being passed into the energy filter, that is, the hemispherical analyzer. Furthermore, different lens modes allow to separate and focus the incoming photoelectrons by their lateral origin (area modes) or emission angle  $\alpha$  (angle modes). Area modes are high-transmission modes, optimized for large spot sizes by maximizing the integral of acceptance area over the illuminated spot, resulting in high counts per second (CPS). Generally, the medium area mode (MA) is used for XPS experiments featuring a monochromated source. The acceptance area is not limited by the lens, but rather by the irradiated area of the source, usually smaller than the sample [10]. The angular acceptance for this mode is  $\pm 8^\circ$ . For ARPES and UPS experiments so called angular modes are used to collect electrons within the angular acceptance. Instead of mapping the lateral distribution, the emission angle distribution is imaged. Together with a 2D-CCD detector, this allows for quick mapping of the valence band structure and Fermi surfaces. The wide-angle mode (WAM) allows to simultaneously image an emission angle

distribution of  $\pm 14^\circ$ .

Followed by the electron lens, the hemispherical electron analyzer will separate the collected electrons by their kinetic energy, acting as the energy filter of the system. The working principle of the analyzer is illustrated in Figure 3.9. The analyzer has an energy dispersive plane (blue) and a non-energy dispersive plane (red to green). An entrance slit is the first stage of the energy filter. A smaller slit will improve the energy resolution, however, less electrons will pass into the filter,

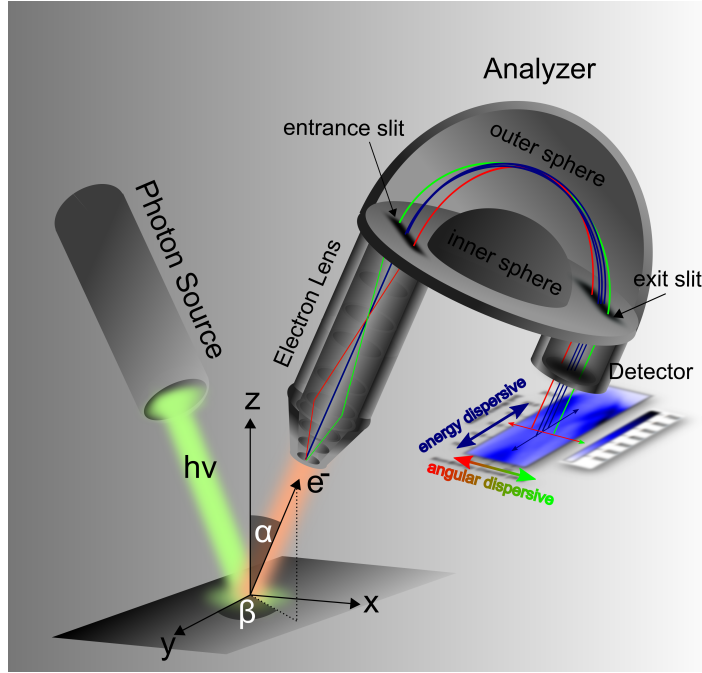


**Figure 3.9:** Basic setup for photoelectron spectroscopy (PES) and working principle of a hemispherical analyzer. A photon source excites electrons via the photoelectric effect from a sample. Photoelectrons  $e^-$  are emitted under the emission angle  $\alpha$  with respect to the surface normal  $z$  and then collected by the analyzer, converting the photoelectrons into a spectroscopic signal. The azimuth angle  $\beta$  describes the in-plane alignment of the sample with respect to the in-plane high symmetry directions, mostly relevant for ARPES.

resulting in lower intensity. The second stage of the energy filter are the two hemispheres. A potential difference, determined by the pass energy, is applied between the outer and inner sphere. Electrons with a certain energy range around the pass energy will be allowed to reach the detector [10], indicated by the blue colored trajectories in Figure 3.9. Smaller pass energies reduce the uncertainty, leading to improved energy resolution at the cost of lower intensity. Electrons with lower or higher kinetic energies will not reach the exit and are instead deflected towards the inner or outer sphere respectively. During this process, the angular distribution imaged by the electrons lens is kept, indicated by the red and green trajectories. Hence, the electrons reach the detector after being sorted by their energy and emission angle. The detector consists of micro channel plates, acting as secondary-electron multipliers. Each of these MCPs is a pixel on the phosphorus screen. The electrons are accelerated towards the screen and result in the emission of light. The emitted light is then captured by a CCD camera, resulting in a spectroscopic signal of the form  $I(E_{kin}, \alpha)$ . Thus, it is possible to directly obtain an image of a certain  $k$ -space and energy range, if the electron distribution for a given pass energy was allowed to reach the detector at once. The analyzer mode allowing for this operation is called the snapshot mode; the pass energy determines the energy window that is seen, while the energy channels of the detector determine the energy steps. At the same time, these are also the main disadvantages of the snapshot mode, as the user



is not free to choose energy resolution and step size for a certain energy of interest. However, the measurement will only take a few seconds, mainly determined by the dwell time, i.e. the amount of time that the energy filter allows electrons to reach the detector. Contrary to the snapshot mode, the fixed analyzer transmission mode (FAT) will scan the electrons by their kinetic energy. The user is free to set the energy steps, i.e. the amount of data points, as well as the pass energy for an optimal ratio of counts and resolution. Measurements in the FAT are, however, more time consuming, as the time is not only determined by the dwell time, but also by the number of scans performed and the step size.

### 3.3 Binding Energy Referencing and Energy Resolution

It is essential to compare binding energies between measurements with the same spectrometer, or even between different spectrometers. An accurate way of binding energy referencing is therefore essential. For example, the binding energy of the Ag 3d<sub>5/2</sub> peak in XPS should always be located at a binding energy of 368.21 eV, independent of the instrument. This is achieved by using the energy conservation of the photoemission process, as illustrated in Figure 3.10. When a conducting sample is put in electric contact with the spectrometer, both Fermi-level ( $E_F$ ) align to the same energy level. The true kinetic energy of the photoelectron is given by [5]

$$E_{kin}^* = h\nu - \Phi_S - E_{bin}, \quad (3.18)$$

where  $h\nu$  is the energy of the photon,  $\Phi_S$  is the work function of the sample and  $E_{bin}$  is the binding

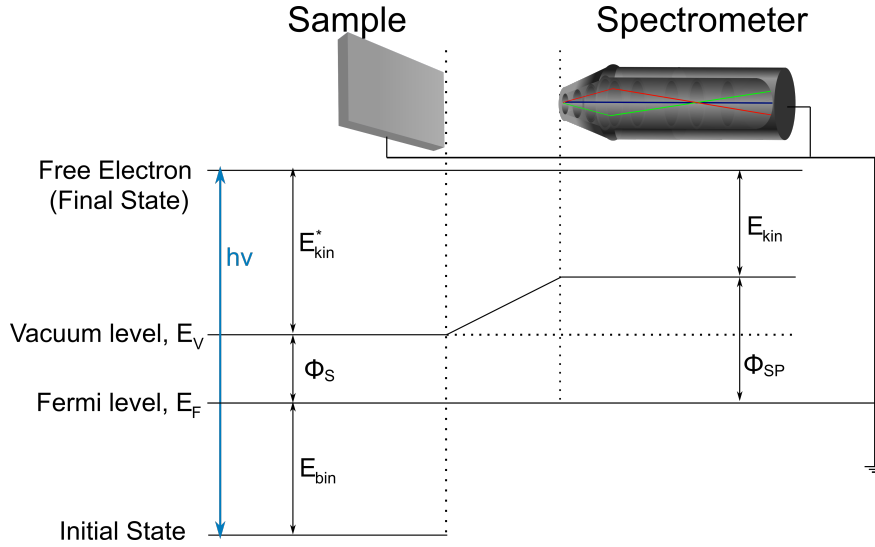


**Figure 3.10:** Energy conservation of the photoemission experiment with respect to the spectrometer. When the sample is in electrical contact with the spectrometer, the Fermi-level  $E_F$  align. When the spectrometer workfunction  $\Phi_{SP}$  is known, the binding energy of the initial state can be determined from the measured kinetic energy of the photoelectron  $E_{kin}$ . After ref. [5].

energy of the electron in the initial state. However, after the alignment of the  $E_F$ , the actual measured kinetic energy  $E_{kin}$  depends on the spectrometer work function  $\Phi_{SP}$ . Since binding energy and photon energy are constant, the sum of the respective workfunction and kinetic energy must be equal [5]:

$$E_{kin}^* + \Phi_S = E_{kin} + \Phi_{SP}. \quad (3.19)$$

In order to achieve the correct binding energy, one needs to determine the work function of the spectrometer. This is achieved by the alignment of a metal Fermi-edge to a binding energy of 0 eV and/or by the alignment of a core-level peaks to known values.

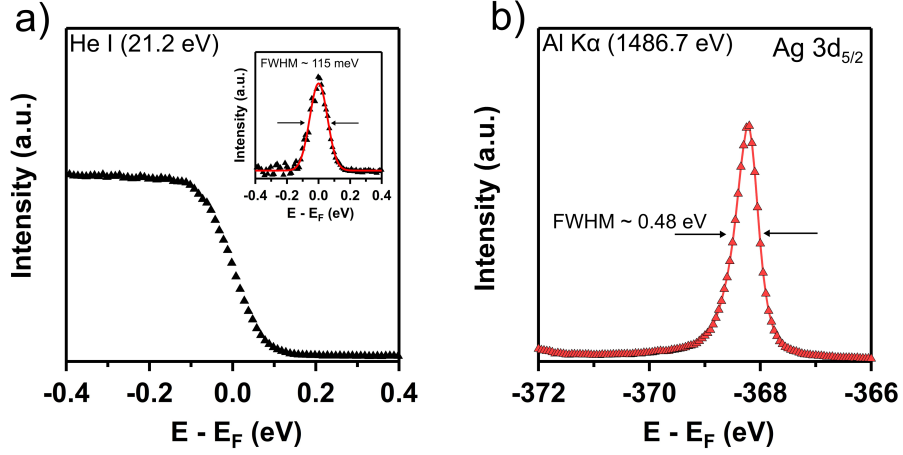


**Figure 3.11:** a) Fermi edge of a sputter cleaned Ag sample, measured with an excitation energy of 21.2 eV and a pass energy of 5 eV at room temperature. The inset shows that the first order derivative is centered on the position of the Fermi-level  $E_F$  with a full width at half maximum (FWHM) of 115 meV. b) Ag  $3d_{5/2}$  peak measured with mono chromated Al  $K\alpha$  (1486.7 eV) and a pass energy of 5 eV at room temperature. The peak is located at 368.21 eV and has a FWHM of 0.48 eV

If the work function of the spectrometer has been calibrated correctly, the spectra of Ag should appear like in Figure 3.11, where a sputter clean Ag foil was measured. Among the noble metals, Ag provides a distinct Fermi-edge under UV-radiation, see Figure 3.11 a). Adjusting the work function of the spectrometer “moves” the position of the Fermi-edge in accordance with the energy conservation law. The inset of Figure 3.11 a) shows the first order derivative of the Fermi-edge fitted by a Voigt-shape peak. The peak maximum corresponds to the center of the Fermi-edge, which is found at a binding energy of 0 eV in this case, thus illustrating a sufficient calibration of the spectrometer. As a result of the correct work function calibration, the Ag  $3d_{5/2}$  peak probed by XPS in Figure 3.11 b) is located at a binding energy of 368.21 eV [10]. Additional information regarding the energy resolution for the respective instrumental settings may also be obtained from the spectra shown in Figure 3.11. The total energy resolution  $E_{total}$  in PES is defined as [10]

$$E_{total}^2 = E_{natural}^2 + E_{instrument}^2, \quad (3.20)$$

where  $E_{natural}$  is the natural line width and  $E_{instrumental}$  is the instrumental energy resolution, influenced by the light source and the spectrometer settings. In case of the Ag  $3d_{5/2}$  peak, the natural line width is 0.33 eV. Using the above equation and the FWHM shown in Figure 3.11 b), the instrumental resolution for XPS becomes 0.35 eV. This extremely high energy resolution comes at the cost of a significant loss in intensity. In practical measurements I typically used an instrumental energy resolution of  $\approx 0.6$  eV, which doubles the FWHM of the silver peak to about 0.7 eV. However, the intensity gained increased by a factor of 10. In case of a Fermi-edge like in Figure 3.11 a),  $E_{natural}$  corresponds to the room temperature broadening, i.e. smearing of the Fermi edge, which is approximately  $4k_B T$ , where  $k_B$  is the Boltzmann constant and  $T$  the temperature. At room temperature,  $4k_B T$  amounts to  $\approx 103$  meV, which means that with  $E_{total}$  corresponding to the FWHM of 115 meV, the instrumental resolution was 50 meV. Further improvement of  $E_{total}$  may be achieved by cooling of the sample to reduce thermal broadening.

### 3.4 Angle-Resolved Photoelectron Spectroscopy

The power of angle-resolved photoelectron spectroscopy for materials science lies in the direct probing of  $E(\mathbf{k})$  of the occupied states at the surface. As already outlined in section 3.1 (Step 3: escape from the surface) this thesis will be restricted to  $E(\mathbf{k}_{||})$ , because  $k_{\perp}$  requires a tunable excitation source.

#### The Importance of UV-Radiation

An important aspect of ARPES is the use of UV radiation for the excitation of photoelectrons, hence, the technique is often also referred to as ARUPS (angle-resolved ultra-violet photoelectron spectroscopy). There are two reasons for the use of electrons in the UV regime. The first reason is the improved energy and momentum resolution. As shown in section 3.3, the energy resolution in UPS is improved by about one order of magnitude compared to XPS. The Momentum resolution is given by [3, 5]

$$\Delta k_{||} = \sqrt{\frac{2m_e E_{kin}}{\hbar^2}} \cos(\alpha) \Delta\alpha \quad (3.21)$$

and a typical angular resolution  $\Delta\alpha$  of the system will be around  $\Delta 0.2^\circ$ . The result is a momentum resolution of  $\Delta k_{||} = 8 \cdot 10^{-3} \text{ \AA}^{-1}$  when He I radiation is used, while in case of Al  $K\alpha$ , the momentum resolution is one order of magnitude worse ( $\Delta k_{||} = 6.8 \cdot 10^{-2} \text{ \AA}^{-1}$ ). The second reason for the use of UV-radiation is the negligible photon momentum in the photoemission process. Strictly speaking, one would have to add the photon momentum in equation (3.12). The photon momentum  $\kappa = \frac{2\pi}{\lambda}$  ( $\lambda$  is the wavelength) becomes  $\approx 0.01 \text{ \AA}^{-1}$  for He I (21.2 eV) and  $\approx 0.02 \text{ \AA}^{-1}$  for He II (40.8 eV) which is negligible compared to the dimensions of the first Brillouin zone in most materials [3] (for Ge it is  $\approx 1 \text{ \AA}^{-1}$ ). However, in case of X-rays with an energy of 1486.7 eV (Al  $K\alpha$ ), the photon momentum becomes  $\approx 0.76 \text{ \AA}^{-1}$ . The transition in the reduced zone scheme is no more vertical, which means that the Brillouin zone is smeared out over the angular range that is probed [3, 5].

#### Data Acquisition and Processing

A set of ARPES data that was obtained with He I radiation on Ge(111) is shown in Figure 3.12. The direction of the non-energy channel is the angular dispersive plane of the analyzer and detector, while the kinetic energy belongs to the energy dispersive plane. Rotation of the sample perpendicular to the non-energy channel direction allows one to move through the surface Brillouin zone and obtain a map of the  $\mathbf{k}_{||}$ -space. A constant energy is then obtained by selecting a certain energy and extracting the intensity profile as a function of the two angles (shown in the right-hand side top of Figure 3.12). Here, a kinetic energy of 20.6 eV was chosen and one can clearly see the 6-fold-symmetry of the band structure due to the hexagonal form of the Ge(111) surface Brillouin zone. At the Fermi-level  $E_F$ , constant energy cuts allow to directly resolve the Fermi-surface. To visualize the energy dispersion  $E(k_{||})$ , one has to take a constant angle cut. If a polar angle of  $0^\circ$  is chosen, the non-energy channel  $0^\circ$  corresponds to the  $\Gamma$ -point. Azimuthal (in-plane) rotation of the sample allows to change the high symmetry direction that is probed. In case of Figure 3.12, the constant angle cut shows the dispersion along the  $\Gamma - K$  direction, indicated by the insets.

The processing and analysis of the energy dispersive ARPES data is illustrated in Figure 3.13 for wide energy range scans of the Ge(111) surface along the  $\Gamma - K$  direction. According to equation (3.16), the experimental data has been transformed and the bottom axis is now in dimensions of  $\mathbf{k}_{||}$ . The energy axis is now given with respect to the Fermi-level  $E_F$ , which means the values are negatives of the binding energy. While most of the features are already visible and show clear

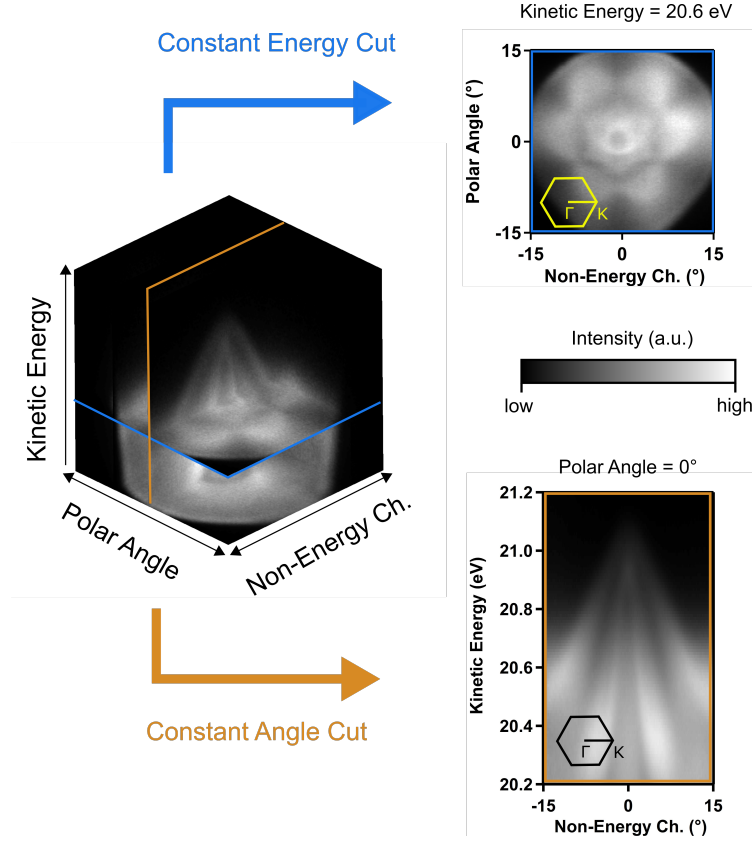


**Figure 3.12:** A Set of ARPES data from a Ge(111) surface is shown on the left side. The non-energy channel corresponds to the angular dispersive plane of the analyzer. Rotation perpendicular to this axis (polar angle) allows to obtain the intensity (gray scale) of photoelectrons as a function of the two angles and the kinetic energy. A constant energy cut (blue) at a kinetic energy of 20.6 eV is shown in the right panel top. The constant angle cut in the right panel bottom corresponds to a polar angle of  $0^\circ$ .

dispersions, high intensity bulk features limit the visibility of low intensity at the valence band maximum. Therefore, it is often times appropriate to enhance spectral features. Figure 3.13 b) shows the same image as a) but after applying a high pass filter, resulting in more pronounced features at the valence band maximum. In order to fit dispersion of bands for quantitative analysis, one has to extract individual curves from the spectra, illustrated in Figure 3.13 a). Energy distribution curves are intensity profiles as a function of  $E - E_F$  (constant  $k_{||}$ ) while momentum distribution curves show the intensity as a function of  $k_{||}$  (constant  $E - E_F$ ). Peak positions can then be extracted by fitting. As such, it is possible to obtain effective mass values, if the fitted dispersion matches a free electron parabola.

### Qualitative Analysis

For the qualitative analysis of ARPES data and the comparison with theoretical calculations, one needs to understand that ARPES is actually measuring a surface projected band structure [1, 3]. At a defined  $k_{||}$ , all energy values of bulk states with the same  $k_{||}$  and an arbitrary  $k_{\perp}$  will appear. If there are no energy values, these will also be projected onto the surface [1]. It is therefore not straight forward to compare bulk calculations with the actual ARPES experiment, as one needs to transition from bulk to surface Brillouin zone and also account for the projection of bands. This becomes particularly important for 3D materials and surface states. Surface states are 2D-states that have no  $k_{\perp}$  dependence. In contrast, 3D dimensional states (bulk states) will show dispersion in  $k_{\perp}$ , even though they are surface projected. Without a continuous light source, the  $k_{\perp}$

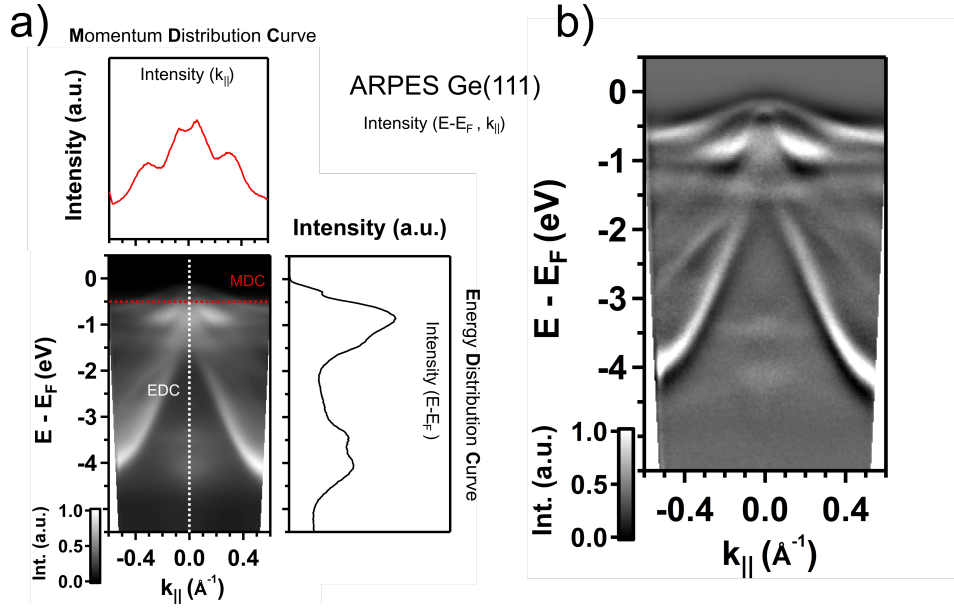


**Figure 3.13:** *a)* shows a wide-energy scan of the Ge(111) valence band structure along the  $\Gamma$ - $K$  direction. Dotted lines indicate the extracted momentum distribution curve (MDC) and energy distribution curve (EDC) that are shown on the top and right-hand side of the intensity map. *b)* The same image as *a)* after applying a high pass filter to enhance spectral features around the valence band maximum.

dependence can hardly be probed, but nevertheless, one can identify surface states by the following characteristics [1]:

- 1) A “true” surface state must lie in the projected bulk gap. As a result of the strong confinement to the surface, the surface state has only  $E(\mathbf{k}_{||})$  dispersion. Along  $k_{\perp}$ , the surface state is dispersion less, essentially like a straight line in direction of  $k_{\perp}$ . For any  $\mathbf{k}_{||}$  and  $E(\mathbf{k}_{||})$  along  $k_{\perp}$ , where the surface states exist, there must not be a single solution for a bulk wave, else the surface state would couple to it. The surface state would not be a true surface state anymore, because it can then penetrate deep into the bulk. In principle, this is a possibility and one then speaks of surface resonances. While they have the  $k_{\perp}$  dependence of bulk states, they have a much stronger amplitude at the surface.
- 2) Surface states are contamination sensitive. If the origin of a surface state is a periodic surface structure, contamination will distort the periodicity and destroy the state. Bulk and surface resonances are less sensitive because they also extend into deeper layers, although a sufficient amount of contamination will also lower their intensity at some point.
- 3) They have a tendency to appear as sharp peaks. What this means is that bulk bands are typically broader due to their projection along  $k_{\perp}$  onto the surface. The overlap of multiple  $k_{\perp}$  values result in energy broadening.

### 3.5 X-Ray Photoelectron Spectroscopy

X-ray photoelectron spectroscopy (XPS) makes use of photons in the X-ray regime in order to excite even deep core-level states and is widely used to study the chemistry at surfaces. Figure 3.14 shows a set of XPS measurements performed on a Ge(001) sample that was just loaded into the UHV-system.

A typical XPS measurement starts with a survey scan for the energy range that can be probed

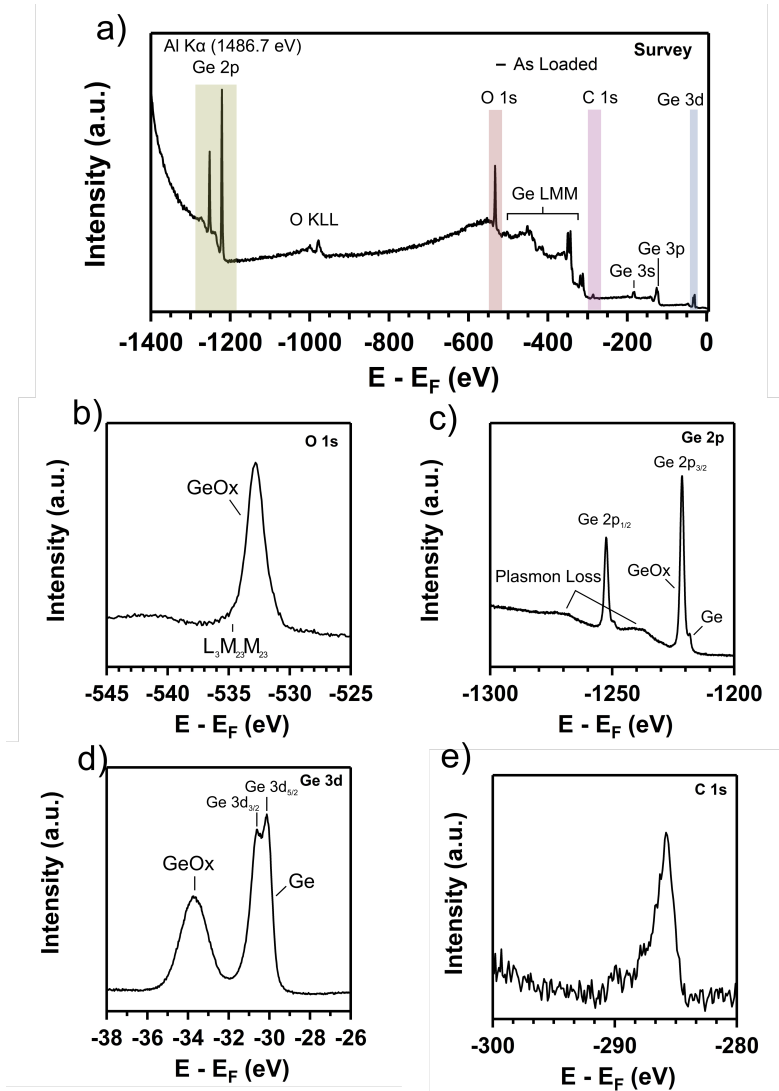


**Figure 3.14:** a) Survey scan of Ge(001) sample without any cleaning treatment, measured with monochromated Al K $\alpha$  (1486.7 eV). Regions used for detail spectra with higher energy resolution are indicated by labels and colored background. b) – e) Detail spectra of the Ge 2p, Ge 3d, O 1s and C 1s core-level regions, respectively.

by the X-rays, as shown in Figure 3.14 a). In this example, monochromated Al K $\alpha$  was chosen as the excitation source, meaning that electrons with a binding energy of up to -1300 eV can be reliably investigated, before the secondary electron background becomes too large (notice the exponential increase of intensity between -1300 eV and -1400 eV). The shown survey scan takes about 5 minutes to measure and is mainly used to obtain a quick overview of the chemical states on the sample. One can quickly identify the core-level peak of O 1s in a region around -530 eV, which belongs to the native Ge oxide that forms when Ge is in contact with air. Besides native oxides, an untreated sample will also have adventitious carbon on the surface. Even short contact with air may form adventitious carbon, which consists of hydrocarbons and carbon with single/double bonds to oxygen. Once a chemical species or core-level region of interest is found, high-resolution scans of that region should be performed. The pass energy will be reduced (in this case from 50 eV down to 15 eV) the step size will be decreased to enhance the number of obtained data points and the dwell time may also be slightly increased. Several scans should be used in order to achieve a good statistic, i.e. a low noise background. A high-resolution scan of the O 1s region is shown

in Figure 3.14 b).

### Auger Peaks

The O 1s peak is overlapping with Auger peaks of Ge, indicated by a marker ( $L_3M_{23}M_{23}$ ). One can also see in Figure 3.14 a) that the region of Auger peaks (indicated by the marker Ge  $LMM$ ) extends over a few hundred eV. Auger electrons can be created as part of the relaxation from the  $N-1$  electron state that is created by photoemission after the electron has left the nucleus. If the x-ray photon ejects a deep core-level electron, the atom being in the  $N-1$  electron state may minimize its energy by the recombination of an electron of a higher energy state with the hole left behind [5]. The recombination will create a photon with an energy equal to the recombination energy, which can then either leave the sample without any interaction or interact with other electrons. The interaction with an electron can then lead to its emission in form of an auger-electron, if energy conservation is still fulfilled. In contrast to regular photoelectrons, auger electrons will always have a characteristic kinetic energy, but their binding energy will change with the excitation energy. This can be used to “move” Auger peaks by switching the excitation energy, if, for example, the auger-peaks interfere with core-level peaks of interest. Therefore, it can be a huge advantage of a dedicated XPS setup to have more than a single excitation energy.

### Chemical Shifts

The Ge 2p and Ge 3d core-level regions are shown in Figure 3.14 c) and d) respectively. Both spectra exhibit Peaks related to pure Ge and to Ge-oxide. Due to charge transfer in the polar bonding, the oxide peak will usually be found at a higher binding energy than the elemental peak. This is commonly referred to as a chemical shift. Comparing the two core-level regions, one will notice that the Ge-oxide peak is much larger with respect to the pure Ge peak in the Ge 2p region compared to the Ge 3d region. This can be explained by the difference in the IMFP of the two regions. The Ge 2p peaks have a higher binding energy, thus a smaller kinetic energy than the Ge 3d peaks. As a result, the Ge 3d peaks are less surface sensitive and since the native oxide is only found at the surface, more percentage of the pure Ge bulk is probed compared to the Ge 2p peaks.

### Spin-Orbit Splitting

While the O 1s peak exhibited only a single peak in the as loaded sample, one can see that the Ge 2p and Ge 3d regions each appear to contain several peaks. The origin of this is the spin-orbit splitting given by the possibility of two final states for the same energy. The spin orbit coupling can be described by the j-j coupling scheme in which total quantum angular momentum  $j$  is used instead of individual numbers  $l$  and  $s$  [5]:

$$j = l + s. \quad (3.22)$$

Here,  $l$  is the angular momentum quantum number and  $s$  is the spin angular momentum number.  $l$  defines the shape of the orbital and is equal to 0 in case of an s-orbital, which means that any orbitals other than s-orbitals (i.e.  $l > 0$ ) have two possible final states by definition. Therefore, one observes two peaks belonging to Ge 2p and Ge 3d. Because  $l$  is 1 in case of the p-orbital, the two peaks for Ge 2p are differentiated by their possible  $j$  value 1/2 and 3/2. For a d-orbital  $j$  is 2, which leads to the labels of 3/2 and 5/2 [1, 5]. The area ratios of the respective doublet pair are given by the orientation possibilities which are  $2j + 1$  for a given  $j$ . In the Ge 2p core-level, there are four possibilities in the 3/2 final state and 2 in the 1/2 final state, giving an area ratio ( $2p_{1/2}: 2p_{3/2}$ ) of 0.5. In case of Ge 3d, there are 6 possibilities for 5/2 and 4 for 3/2, making the respective area ratio 0.67. These can be considered universal for all p- and d-orbitals of all elements. The

energy value of the splitting, i.e. the separation of the peaks, depends on the doublet and the material itself, making it have a similar signature like the core-level binding energy. Even for all compounds of a given material, the splitting is constant. For the Ge 2p peaks the splitting is 31 eV, while in the case of Ge 3d, the splitting is only 0.59 eV. The clear observation of the latter in Figure 3.14 d) also highlights the extremely good energy resolution of the experimental setup.

### **Plasmon Loss Features**

In addition to the spin-orbit splitting, several peaks can be found in the Ge 2p region. These do not belong to auger lines of Ge, which are found at a much lower binding energy. Instead, they belong to plasmon loss features. These occur in conductive samples, where the excitation of photoelectrons may lead to collective oscillations of conduction band electrons. A photoelectron will then suffer from discrete energy losses, in multiples of the characteristic plasmon frequency [5].

### **C 1s for Binding Energy Referencing**

Finally, the C 1s high-resolution scan is shown in Figure 3.14 e). The C 1s core-level is commonly used for binding energy referencing and actually an ISO standard [11], but it was recently reported that this may lead to inaccuracies of up to 1 eV [12]. Therefore, the binding energy referencing using C 1s should be avoided and instead metals in electrical contact with the sample should be used.

### **Peak Fitting**

An essential part of the core-level peak analysis in XPS and UPS is the fitting of peaks for a detailed analysis. A detailed review on how to proceed with such an analysis can be found in ref. [13] and I will only summarize here the most important aspects. The first step of fitting requires an appropriate background. The commonly used types of background subtraction are (1) linear background, (2) Shirley background and (3) Tougaard background [13, 14]. Without going into the mathematical details, Figure 3.15 a) illustrates the three types of backgrounds subtraction on the Ge 2p core-level region. The linear background has the shape of a straight line going through the intensity starting and endpoints and has essentially not physical meaning to it (it is pure mathematics). For simple backgrounds, this can still be an appropriate way to handle data, although it is not recommended for most core-level data.

Peaks where the linear background may still find application generally originate from s-orbitals. Due to the complexity of the Ge 2p core-level region and its background, this procedure clearly fails: An ideal background should pass through the noise outside the peak area and this is clearly not the case.

While the Shirley background has also a more mathematical origin compared to the more physical Tougaard background, it still is not as arbitrary as the linear background. The reason for this is that the Shirley background uses the overlying intensities to approximate the steps in the background. However, it also fails to estimate the correct background of the entire region. One may obtain better results by splitting the region into smaller parts and apply multiple fits. In general, the Shirley background and its iterations are widely used.

The Tougaard background has actually a physical meaning attached to it, in the sense that it accounts mathematically for the inelastic scattering and implementing the cross-section [15]. Generally, this results in the most accurate way of describing a background, but the use of the Tougaard background is not straight forward. The parameters for Ge are known and shown as the Ge



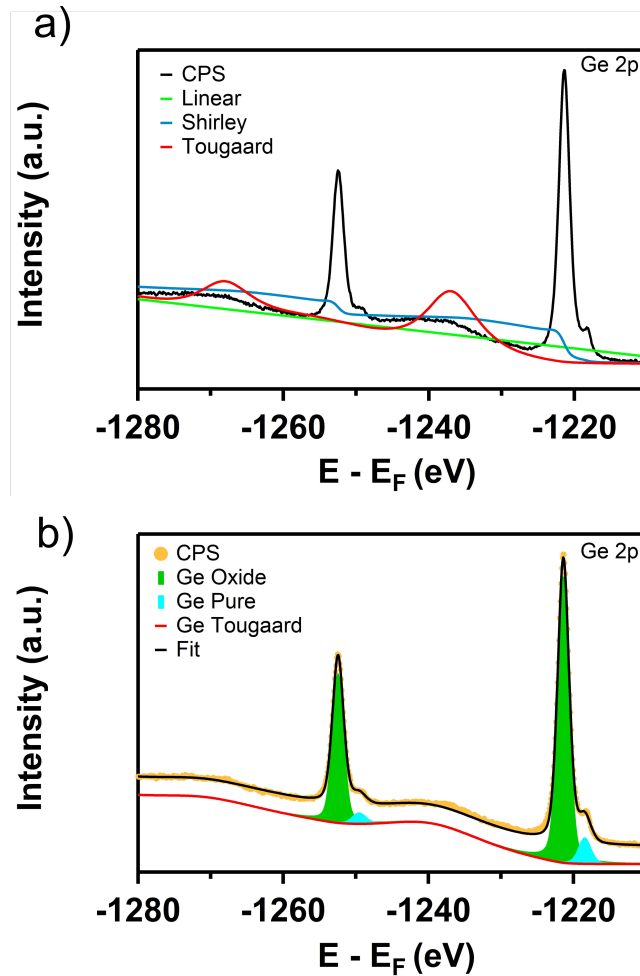


**Figure 3.15:** a) Showing that the three main types of background subtraction (Linear, Shirley and Tougaard) not match the background of the Ge 2p core-level region. b) The Ge Tougaard background after parameter adjustment and the resulting fit of the Ge 2p core-level region with two components.

Tougaard in Figure 3.15 a). The background also accounts for plasmon loss features, although overestimating them because the sample is oxidized. Adjusting the parameters, Figure 3.15 b) shows now a background (red line) that matches perfectly with the signal surrounding the peaks.

The next step is to choose how many components are used to fit the peaks. In general, once can fit any number and obtain a good residual. However, the peaks should also have a physical meaning [13]. For known materials and components, one should first refer to the literature. Since the surface is oxidized, it is clear that two components are required: one for pure Ge and another one for Ge-oxides. The latter could in theory also be present as Ge mono-oxide on the surface, but the fitting was found sufficient for just the Ge di-oxide component, separated by 2.9 eV from the Ge line. As a general guideline, the physical meaning of each component always needs to be justified.

The last important aspect of peak fitting is the actual shape of the peak. Core-level peaks do not appear as sharp lines for two reasons:

- (1) The life time of the core-level leads to a broadening that has a Lorentzian shape [13]. This depends on the material and the core-level itself. For example, the Ge 3d core-hole has a shorter life time than the Ge 2p core-hole, which makes the Ge 2p about 3 times broader.
- (2) The instrument will add broadening to the core-level peak in the form of a Gaussian shape [13].

This total Gaussian-broadening is given by the energy resolution of the instrument (see section 3.3).

The result of (1) and (2) is that a core-level peak is usually best described by a convolution of Gaussian and Lorentzian peak shape, where the exact contribution needs to be individually determined. Finally, the fitting procedure needs to obey the criteria for spin-orbit splitting components, meaning the separation of Ge-oxide and pure Ge  $2p_{3/2}$  and  $2p_{1/2}$  components is constant, as well as the area ratios [13].

## Chapter 4

# Surface Structure Characterization

In this thesis, the investigation of the surface electronic structure will be accompanied by surface structure characterization methods such as low-energy electron diffraction (LEED) and scanning tunneling microscopy (STM). Both techniques were readily available for in-situ characterization of my samples. Combining these two techniques with PES will allow for a more detailed analysis and robust interpretation of the results in the following chapters.

### 4.1 Low-Energy Electron Diffraction

LEED is an easy-to-setup surface structure probing technique, which is found in many laboratories carrying out surface science. The main advantages are the high reliability and the short measurement durations. As such, LEED is used in this thesis as a first probe to the surface structure.

At low-kinetic energy, the de Broglie wavelength of electrons is comparable to the interatomic distances and diffraction phenomena can be expected. Using electrons instead of photons also means a high surface sensitivity of these experiments because of the IMFP, similarly to PES from the previous section. In fact, most LEED data is acquired with electrons that have a kinetic energy somewhere between 30 to 150 eV, which means that the IMFP is at its minimum. The LEED diffraction pattern holds information about the symmetry of the surface atomic arrangement, as well as the surface unit cell. The spot size in LEED is comparable to the dimensions of ARPES and XPS spot sizes, therefore LEED provides valuable structural information of the surface by probing at a similar scale.

The experimental setup for LEED is illustrated in Figure 4.1. An electron gun delivers an electron beam of variable energy by accelerating the electrons from a cathode. The beam is directed on a sample surface in normal emission (the angle between surface normal and beam is  $0^\circ$ ) and electrons are backscattered to a detector system, which consists of four grids and a fluorescent screen. From sample towards screen, the first grid G1 is grounded, while the next two grids (G2 and G3) have a retarding voltage  $U_R$ , set slightly lower than the kinetic energy of the electron beam. This ensures that electrons with a lower kinetic energy than the incident electron beam (i.e. inelastically scattered electrons) do not reach the next stage of the detector system and are filtered out from the measured signal. The final stage is another grounded grid G4 and the fluorescent screen. The latter has also a voltage applied to it and the larger this voltage, the larger the overall intensity gets (typically 1 – 4 kV are used). The light emission from the screen is then captured by a CCD-camera behind the view port of the screen.

The appearing LEED spots are due to constructive interference of the backscattered electrons at

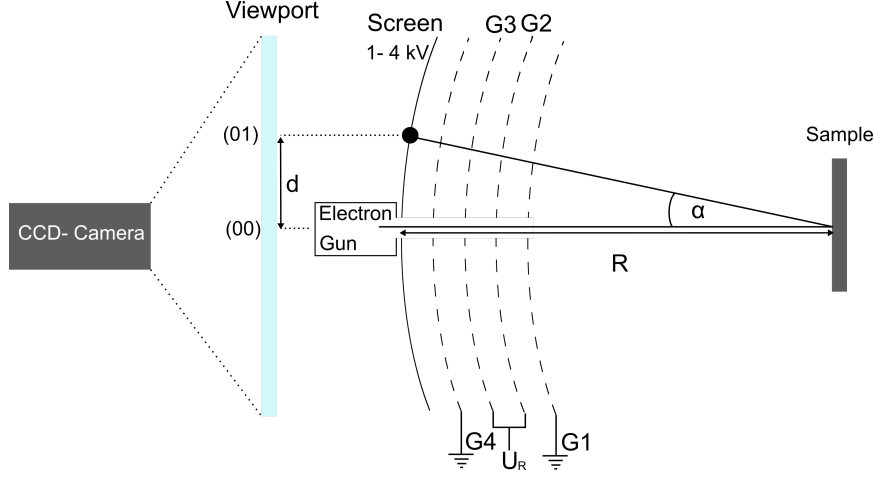


**Figure 4.1:** Basic experimental setup and geometry of the LEED experiment. An electron gun delivers an electron beam, with controllable kinetic energy. A crystalline sample will backscatter electrons under different angles  $\alpha$ .  $G1$  and  $G4$  are grounded grids, while a retarding voltage  $U_R$  is applied between  $G2$  and  $G3$ . The screen has a voltage applied to it (1 - 4 kV) and the emitted light is captured by a camera through the view port. The distance between diffraction spots is  $d$  and the screen radius is  $R$ . After ref. [1].

the surface crystal lattice. At a surface, i.e. a two-dimensional lattice, the diffraction condition is given by the Laue condition [1, 5]

$$\mathbf{k}_s^{\parallel} - \mathbf{k}_i^{\parallel} = \Delta \mathbf{k}^{\parallel} = \mathbf{g}, \quad (4.1)$$

where  $\mathbf{k}_i^{\parallel}$  and  $\mathbf{k}_s^{\parallel}$  are the components of the incident and scattered electron wave vectors parallel to the surface and  $\mathbf{g}$  is the vector of the surface reciprocal lattice. Due to energy conservation, the length of the elastically scattered electron wave vector must be the same as the incident electron wave vector length

$$|\mathbf{k}_i| = |\mathbf{k}_s|. \quad (4.2)$$

A useful tool to illustrate the diffraction condition at a crystal lattice is the Ewald-Sphere, shown in Figure 4.2 a) for the bulk case and in Figure 4.2 b) for a surface. The bulk case is depicted in two dimensions by only showing a single cut through the reciprocal lattice, allowing a more convenient illustration of the sphere construction. A  $\mathbf{k}_i$  vector is drawn with the correct direction and length, pointing with its tip at the origin of the reciprocal lattice. Then, a circle is drawn with

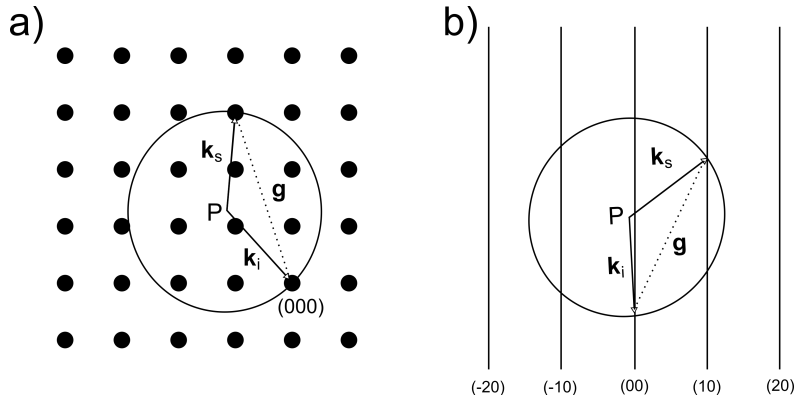


**Figure 4.2:** Illustration of the Ewald Sphere construction a) for the bulk case in two-dimensions and b) for the case at a surface. The incident electron wave vector  $\mathbf{k}_i$ , the wave vector of the scattered electron wave  $\mathbf{k}_s$  and the reciprocal lattice vector  $\mathbf{g}$  are indicated.  $P$  is the center of the Ewald Sphere. After ref. [1].

the radius  $|\mathbf{k}_i|$  and the origin at  $P$ . The principle of the Ewald sphere works intuitively: Any point

that intersects the circle follows the conservation rules from equation (4.1) and (4.2) and can thus be observed by constructive interference. Transitioning the construction to the surface means that the lattice points have now become rods, which also illustrates the missing  $k_{\perp}$  dependence from equation (4.1). The reason for this is the two-dimensional confinement of the surface in real space, or rather, its infinitely high symmetry in the perpendicular direction by being just one atomic layer. This results in an infinite number of  $k$ -points perpendicular to the surface, forming the rods [1, 5]. Similar to the bulk case, constructive interference is expected as soon as a rod is intersected. The Ewald-sphere construction at a surface nicely illustrates a common observation in LEED. Generally, more diffraction spots are visible at higher kinetic energies, because the sphere radius is increased and thus cutting more rods ( $|\mathbf{k}_i| = \frac{\hbar}{2m_e} \sqrt{E_{kin}}$ ). See for example Figure 4.3, showing the LEED pattern of the Ge(001) surface taken with 75 eV and 110 eV electron kinetic energy. More

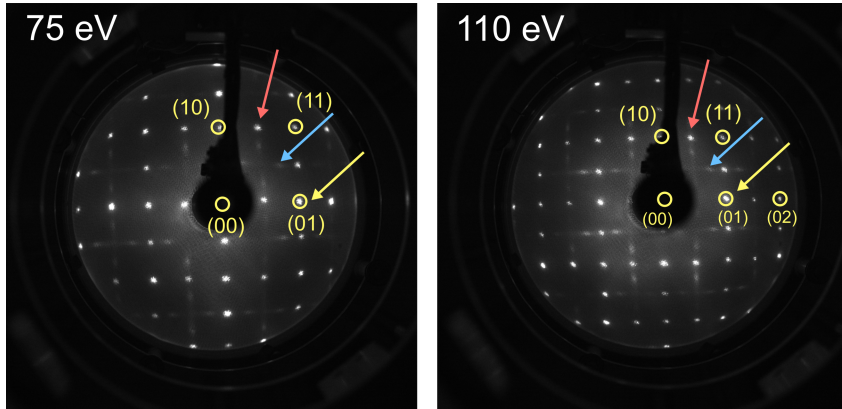


**Figure 4.3:** LEED raw data of a clean Ge(001) surface captured with different electron kinetic energies (75 eV and 110 eV). Yellow circles indicate the position of full-order diffraction spots of the upper right quadrant. The red arrow points at the position of a half-order spot and the blue arrow points at a quarter-order spot. The presence of half- and quarter-order spots is a sign of a reconstruction of the surface. The yellow arrow indicates the position of the (01) spot in each image to guide the eye. Upon increasing the electron kinetic energy, the (01) spot moves towards the (00) spot, while also higher order spots appear. Some spots, for example the (00) spot, are hidden behind the electron gun.

spots are present in the image taken with 110 eV electron kinetic energy. An electron beam of normal incidence means that  $\mathbf{k}_i^{\parallel} = 0$ . According to equation 4.1 and the Ewald sphere construction, the distances between points are then equal to the reciprocal lattice vector because  $\mathbf{k}_s^{\parallel} = \mathbf{g}$ . Using the geometry of the LEED experiment ( $\sin\alpha = \frac{|g|}{|k_s|} = \frac{d}{R}$ ), depicted in Figure 4.1, one can actually measure the length of the reciprocal lattice vector according to

$$d = R \frac{\hbar}{\sqrt{2m_e}} \frac{1}{\sqrt{E}} |g|, \quad (4.3)$$

where  $d$  is the spot distance (in this example from the zeroth order (00) to a first order spot (01) on the screen) and  $R$  is the distance between screen and sample surface. Equation 4.3 also explains another observation in Figure 4.3: With increasing kinetic energy, not only do more spots appear, they also move towards the zeroth order, see for example the spots that are highlighted by arrows in both images. Furthermore, the distances between the spots become smaller on the screen. When analyzing a LEED diffraction pattern, one of the first questions should be if the surface is reconstructed or not. It is therefore useful to estimate the lowest energy when a  $(1 \times 1)$  diffraction pattern should be observed. For the Ge(001) surface, this is around 35 - 45 eV. The  $(1 \times 1)$  diffraction spots have been marked yellow in Figure 4.3 for the upper right quadrant. The additional spots in between are a sign for a reconstruction of the surface. At half-order, these

correspond to the  $p(2\times 1)$  reconstruction (red arrow) and the streaky spots at quarter-order (blue arrow) correspond to the  $c(4\times 2)$  reconstruction [16, 17].

Figure 4.4 illustrates how the Ge(001)  $p(2\times 1)$  and  $c(4\times 2)$  reconstructions transition into a LEED diffraction pattern. Their appearance in between the  $(1\times 1)$  spots can be rationalized by their larger surface unit cells in real space compared to  $(1\times 1)$  and the real space shape also transitions into the reciprocal space. However, the final LEED pattern also includes diffraction spots related

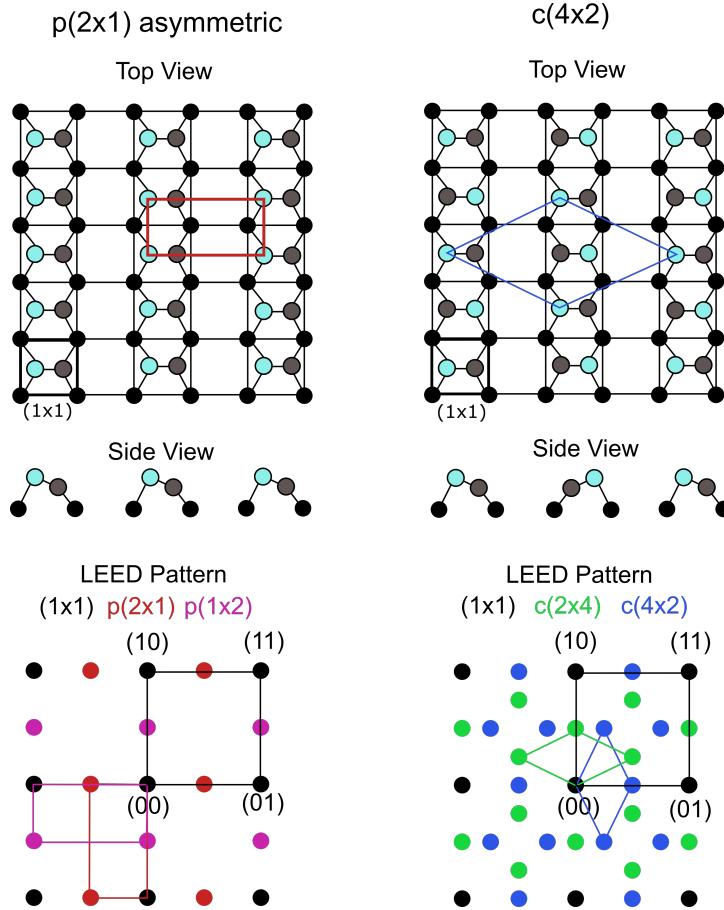


**Figure 4.4:** Illustration of the relation between Ge(001) surface reconstructions and the observed LEED pattern. The top panel shows the surface models of the  $p(2\times 1)$  symmetric and  $c(4\times 2)$  reconstructions, after ref. [18]. In the top view, the surface unit cells are indicated in red and blue, while a thick black solid square indicates the size of the  $(1\times 1)$  surface unit cell. The bottom panel shows the LEED pattern corresponding to the  $(1\times 1)$ ,  $p(2\times 1)$  and  $c(4\times 2)$  reconstructions, also including domains ( $p(1\times 2)$  and  $c(2\times 4)$ ). Lines indicate the basis of the diffraction pattern in the respective colors.

to the  $p(1\times 2)$  and  $c(2\times 4)$  domains. This is explained by large spot size of the electron beam ( $1\text{ mm}^2$ ) compared to the dimensions of the Ge(001) terraces ( $100\text{ nm}^2$ ). As such, LEED will probe multiple terraces and domains at the same time. However, the coherence length of electrons in LEED is only about  $50\text{ \AA} - 100\text{ \AA}$ , which is smaller than the size of terraces and the residing domains. Therefore, the interference between electrons from different domains is neglected and the final LEED pattern emerges as an incoherent sum of the possible domains and their intensities [1, 5], indicated in the bottom panel of Figure 4.4.

The small coherence length of LEED also indicates some of its limitations in the surface structure analysis. Islands and smaller defects may not be identified if their density is lower than the coherence length. It is therefore important to keep in mind that “basic” LEED does not allow finite conclusion on the surface quality by itself.

## 4.2 Scanning Tunneling Microscopy

To cover some of the limitations inherent to LEED, STM will be employed in this thesis. STM allows to spatially resolve the surface structure at the atomic scale in real space, which will nicely complement LEED in the surface structure analysis.

In STM, a stylus type, atomically sharp tip is brought close to a surface and a voltage is applied, shown in Figure 4.5 a). The physical phenomenon that now enables the working principle of STM is the quantum mechanical tunneling effect [5]. A finite potential, such as the vacuum between probe and surface, is not able to fully contain the wave functions of the electrons and there is a decaying leakage of the wave function. The decay length is given by [1, 5]

$$\kappa = \sqrt{\frac{2m_e\Phi_s}{\hbar^2}}, \quad (4.4)$$

where  $m_e$  is the electron mass,  $\Phi_s$  is the sample work function and  $\hbar$  is the reduced Planck's constant. With a typical work function of about 4 eV, the decay length is in the order of 1 Å [1]. Bringing tip and surface close enough to each other means that the decaying wave functions

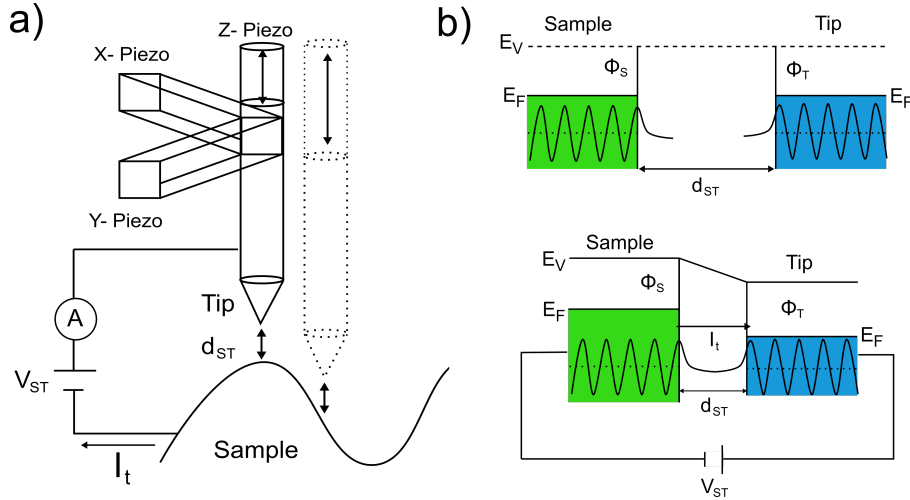


**Figure 4.5:** a) The schematic figure illustrates the basic principle of STM in the constant current mode: a stylus-type tip is brought close to a surface. Applying a voltage  $V_{ST}$  between sample and tip, a tunneling current  $I_t$  can flow. A feedback loop with the z-piezo ensures that the sample to tip distance  $d_{ST}$  is held constant when the surface is raster-scanned. After Ref. [1]. b) The schematic figure illustrates the role of quantum mechanical tunneling in STM. Sample and tip are made of the same material and the wave functions of their electrons close to the Fermi-level ( $E_F$ ) decays into the forbidden region, through a finite potential barrier. If sample and tip are close enough, the penetrating wave functions can overlap and applying a voltage permits the flow of a tunneling current  $I_t$ . After Ref. [5].

can overlap, as illustrated in Figure 4.5 b). In this example, sample and tip are made of the same material, meaning their  $E_F$  are at the same energy level. After applying a sufficiently high voltage (a few mV to several V), a tunneling current can flow between the occupied states of the sample and the unoccupied states of the tip. The tunneling current  $I_t$  depends exponentially on the sample to tip distance  $d_{ST}$  and the decay length  $\kappa$

$$I_t \propto \exp(-2 \cdot \kappa \cdot d_{ST}). \quad (4.5)$$

Typical values for the tunneling current range from 0.5 to 5 nA [1]. A common mode of operation is to keep the tunneling current constant and adjust the height of the tip. During operation  $d_{ST}$  is adjusted to achieve a constant  $I_t$  by a feedback loop, as the  $x - y$  plane is scanned. Precise control

of the tip movement is achieved by piezo-electric motors, as indicated in Figure 4.5 a). The piezo extension in  $z$ -direction is proportional to the applied voltage, hence any added correction voltage to keep  $d_{ST}$  constant will result in a direct measurement of the height profile. The height profile can depend on the actual roughness, i.e. height differences and/or the changes in the local density of states (LDOS) (usually a mixture of both).

In fact, the tunneling current is also proportional to the density of states at the  $E_F$  of the sample and at the center of the tip [19]. Therefore, STM does actually not directly resolve the atomic structure, but more so the LDOS. This is important to keep in mind, especially for reconstructed semiconductor surfaces such as the Ge(001) surface. In Figure 4.6 a) a  $5 \times 5 \text{ nm}^2$  STM image of the Ge(001) surface is shown, capturing a  $c(4 \times 2)$  reconstructed area. As indicated by the model of the buckled dimer in Figure 4.6 b) charge is transferred from the down-tilted atom ( $D_{down}$ , gray) to the up-tilted atom ( $D_{up}$ , turquoise), leading to the formation of a  $\pi$ -bond [18]. The applied voltage of  $-1 \text{ V}$  results in a probe of the occupied states (turquoise arrow), which appear as brighter areas in the STM image. The dark areas (gray arrow) do not correspond to holes in the surface, but to the  $D_{down}$  atoms with a lower LDOS at the  $E_F$ . With this in mind, the periodicity of the LDOS corresponds to the periodicity of the individual atoms and one can draw the  $c(4 \times 2)$  surface unit cell in real space, indicated by the blue rhombus. While the resolving the surface structure at

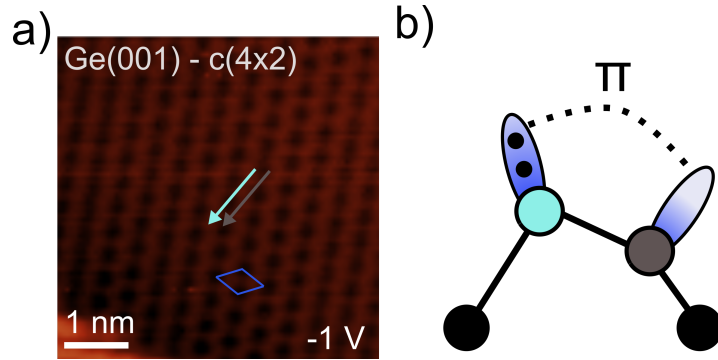


**Figure 4.6:** a)  $5 \times 5 \text{ nm}^2$  STM image of a  $c(4 \times 2)$  reconstructed area of the Ge(001) surface obtained at  $-1 \text{ V}$ . Negative bias means that occupied states (turquoise arrow) are probed and the unoccupied states (gray arrow) appear dark. A surface unit cell of the  $c(4 \times 2)$  reconstruction is indicated by a blue rhombus. b) Side-view of the buckled dimer model of the reconstructed Ge(001) surface. The dangling bonds form a  $\pi$ -bond and charge transfer occurs from the down-tilted (gray) to the up-tilted (turquoise) atom, symbolized by two electrons (black dots). Therefore, the down-atoms appear dark in STM image when the occupied states are probed.

atomic scale is pretty powerful, obtaining STM images of high quality (atomic resolution) is not straightforward due to several challenges that have to be faced:

The first is the inherent sensitivity of STM to any vibrations, since the tunneling current depends exponentially on  $d_{ST}$ . It requires sufficient vibration insulation of the instrument, which can also mean that mechanical pumps (turbo- and scroll-pumps) need to be switched off during measurement. Occasionally samples and parts of sample holders may also start to vibrate if they are insufficiently fixed.

The second is a sufficient tip. STM requires an atomically sharp tip that also needs to be stable during the measurement. Contaminations may attach during the scanning to the tip, distorting the images. Additionally, a double-tip may result in the creation of artefacts during the measurement.

The third is the distortion of STM images by piezo actuator creep and by thermal drifts. The origin of piezo actuator creep is a hysteresis effect of the scanner movement. It usually occurs



when a voltage is applied to move to a different scanning location. When the location is reached and the scan begins, the piezo may still try to “move” away from the location. The problem is usually solved by repeated scanning. Thermal drift is caused by the relative movement of sample and tip due to expansion and/or contraction.

These challenges illustrate why STM can be considered as an extremely time-consuming measurement technique to obtain atomically resolved images.



## Chapter 5

# New Insights into the Electronic States of the Ge(001) Surface by Joint Angle-Resolved Photoelectron Spectroscopy and First-Principle Calculation Investigation

Ge is a group IV semiconducting material that crystallizes in the diamond cubic structure, in which a Ge atom has four nearest neighbors connected by covalent bonds. Due to this diamond cubic structure, a Ge atom will have two missing bonds at the technological relevant (001) surface, the so-called dangling bonds. To minimize the surface energy, additional bonds are created between the dangling bonds, leading to the dimerization of neighboring surface atoms and the reconstruction of the surface. The dimerization reduces the number of dangling bonds per surface atom from two down to one, gaining 0.66 eV per  $(1 \times 1)$  surface unit cell [20]. The atoms of a dimer are bonded by a  $\sigma$ -bond, and the remaining pair of dangling bonds, each still carrying their electrical charge, form a  $\pi$ -bond. This atomic configuration is known as the symmetric dimer.

However, there is an energetically more favorable atomic configuration, gaining about 0.24 eV per dimer [21]. The dimer atoms buckle, leading to an up-tilted ( $D_{up}$ ) and down-tilted ( $D_{down}$ ) atom and charge is transferred from  $D_{down}$  to  $D_{up}$ . The result of this buckling are the two main reconstructions of the Ge(001) surface:  $p(2 \times 1)$  and  $c(4 \times 2)$ , which were already encountered in chapter 4. To understand the consequences of the Ge(001) surface reconstruction for the electronic structure, many studies were conducted in the past and the assignment of surface and bulk states has led to controversial discussions in the literature.

Several groups assigned the valence band maximum (VBM) to the filled surface state of  $D_{up}$  [22, 23, 24], while Nakatsuji et al. [25] argued that the VBM is exclusively bulk states. A more recent report by Seo et al. [26] stated that the VBM originates from bulk states and the  $D_{up}$  surface state forms a surface resonance with the heavy hole (HH) band, approaching the VBM. However, one may argue that the dispersions of the HH band and the  $D_{up}$  state don't match, which may indicate that the valence band structure is bulk dominated.

Whether the Ge(001) surface is of semi-conducting or conducting nature at RT has been another

point of discussion for decades. Back in 1984, Kevan and Stoffel [17] reported the observation of a state above the VBM (below the Fermi-level  $E_F$ ) occupied at room temperature (RT), which I am going to label  $SS_1$ .  $SS_1$  was assigned to a metallic surface state that originates from the partially filled bands of dimers in the  $(2 \times 1)$  domains, due to their flip flop motion [27]. Following the initial reports [17, 28], later ARPES studies found  $SS_1$  above  $E_F$ , but unoccupied at RT [24, 25, 29, 30]. The state was then assigned to the unoccupied band of  $D_{down}$  of the  $p(2 \times 1)$  reconstruction, due to the separation of  $SS_1$  and VBM of  $0.4 - 0.5$  eV [24, 30], and the Ge(001) surface was considered semi-conducting at RT. However, the VBM was positioned too far below  $E_F$ , because the actual VBM was assigned to the  $D_{up}$  surface states [24, 30]. In fact, the separation of  $SS_1$  and VBM is only about  $0.2 - 0.3$  eV [25], indicating that the origin could be the  $c(4 \times 2)$  reconstruction, as recently reported by Kanasaki et al. [31].

The controversy in the literature implies the need for my own study on the Ge(001) surface, not only to obtain a reference for the modification upon adsorption of Sn, but also to clarify long standing misconceptions regarding the electronic structure.

## Chapter 5: Publication Contribution Statement

This Chapter has been published in Applied Surface Science, 571 (2022) 151264, <https://doi.org/10.1016/j.apsusc.2021.151264> as a subscription article [32]. Any use of this article requires the explicit written permission of Elsevier. For details, please refer to ScienceDirect "get rights and content".

The surface cleaning of samples that were analyzed in the results section of this chapter was performed by me. The sputtering and annealing parameters were refined in multiple trial sessions and in close collaboration with Andreas P. Becker and Emily V. S. Hofmann, using feedback loops of ARPES, STM and LEED.

In the results section, the ARPES and LEED raw data were obtained by me. I performed the sample transfer in the system and the alignment for the two characterization methods. In addition, the measurement parameters were chosen entirely by me.

The STM raw data was obtained with the help of Andreas P. Becker. During the measurements, I assisted Andreas P. Becker.

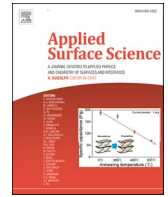
The raw data of ARPES, LEED and STM were analyzed by me and I created the figures that show their results. A first draft of the experimental results, including preliminary interpretation was provided by me and discussed with all co-authors. I was in charge to organize these meetings and led the scientific discussion.

The calculations were performed by Dr. Emilio Scalise and I only contributed in their discussion.

With the experiments and calculations finished, I prepared a first written draft of this publication. While I have written the abstract, introduction, experimental methods, experimental results and discussion & conclusion by myself, I received text passages of the theory related sections from Dr. Emilio Scalise. After merging them, the draft was reviewed by all authors and I included all remarks and changes requested by the co-authors.

I handled the submission process and was in charge to communicate with editor and reviewers. Furthermore, I led the revision of the article based on the reviewer's comments and took care of the re-submission.





## Full Length Article

# New insights into the electronic states of the Ge(001) surface by joint angle-resolved photoelectron spectroscopy and first-principle calculation investigation

Felix Reichmann<sup>a,\*</sup>, Emilio Scalise<sup>b,\*</sup>, Andreas P. Becker<sup>a</sup>, Emily V.S. Hofmann<sup>a,c,d</sup>, Jaroslaw Dabrowski<sup>a</sup>, Francesco Montalenti<sup>b</sup>, Leo Miglio<sup>b</sup>, Mattia Mulazzi<sup>e</sup>, Wolfgang M. Klesse<sup>a</sup>, Giovanni Capellini<sup>a,f</sup>

<sup>a</sup> IHP – Leibniz-Institut für innovative Mikroelektronik, Im Technologiepark 25, 15236 Frankfurt (Oder), Germany

<sup>b</sup> L-NESS and Dipartimento di Scienza dei Materiali, Università di Milano-Bicocca, Via R. Cozzi 55, I-20125 Milano, Italy

<sup>c</sup> London Centre for Nanotechnology, University College London, 17-19 Gordon Street, London WC1H 0AH, UK

<sup>d</sup> Department of Electronic and Electrical Engineering, University College London, London WC1E 7JE, UK

<sup>e</sup> Humboldt-Universität zu Berlin, Unter den Linden 6, 10099 Berlin, Germany

<sup>f</sup> Dipartimento di Scienze, Università Roma Tre, Viale G. Marconi 446, I-00146 Rome, Italy

## ARTICLE INFO

## Keywords:

Germanium  
Ge(001)  
Surface  
ARPES  
DFT

## ABSTRACT

While the Ge(001) surface has been extensively studied, it is still debated whether it is of conducting or semiconducting nature at room temperature. The evidence collected by angle-resolved photoelectron spectroscopy experiments in the past has led to the preliminary attribution of a semiconducting nature at room temperature. In contrast, we show in this work that the pristine Ge(001) surface is conducting at room temperature by using temperature-dependent angle-resolved photoelectron spectroscopy, scanning tunneling microscopy and first principles calculations. Specifically, a surface band located  $\sim 200$  meV above the valence band maximum has been observed at room temperature. This surface band shows anisotropic dispersions along the [010] and [110] directions, but it disappears at lower measurement temperature, which indicates its occupation by thermally excited electrons. State-of-the-art density functional theory calculations undoubtedly attribute this surface band to the unoccupied  $\pi^*$ -band formed by dangling bonds on the  $c(4 \times 2)$  surface reconstruction, while evidencing fundamental differences with the  $p(2 \times 1)$  reconstruction. Furthermore, the calculations demonstrate that the valence band structure observed in angle-resolved photoelectron spectroscopy experiments arise from projected bulk states and is thus insensitive to surface contamination. Our results contribute to the fundamental knowledge of the Ge(001) surface and to a better understanding of its role in micro- and opto-electronic devices.

## 1. Introduction

While silicon wafers remain the established workhorse in complementary metal-oxide-semiconductor (CMOS) technology, epitaxial Ge is receiving more and more attention. In particular, the high carrier mobilities of Ge (specifically holes) have sparked interest for the use in advanced field effect transistors [1]. Ge, and its alloys with Si and Sn, have also shown a great potential in optoelectronic devices, in particular for photodetectors [2] and integrated infrared lasers [3–5]. More recently, Ge has been highlighted as a candidate for the manufacturing of scalable quantum computing [6] and spintronic [7] devices.

On the technologically-relevant Ge(001) surface, dangling bonds form buckled (asymmetric) dimers, which align parallel to the [110] and  $[\bar{1}10]$  directions, leading to high order reconstructions like  $p(2 \times 1)$ ,  $p(2 \times 2)$  and  $c(4 \times 2)$  [8]. The dimerization reduces the surface energy by the formation of bonding  $\sigma$  and antibonding  $\sigma^*$  states from the two hybridized  $sp^3$  orbitals of the backbonds, while bonding  $\pi$  and antibonding  $\pi^*$  states are formed by the orbital overlapping of the two dangling bonds. The surface energy is lowered further by buckling the two atoms of the dimers. The buckling causes a charge transfer from the down-atom ( $D_{\text{down}}$ ) to the up-atom ( $D_{\text{up}}$ ), resulting in filled ( $\pi$ ) bonding states of the  $D_{\text{up}}$ , which manifest themselves in an energy band lying

\* Corresponding authors.

E-mail addresses: E-mail address: [reichmann@ihp-microelectronics.com](mailto:reichmann@ihp-microelectronics.com) (F. Reichmann), [emilio.scalise@unimib.it](mailto:emilio.scalise@unimib.it) (E. Scalise).

<https://doi.org/10.1016/j.apsusc.2021.151264>

Received 10 July 2021; Received in revised form 6 September 2021; Accepted 10 September 2021

Available online 14 September 2021

0169-4332/© 2021 Elsevier B.V. All rights reserved.

below the Fermi-level ( $E_F$ ), while unoccupied ( $\pi^*$ ) states of the  $D_{\text{down}}$  are located above  $E_F$ .

The electronic structure of the Ge(001) surface has been the subject of multiple investigations by angle-resolved photoelectron spectroscopy (ARPES) over the last decades and the assignment of bulk and surface states (in particular the states related to the  $D_{\text{up}}$  and  $D_{\text{down}}$ ) has led to controversial discussion [8–16].

It was generally reported that the valence band maximum (VBM) probed by ARPES originates from the filled  $D_{\text{up}}$  surface states of the  $p(2 \times 1)$  reconstruction [11,12,15], while Nakatsuji et al. [13] argued that the observed VBM arises mainly from bulk states. In contrast, Radny et al. [17] argued, by using density functional theory and scanning tunneling microscopy, that the VBM is formed by the dimer back-bond surface states. However, a recent experimental and theoretical investigation by Seo et al. [16] has shown that the VBM is mainly related to bulk states, with the  $D_{\text{up}}$  surface state approaching the heavy hole band to form a surface resonance around the VBM.

Another key issue heavily debated in literature is related to the unoccupied  $\pi^*$ -band of  $D_{\text{down}}$  and its occupation at room temperature (RT) [8,13–15]. Kevan and Stoffel [8] observed this state at an energy below  $E_F$  at RT, leading to the assignment of a metallic state formed by partially filled bands in the  $(2 \times 1)$  domains due to the buckling oscillation of dimers [18]. Subsequent ARPES studies found the same state above  $E_F$ , assigning it to the unoccupied  $\pi^*$ -band of the asymmetric  $p(2 \times 1)$  reconstruction, which lies around 0.4–0.5 eV above the VBM [14,15]. However, the VBM was positioned too far below  $E_F$  due to an incorrect assignment of the  $D_{\text{up}}$  states, resulting in an overestimation of the VBM to  $\pi^*$  separation. In fact, the state lies only about 0.2 eV–0.3 eV above the VBM [13], which indicates that the origin is not the  $(2 \times 1)$  phase with its  $\pi^*$ -band 0.5 eV above the VBM [16]. A very recent study by Kanasaki et al. [19] assigns the same feature to unoccupied  $\pi^*$  band formed by  $c(4 \times 2)$  reconstructed surface by employing time- and angle-resolved two-photo photoelectron spectroscopy, finding a separation of 0.22 eV.

Differences in the Ge(001)  $c(4 \times 2)$  and  $p(2 \times 1)$  surface electronic structure could impact the  $\pi^*$  occupation at RT by thermally excited electrons and thus its conducting or semiconducting nature. To address this dispute, we report here a combined experimental and theoretical investigation based on time- and temperature-dependent ARPES, scanning tunneling microscopy (STM), and density functional theory (DFT).

In the first section, using STM and low-energy electron diffraction (LEED) we demonstrate a clean Ge(001) surface prepared by sputtering and annealing.

In the second section, we focus on the experimentally probed surface electronic structure by ARPES at RT. Probing along the  $[010]$  and  $[\bar{1}10]$  directions allows the observation of anisotropic dispersion, which indicates a relation to the surface reconstruction of Ge(001). Time-dependent measurements confirm the surface nature of the observed state and temperature-dependent measurements, particularly at low-temperatures, provide evidence for the occupation by thermally excited electrons.

In the third section, state-of-the-art DFT is used for detailed insights on the Ge(001) surface electronic structures. The large number of atomic layers included in the slab calculations, together with the possibility to have an accurate prediction of the bandgap, allowed a direct comparison of the surface states of  $p(2 \times 1)$  and  $c(4 \times 2)$  reconstructions. We find key differences that are crucial to identify and understand the origin of the observed features in ARPES.

In the fourth and final section, we compare our findings to the literature and outline the importance of the work shown here.

## 2. Methods

### 2.1. Experimental

Clean Ge(001) substrates were prepared from  $n$ -type (1–10  $\Omega$  cm),  $p$ -

type (1–10  $\Omega$  cm), and  $i$ -Ge(001) (35  $\Omega$  cm) pieces extracted from 2" wafers. Samples were loaded into a UHV system, comprising a preparation chamber and two analysis chambers, with base pressures below  $5 \cdot 10^{-10}$  mbar and degassed for 2 h at 300 °C. After cooldown, the cleaning treatment continued with repeated cycles of  $\text{Ar}^+$  sputtering with 500 eV ion energy and annealing. Each sputtering step was followed by a resistive heating to 600 °C for 1 min and subsequent cooldown lasting for 10 min, to avoid surface re-contamination. In the final cleaning cycle, the sputtering was followed by a resistive heating to 750 °C for 2 min. An at least 30 min cool down was ensured before the sample was transferred for investigation into the analysis chamber.

The valence band structure was studied by ARPES using a SPECS Phoibos 150 spectrometer. The He I line with an energy of 21.2 eV was used to excite photoelectrons. The angular resolution was better than  $0.15^\circ$  and the total energy resolution was better than 120 meV, dominated by the thermal broadening at room temperature. The work function of the spectrometer was calibrated by measuring the Fermi edge of a sputter-cleaned Ag foil (99.99% purity). STM was performed in a separate chamber on a SPECS SPM Aarhus 150 HT, equipped with a tungsten tip, in constant current mode with a sample bias of  $-1$  V. An ErLEED 150 optics from SPECS was used to acquire low energy electron diffraction (LEED) data.

### 2.2. First-principles calculations

The first-principles calculations were performed within the density functional theory (DFT) using planewave basis sets as implemented in the Quantum Espresso code [20]. A kinetic energy cutoff of 80 Ry was used, with projector augmented wave (PAW) pseudopotentials [21] and a  $8 \times 16 \times 1$  Monkhorst-Pack grid for sampling the Brillouin zone of the  $p(2 \times 1)$  Ge supercell, adequately reduced for the larger supercells. We carefully checked the convergence of the band-structure energy values and found that we needed at least 36 Ge layers for the slab models of the Ge(001) surfaces to have converged results. The importance of the slab thickness on the DFT calculations of the surface band structure, particularly the dangling bond states of the surface dimers near the Fermi level, have been clearly shown by Sagika et al. [22] for the Si (001) surface. We confirm the crucial influence of the slab thickness also on the band structure of Ge (001), due to surface resonances [17] and mixed states between the dangling-bonds  $\pi$  states and bulk states near the band edges [23]. In fact, we show that in order to calculate pure bulk states, one needs to go deeper than 30 atomic layers from the surface.

The bottom atoms of the Ge slab were saturated by H atoms and we added about 15 Å of vacuum to prevent interactions between the replica in the non-periodic direction. The structural relaxations were performed until the average atomic force was lower than 10<sup>-4</sup> Ry/Bohr, using a conjugate gradient method and the Perdew-Zunger (LDA) exchange-correlation functional [24], providing a lattice parameter for the bulk Ge of 5.622 Å, which slightly underestimates the experimental value of 5.652 Å [25]. For the band structure and the LDOS calculations, meta-GGA exchange-correlation functionals were exploited in order to improve the bandgap prediction. In particular, by using recently developed non-empirical strongly constrained and appropriately normed (SCAN) meta-GGA functionals [26] a bandgap of about 0.66 eV has been obtained for the bulk Ge, which improve substantially the completely wrong GGA prediction showing only a few meV of bandgap, and it is very close to the experimental room temperature value [27] (0.6643 eV) or the value obtained by the more computationally demanding HSE06 calculations (0.675 eV) [28]. Note that the presented calculations do not include spin-orbit coupling and this do not allow for a correct prediction of the split-off band. Still, this do not affect much the valence and conduction band edges, nor the surface states as concluded by Seo et al. [16] or Sheverdyaeva et al. [29]. The latter work shows that the inclusion of spin-orbit coupling may lead only to a slight broadening (few tens of meV) of the surface bands.



### 3. Results

#### 3.1. Experimental characterization of the surface structure

In Fig. 1 we show the surface structure of the clean Ge(001) surface, characterized by STM and LEED. The  $50 \times 50 \text{ nm}^2$  STM image of the as-cleaned Ge(001) surface in the left panel of Fig. 1 a) shows terraces with dimer rows and the typical  $c(4 \times 2)$  and  $p(2 \times 1)$  reconstruction. The left panel of Fig. 1 a) shows enlarged images of the  $p(2 \times 1)$  and  $c(4 \times 2)$  reconstructions. Under a sample bias of  $-1 \text{ V}$ , the buckled dimers of the  $c(4 \times 2)$  reconstruction appear in honeycomb arrangements, while the symmetric dimers of the  $p(2 \times 1)$  are arranged in linear dimer rows [30]. A closer look at the surface reveals an ordered pattern consisting of different  $c(4 \times 2)$  and  $p(2 \times 1)$  domains several dimer rows wide, occupying the same terrace. We point out that this highly ordered  $(4 \times 2)/(2 \times 1)$  domain pattern is consistent with extremely clean Ge(001) surfaces [30–32]. In Fig. 1 b), we show the LEED pattern acquired with an electron kinetic energy of  $110 \text{ eV}$ . We observe half-order diffraction spots corresponding to the  $p(2 \times 1)$  and  $p(1 \times 2)$  double domain pattern, labeled in black and red respectively (see Fig. 1 c for a labelling of the surface Brillouin zones). At quarter-order position, streaky diffraction spots indicate the presence of the double domain reconstruction related to  $c(4 \times 2)$  [8,9,15,33]. The SPM data in combination with the presented LEED pattern indicates the presence of a clean Ge(001) surface suitable for the subsequent photoemission study.

#### 3.2. Experimental valence band structure

In Fig. 2 we show the experimental valence band structure of the clean Ge(001) surface probed by ARPES at RT. The energy scale of each

plot is referenced to the position of the Fermi-level ( $E_F$ ), while the  $\Gamma$ -point is located at  $0 \text{ \AA}^{-1}$ . As can be seen from Fig. 1 c), an ARPES measurement aligned with the  $[010]$  in-plane crystallographic direction corresponds to  $\Gamma J'_2$  k-path, while the  $[110]$  direction corresponds to  $\Gamma J$  and  $\Gamma J'$  k-paths.

Intensity normalized ARPES spectra are shown in Fig. 2 a) and b) along the  $[010]$  and  $[110]$  directions. The valence band maximum (VBM) is found to be  $120 \text{ meV}$  below  $E_F$ . To better highlight the features of the valence band structure a high-pass filter was applied to Fig. 2 a) and b) and the results are shown in Fig. 2 c) and d), respectively. First, we highlight the three typical Ge hole bands along  $[010]$  in Fig. 2 c): one heavy hole band (HH), one light hole band (LH) and one split-off band (SO). HH and LH degenerate in the VBM, while SO is separated from the VBM by  $0.26 \text{ eV}$ , close to the expected value of  $0.29 \text{ eV}$  [13,16,34].

A notable feature in all graphs of Fig. 2 is located  $200 \text{ meV}$  above the VBM, labeled as  $SS_1$ , which shows a clear difference in the state dispersion along the  $[010]$  and  $[110]$  directions. Both the energy and the dispersion anisotropy are compatible with those of the surface unoccupied band of the  $c(4 \times 2)$  surface [13,19]. We also argue that this is the same feature as previously reported by standard ARPES experiments as occupied at RT by Kevan and Stoffel [8], while later being reported to be unoccupied at RT [14,15].

In Fig. 3 a) we show the evolution of the energy distribution curves (EDCs) around  $\Gamma$  as a function of sample temperature. The sample was cooled to liquid nitrogen ( $70 \text{ K}$ ) and subsequently measured at increasing temperatures, until RT was reached. The  $SS_1$  intensity vanishes at low temperatures and monotonically increases as the temperature ( $T$ ) is increased, indicating occupation by thermally excited electrons. Taking the natural logarithm of the  $SS_1$ -intensity and plotting it against  $1/T$  gives the Arrhenius plot shown as the inset in Fig. 3 a). The

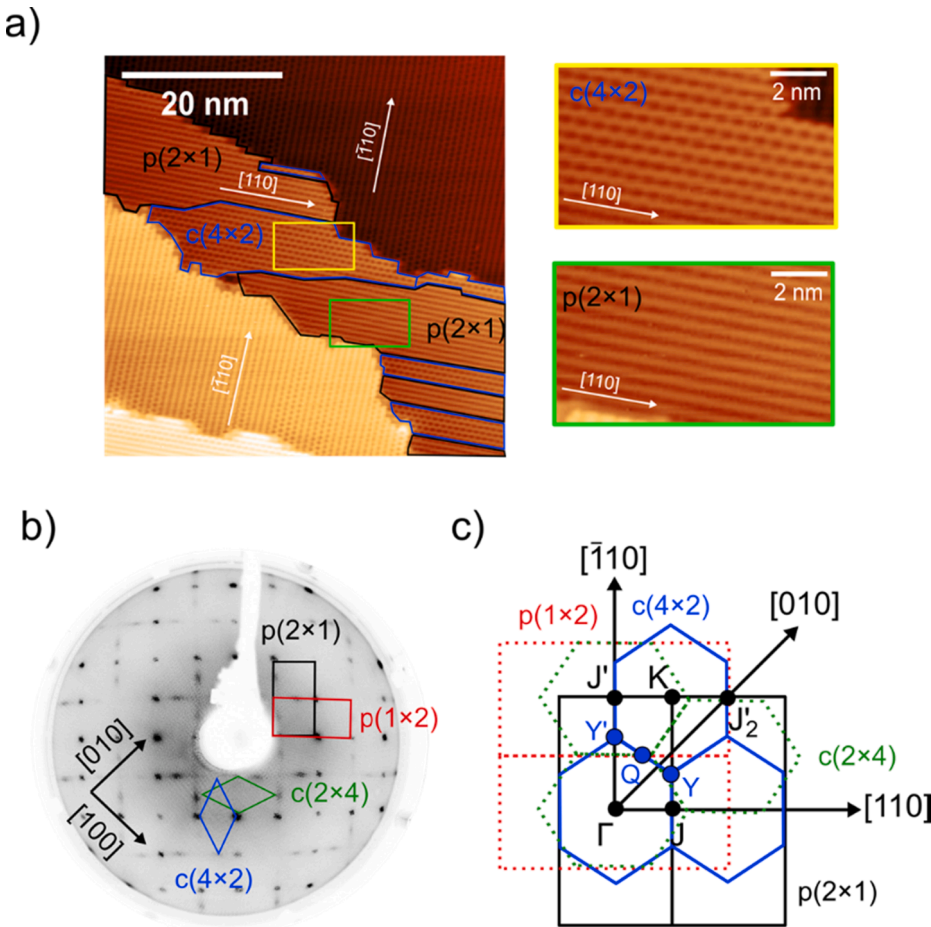


**Fig. 1.** a) The left panel shows an STM image of the clean Ge(001) surface, captured at a sample bias of  $-1 \text{ V}$  at room temperature. Examples of areas with the  $p(2 \times 1)$  and  $c(4 \times 2)$  reconstructions of the Ge(001) surface are marked. White arrows indicate the orientations of the dimer rows on each terrace with a rotation of  $90^\circ$  between the terraces. The right panel shows enlarged images of areas of the  $p(2 \times 1)$  (green) and  $c(4 \times 2)$  (yellow) reconstructions. b) LEED pattern of the cleaned Ge(001) at  $110 \text{ eV}$  kinetic energy captured at room temperature. Diffraction spots related to the  $p(2 \times 1)$  and  $c(4 \times 2)$  double domains are labeled. Schematics corresponding to the surface Brillouin zones of the respective Ge(001) surface reconstructions are shown in c). (For interpretation of the references to colour in this figure legend, the reader is referred to the web version of this article.)

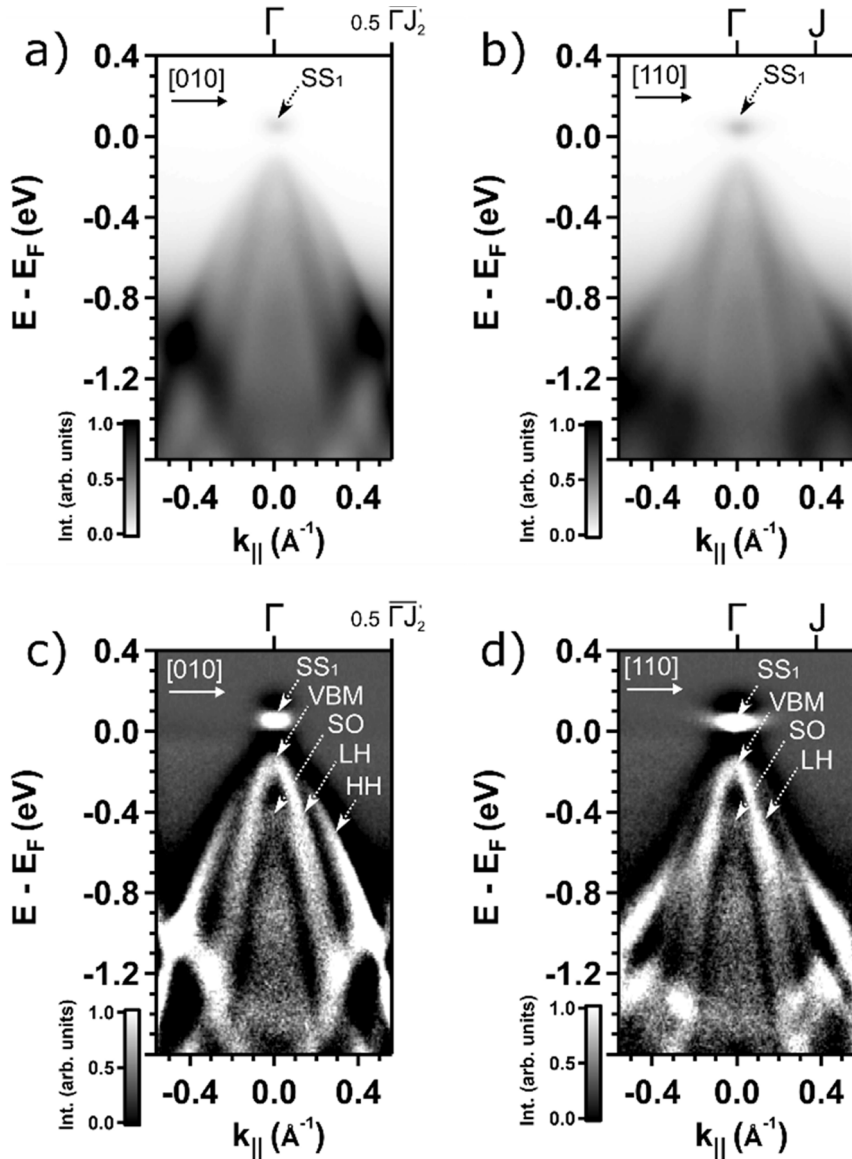


**Fig. 2.** a) and b) Show ARPES intensity plots of the clean Ge(001) valence band maximum measured with an excitation energy of 21.2 eV at room temperature along [010] and [110] direction respectively. The energy scale has been referenced to the position of the Fermi-level ( $E_F$ ) and the  $\Gamma$ -point is located at  $0 \text{ \AA}^{-1}$ . c) and d) show the same images as a) and b) after applying a high-pass filter to enhance visibility of features. The observation of a surface state  $SS_1$  is indicated in all figures. Valence band top (VBM), as well as the light hole (LH), heavy hole (HH) and split-off (SO) band are labeled in c) and d).

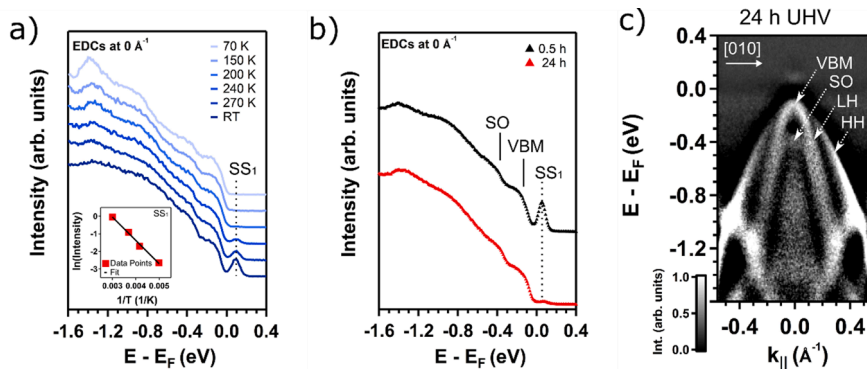


**Fig. 3.** a) Temperature-dependent energy distribution curves (EDCs) at  $0 \text{ \AA}^{-1}$  after cooling to liquid nitrogen temperatures (70 K) and repeated measurement while gradually increasing the sample temperature back to room temperature (RT). The inset shows the Arrhenius plot of the  $SS_1$  intensity between RT to 200 K, with error bars indicated by the symbol size. b) Comparison of EDCs at  $0 \text{ \AA}^{-1}$  at about 0.5 h (black) after the sample was cleaned and after 24 h in UHV (red). c) ARPES intensity plot of Ge(001) along [010] measured with an excitation energy of 21.2 eV at room temperature after the sample was cleaned and left in UHV for 24 h. (For interpretation of the references to colour in this figure legend, the reader is referred to the web version of this article.)

slope of the linear fit was multiplied by the Boltzmann constant, which gives an activation energy of  $\sim 100 \text{ meV}$ . This result indicates that the energy barrier to occupy  $SS_1$  is smaller than its 200 meV separation from the VBM.

Leaving a sample in UHV for 24 h after cleaning resulted in the

vanishing of  $SS_1$ , except for an almost unnoticeable shoulder, shown in Fig. 3 b). Nonetheless, the main features of the as-cleaned Ge(001) valence band structure shown in Fig. 2 still remain clearly visible (see Fig. 3 c). These results demonstrate that  $SS_1$  is a true surface state, sensitive to the adsorption of contaminants naturally present in the UHV

system. Furthermore, most of the observed Ge(001) surface band structure appears bulk-related, as its observation is not affected by surface contamination from the residual gas of the UHV.

### 3.3. First-principles calculations

To better interpret our experimentally derived spectral features, we calculated the surface band structure of Ge(001). We put a particular emphasis on the accurate description of the surface band structure of the  $c(4 \times 2)$  reconstruction and the differences from the  $p(2 \times 1)$  reconstruction with dimers in a buckled configuration. Note that the dimers of  $p(2 \times 1)$  on a real surface are constantly flip-flopping between the two buckled states [35], thus actually appearing symmetric under STM, as shown in Fig. 1 a). The top panels in Fig. 4 show the results of the calculations for the  $p(2 \times 1)$  reconstructed surface while in the bottom panels we report on the  $c(4 \times 2)$  reconstruction. In Fig. 4 a) - c) and e) - g), the partial density of states (DOS) has been weighted for  $D_{up}$ ,  $D_{down}$  and for atoms in the bulk-like position (Bulk). The  $k$ -axis is oriented along the  $\Gamma J_2$  direction, for comparison with dispersion along the  $[010]$  direction probed by ARPES. The partial DOS around  $\Gamma$  are compared to the experimental EDC in Fig. 4 d) and h). In the case of the  $p(2 \times 1)$  reconstructed surface, we observe the  $\pi$ -like states of the  $D_{up}$  at the valence band edge, which merge with the heavy hole bands of the bulk in the vicinity of the  $\Gamma$  point, thus becoming a surface resonance. As expected, and discussed in the introduction, the surface states of the  $D_{down}$  clearly manifest their antibonding  $\pi^*$  nature in contributing strongly to the conduction band edge. This reduces the gap around  $\Gamma$  to about 0.5 eV, but it is clearly observable in Fig. 4 d) that the conduction band edge is quite far from  $E_F$ . In fact, the buckling and the consequent charge transfer between the atoms of the dimers induce an energy separation between the  $\pi$ - and  $\pi^*$ -like surface states, which is large enough to preserve the semiconducting nature of the material even at its surface. These observations are in excellent agreement with the previous work by Seo et al. [16]. Notably, the  $\pi^*$ -like surface states nearly cross  $E_F$  in the case of the  $c(4 \times 2)$  terminated surface, as evidenced by the high intensity features in Fig. 4 f). The  $D_{down}$  generates two states close to the VBM, one being located about 0.6 eV above  $E_F$  and the other much closer to  $E_F$ . The latter nearly closes the surface energy gap but can be located at about 0.15 eV from the bulk-like VBM. In fact, we attribute this feature of the calculated surface band structure to the  $SS_1$  peak observed in the experiments, as shown in the DOS analysis of Fig. 4 h). The states nearly crossing  $E_F$  explains why the experimentally determined energy

barrier for the occupation of  $SS_1$  is smaller than the separation from the VBM.

This theoretical analysis highlights how crucial the differences between the two surface reconstructions are to understand the experimental evidence and the true electronic nature of the Ge(001) surface. To the best of our knowledge, a detailed direct comparison between the different surface reconstructions, based on first-principle calculations of the electronic band structure, has never been presented. The need for a very thick slab model combined with an advanced theoretical approach to get an accurate estimation of the bandgap are two major difficulties that we overcome here. Nevertheless, the physical origin of the different surface electronic properties of the  $p(2 \times 1)$  and the  $c(4 \times 2)$  surface reconstructions of the Ge(001) is fundamental and can be understood by a simple GGA based DFT calculation, as presented in the following. While not shown in this work, we calculated the  $p(2 \times 2)$  reconstruction electronic properties. In essence, they are identical to the  $c(4 \times 2)$  surface, which can be rationalized by the fact that the coupling within a dimer row is stronger than between adjacent rows. Therefore, the arguments that we will discuss to explain the differences between the  $p(2 \times 1)$  and the  $c(4 \times 2)$  reconstructions remain valid when comparing the  $p(2 \times 1)$  and the  $p(2 \times 2)$  reconstruction.

The first major difference between the surface states of the  $p(2 \times 1)$  and the  $c(4 \times 2)$  reconstruction originates from their different primitive cells and Brillouin zones, as shown in Fig. 1 c). In particular, there are  $k$ -vectors that are distinct in the  $p(2 \times 1)$  Brillouin zone but are equivalent in the  $c(4 \times 2)$  Brillouin zone: as a result of the  $(2 \times 1)$  Brillouin zone folding into the  $c(4 \times 2)$  one,  $K \equiv \Gamma$ ,  $Y \equiv Y'$  and  $J \equiv J'$  [36]. This is evident in Fig. 5 b), in which the gray lines are the band structure of the  $p(2 \times 1)$  reconstruction, but calculated by using the rhomboidal  $c(4 \times 2)$  unit cell. The band folding explains the formation of the two subbands from the initial conduction band (CB) of the “true”  $p(2 \times 1)$  surface (see Fig. 5 a). One may also note that these two subbands cross each other at different points of the reciprocal space, thus becoming degenerate. This degeneration is not allowed at the irreducible wedges of the first Brillouin zone, such as along  $\overline{Y\overline{Y}}$   $k$ -path of the  $c(4 \times 2)$  Brillouin zone. In fact, the crossing at the Q point of the two subbands of the folded  $p(2 \times 1)$  band structure is not existent in the  $c(4 \times 2)$  band structure. But the band folding and the rearrangement of the subbands, to avoid the band crossing, only partially explains the differences between the  $p(2 \times 1)$  and  $c(4 \times 2)$  surface states.

One of the most important aspects is the “repulsion” of the two subbands at  $\Gamma$ , causing the reduction of the  $c(4 \times 2)$  surface band gap

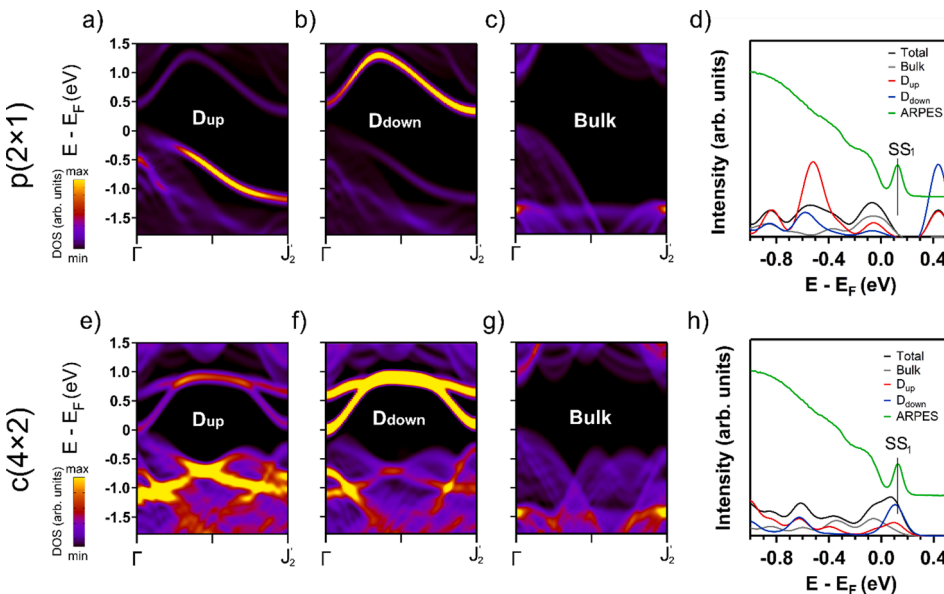
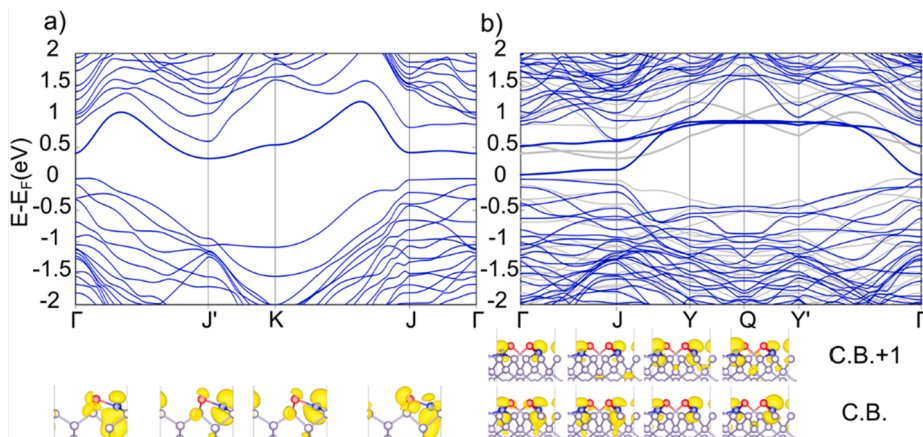


Fig. 4. The top panel shows the calculated band structure and partial density of states (DOS) of the Ge(001)  $p(2 \times 1)$  reconstructed surface, while the bottom panel shows the same for the Ge(001)  $c(4 \times 2)$  reconstructed surface. The intensities in a) - c) and e) - g) of the bands have been weighted by the partial DOS derived from the  $D_{up}$  atom, the  $D_{down}$  atom and an atom in the bulk-like position respectively. The images show the bands along the  $[010]$  direction. d) and h) show the DOS of the respective reconstructions around  $\Gamma$  in comparison with the experimental (ARPES) energy distribution curve around  $\Gamma$ . The Fermi-level ( $E_F$ ) is aligned to the VBM.



**Fig. 5.** The left panel a) shows the calculated band structure of Ge(001) p(2 × 1) and the right panel b) shows the calculated band structure of the Ge(001) c(4 × 2) reconstructed surface at the GGA level and by using slabs with only 12 atomic layers. Gray lines in the right panel show the band structure of the p(2 × 1) reconstruction modelled by using a rhomboidal supercell identical to the primitive cell of the c(4 × 2) reconstruction. The insets below each figure show the isosurface of the (pseudo-)charge density with the contribution of the wavefunction at the corresponding high symmetry points and for the conduction band (CB) or CB+1 states (thicker lines in the band structure plots). The  $D_{\text{up}}$  atoms are red, while the  $D_{\text{down}}$  atoms are colored blue.  $E_F$  is aligned to the VBM. (For interpretation of the references to colour in this figure legend, the reader is referred to the web version of this article.)

and thus the appearance of the  $SS_1$  peak in the experiments. The physical origin of can be understood by studying the contribution of the wavefunctions at each high-symmetry points to the charge density, plotted in the insets of Fig. 5. One may realize that the depiction of the formation of bonding (and antibonding)  $\sigma$ - and  $\pi$ -like band described in the introduction is oversimplified. The (lowest) CB state of the p(2 × 1) reconstruction also has contributions that originate from the hybridized  $sp^3$  orbitals of the dimer atoms, thus involving the back bonding atoms, particularly at the  $\Gamma$  and J points. By contrast, at  $J'$  and K the pure  $\pi^*$ -like character of the CB state is more faithful. This affects the c(4 × 2) surface states too: at the  $\Gamma$  and J points the CB state has a more  $\sigma^*$ -like character, as for the p(2 × 1) CB states; but for the CB+1 state the  $\pi^*$ -like bonding emerges, reflecting the folding of the p(2 × 1) CB states at K and  $J'$ .

In Table 1 the bond angles for the p(2 × 1) and c(4 × 2) surfaces are reported. A substantial difference between the two reconstructions is observed, particularly for the angle between the two hybrid  $sp^3$  bonds of the dimer atoms (backbonds, BB). The angles reveal that these bonds with the back bonding atoms are truly  $sp^3$ -like for the p(2 × 1) surface, while are much closed to an  $sp^2$ -like hybridization for the  $D_{\text{down}}$  of the c(4 × 2) surface, with p-like orbitals for the  $D_{\text{up}}$  dangling bonds. In fact, the bond angle difference also manifests in the charge density plots of Fig. 5. For instance, the charge density corresponding to the CB state at  $\Gamma$  for the c(4 × 2) surface, although evidencing a hybridization with the back bonding orbitals, has a shape much more similar to a  $p_z$ -like orbital than the corresponding state for the p(2 × 1) surface. In other words, the CB state of the c(4 × 2) surface has a more accentuated  $\pi^*$ -like (and less  $\sigma^*$ -like) character as compared to the p(2 × 1) CB state. As a result, its energy is lower in the c(4 × 2) band structure, getting closer to the  $E_F$ . The larger angle formed between the BB- $D_{\text{down}}$ -BB atoms of the c(4 × 2) reconstruction cause a reduced tilting of the  $p_z$ -like orbital of the  $D_{\text{down}}$  as compared to the p(2 × 1) reconstruction, leading to an higher energy of the  $\pi^*$ -like state (CB+1). In fact, the CB+1 state at  $\Gamma$  is at higher energy than it would be by simply folding the p(2 × 1) CB state (see Fig. 5 b). Finally, note the inversion of the charge density behavior between the CB and the CB+1 for the c(4 × 2) states at Y, as compared to the  $\Gamma$  and J point, due to the crossing between J and Y points. The two charge densities referred to as the CB and CB+1 state become almost identical

**Table 1**

Bond angles for the p(2 × 1) and c(4 × 2) surfaces. The first column shows the bonding angles between  $D_{\text{down(up)}}$ - and  $D_{\text{up(down)}}$ -backbonding (BB) atoms, while the second one shows the angles between BB- $D_{\text{down(up)}}$ -BB atoms.

Pivoting atom	$D_{\text{atom}}$ -BB atom	BB atom- BB atom
p(2 × 1) $D_{\text{down}}$	123.6°	110°
p(2 × 1) $D_{\text{up}}$	86°	104.5°
c(4 × 2) $D_{\text{down}}$	117°	122.3°
c(4 × 2) $D_{\text{up}}$	89.3°	95°

at the Q point. This theoretical analysis is crucial to understand the disappearance of the surface state  $SS_1$  with adsorption of contaminants. In fact, any adatom on the c(4x2) surface reconstruction breaks its periodicity and consequently the band folding discussed above, and at the origin  $SS_1$  state, becomes nonexistent.

Previous studies [16] of the Ge(001) surface concluded that the HH band shown in the ARPES spectra is heavily surface related, but a marked discrepancy between the dispersion of the experimental valence bands and the theoretical one was evidenced, needing further analysis. Thus, we show a direct comparison of the experimental dispersion in ARPES with the calculated band structures for c(4 × 2) and p(2 × 1) reconstructed surfaces in Fig. 6, in order to understand better the impact of the surface states on the valence band structure observed by ARPES, in particular HH and LH. The left panel shows the respective slab and the number of layers is indicated, while the center panel shows an array of the partial density of states (DOS) from atomic layers one to 31 of the slab, weighted by their intensity. The right panel shows enlarged figures of one surface and one bulk layer for each reconstruction. Surface features clearly vanish with deeper layers and around atomic layer 31, only bulk bands remain. Overlaying the experimental dispersion of HH and LH by grey lines, we show that the dispersion matches well with the bulk signal. While it appears that  $D_{\text{up}}$  of the p(2 × 1) reconstruction approaches HH at the VBM to form a surface resonance, the dispersion of  $D_{\text{up}}$  does actually not match well with HH. Thus, the valence band structure of Ge(001) mainly derives from bulk states, which also explains why after 24 h in UHV, the band structure remains clearly resolved, with only the true surface state  $SS_1$  vanishing due to adsorption of contaminants.

The analysis in Fig. 6 elucidates the need for a thick slab for accurate DFT calculations. The wavefunctions of the surface resonant states, particularly in the VB, penetrate very deep into the slab layers and their effects on the slab electronic states are discernible up to about 30 atomic layers from the surface. Thus, truncating these wavefunctions by using a thinner slab will affect the surface electronic states and introduce a significant error in the prediction of the surface bandgap, which has been estimated in about 0.25 eV for our 12-layers slab calculations.

#### 4. Discussion and conclusions

Our investigation of the pristine Ge(001) surface by ARPES show the occupation of a surface band ( $SS_1$ ) above the VBM at RT. This observation is in significant contrast to previous ARPES studies, reporting the state as only occupied at elevated temperatures [13–15]. The band is located above  $E_F$ , which excludes the flip-flop motion of the (2 × 1) domains as a possible origin, since the partially filled bands would have to be located at or slightly below  $E_F$  [18]. In the previous work by Jeon et al. [14] and Eriksson et al. [15], the band was argued to originate from the unoccupied band of  $D_{\text{down}}$  in the asymmetric p(2 × 1) reconstruction

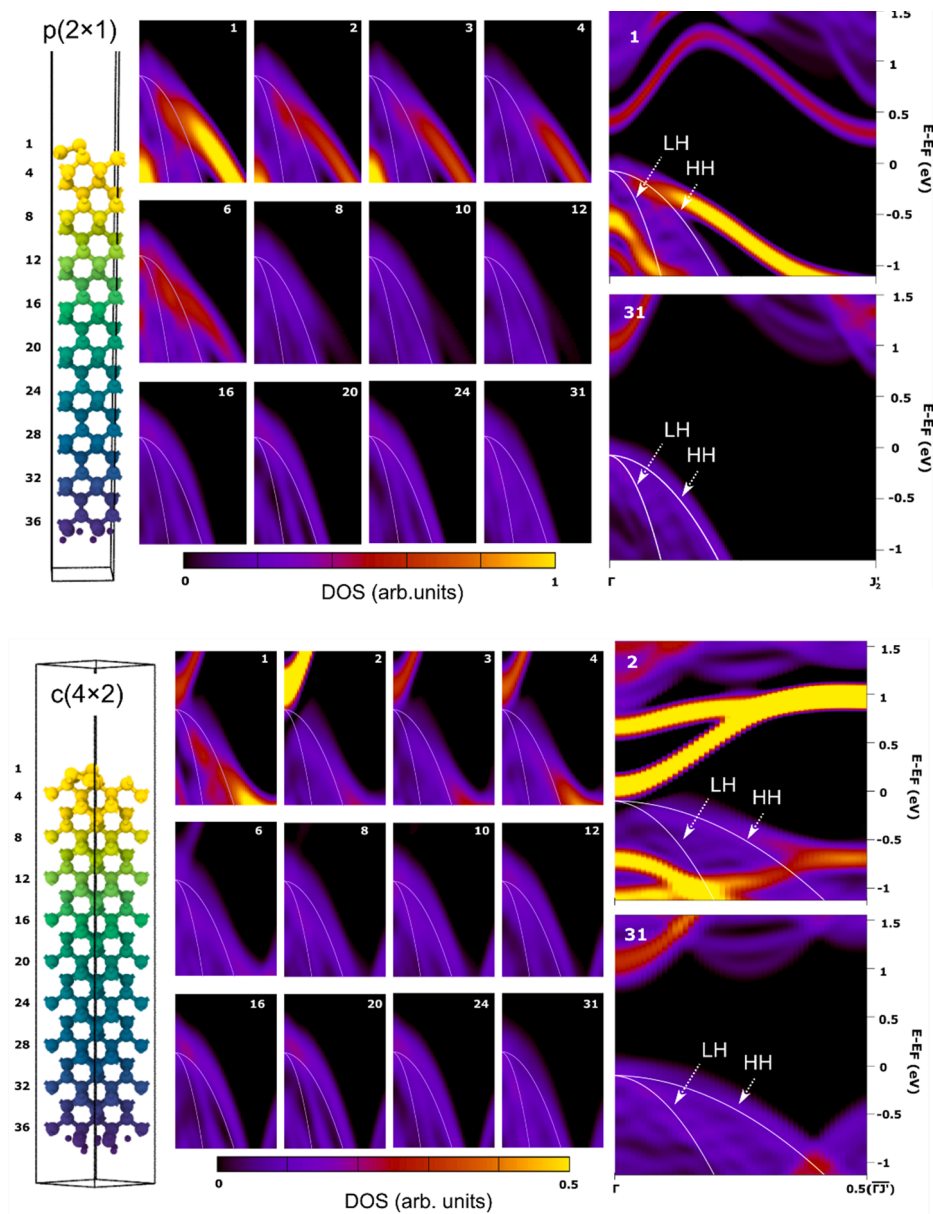


**Fig. 6.** The top panel shows the calculated band structure of the Ge(001)  $p(2 \times 1)$  reconstructed surface and the bottom panel shows the calculated band structure of the Ge(001)  $c(4 \times 2)$  reconstructed surface. On the left side of each panel is the atomistic slab model of the respective reconstruction and numbers indicate the atomic layers from surface (top) to bulk (bottom). The center part of each panel shows an array of the partial density of states (DOS) from atomic layers 1 to 31 of the slab, weighted by their intensity. Each of these figures has an energy scale ranging from 0.2 eV to  $-0.6$  eV and a  $k$ -path ranging from  $\Gamma$  to half the distance to  $J_2$ . The right side of each panel shows enlarged figures of the surface layer (layer 1 for  $p(2 \times 1)$  and layer 2 for  $c(4 \times 2)$ ) and bulk layer (layer 31) of the respective slabs. Solid grey lines in each figure indicate the experimental dispersion of the HH and LH.  $E_F$  is aligned to the VBM.

with a separation of 0.4–0.5 eV from the VBM. However, the SO reported here was assigned as the VBM in their reports, which led to an overestimation of the separation.

We observe a separation of 0.2 eV between VBM and  $SS_1$ , as well as anisotropic dispersions along the  $[010]$  and  $[110]$  directions whose origin was understood and explained by state-of-the-art DFT calculations. By comparing the surface electronic band structure of the  $p(2 \times 1)$  and  $c(4 \times 2)$  reconstructed surfaces, one may realize that in the former reconstruction, a sizable gap of 0.5 eV is formed by the bulk and surface states, and no features that could be related to  $SS_1$  are present. However, the  $c(4 \times 2)$  reconstruction shows two states within the bulk bandgap, one of which lies about 0.15 eV above the VBM and thus in excellent agreement with the  $SS_1$  probed experimentally. The detailed theoretical investigation also elucidates the physical origin of the surface states of the two reconstructions and explains the disappearance of the  $SS_1$  band upon surface contamination, essentially due to the lack of the  $(4 \times 2)$  surface periodicity.

The CB surface state of the  $c(4 \times 2)$  reconstruction, which nearly cross  $E_F$ , enables the occupation of the observed feature in ARPES by thermally excited electrons, even at RT. We proved thermal occupation

of  $SS_1$  by temperature-dependent measurements, giving an energy barrier of about 100 meV. In fact,  $SS_1$  is still observable at a sample temperature of 240 K. These observations are in agreement with report by Kanasaki et al. [19]. In their report, the relaxation pathways of electrons in unoccupied  $D_{\text{down}}$ -band of the  $c(4 \times 2)$  reconstruction were probed by time- and angle-resolved two-photo photoelectron spectroscopy, which also enables the probing of unoccupied states in contrast to the standard ARPES used here. In fact, in standard ARPES states above  $E_F$  should only be observable at elevated temperatures or in the case of conducting surface at RT. We ensured that the surface did not exceed RT during measurements, which implies that the Ge(001) surface must be conducting at RT due to the observation of  $SS_1$ .

Probing the surface after 24 h in UHV means that residual gas contaminates the surface and consequently  $SS_1$  disappears. However, the important features of the valence band structure could still be resolved by ARPES. If we compare the calculated dispersion of the  $(2 \times 1)$ - $D_{\text{up}}$  state with our experimental curvature, the dispersions do not fit [16]. We argue that the experimentally observed valence band features in ARPES mainly arise from the projected bulk states and that the  $(2 \times 1)$ - $D_{\text{up}}$  state barely contributes to the observed signal. This result also

implies that the observation of valence band features in ARPES is no guarantee for a pristine Ge(001) surface, since the bulk states are less sensitive to contamination compared to  $SS_1$ .

In conclusion, the observation of a surface state above the valence band top of Ge(001) surface probed by ARPES clashes with previous interpretations of a semiconducting Ge(001) surface at RT. We combined an experimental and theoretical approach to demonstrate a reduced gap in the Ge(001) subsurface band structure at RT. The gap is formed by the projected bulk states and the surface conduction band related to the  $c(4 \times 2)$  reconstruction. States nearly crossing the Fermi-level allow the occupation of the surface conduction band already at temperatures below RT, which implies that the Ge(001) surface must be conducting at RT. Thus, our results have important implications for the fundamental understanding of the Ge(001) surface electronic structure.

### CRediT authorship contribution statement

**Felix Reichmann:** Conceptualization, Validation, Formal analysis, Investigation, Writing – original draft. **Emilio Scalise:** Conceptualization, Validation, Formal analysis, Writing – original draft. **Andreas P. Becker:** Investigation, Writing – review & editing. **Emily V.S. Hofmann:** Writing – review & editing. **Jaroslav Dabrowski:** Writing – review & editing. **Francesco Montalenti:** Conceptualization, Supervision. **Leo Miglio:** Conceptualization. **Mattia Mulazzi:** Writing – review & editing. **Wolfgang M. Klesse:** Resources, Supervision. **Giovanni Capellini:** Formal analysis, Conceptualization, Supervision, Writing – review & editing.

### Declaration of Competing Interest

The authors declare that they have no known competing financial interests or personal relationships that could have appeared to influence the work reported in this paper.

### Acknowledgements

E.S. acknowledges the CINECA award under the ISCRA initiative, for the availability of high-performance computing resources and support. E.V.S.H. is partly supported by the EPSRC Centre for Doctoral Training in Advanced Characterisation of Materials (grant number EP/L015277/1).

### References

- [1] R. Pillarisetty, Academic and industry research progress in germanium nanodevices, *Nature* 479 (7373) (2011) 324–328, <https://doi.org/10.1038/nature10678>.
- [2] M. Hochberg, T. Baehr-Jones, Towards fabless silicon photonics, *Nat. Photonics* 4 (8) (2010) 492–494, <https://doi.org/10.1038/nphoton.2010.172>.
- [3] R. Geiger, T. Zabel, H. Sigg, Group-IV direct band gap photonics: methods, challenges, and opportunities, *Front. Mater.* 2 (2015) 1–18, <https://doi.org/10.3389/fmats.2015.00052>.
- [4] J. Chrétién, N. Pauc, F. Armand Pilon, M. Bertrand, Q.-M. Thai, L. Casiez, N. Bernier, H. Dansas, P. Gergaud, E. Delamadeleine, R. Khazaka, H. Sigg, J. Faist, A. Chelnokov, V. Reboud, J.-M. Hartmann, V. Calvo, GeSn lasers covering a wide wavelength range thanks to uniaxial tensile strain, *ACS Photonics* 6 (10) (2019) 2462–2469, <https://doi.org/10.1021/acsphotonics.9b00712>.
- [5] Y. Zhou, W. Dou, W. Du, S. Ojo, H. Tran, S.A. Ghetmiri, J. Liu, G. Sun, R. Soref, J. Margetis, J. Tolle, B. Li, Z. Chen, M. Mortazavi, S.-Q. Yu, Optically pumped GeSn lasers operating at 270 K with broad waveguide structures on Si, *ACS Photonics* 6 (6) (2019) 1434–1441, <https://doi.org/10.1021/acsphotonics.9b00030>.
- [6] G. Scappucci, C. Kloeffel, F.A. Zwaneburg, D. Loss, M. Myronov, J.-J. Zhang, S. De Franceschi, G. Katsaros, M. Veldhorst, The germanium quantum information route, *Nat. Rev. Mater.* (2020), <https://doi.org/10.1038/s41578-020-00262-z>.
- [7] F. Bottegoni, M. Celebrano, M. Bollani, P. Biagioni, G. Isella, F. Ciccacci, M. Finazzi, Spin voltage generation through optical excitation of complementary spin populations, *Nat. Mater.* 13 (8) (2014) 790–795, <https://doi.org/10.1038/nmat4015>.
- [8] S.D. Kevan, N.G. Stoffel, Metal-insulator transition on the Ge(001) surface, *Phys. Rev. Lett.* 53 (7) (1984) 702–705, <https://doi.org/10.1103/PhysRevLett.53.702>.
- [9] S.D. Kevan, Surface states and reconstruction on Ge(001), *Phys. Rev. B* 32 (4) (1985) 2344–2350, <https://doi.org/10.1103/PhysRevB.32.2344>.
- [10] E. Landemark, C.J. Karlsson, L.S.O. Johansson, R.I.G. Uhrberg, Electronic structure of clean and hydrogen-chemisorbed Ge(001) surfaces studied by photoelectron spectroscopy, *Phys. Rev. B* 49 (23) (1994) 16523–16533, <https://doi.org/10.1103/PhysRevB.49.16523>.
- [11] L. Kipp, R. Manzke, M. Skibowski, The surface band gaps of Ge(001)  $2 \times 1$ , *Surf. Sci.* 269 (1992) 854–859, [https://doi.org/10.1016/0039-6028\(92\)91361-E](https://doi.org/10.1016/0039-6028(92)91361-E).
- [12] L. Kipp, R. Manzke, M. Skibowski, An intrinsic metallic surface state on Ge(001)  $2 \times 1$ , *Solid State Commun.* 93 (7) (1995) 603–607, [https://doi.org/10.1016/0038-1098\(94\)00598-7](https://doi.org/10.1016/0038-1098(94)00598-7).
- [13] K. Nakatsuji, Y. Takagi, F. Komori, H. Kusunohara, A. Ishii, Electronic states of the clean Ge(001) surface near Fermi energy, *Phys. Rev. B* 72 (2005), 241308, <https://doi.org/10.1103/PhysRevB.72.241308>.
- [14] C. Jeon, C.C. Hwang, T.-H. Kang, K.-J. Kim, B. Kim, Y. Chung, C.Y. Park, Evidence from ARPES that the Ge(001) surface is semiconducting at room temperature, *Phys. Rev. B* 74 (12) (2006), <https://doi.org/10.1103/PhysRevB.74.125407>.
- [15] P.E.J. Eriksson, M. Adell, K. Sakamoto, R.I.G. Uhrberg, Origin of a surface state above the Fermi level on Ge(001) and Si(001) studied by temperature-dependent ARPES and LEED, *Phys. Rev. B* 77 (2008), 085406, <https://doi.org/10.1103/PhysRevB.77.085406>.
- [16] H. Seo, R.C. Hatch, P. Ponath, M. Choi, A.B. Posadas, A.A. Demkov, Critical differences in the surface electronic structure of Ge(001) and Si(001): ab initio theory and angle-resolved photoemission, *Phys. Rev. B* 89 (2014), 115318, <https://doi.org/10.1103/PhysRevB.89.115318>.
- [17] M.W. Radny, G.A. Shah, S.R. Schofield, P.V. Smith, N.J. Curson, Valence Surface Electronic States on Ge(001), *Phys. Rev. Lett.* 100 (2008), 246807, <https://doi.org/10.1103/PhysRevLett.100.246807>.
- [18] O. Gurlu, H.J.W. Zandvliet, B. Poelsema, Electronic properties of  $(2 \times 1)$  and  $c(4 \times 2)$  domains on Ge(001) studied by scanning tunneling spectroscopy, *Phys. Rev. Lett.* 63 (2004), 066101, <https://doi.org/10.1103/PhysRevLett.93.066101>.
- [19] J. Kanasaki, I. Yamamoto, J. Azuma, S. Fukatsu, Electronic structure of the surface unoccupied band of Ge(001)- $c(4 \times 2)$ : direct imaging of surface electron relaxation pathways, *Phys. Rev. B* 96 (2017), 115301, <https://doi.org/10.1103/PhysRevB.96.115301>.
- [20] P. Giannozzi, S. Baroni, N. Bonini, M. Calandra, R. Car, C. Cavazzoni, D. Ceresoli, G.L. Chiarotti, M. Cococcioni, I. Dabo, A. Dal Corso, S. de Gironcoli, S. Fabris, G. Fratesi, R. Gebauer, U. Gerstmann, C. Gougousis, A. Kokalj, M. Lazzeri, L. Martin-Samos, N. Marzari, F. Mauri, R. Mazzarello, S. Paolini, A. Pasquarello, L. Paulatto, C. Sbraccia, S. Scandolo, G. Sclauzero, A.P. Seitsonen, A. Smogunov, P. Umari, R.M. Wentzcovitch, QUANTUM ESPRESSO: a modular and open-source software project for quantum simulations of materials, *J. Phys. Condens. Matter* 21 (39) (2009) 395502, <https://doi.org/10.1088/0953-8984/21/39/395502>.
- [21] F. Han, Problems in solid state physics with solutions, *Illustrated ed.*, World Scientific, 2011, pp. 391, <https://doi.org/10.1142/8218>.
- [22] K. Sagisaka, J. Nara, D. Bowler, Importance of Bulk States for the Electronic Structure of Semiconductor Surfaces: Implications for Finite Slabs, *J. Phys.: Condens. Matter* 29 (2017), 145502, <https://doi.org/10.1088/1361-648X/aa5f91>.
- [23] M. Kuzmin, J. Mäkelä, J.P. Lehtiö, M. Yasir, M. Tuominen, Z.S. Jahanshah Rad, A. Lahti, M.P.J. Punkkinen, P. Laukkanen, K. Kokko, Imaging Empty States on the Ge(100) Surface at 12 K, *Phys. Rev. B* 98 (2018) 155322, <https://doi.org/10.1103/PhysRevB.98.155322>.
- [24] J.P. Perdew, A. Zunger, Self-interaction correction to density-functional approximations for many-electron systems, *Phys. Rev. B* 23 (1981) 5048, <https://doi.org/10.1103/PhysRevB.23.5048>.
- [25] M.Y. Hu, H. Sinn, A. Alatas, W. Sturhahn, E.E. Alp, H.-C. Wille, Y.V. Shyvd'ko, J. P. Sutter, J. Bandaru, E.E. Haller, V.I. Ozogin, S. Rodriguez, R. Colella, E. Kartheuser, M.A. Villeret, Effect of isotopic composition on the lattice parameter of germanium measured by x-ray backscattering, *Phys. Rev. B* 67 (2003) 113306, <https://doi.org/10.1103/PhysRevB.67.113306>.
- [26] Y.i. Yao, Y. Kanai, Plane-wave pseudopotential implementation and performance of SCAN meta-GGA exchange-correlation functional for extended systems, *J. Chem. Phys.* 146 (22) (2017) 224105, <https://doi.org/10.1063/1.4984939>.
- [27] G.G. Macfarlane, T.P. McLean, J.E. Quarrington, V. Roberts, Fine Structure in the Absorption-Edge Spectrum of Ge, *Phys. Rev.* 108 (6) (1957) 1377–1383, <https://doi.org/10.1103/PhysRev.108.1377>.
- [28] C. Rödl, J. Furthmüller, J.R. Suckert, V. Armuzza, F. Bechstedt, S. Botti, Accurate electronic and optical properties of hexagonal germanium for optoelectronic applications, *Phys. Rev. Mater.* 3 (2019), 034602, <https://doi.org/10.1103/PhysRevMaterials.3.034602>.
- [29] P.M. Sheverdyaeva, C. Hogan, A. Sgarlata, L. Fazi, M. Fanfoni, L. Persichetti, P. Moras, A. Balzarotti, Electronic structure of the Ge/Si(1 0 5) hetero-interface: an ARPES and DFT study, *J. Phys.: Condens. Matter* 30 (46) (2018) 465502, <https://doi.org/10.1088/1361-648X/aae66f>.
- [30] H.J.W. Zandvliet, The Ge(001) surface, *Phys. Rep.* 388 (1) (2003) 1–40, <https://doi.org/10.1016/j.physrep.2003.09.001>.
- [31] H.J.W. Zandvliet, B.S. Swartzentruber, W. Wulfhekel, B.J. Hattnik, B. Poelsema, Spontaneous formation of an ordered  $c(4 \times 2)$ - $(2 \times 1)$  domain pattern on Ge(001), *Phys. Rev. B* 57 (1998) R6803, <https://doi.org/10.1103/PhysRevB.57.R6803>.
- [32] W.M. Klesse, G. Scappucci, G. Capellini, M.Y. Simmons, Preparation of the Ge(001) surface towards fabrication of atomic-scale germanium devices, *Nanotechnology* 22 (14) (2011) 145604, <https://doi.org/10.1088/0957-4484/22/14/145604>.
- [33] R.J. Culbertson, Y. Kuk, L.C. Feldman, Subsurface strain in the Ge(001) and Ge(111) surfaces and comparison to Silicon, *Surf. Sci.* 167 (1) (1986) 127–140, [https://doi.org/10.1016/0039-6028\(86\)90789-2](https://doi.org/10.1016/0039-6028(86)90789-2).
- [34] T. Sakata, S.N. Takeda, K. Kitagawa, H. Daimon, Interband interaction between bulk and surface resonance bands of a Pb-adsorbed Ge(001) surface, *Semicond. Sci.*

- Technol. 31 (8) (2016) 085012, <https://doi.org/10.1088/0268-1242/31/8/085012>.
- [35] A. van Houselt, R. van Gastel, B. Poelsema, H.J.W. Zandvliet, Dynamics and Energetics of Ge(001) Dimers, Phys. Rev. Lett. 97 (2006), 266104, <https://doi.org/10.1103/PhysRevLett.97.266104>.
- [36] J. Dabrowski, H.-J. Müssig, Silicon Surfaces and Formation of Interfaces: Basic Science in the Industrial World, World Scientific, River Edge (2000), <https://doi.org/10.1142/3615>.





## Chapter 6

# Modification of the Ge(001) Subsurface Electronic Structure after Adsorption of Sn

The GeSn alloy offers carrier mobilities exceeding those of pure Ge, Si and their alloy [33, 34, 35], in addition to a band gap, tunable by variation of the Sn content [36, 37]. These promising characteristics have attracted the micro- and optoelectronic research communities [38], leading to the demonstration of GeSn-based photodiodes [39], light emitting diodes [40], photodetectors [41, 42], transistors [37, 43]. Ultimately, the first CMOS-integrable group IV laser was demonstrated and recent developments already show near to room temperature (RT) operation and electrical pumping [44, 45].

However, Sn contents in excess of 6 at.% [36, 46, 47] are necessary in the GeSn alloy in order to achieve both the fundamental direct band gap required for lasing and to improve carrier mobilities beyond those of strained Ge [48]. In view of a low solid solubility of Sn in Ge (1 % at thermodynamic equilibrium) [49], a large lattice mismatch (14.7 %) [50] and the relative thermal instability of the epitaxial GeSn alloy [51], these rather high Sn contents present a challenging task for fabrication of GeSn based devices. Non-equilibrium growth conditions can be chosen to achieve high Sn contents, at the cost of layer quality. Layer quality may be improved by step graded growth with gradually increasing Sn contents [52]. However, these structures can suffer from non-radiative recombination and leakage currents in the defective, low Sn-content buffer layers, resulting in detrimental effects on the device performance [38]. Another approach is the growth of multi-quantum well structures, which can suppress the formation of defects and separate carriers from defect interfaces, thus providing a novel pathway towards the achievement of GeSn-based RT lasing devices [53, 54, 55].

Fabrication of these multi-quantum structures requires deposition of very thin Sn layers [56] and, consequently, the adsorption mechanism of Sn on Ge(001) has been extensively studied by STM [57, 58, 59, 60]. However, a detailed investigation of the sub-surface structure as well as the modification of the Ge electronic states after adsorption of Sn has been missing.

Photoemission studies with a high sensitivity to surface core-level shifts could help to obtain structural details of the subsurface layers [61, 62, 63] and ARPES would permit to obtain details about the electronic states at the interface. The importance of such investigations becomes particularly evident in view of the strong Fermi-level pinning (FLP) at the Ge(001) surface, resulting in large

Schottky barrier heights of metal/n-Ge contacts [64]. The origin of the FLP has been the subject of multiple investigations [65, 66, 67] and was attributed to bulk evanescent states in the latest photoemission investigations [26, 68].

Therefore, a detailed understanding of the sub-surface (electronic) structure after adsorption of Sn would certainly help the fundamental research activities. Accordingly, I am presenting such an investigation in this chapter.

## Chapter 6: Publication Contribution Statement

This Chapter has been published in Applied Surface Science 599 (2022) 153884, <https://doi.org/10.1016/j.apsusc.2022.153884> as a subscription article [69]. Any use of this article requires the explicit written permission of Elsevier. For details, please refer to ScienceDirect "get rights and content".

The deposition of Sn relayed on the correct alignment of the sample to the Sn source, checking the homogeneity of the growth as well as a calibration of the deposition rate. Hence, I used a multi-technique approach by XPS, secondary ion-mass spectroscopy (SIMS) and STM.

The SIMS raw data were obtained by a commercial supplier (EAG Laboratories) on dummy-samples that I prepared. The XPS measurements and analysis was done by myself. STM was performed by Emily V. S. Hofmann and I analyzed the data together with her.

The surface cleaning of samples that were analyzed in the results section of this chapter was performed by me. The sputtering and annealing parameters were refined in multiple trial sessions and in close collaboration with Andreas P. Becker and Emily V. S. Hofmann, using feedback loops of ARPES, STM and LEED. The deposition of Sn with different thicknesses and the post-growth annealing were done by me.

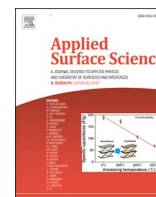
In the results section, the UPS, ARPES and LEED data were measured and analyzed by me. I performed the sample transfer in the system and the alignment for the three characterization methods. In addition, the measurement parameters were chosen entirely by me.

The STM raw data was obtained by Emily V. S. Hofmann and Andreas P. Becker, while I assisted during the measurements.

Using the UPS, ARPES, LEED and STM data, I prepared figures and a first draft of the results, which was then discussed with the co-authors. While drafting the manuscript, I was in charge to handle the communication and include the co-authors remarks.

I handled the submission process and was in charge to communicate with editor and reviewers. Furthermore, I led the revision of the article based on the reviewer's comments and took care of the re-submission.





## Full Length Article

## Modification of the Ge(001) subsurface electronic structure after adsorption of Sn

Felix Reichmann<sup>a,\*</sup>, Andreas P. Becker<sup>a</sup>, Emily V.S. Hofmann<sup>a,b,c</sup>, Neil J. Curson<sup>b,c</sup>, Wolfgang M. Klesse<sup>a</sup>, Giovanni Capellini<sup>a,d,\*</sup><sup>a</sup> IHP – Leibniz-Institut für innovative Mikroelektronik, Im Technologiepark 25, 15236 Frankfurt (Oder), Germany<sup>b</sup> London Centre for Nanotechnology, University College London, 17-19 Gordon Street, London WC1H 0AH, UK<sup>c</sup> Department of Electronic and Electrical Engineering, University College London, London WC1E 7JE, UK<sup>d</sup> Dipartimento di Scienze, Università Roma Tre, V.le G. Marconi 446, I-00146 Rome, Italy

## ARTICLE INFO

## Keywords:

(AR)PES

STM

GeSn

Thin-Films

Electronic Structure

## ABSTRACT

In this work, we investigate how the electronic structure of the Ge(001) surface is modified by the adsorption of Sn atoms. We extend a previously established growth model of the Sn layer formation on Ge(001) with a detailed analysis of surface core-level shifts, observing a prevalence of symmetric Sn ad-dimers at a Sn coverage above one monolayer. The valence band structure of Ge(001) reveals the appearance of a non-dispersive electronic state after the adsorption of Sn. We correlate the presence of this state to the interaction of electronic states from a Sn ad-dimer configuration with the surface resonances of the Ge up-dimer. Post-deposition annealing leads to full incorporation of Sn and, consequently, to the disappearance of valence band state attributable to Sn ad-atoms. Notably, the adsorption and/or incorporation of Sn removes a Ge(001) surface state above the valence band maximum. The Fermi-level remains pinned close to the valence band maximum, indicating the initial stages of a Schottky barrier formation. Overall, these results provide new fundamental insights into the electronic structure of Sn on Ge(001), crucial for the development of SnGe electronics devices, and more generally of use for understanding the controlled alloying of isoelectronic layered materials.

## 1. Introduction

GeSn alloys feature carrier mobilities exceeding those of Ge, Si, and their alloy [1,2]. Furthermore, the alloying of Ge with Sn induces a remarkable modification of the electronic band structure, enabling the formation of Group IV direct band gap materials [3,4]. These very promising characteristics have attracted the attention of the opto- and micro-electronic research communities [5]. This has led to the demonstration of a plethora of different GeSn-based devices, such as photodiodes [6], light emitting diodes [7], photodetectors [8,9], transistors [4,10] and, ultimately, to the first demonstration of a CMOS-integrable Group IV laser, with the recent achievements of both near-to-room-temperature (RT) operation [11] and electrical pumping [12].

Nonetheless, Sn contents in excess of 6 at.% [3,13,14] in the  $\alpha$ -GeSn alloy are necessary to achieve both the fundamental direct band gap required for lasing and to increase the carrier mobility beyond those of strained Ge [15]. Unfortunately, alloys with these apparently moderate Sn contents are challenging to obtain, owing to the extremely low solid

solubility of Sn in Ge (1% at thermodynamic equilibrium), the large Sn-Ge lattice mismatch (14.7%) [16,17] and the relative thermal instability of the epitaxial GeSn alloy [18]. Consequently, high Sn contents can be obtained only relying on non-equilibrium growth conditions, at the expenses of the epitaxial layer quality. The latter can be improved by step-graded growth GeSn layers with increasing Sn content [19,20,21]. However, these structures can suffer from non-radiative recombination and leakage currents in the defective, low Sn-content buffer layers, resulting in detrimental effects on the device performance [5].

Another approach to suppress the formation of defects is the growth of multi-quantum well (MQW) structures. MQW structures have the additional advantage of separating carriers from defect interfaces, providing a novel pathway towards the achievement of GeSn-based RT lasing devices [21,22,23,24]. Sn/Ge MQW structures can be grown by repeated cycles of few monolayer (ML) Sn deposition and subsequent Ge overgrowth, which result in the formation of thin, Sn-rich GeSn layers, thanks to the intermixing process [25]. Growing few-MLs of Sn on Ge requires precise control of the growth parameters and consequently

\* Corresponding author.

E-mail addresses: [reichmann@ihp-microelectronics.com](mailto:reichmann@ihp-microelectronics.com) (F. Reichmann), [capellini@ihp-microelectronics.com](mailto:capellini@ihp-microelectronics.com) (G. Capellini).<https://doi.org/10.1016/j.apsusc.2022.153884>

Received 21 January 2022; Received in revised form 31 May 2022; Accepted 31 May 2022

Available online 3 June 2022

0169-4332/© 2022 Elsevier B.V. All rights reserved.

understanding of the underlying growth mechanism of Sn on Ge(001).

First surface science studies by scanning tunneling microscopy (STM) have targeted the initial stages of the Sn layer formation on Ge(001) at the atomic scale [26,27,28,29]. However, an extension of this model towards Sn coverages above 1 ML is up to date missing. STM studies are also limited to the very surface layer, which means that photoemission studies with a high sensitivity to surface core-level shifts could help to obtain structural details of the sub-surface layers [30,31,32]. Furthermore, angle-resolved photoelectron spectroscopy (ARPES) would enable details about the electronic states at the interface to be obtained. The importance of such investigations becomes particularly evident in view of the strong Fermi-level pinning (FLP) at the Ge(001) surface, resulting in large Schottky barrier heights of metal/n-Ge contacts [33]. The origin of the FLP has been the subject of multiple investigations [34,35,36] and was attributed to bulk evanescent states in the latest photoemission investigations [37,38].

We believe that an improved understanding of the above-mentioned points would significantly contribute to both applied and fundamental research on Sn(Ge) nano- and MQW structures. Accordingly, we shall exploit in this article a multi-technique surface science approach that combines low-energy electron diffraction (LEED), STM microscopy and photoemission studies to address these open questions.

To compare the preparation of our samples with previous studies, we show in section 3.1 the surface structure analyzed by STM and LEED. We confirm a pristine Ge(001) surface after cleaning and the adsorption of Sn lines, eventually merging to a closed layer with increasing Sn coverage.

We will then discuss in section 3.2 the electronic structure after the adsorption of 0.3 ML, 0.6 ML and 1.2 ML Sn at RT by employing ultraviolet photoelectron spectroscopy (UPS) and angle-resolved photoelectron spectroscopy (ARPES). We extend the growth model initially proposed by STM studies with a detailed analysis of the UPS probed surface core-level shifts and explain the origin of a new Sn-related surface resonance, probed by ARPES after deposition of 0.3 ML Sn. In view of vanishing surface states related to the pristine Ge(001) surface, we go on to explain the persisting FLP after Sn adsorption.

The influence of post-growth annealing at 150 °C and 450 °C will be studied on samples with 0.3 ML Sn coverage in section 3.3. Investigation of the surface structure and electronic structure reveals the full incorporation of Sn at both temperatures and a vanishing of the Sn-related surface resonance, allowing us to conclude its origin.

Finally, we shall summarize our results and discuss the relevance of this work within research on GeSn.

## 2. Methods

Clean Ge(001) substrates were cut from an *n*-type (1–10 Ω·cm) 2" wafer. Samples were loaded into an UHV-system with an operating base pressure < 5·10<sup>-10</sup> mbar. The UHV-system comprises different chambers for 1) sample cleaning, 2) growth by MBE and characterization by LEED, 3) characterization by photoelectron spectroscopy (PES) and 4) STM. Chambers are connected to allow in-situ transfer of samples. After loading, samples were initially degassed for 2 h at 300 °C followed by a cool down. A clean and well-reconstructed surface was obtained by repeated cycles of Ar<sup>+</sup> ion sputtering and annealing, as we detailed in a previous paper [39].

Sn was deposited by molecular beam epitaxy with an electron-beam evaporator. A beam accelerating voltage of ~ 700 V and an emission current of ~ 36 mA resulted in a constant flux of 10 nA ± 0.1 nA. The deposition rate of Sn on Ge(001) at RT was calibrated by STM, secondary ion mass spectroscopy (SIMS) and X-ray photoelectron spectroscopy (XPS). With STM, individual Sn atoms were counted in several STM images after deposition on the Ge(001) substrate. For the calibration with SIMS, Sn was grown on the Ge(001) substrate and overgrown by Ge at RT, resulting in Ge/Sn/Ge(001) stacks and allowing to determine the dose (atoms/cm<sup>2</sup>) of Sn atoms for different Sn deposition

times. The atoms per cm<sup>2</sup> obtained by STM and SIMS were about equal for a given deposition time. Intensity ratios of Sn 4d and Ge 3d core-level in XPS were checked after 5 different deposition times of Sn on Ge(001), showing a linear dependence of deposition time and intensity ratios.

Based on these methods, a deposition rate of 0.002 ML/s was determined. Here, 1 ML is defined by the number of surface atoms of the Ge(001) surface (i.e. 6.24 × 10<sup>14</sup> cm<sup>-2</sup>). Since the initial stages of the Sn/Ge(001) interface formation are of particular interest for this study, Sn coverages of 0.3 ML, 0.6 ML and 1.2 ML have been deposited at RT. The influence of annealing steps at 150 °C and 450 °C were studied on samples with 0.3 ML Sn coverage and the annealing temperature was monitored by a low temperature pyrometer.

For all the photoemission experiments, we used the same Phoibos 150 spectrometer. The k-space resolved valence band structure was investigated by ARPES, using the He I line with an energy of 21.2 eV. The angular resolution in the ARPES experiments was better than 0.25° and the total energy resolution was better than 120 meV. Surface core-level shifts were studied by employing the He II line (40.8 eV) with a total energy resolution better than 140 meV and the angular acceptance of the electron lens was limited to ± 2°. For the investigation of Ge 3d and Sn 4d intensity ratios in dependence of the annealing temperature, we also used the monochromated Al Kα line (1486.7 eV), with a total energy resolution of the XPS experiments better than 600 meV. The work function of the spectrometer was calibrated by measuring the Fermi edge of a sputter-cleaned, polycrystalline Ag foil (99.99% purity). Binding energies in the photoemission experiments were referenced to the Fermi-level (E<sub>F</sub>) position of a Mo plate in electrical contact with the samples.

STM was performed on a SPECS SPM Aarhus 150 HT, equipped with a tungsten tip and in constant current mode with a sample bias of -1 V. An ErLEED 150 optics from SPECS was used to acquire the LEED images.

## 3. Results

### 3.1. Surface structure after adsorption of Sn at room temperature

First, we show in Fig. 1(a) the starting point for the subsequent investigation of the Sn/Ge(001) heterointerfaces, i.e. the pristine Ge(001) surface. In the 50 × 50 nm<sup>2</sup> STM image we can observe a well-ordered (4 × 2)/(2 × 1) domain pattern. In the corresponding LEED pattern (inset) half- and quarter-order spots can be observed, corresponding to the p(2 × 1) and c(4 × 2) reconstructions, respectively. These results are consistent with previous reports of atomically-clean Ge(001) surfaces [40,41,42].

In Fig. 1(b)–(d) we show 50 × 50 nm<sup>2</sup> STM images of the sample surface after adsorption of 0.3 ML, 0.6 ML and 1.2 ML Sn on Ge(001). Sn atoms are adsorbed predominantly in three distinct ad-dimer configurations, labeled here as Sn A, Sn B and Sn C features, respectively [28,29]. Fig. 1(e) illustrates the atomic configurations of these features. Their appearance in STM is indicated by magnified images in Fig. 1(e). The Sn A and Sn B features are oriented perpendicular to the Ge dimer rows, while their individual ad-dimers align parallel to the Ge dimers. However, there are two noticeable differences [28]: 1) The Sn A feature consists of symmetric ad-dimers, while Sn B feature consists of asymmetric (buckled) dimers, i.e. one atom is tilted upwards and the other is tilted downwards with respect to the (001) surface. The latter is accompanied by an electrical charge transfer from the dangling bond of the down-tilted atom to that of the up-tilted atom [28]. 2) The Sn B features form straight lines, while two ad-dimers of the Sn A feature are offset by one Ge-dimer.

Sn C features consist of buckled Sn ad-dimers that are oriented perpendicular to the Ge dimers (Fig. 1(e)). Notably, the Sn C feature ad-dimers reside between the Ge dimer rows and in between a Ge dimer, splitting the dimer and pushing the atoms back in bulk-like positions. In STM, the Sn C feature appears as a "zig-zag" row and/or in a honeycomb arrangement (Fig. 1(e), dotted rectangle). We notice that the up-tilted

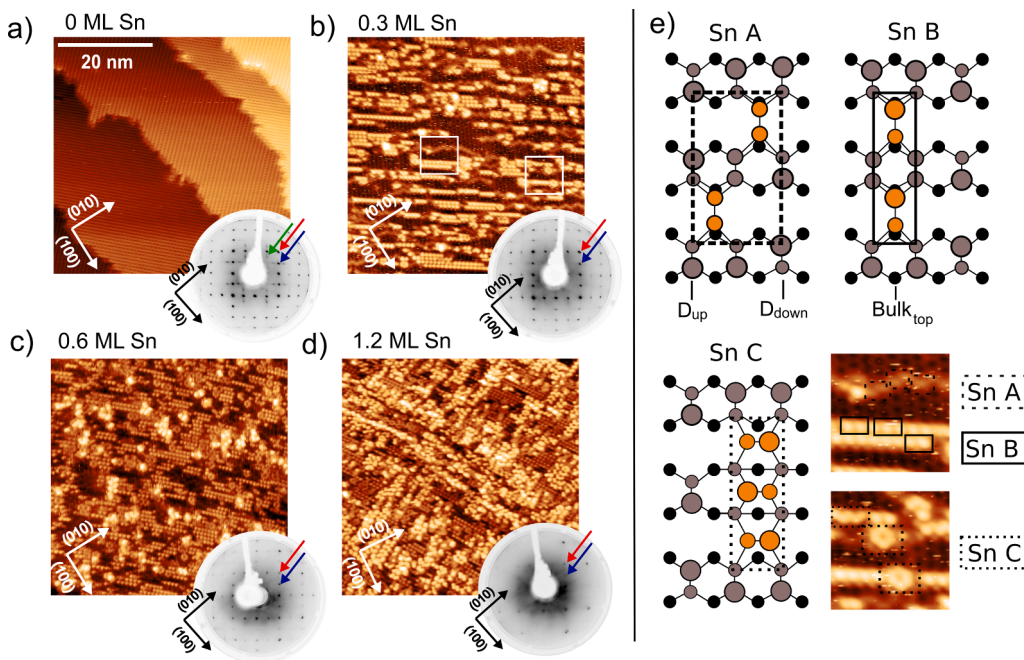


**Fig. 1.** a) – d) STM images measured at  $-1.0$  V sample bias (filled states) of the clean Ge(001) surface and after deposition 0.3 ML, 0.6 ML and 1.2 ML Sn at RT. The corresponding LEED patterns are shown in the bottom right of each image, captured with electron kinetic energies of a), b) 115 eV and c), d) 110 eV. Arrows indicate the presence of quarter-, half- and full-order diffractions spots (green, blue and red respectively). e) Atomic configurations of the Ge(001) surface with the Sn A, Sn B and Sn C features. The top-layer of the Ge bulk ( $\text{Bulk}_{\text{top}}$ ) and the up- ( $\text{D}_{\text{up}}$ ) and down-tilted ( $\text{D}_{\text{down}}$ ) dimer atoms are labeled. Sn ad-dimers are shown in orange. The Sn A feature is a symmetric ad-dimer, while the Sn B feature consists of up- and down-tilted Sn atoms. Both features align perpendicular to the Ge(001) dimer-rows. The Sn C features consists of up- and down-tilted atoms, oriented parallel to the Ge(001) dimer-rows. Images showing magnified regions of b) indicate the appearance of the Sn A (dashed), Sn B (solid) and Sn C (dotted) features in STM.

atoms of the Sn B and Sn C feature have almost the same apparent STM height, which may indicate a similar local density of states [29]. While all three features are generally observable at sub-ML coverage (0.3 ML), one can notice a prevalence of the Sn B feature, leading to the formation of Sn lines [28,29]. The relative abundance of Sn A and Sn C features is nearly equal. As the Sn coverage increases to 0.6 ML and then to 1.2 ML, the Sn lines merge and form a closed layer. While this doesn't affect the prevalence of the Sn B feature, the number of Sn C features grows about two times faster than the number of Sn A features towards a closing layer [29].

Looking at the LEED patterns in Fig. 1(a)–(d) we note a gradual change with increasing Sn coverage. The quarter-order diffraction spots, corresponding to the  $c(4 \times 2)$  reconstruction, vanish after deposition of 0.3 ML Sn. As the Sn coverage increases to 0.6 ML, the full- and half-order spots, corresponding to the  $(1 \times 1)$  and  $(2 \times 1)$  reconstructions begin to fade, and almost completely disappear after a Sn coverage of 1.2 ML. These findings are in good agreement with the report by Timofeev *et al.* [43], in which they studied the adsorption of Sn on Ge(001) with reflection high-energy electron diffraction, obtaining a phase diagram of the surface reconstructions. However, the absence of any additional diffraction spots in our LEED data indicates that growth of Sn at RT does not result in an ordered superstructure at the scale of the coherence length in LEED, which is about 10 – 20 nm [44]. As a result, the coherent diffraction of the Ge(001) substrate fades out against the scattering background produced by the Sn layer.

Overall, our results are in good agreement with the previous investigations by Tomatsu *et al.* [28] and Hofmann *et al.* [29].

### 3.2. Electronic structure after adsorption of Sn at room temperature

We shall now investigate the modification of the (sub-)surface electronic structure at the different stages of the Sn layer formation. Photoemission techniques are perfectly suited for this purpose, as they provide a direct way of probing the electronic structure of the occupied states. Since we employ excitation energies of 40.8 eV (UPS) and 21.2 eV (ARPES), our experiments combine high-energy resolution with high surface sensitivity. As a result, they are not only sensitive to the chemical environment of atoms at the surface, but also to their geometric arrangement.

In Fig. 2, the core-level analysis of the UPS Ge 3d core-level at the different stages of the Sn layer formation is presented. In Fig. 2(a) we show a side-view model of the atomic configurations at the Ge(001) surface and we can identify four non-equivalent atom positions: atoms in bulk position (Bulk), atoms in bulk-like position ( $\text{Bulk}_{\text{top}}$ ) and dimer atoms in the up- ( $\text{D}_{\text{up}}$ ) and down-tilted ( $\text{D}_{\text{down}}$ ) position. According to recent studies, a different binding energy (BE) of the Ge 3d core-level corresponds to each of these atomic configurations [31,32,45]. Consequently, we fitted the Ge 3d core-level with three surface related components ( $\text{D}_{\text{up}}$ ,  $\text{D}_{\text{down}}$  and  $\text{Bulk}_{\text{top}}$ ) and one bulk component (Bulk), as shown in Fig. 2(b) for the pristine Ge(001) surface.

Due to the spin-orbit splitting, each fitting component consists of two peaks, Ge  $3d_{5/2}$  and Ge  $3d_{3/2}$ , separated by 0.59 eV. For the branching ratio (BR), i.e. the intensity ratio of the  $3d_{3/2}$  to  $3d_{5/2}$  peaks, we obtained the lowest residuals when using a value of 0.55. Note that this experimental value is lower than the theoretical value of 0.67 due to the nearness of the photoelectron kinetic energy to the photoemission threshold [46,47]. Peak shapes were approximated by a Voigt-like convolution of Lorentzian and Gaussian peaks with full width at half maximum (FWHM) of 0.16 eV and 0.35 eV, respectively [31,45,48]. The final constraint assumes an equal population of  $\text{D}_{\text{up}}$  and  $\text{D}_{\text{down}}$  atoms at the surface, meaning their respective photoemission intensities should be the same. Therefore, the only free parameters of the fit in Fig. 2(b) were the  $3d_{5/2}$  peak positions and the intensities of Bulk,  $\text{Bulk}_{\text{top}}$  and  $\text{D}_{\text{down}}$ .

Based on previous reports, we can attribute the low BE shoulder of the spectrum to  $\text{D}_{\text{up}}$  [31,32,45,48]. The charge transfer from  $\text{D}_{\text{down}}$  to  $\text{D}_{\text{up}}$  leads to the lowest BE. Consequently, electrons from  $\text{D}_{\text{down}}$  should experience a higher BE [30]. In fact, initial state theory predicts a BE higher than the Bulk component, but Pehlke and Scheffler [49] have demonstrated the importance of screening effects in the photoemission process for the final state BE. The calculated values for the final state surface core-level shift of  $\text{D}_{\text{up}}$ ,  $\text{D}_{\text{down}}$  and  $\text{Bulk}_{\text{top}}$  with respect to Bulk were reported to be  $-0.67$  eV,  $-0.39$  eV and  $-0.16$  eV, respectively [49]. We have summarized the peak positions of the fit in Fig. 2(b) in Table 1: the Bulk component is located at  $-29.3$  eV, while  $\text{D}_{\text{up}}$ ,  $\text{D}_{\text{down}}$ , and  $\text{Bulk}_{\text{top}}$  are shifted by  $-0.51$  eV,  $-0.21$  eV, and  $0$  eV from Bulk towards lower BE, respectively. While these absolute values differ from Pehlke and Scheffler [49], their separation is in excellent agreement within an error

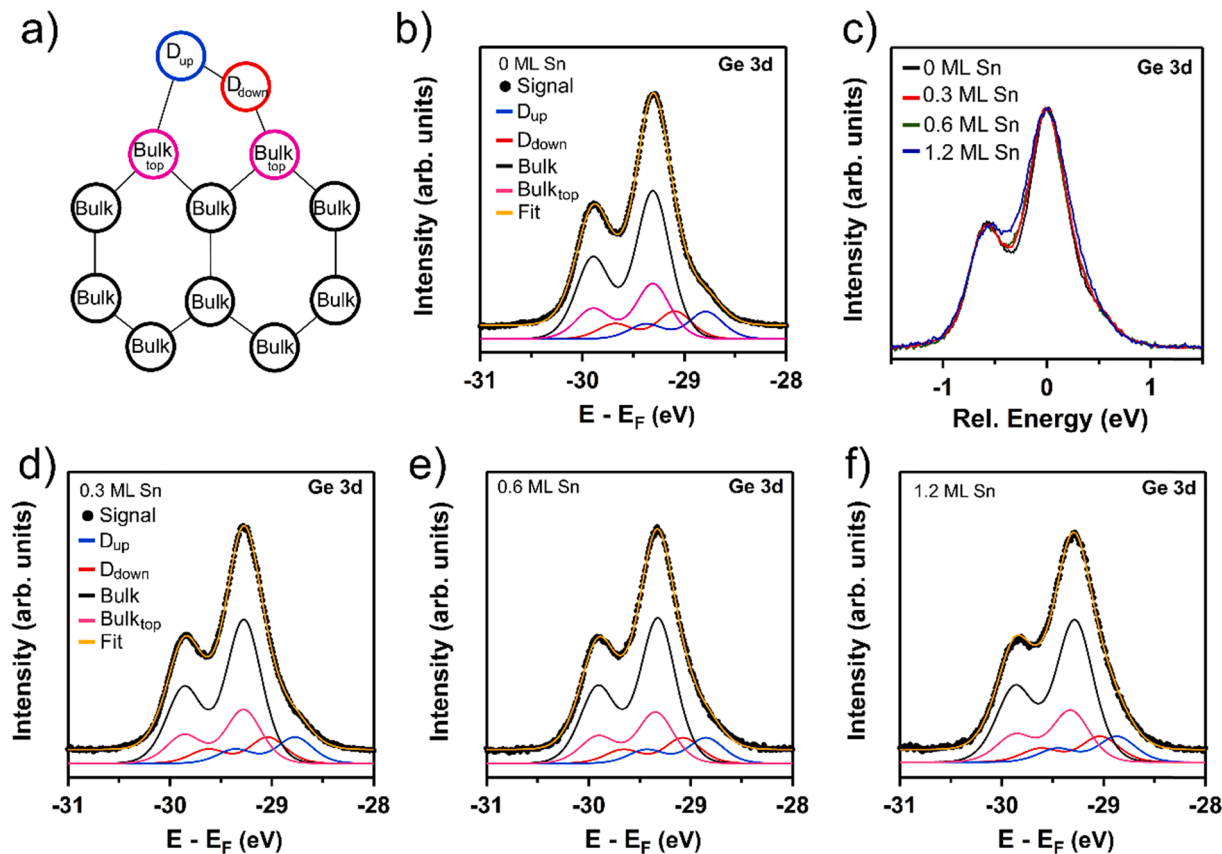


**Fig. 2.** a) Side-view model of the Ge crystal structure. Bulk atoms are labeled as “Bulk”, the top layer of bulk atoms as “Bulk<sub>top</sub>” and the down-atom of the dimer as “D<sub>down</sub>” and the up-atom of the dimer as “D<sub>up</sub>”. b) Ge 3d core-level region of the clean Ge(0 0 1) surface (0 ML Sn), measured with an excitation energy of 40.8 eV (normal emission). Four components are used to fit the spectrum, corresponding to D<sub>up</sub>, D<sub>down</sub>, Bulk<sub>top</sub> and Bulk. c) Ge 3d core-level region after deposition of 0 ML, 0.3 ML, 0.6 ML and 1.2 ML Sn at RT. The energy scale is referenced to the Ge 3d<sub>5/2</sub> Bulk position at -29.3 eV to highlight changes in the peak shape with increasing Sn coverage. d) –f) Peak fitting of the Ge 3d core-level region after deposition of 0.3 ML, 0.6 ML and 1.2 ML Sn at RT. The energy scale is referenced to the Fermi-level (E<sub>F</sub>).

**Table 1**

Surface core-level shifts of the Ge 3d core-level spectra with increasing Sn coverage. Fitting of the core-level yields components related to the up-atom of the dimer (D<sub>up</sub>), the down-atom of the dimer (D<sub>down</sub>), the top layer of the bulk atoms (Bulk<sub>top</sub>) and the bulk atoms (Bulk).

	Bulk <sub>top</sub> -Bulk (eV)	D <sub>down</sub> -Bulk (eV)	D <sub>up</sub> -Bulk (eV)
0 ML Sn	0	-0.21	-0.51
0.3 ML Sn	0.01	-0.23	-0.5
0.6 ML Sn	0.02	-0.24	-0.47
1.2 ML Sn	0.04	-0.26	-0.42

of ± 20 meV. A good agreement of our fit is also found with more recent experimental reports [31,45,48].

In Fig. 2(c) we display the comparison of the Ge 3d core-level of the clean Ge surface and after deposition of 0.3 ML, 0.6 ML and 1.2 ML Sn, respectively. The intensity was normalized to the largest peak height and the energy scale is referenced to the Bulk component, allowing for a better observation of peak shape changes. We note an enhanced broadening on both sides of the 3d<sub>5/2</sub> component with increasing Sn coverage, resulting in significantly less pronounced splitting of the 3d<sub>5/2</sub> and 3d<sub>3/2</sub> peaks at 1.2 ML Sn coverage. Fig. 2(d)–(f) show the Ge 3d spectra after adsorption of 0.3 ML, 0.6 ML and 1.2 ML Sn without any normalization of the BE. The same constraints as in Fig. 2(b) were applied to fit the spectra. Peak shifts with respect to the Bulk component are summarized in Table 1. We observe a shift of D<sub>down</sub> towards lower BE, while D<sub>up</sub> shifts towards higher BE with increasing Sn coverage, i.e. the components become closer in energy. This leads to the observed

broadening on the low BE side of the Ge 3d<sub>5/2</sub> peak. The broadening at high BE is related to the + 0.04 eV shift of the Bulk<sub>top</sub>. Independent of the Sn coverage, the intensity contributions of all components remain constant within ± 1 %. To better understand the driving force of the Sn coverage-dependent changes, we now examine the Sn 4d core-level.

Similar to the Ge 3d analysis, the first step in the UPS Sn 4d core-level analysis is to identify the BE states of Sn atoms at the surface and assign them to the fitting components. While Sn can be incorporated in the Ge (001) dimers already at RT, the intermixing was observed to be below 2% [29]. We can thus assume that the Sn 4d spectra in Fig. 3(a)–(c) for Sn coverages of 0.3 ML, 0.6 ML and 1.2 ML will almost exclusively originate from Sn atoms on top of the Ge(001) surface. Fig. 3(d) shows the side-view models of the atomic configurations of the Ge surface with the Sn A, Sn B and Sn C features according to Tomatsu et al. [28].

We could assume that each Sn feature corresponds to a component in the Sn 4d spectra. However, this assumption would completely neglect the buckling of the Sn ad-dimer atoms in the Sn B and Sn C features. The down-tilted and up-tilted Sn atoms would correspond to the same BE value, even though the up-tilted atoms receive additional charge from the down-tilted Sn atoms [28]. This should, within the initial state picture, result in a significantly lower BE [30]. Splitting up the Sn B and Sn C components into two components each, in order to account for the buckling, would result in a total of five fitting components (two for Sn B, two for Sn C and one for Sn A). Given the limited number of resolvable features in Fig. 3 (a)–(c) this appears unreasonable. Furthermore, it is not apparent why an up-tilted Sn atom in the Sn C feature would experience a different BE than an up-tilted Sn atom in the Sn B feature given their similar heights in STM [29]. Therefore, we are going to



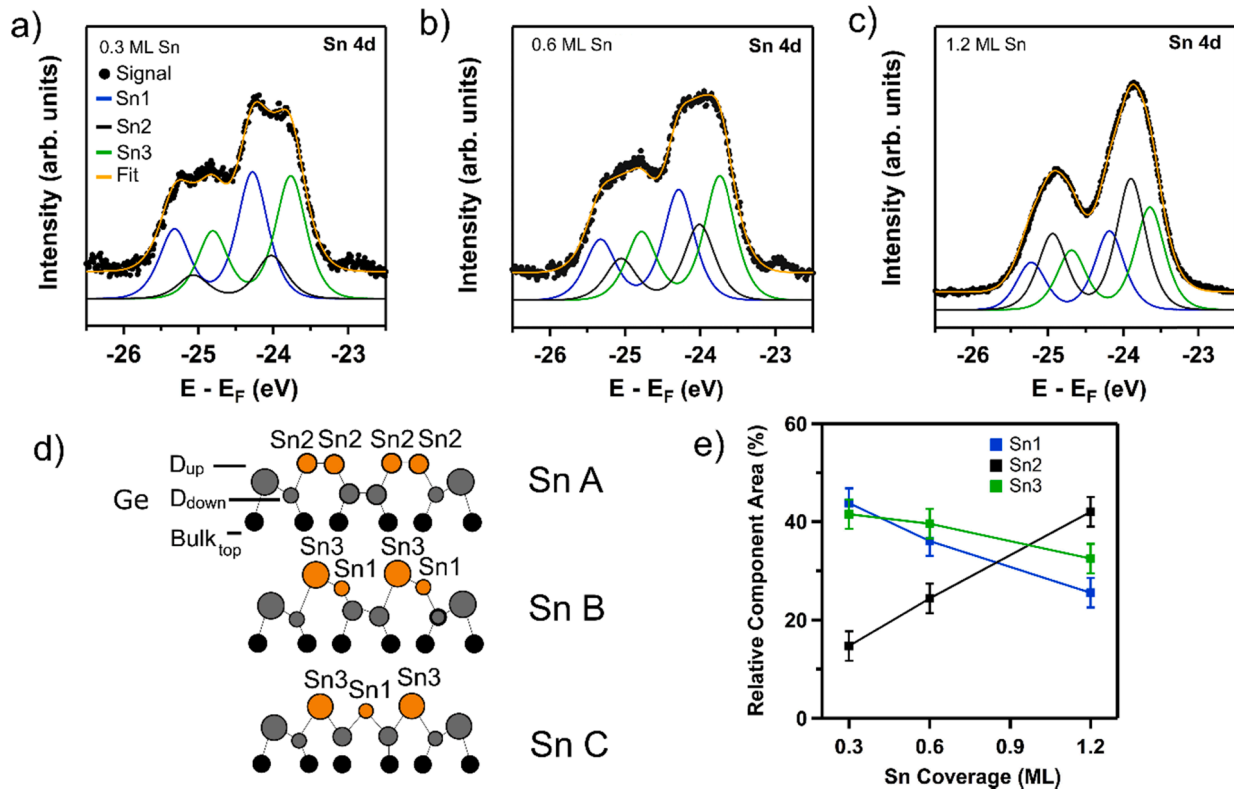


**Fig. 3.** a) – c) Sn 4d core-level regions measured with an excitation energy of 40.8 eV (normal emission) after deposition of 0.3 ML, 0.6 ML and 1.2 ML Sn at RT. The spectra were fitted with three components, labeled as Sn1, Sn2 and Sn3. d) Three side-view schematics of the Ge(001) dimer rows with Sn ad-dimers forming the Sn A, Sn B and Sn C features respectively, after Tomatsu *et al.* [28]. Sn atoms are shown in orange. Top-layer atoms of the Ge bulk are labeled as “Bulk<sub>top</sub>”, the down-atom of the Ge dimer as “D<sub>down</sub>” and the up-atom of the Ge dimer as “D<sub>up</sub>”. The Sn atoms have additional tags, indicating their correspondence with the Sn1, Sn2 and Sn3 components of the photoemission fits. e) Relative peak areas of the Sn1, Sn2 and Sn3 components with respect to the total Sn 4d peak intensity, shown as a function of the Sn coverage.

attribute fitting components to atomic positions of individual Sn atoms, rather than entire features.

Based on these assumptions, we identify three different BE components: down-tilted Sn atoms are labeled as Sn1, atoms in the symmetric configuration as Sn2, and the Sn atoms in the up-tilted position as Sn3. The lowest BE component is assigned to Sn3, while Sn2 and Sn1 should feature higher BE values. Not accounting for screening effects, we can assume that Sn2 experiences a lower BE because the dangling bonds are at least partially occupied. Therefore, we assign the highest BE value to the Sn1 component. We have fitted the 4d Sn core-level in Fig. 3(a)–(c) with the three components (Sn1, Sn2 and Sn3) following the same procedures used in the Ge 3d core-level case. The separation of the 4d<sub>5/2</sub> and 4d<sub>3/2</sub> spin-orbit components were fixed to be 1.04 eV and the BR was again 0.55 [47]. For the Voigt-like peak shapes, a Lorentzian FWHM of 0.22 eV and Gaussian FWHM of 0.42 eV were chosen, both of which lie in the range of experimentally reported values of Sn on Ge(1 1 1) [30]. The free parameters were the relative intensities of each component and the 4d<sub>5/2</sub> peak positions.

We note that the BE values do not shift in dependence of the Sn

**Table 2**

Relative spacing of the Sn1, Sn2 and Sn3 components that were used to fit the Sn 4d spectra. Sn1 corresponds to atoms in down-tilted position, while Sn2 corresponds to atoms in symmetric and Sn3 to atoms in up-tilted position in the Sn ad-dimers.

	Sn2-Sn1 (eV)	Sn3-Sn1 (eV)	Sn3-Sn2 (eV)
0.3 ML Sn	0.26	0.51	0.25
0.6 ML Sn	0.27	0.53	0.26
1.2 ML Sn	0.27	0.51	0.24

coverage and thus their relative spacing remains fairly constant at a value of about 0.26 eV (see Table 2). However, changes occur in their relative contribution to the total peak intensity, as shown in Fig. 3(e). Notably, Sn1 and Sn3 contributions are about equal at sub-ML coverages, which nicely fits with our assumption that Sn1 and Sn3 are assigned to the down- and up-tilted atoms of buckled dimers. Due to the adsorption of Sn in ad-dimers, down- and up-tilted Sn atoms should always exist in equal numbers. A larger contribution of Sn3 at 1.2 ML Sn can be attributed to an increasing amount of incorporated Sn, which prefers the up-position in the heterodimer [27,50]. Due to the limited resolution, it is not possible to discriminate between the Sn-Sn and Sn-Ge ad-dimers in terms of BE in the Sn 4d spectra. Likewise, it will be difficult to justify a separate component in the Ge 3d spectra. Instead, a larger contribution of D<sub>down</sub> compared to D<sub>up</sub> in the Ge 3d spectra could be expected. However, based on the intensity difference between Sn1 and Sn3, only 5 % of the Sn atoms have incorporated at a Sn coverage of 1.2 ML. The contribution of dimer components in the Ge 3d spectra is about 22 % in total, which means at a Sn coverage of 1.2 ML the intensity difference between D<sub>up</sub> and D<sub>down</sub> would have to be ~ 1 %, e.g. at the scale of the intensity error bar.

We proceed with the analysis of the relative component areas in Fig. 3(e) and a comparison with the fractions reported by STM [29]. Since the Sn1 and Sn3 components in UPS share the Sn B and Sn C features observed by STM, it is not possible to compare them individually. However, it is possible to directly compare the fraction of Sn A to the contribution of Sn2, because there is no overlap with other features in UPS. Based on the report by Hofmann *et al.* [29], the fraction of symmetric Sn A features at a Sn coverage of 0.5 ML can be estimated to be 23 %, which is in very good agreement with the Sn2 contribution of 24% in UPS at a Sn coverage of 0.6 ML. However, at a Sn coverage of 1.2

ML, the UPS measured contribution of Sn<sub>2</sub> is about 42 %. This value is much larger than the fraction of symmetric Sn A features reported by Hofmann *et al.* [29] with STM, which we estimated to be around 18 % at Sn coverage of 1.24 ML. Furthermore, a relative increase of the symmetric Sn ad-dimers between 0.5 ML and 1.2 ML was not reported. We explain this mismatch of results between STM and UPS for Sn coverages approaching 1.2 ML by the formation of the second Sn layer: Buckled Sn ad-dimers of the first layer change into symmetric configuration underneath the Sn ad-dimers of the second layer. This observation remained hidden in STM, because only the very surface atoms can be probed, while UPS probes a sub-surface region.

According to Fig. 3(d), adjacent symmetric Sn ad-dimers in the Sn A feature cause the formation of symmetric Ge dimers ( $D_{\text{sym}}$ ). Going back to our analysis of the Ge 3d core-level, we argue that the gradual shift of  $D_{\text{down}}$  and  $D_{\text{up}}$  towards each other with increasing Sn coverage can be interpreted by a growing number of  $D_{\text{sym}}$ . The BE of  $D_{\text{sym}}$  is expected to lie between  $D_{\text{down}}$  and  $D_{\text{up}}$ , but since we did not assign a separate component for  $D_{\text{sym}}$ , the fit accounts for their increasing contribution by shifting  $D_{\text{down}}$  and  $D_{\text{up}}$ . In fact, when we added a fifth component related to  $D_{\text{sym}}$ , we obtained a good fit that supports our interpretation (see supporting information). However, adding additional components also

increases the danger of overfitting. Therefore, we infer that the more robust fit is based on the four components shown here.

Whether the formation of  $D_{\text{sym}}$  is induced by charge transfer, stress or a mixture of both remains an open question without any dedicated first-principles calculations. Recently, Ponath *et al.* [32] explained the formation  $D_{\text{sym}}$  after adsorption of Eu at sub-ML coverages by a charge transfer from Eu to Ge. The conclusion was rationalized by the higher electronegativity of Ge (2.02) compared to Eu (1.01) and changes in the Eu chemical state. Additionally, a breakup of dimers at coverages of 1 ML was observed. Since Ge (2.02) is only slightly more electronegative than Sn (1.73) [51], a BE shift solely based on charge transfer appears unlikely. Noteworthy is the observation that Sn can induce enough stress on the Ge(001) surface to break up the Ge dimers as part of the Sn C feature formation [28]. Therefore we propose that the formation of  $D_{\text{sym}}$  is mainly driven by the stress that Sn induces on the Ge(001) surface. Since several features in Ge(001) valence band structure are related with the dimerization and reconstruction of the surface, it is then worthwhile to investigate the valence electronic states by ARPES, which can directly probe the k-space resolved valence band structure.

To address the modification of the valence states upon adsorption of Sn, we show in Fig. 4(a)–(d) the ARPES intensity maps of the valence

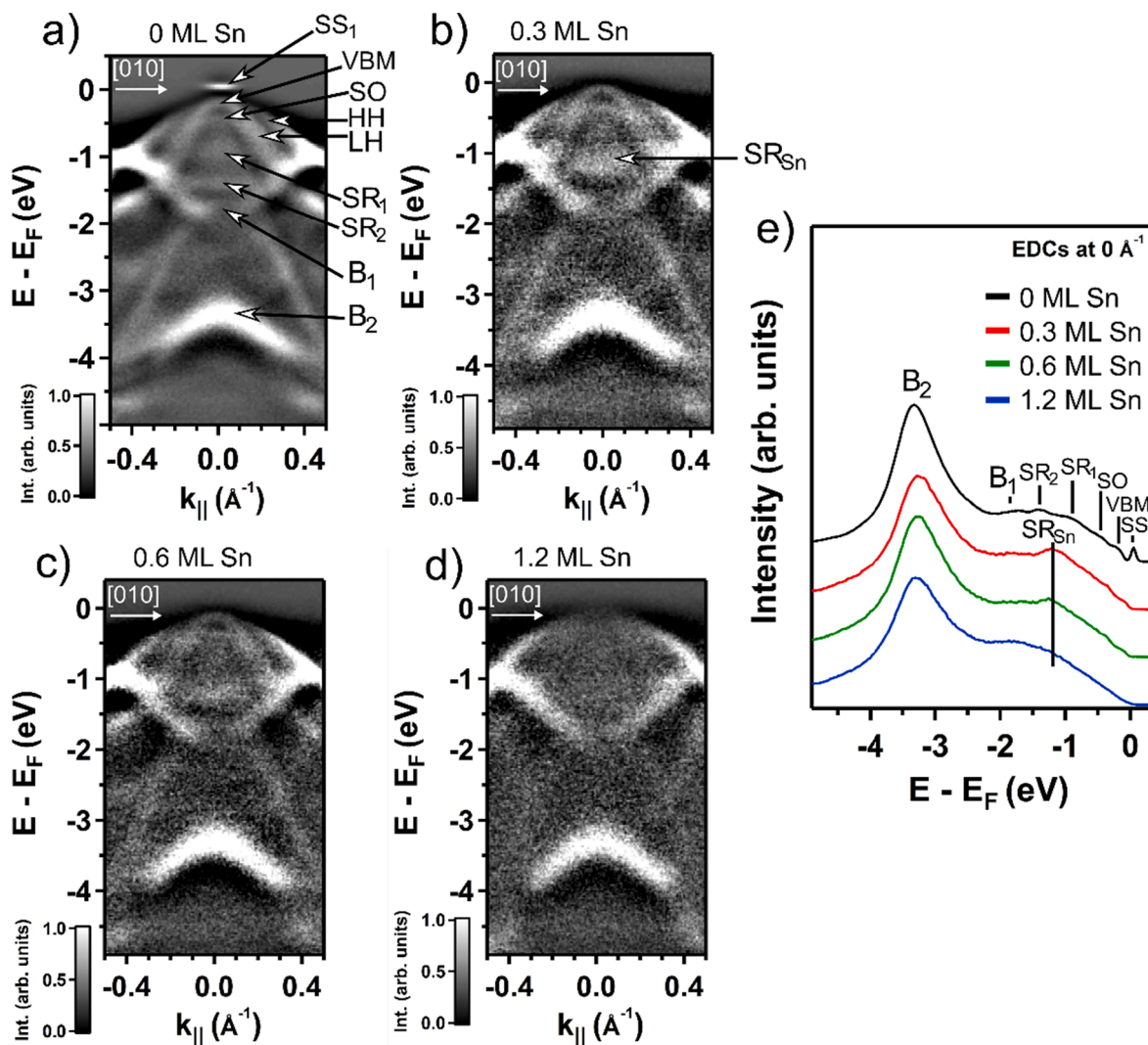


Fig. 4. a) – d) Grey scale ARPES intensity maps of the clean Ge(001) surface (0 ML Sn) and after deposition of 0.3 ML, 0.6 ML and 1.2 ML Sn at room temperature (RT), measured with an excitation energy of 21.2 eV. The images were modified by a high-pass filter to enhance the visibility of spectral features. Ge bulk states ( $B_x$ ), surface resonances ( $SR_x$ ), a surface state ( $SS_1$ ) as well as the typical light hole (LH), heavy hole (HH) and split-off band (SO) and valence band maximum (VBM) are indicated in a). e) Shows a comparison of the energy distribution curves (EDCs) extracted around the  $\Gamma$ -point ( $0 \text{ \AA}^{-1}$ ) of the clean Ge(001) surface and after deposition of 0.3 ML, 0.6 ML and 1.2 ML Sn at RT. A Sn-related state ( $SR_{\text{Sn}}$ ) can be observed for Sn coverages of 0.3 ML and 0.6 ML.

band structure with increasing Sn coverage. A high-pass filter was applied to highlight spectral features, similar to what we have done in our previous report [39]. The  $\Gamma$ -point of the surface Brillouin zone is located at  $0 \text{ \AA}^{-1}$  on the  $k$ -axis and the direction is oriented along  $[010]$ , which corresponds to the  $\Gamma J_2$ -path in the surface Brillouin zone. Fig. 4 (e) shows a comparison of the corresponding energy distribution curves (EDCs) extracted from the ARPES raw-data at the  $\Gamma$ -point.

Starting with the pristine Ge (001) surface, we can observe in Fig. 4 (a) the typical features related to light hole (LH), heavy hole (HH) and split-off band (SO). SO is separated from the valence band maximum (VBM) by 0.26 eV, which is close to the theoretical value of 0.29 eV [52,53]. The surface state  $SS_1$  0.2 eV above the VBM is ascribed to the surface conduction band formed by  $c(4 \times 2)$  reconstruction and the occupation by thermally excited electrons at RT [39]. Notably,  $SS_1$  vanishes after adsorption of Sn, as expected from its true surface state nature. Sn can be considered to act as an "impurity" to the Ge surface reconstruction, interfering with the conduction band formed by the unoccupied orbitals of the  $D_{\text{down}}$  atoms. We observe a gradual smearing of bands with increasing Sn coverage, which becomes particularly evident at a Sn coverage of 1.2 ML in Fig. 4(d) and (e). Even bulk-related features such as the VBM and SO seem to disappear at this stage. The separation of 0.26 eV between VBM and SO remains constant in the range of 0.3 ML and 0.6 ML, where the features were still resolvable. The observed smearing and broadening of bands is consistent with the observations from the surface structure in section 3.1: the growth of Sn layers dissolves the Ge(001) surface reconstructions, thus broadening the valence states.

After Sn deposition of 0.3 ML, an additional surface feature  $SR_{\text{Sn}}$  appears in Fig. 4 (b), (e) and is located at  $-1.2 \text{ eV}$  around  $0 \text{ \AA}^{-1}$ , showing no dispersion. Remarkably, this feature is located between the Ge(001)  $SR_2$  and  $SR_1$  surface resonances, which have been reported to originate from  $D_{\text{up}}$  [37,39]. The intensity of the feature decreases at a Sn coverage of 0.6 ML, eventually vanishing at 1.2 ML Sn coverage. These findings correlate with the observations from the Ge 3d and Sn 4d core-level analysis: the coverage with symmetric Sn ad-dimers (Sn2 component in the Sn 4d spectra) is below 20% at a Sn coverage of 0.3 ML and we observed only small BE shifts of the Ge dimer components. As the Sn coverage increases to 0.6 ML and 1.2 ML, a relative growth of Sn2 in the Sn 4d spectra and larger BE shifts of the Ge dimer components in the Ge 3d spectra were found. Given these observations and a BE that lies between the  $D_{\text{up}}$  surface resonances  $SR_1$  and  $SR_2$ , we argue that the origin of  $SR_{\text{Sn}}$  may be an interaction of Sn with  $D_{\text{up}}$ . From the dispersion-less characteristic of  $SR_{\text{Sn}}$  and the high localization in  $k$ -space, we conclude that a certain ad-dimer configuration within the Sn-lines leads to the observed state. We assume that the Sn B feature could be responsible for this interaction, as it is by far the most abundant feature at a Sn coverage of 0.3 ML, at which  $SR_{\text{Sn}}$  showed the highest intensity. Additionally, the vanishing of  $SR_{\text{Sn}}$  correlates with an increasing population of Sn A and Sn C features. The tilt angle of the  $D_{\text{up}}$  atoms is only slightly changed underneath the Sn B feature, while more forceful changes are observed as part of the Sn A and Sn C feature formation [28]. A definitive conclusion will require theoretical calculations, now ongoing.

Notably, we observe no significant changes in the BE positions of valence band features with increasing Sn coverage. While some of the qualitative changes, such as the smearing of states close to the VBM, could influence this observation, the  $B_2$  bulk-related feature remains well resolvable up to a Sn coverage of 1.2 ML and shows no significant shifts within  $\pm 20 \text{ meV}$ . The same holds for the Bulk component of the Ge 3d core-level in Fig. 2, which showed the same BE of  $-29.3 \text{ eV}$ . Based on these observations we conclude that  $E_F$  remains pinned close to the VBM and that no significant band bending changes occur. In a previous work [39], we showed with first-principle calculations that the occupation of  $SS_1$  by thermally excited electrons can be explained by  $c(4 \times 2)$  related-states nearly crossing  $E_F$ . Our observations here indicate that

these surface states are not related to the strong FLP, due to the vanishing of  $SS_1$  with increasing Sn coverage. It is therefore reasonable to assume that the strong FLP at the surface stems from bulk evanescent states that show lower sensitivity to the adsorption of Sn.

So far, we have investigated the modifications of the electronic structure after adsorption of Sn at RT with limited incorporation of Sn. We observed changes in the relative population of symmetric and buckled Sn ad-dimers in our core-level analysis. While the valence band structure exhibits a Sn-related feature at sub-ML coverage, a vanishing is observed at 1.2 ML Sn. Furthermore, no Sn coverage dependent changes in the position of  $E_F$  were observed, indicating that the strong FLP is unaffected by the adsorption of Sn. Keeping these observations in mind, we are now going to examine the electronic structure changes after Sn adsorption and post-growth annealing.

### 3.3. Post-growth annealing after adsorption of Sn

Before we inspect the electronic structure of two 0.3 ML Sn samples after post-growth annealing at  $150 \text{ }^\circ\text{C}$  and  $450 \text{ }^\circ\text{C}$ , we reference their surface structures. For this reason, we show in Fig. 5 the STM images of these surfaces with the corresponding LEED patterns as insets. Since both surfaces exhibit asymmetric dimer configurations, it is no surprise that we observe no qualitative change in the corresponding LEED patterns in dependence of the annealing temperature. We can observe in the STM image of Fig. 5(a) that the Sn lines have transformed into clusters after annealing at  $150 \text{ }^\circ\text{C}$  and we notice some protrusions in the Ge dimer rows (dotted circles), which we attribute to incorporated Sn atoms. The clusters appear to consist of zig-zag rows, similar to the Sn C feature.

Annealing to  $450 \text{ }^\circ\text{C}$  (Fig. 5(b)) results in the formation of comb-teeth like structures with no large terraces observable. Yamazaki *et al.* [26] reported similar structures after post-growth annealing at  $250 \text{ }^\circ\text{C}$ , indicating that no substantial change in the surface morphology is expected within the temperature range of  $250 \text{ }^\circ\text{C}$  to  $450 \text{ }^\circ\text{C}$ . The formation of the comb-teeth structures is explained by the incorporation of Sn into the Ge dimer rows, which increases the compressive stress in the Ge surface layer. Eventually, this results in a stress relief mechanism leading to undulating step edges. The surface structure after post-growth annealing at  $150 \text{ }^\circ\text{C}$  appears as an intermediate between RT and  $450 \text{ }^\circ\text{C}$ . This indicates that the compressive stress is not entirely elastically relaxed at this stage. Certainly, the analysis of the electronic structure will help to put this into perspective.

We identify two main atomic configurations, one resembling zig-zag chains (blue dotted square), similar to the Sn C feature, and the other one in honeycomb arrangement (black dotted square). Their different appearance in STM is explained by the inter dimer-row configurations of up- and down-tilted atoms. Based on the observation of protrusions in these features, both seem to include Ge-Sn dimers.

Fig. 6 shows the core-level analysis of the Ge 3d and Sn 4d core-level after deposition of 0.3 ML Sn and post-growth annealing at  $150 \text{ }^\circ\text{C}$  and  $450 \text{ }^\circ\text{C}$ . In panel a), we show a comparison of the Ge 3d spectra after deposition at RT and annealing. The intensity was normalized to the maximum peak height and BE is referenced to the  $3d_{5/2}$  Bulk BE. No significant peak shape changes are observable. However, it appears from Fig. 5, that no symmetric Sn ad-dimers are left at the surface and we shall find further evidence in the Sn 4d core-level. After fitting the Ge 3d core-level, a relative increase of  $D_{\text{down}}$  compared to  $D_{\text{up}}$  can be observed in Fig. 6(b) and (c). The relative increase of  $D_{\text{down}}$  may be explained by a preference of Sn to occupy the up-position in the Ge-Sn heterodimer. Surface core-level shifts relative to Bulk are summarized in Table 3 and the values remain fairly constant. These observations are consistent with the  $(2 \times 1)$  LEED patterns, which remains effectively temperature independent at these Sn coverages [43].

A notable change occurs in the Sn 4d core-level after annealing. Peak fits of the Sn 4d core-level are shown in Fig. 6(d)–(e) for the respective post-growth annealing temperatures. After applying the same parameters and constraints as in section 3.2, fitting the spectra with two

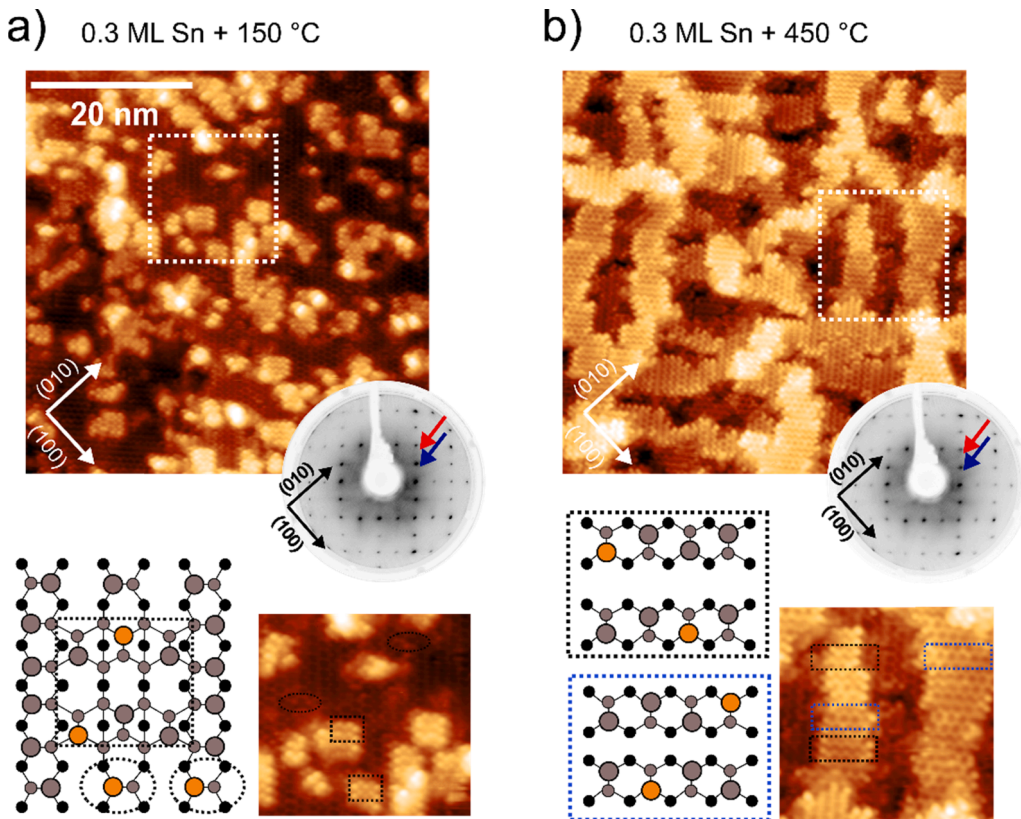


**Fig. 5.** STM images measured at  $-1$  V sample bias (filled states) after deposition of 0.3 ML Sn at RT on Ge(001) and post-growth annealing at a) 150 °C and b) 450 °C. The corresponding LEED patterns are shown as insets and were captured with an electron kinetic energy of 110 eV. Blue and red arrows mark the position of full- and half-order spots, respectively. The bottom panel in a) shows a model of the Ge(001) surface with incorporated Sn, leading to single Ge-Sn heterodimers (dotted circle) and to structures that resemble the Sn C feature but consist presumably of Ge-Ge and Ge-Sn heterodimers (dotted squares). The location of Sn in these features was chosen randomly for this image. Some possible examples of these features are marked in the magnified STM image on the right-hand side. In the bottom panel of b) the proposed atomic configurations of honeycomb (black dotted square) and Sn C feature like (blue dotted square). Features were marked in the magnified STM image on the right-hand side. Note that the location of incorporated Sn atoms in the models of the atomic configurations is arbitrary.

components,  $\text{Sn1}^*$  and  $\text{Sn3}^*$  was sufficient. The  $\text{Sn1}^*$  and  $\text{Sn3}^*$  components are shifted towards higher BE with respect to  $\text{Sn1}$  and  $\text{Sn3}$  from the RT sample by about the same value, i.e. 0.05 eV. Together with the vanishing of the symmetric dimer  $\text{Sn2}$  component, this observation indicates the full incorporation of Sn already at 150 °C. About 80% of the spectra contribution arises from Sn that is in the up-position of the Ge-Sn heterodimer ( $\text{Sn3}^*$ ). The smaller component arises from Sn in the down-position of a heterodimer ( $\text{Sn1}^*$ ). These results are consistent with our observations from the Ge 3d core-level analysis, showing a relative increase of  $D_{\text{down}}$  compared to  $D_{\text{up}}$ . The sum of these findings supports previous reports, stating that the up-position in the heterodimer is energetically more favorable for the Sn [27,50].

To check whether the amount of Sn at the surface remains constant in dependence of the post-growth annealing temperature, we show in Fig. 6(f) the intensity ratio of the Sn 4d and Ge 3d core-level, determined by measurements with UPS and XPS. The constant ratios indicate that the deposited Sn entirely remains in the probed subsurface region after annealing at either temperature. This observation may be reasoned with the incorporation of Sn, which starts already at RT. By ramping the temperature to 150 °C, full incorporation takes place and it appears that the Ge-Sn heterodimer is stable up to 450 °C.

Our previous analysis of the surface after post-growth annealing indicates that the stress relief mechanism observed in STM seems to have negligible effects on the electronic structure. For a final verification, we show in Fig. 7(a)–(b) the ARPES intensity maps after post-growth annealing at 150 °C and 450 °C of 0.3 ML Sn deposited on Ge(001). We can immediately note a vanishing of the  $\text{SR}_{\text{Sn}}$  feature, emphasized by the  $\Gamma$ -EDCs in Fig. 7(c). This result proves the dependence of this feature on a certain Sn ad-dimer configuration on top of the Ge dimers. As the surface is annealed, Sn ad-dimers break up and incorporate. Consequently, the interaction with the Ge up dimer that gives rise to this state does not exist anymore. In correlation with the absence of any  $c(4 \times 2)$  related diffraction spots in the LEED patterns of Fig. 5, we note that the  $\text{SS}_1$  feature does not reappear after the incorporation of Sn. We thus

found additional proof that this surface state requires a well-ordered surface. Features related to the Ge(001) bulk states appear unaffected by the incorporation of Sn, and we see no change of the SO to VBM separation of 0.26 eV. Similar to our observations in section 3.2, we do not observe any substantial change of the BE values of bulk related components in the UPS Ge 3d and the ARPES valence band spectra, indicating that the  $E_{\text{F}}$  remains pinned at about 0.1 eV above the VBM.

#### 4. Summary and conclusion

In this work we have thoroughly investigated the modification of the Ge(001) surface electronic structure upon adsorption of Sn atoms.

Analysis of the Ge 3d core-level revealed a shift of  $D_{\text{down}}$  and  $D_{\text{up}}$  towards each other with increasing Sn coverage. We argue that the origin of this observation is an increasing number of symmetric Ge dimers. This observation correlates with a change in the intensity contributions of the Sn 4d core-level, favoring a component related to the symmetric Sn ad-dimers with increasing Sn coverage, which also forces the formation of symmetrical Ge dimers [28]. A relative increase of symmetric Sn ad-dimers was not reported in previous STM investigations [28,29], which indicates to us that these are formed beneath the second Sn layer. Thus, they remained hidden in STM because only the very surface atoms are probed. Whether these changes are driven by charge transfer, stress induced by the Sn or a mixture of both remains open for future investigations supported by theory.

Post-growth annealing of samples with a Sn coverage of 0.3 ML at 150 °C and 450 °C results in the complete incorporation of Sn at these temperatures, leading to the formation of Ge-Sn dimers. This conclusion is driven by the vanishing of Sn lines in STM, the higher binding energies of Sn components in the Sn 4d spectra compared to RT, a vanishing of the Sn 4d component related to symmetric Sn and an increase of  $D_{\text{down}}$  relative to  $D_{\text{up}}$  in the Ge 3d core-level. We quantify that about 80 % of the atoms reside in the energetically more favorable up-tilted position of the heterodimer. Based on constant Ge 3d and Sn 4d intensity ratios, we

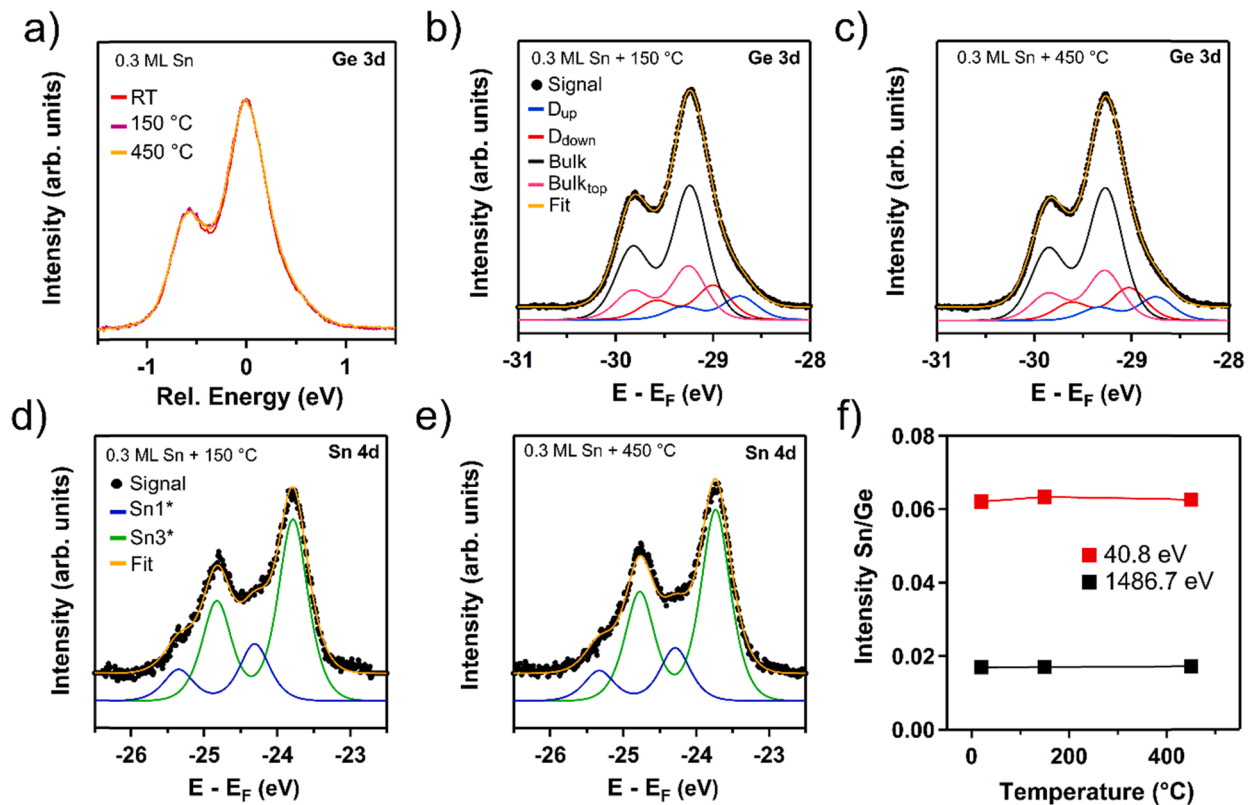


**Fig. 6.** a) Comparison of the Ge 3d core-level measured with an excitation energy of 40.8 eV (normal emission) after deposition of 0.3 ML Sn for different post-growth annealing temperatures. The intensity was normalized to the maximum intensity and the energy scale is referenced to the Ge 3d bulk component. b) and c) Ge 3d core-level region after deposition of 0.3 ML Sn on Ge(001) at RT, followed by post-growth annealing at 150 °C and 450 °C. Four components were used to fit the core-level, indicated by different colors. The energy scale is referenced to the Fermi-level ( $E_F$ ). d) and e) Sn 4d core-level regions measured with an excitation energy of 40.8 eV (normal emission) after deposition of 0.3 ML Sn and post-growth annealing of 150 °C and 450 °C, fitted with two components Sn1\* and Sn3\*. These components correspond to Sn atoms in the down- (Sn1\*) and up-tilted (Sn3\*) position of the Ge-Sn heterodimers. f) Plot of the Sn 4d and Ge 3d intensity ratios measured by UPS (40.8 eV) and XPS (1486.7 eV) vs post-growth annealing temperature.

**Table 3**

Surface core-level shifts of the Ge 3d core-level spectra after deposition of 0.3 ML Sn at RT and post-growth annealing at 150 °C and 450 °C. Fitting of the core-level yields components related to the up-atom of the dimer ( $D_{up}$ ), the down-atom of the dimer ( $D_{down}$ ), the top layer of the bulk atoms ( $Bulk_{top}$ ) and the bulk atoms (Bulk).

	Bulk <sub>top</sub> -Bulk (eV)	D <sub>down</sub> -Bulk (eV)	D <sub>up</sub> -Bulk (eV)
0.3 ML Sn, RT	0.01	-0.23	-0.5
0.3 ML Sn, 150 °C	0.01	-0.24	-0.51
0.3 ML Sn, 450 °C	0.01	-0.23	-0.52

conclude that annealing up to 450 °C does not result in any significant desorption of Sn.

By probing the valence band structure with ARPES, we observed a surface resonance formed between Ge(001)  $D_{up}$  states and a Sn ad-dimer configuration, labeled as  $SR_{Sn}$ . A gradual decrease of its intensity, with increasing Sn coverage, can be explained by a growing number of symmetric dimers. We propose that the Sn B feature is responsible for the observed state, as it has less detrimental effects on the buckling of the Ge dimer compared to the Sn A and Sn C features. Furthermore, it is by far the most abundant feature at a Sn coverage of 0.3 ML, which also featured the highest  $SR_{Sn}$  intensity. Annealing breaks the Sn ad-dimers, leading to incorporation of Sn and consequently a vanishing of  $SR_{Sn}$ .

Bulk-related features in ARPES and UPS did not shift after Sn adsorption and/or Sn incorporation, indicating that the  $E_F$  remains pinned close to the VBM. In conjunction with the vanishing of the  $SS_1$  surface state after Sn adsorption, our results support previous

conclusions that the strong FLP originates from bulk evanescent states [37,38].

Our detailed analysis of the Ge 3d and Sn 4d core-level extends the interpretation of previous STM studies and can be utilized in ongoing research activities that focus on the growth of Sn thin-films on Ge(001). Examination of the valence states revealed interactions of the Ge  $D_{up}$  surface resonances with Sn, apparently limited to a certain Sn ad-dimer configuration, presumably the Sn B feature. Furthermore, we find compelling evidence that the origin of the strong FLP at the Ge(001) surface originates from bulk evanescent states and not from the surface states. Owing to the strong FLP close to the VBM, the initial stages of the Schottky barrier formation at the interface were probed. Overall, our results provide a fundamental understanding of the electronic structure at the Ge/Sn interface, which can be beneficial to the research activities on this and similar material systems.

#### CRediT authorship contribution statement

**Felix Reichmann:** Validation, Formal analysis, Investigation, Writing – original draft. **Andreas P. Becker:** Investigation, Writing – review & editing. **Emily V.S. Hofmann:** Investigation, Writing – review & editing. **Neil J. Curson:** Conceptualization, Supervision, Writing – review & editing. **Wolfgang M. Klesse:** Conceptualization, Writing – review & editing. **Giovanni Capellini:** Conceptualization, Resources, Project administration, Funding acquisition, Supervision, Writing – review & editing.

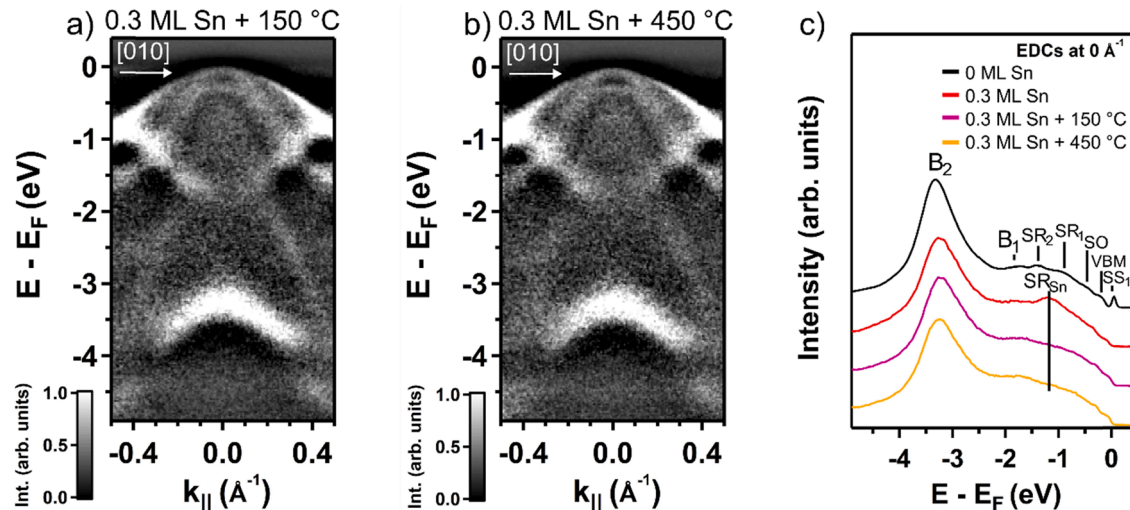


Fig 7. a) – b) ARPES intensity maps of the Ge(001) surface measured with an excitation energy of 21.2 eV after deposition of 0.3 ML and post-growth annealing at 150 °C and 450 °C. c) Comparison of the energy distribution curves (EDCs) extracted around the  $\Gamma$ -point ( $0 \text{ \AA}^{-1}$ ) of the clean Ge(001) surface, after deposition of 0.3 ML Sn and post-growth annealing at 150 °C and 450 °C. The Sn-related state ( $SR_{Sn}$ ) vanishes after annealing.

### Declaration of Competing Interest

The authors declare that they have no known competing financial interests or personal relationships that could have appeared to influence the work reported in this paper.

### Acknowledgment

The authors want to thanks Dr. Emilio Scalise and Prof. Dr. Francesco Montalenti from the Università di Milano-Bicocca for the scientific discussion. E.V.S.H. is partly supported by the EPSRC Centre for Doctoral Training in Advanced Characterisation of Materials (grant number EP/L015277/1) and also IHP – Leibniz-Institut für innovative Mikroelektronik.

### Appendix A. Supplementary material

Supplementary data to this article can be found online at <https://doi.org/10.1016/j.apsusc.2022.153884>.

### References

- [1] R. Pillarisetty, Academic and industry research progress in germanium nanodevices, *Nature* 479 (2011) 324, <https://doi.org/10.1038/nature10678>.
- [2] S. Wirths, D. Buca, S. Mantl, Si-Ge-Sn alloys: from growth to applications, *Progress in Crystal Growth and Characterization of Materials*, 62 (2016) 1, doi: 10.1016/j.pcrysgrow.2015.11.001.
- [3] S. Wirths, R. Geiger, N. von den Driesch, G. Mussler, T. Stoica, S. Mantl, Z. Ikonik, M. Luysberg, S. Chiussi, J.M. Hartmann, H. Sigg, J. Faist, D. Buca, D. Grützmacher, Lasing in direct-bandgap GeSn alloy grown on Si, *Nat. Photonics* 9 (2015) 88, <https://doi.org/10.1038/nphoton.2014.321>.
- [4] S. Gupta, Y. Huang, Y. Kim, E. Sanchez, K.C. Saraswat, Hole mobility enhancement in compressively strained  $\text{Ge}_{0.93}\text{Sn}_{0.07}$  pMOSFETs, *IEEE Electron Device Lett.* 34 (2013) 831, <https://doi.org/10.1109/LED.2013.2259573>.
- [5] O. Moutanabbir, S. Assali, X. Gong, E. O'Reilly, C.A. Broderick, B. Marzban, J. Witzens, W. Du, S.-Q. Yu, A. Chelnokov, D. Buca, D. Nam, Monolithic infrared silicon photonics: the rise of (Si)GeSn semiconductors, *Appl. Phys. Lett.* 118 (2021), 110502, <https://doi.org/10.1063/5.0043511>.
- [6] J. Mathews, R. Roucka, C. Weng, R. Beeler, J. Tolle, J. Menéndez, J. Kouvetakis, Near IR photodiodes with tunable absorption edge based on Ge<sub>1-y</sub>Sn<sub>y</sub> alloys integrated on silicon, *ECS Trans.* 33 (2010) 765, <https://doi.org/10.1149/1.3487607>.
- [7] M. Oehme, J. Werner, M. Gollhofer, M. Schmid, M. Kaschel, E. Kasper, J. Schulze, Room-temperature electroluminescence from GeSn light-emitting pin diodes on Si, *IEEE Photonics Technol. Lett.* 23 (2011) 1751, <https://doi.org/10.1109/LPT.2011.2169052>.
- [8] R.T. Beeler, C. Xu, D.J. Smith, G. Grzybowski, J. Menéndez, J. Kouvetakis, Compositional dependence of the absorption edge and dark currents in Ge<sub>1-x-y</sub>Si<sub>6xSn<sub>y</sub></sub>/Ge(100) photodetectors grown via ultra-low-temperature epitaxy of Ge<sub>4</sub>H<sub>10</sub>, Si<sub>4</sub>H<sub>10</sub>, and SnD<sub>4</sub>, *Appl. Phys. Lett.* 101 (2012), 221111, <https://doi.org/10.1063/1.4768217>.
- [9] A. Gassenq, F. Gencarelli, J. Van Campenhout, Y. Shimura, R. Loo, G. Narcy, B. Vincent, G. Roelkens, GeSn/Ge heterostructure short-wave infrared photodetectors on silicon, *Opt. Express* 20 (2012) 27297, <https://doi.org/10.1364/OE.20.027297>.
- [10] D. Lei, K.H. Lee, Y. Huang, W. Wang, S. Masudy-Panah, S. Yadav, A. Kumar, Y. Dong, S. Xu, Y. Wu, C.S. Tan, X. Gong, Y. Yeo, Germanium-tin (GeSn) p-channel fin field-effect transistor fabricated on a novel GeSn-on-insulator Substrate, *IEEE Trans. Electron Devices* 65 (2018) 3754, <https://doi.org/10.1109/TED.2018.2856738>.
- [11] J. Chrétien, N. Pauc, F.A. Pilon, M. Bertrand, Q. Thai, L. Casiege, N. Bernier, H. Dansas, P. Gergaud, E. Delamadeleine, R. Khazaka, H. Sigg, J. Faist, A. Chelnokov, V. Reboud, J.-M. Hartmann, V. Calvo, GeSn lasers covering a wide wavelength range thanks to uniaxial tensile strain, *ACS Photonics* 6 (2019) 2462, <https://doi.org/10.1021/acsp Photonics.9b00712>.
- [12] Y. Zhou, W. Dou, W. Du, S. Ojo, H. Tran, S.A. Ghetmiri, J. Liu, G. Sun, R. Soref, J. Margetis, J. Tolle, B. Li, Z. Chen, M. Mortazavi, S.-Q. Yu, Optically pumped GeSn lasers operating at 270 K with broad waveguide structures on Si, *ACS Photonics* 6 (2019) 1434, <https://doi.org/10.1021/acsp Photonics.9b00030>.
- [13] A. Elbaz, D. Buca, N. von den Driesch, K. Pantzas, G. Patriarche, N. Zerounian, E. Herth, X. Checoury, S. Sauvage, I. Sagnes, A. Foti, R. Ossikovskii, J.-M. Hartmann, F. Boeuf, Z. Ikonik, P. Boucaud, D. Grützmacher, M. El Kurdi, Ultra-low-threshold continuous-wave and pulsed lasing in tensile-strained GeSn alloys, *Nat. Photonics* 14 (2020) 375, <https://doi.org/10.1038/s41566-020-0601-5>.
- [14] D. Rainko, Z. Ikonik, A. Elbaz, N. von den Driesch, D. Stange, E. Herth, P. Boucaud, M. El Kurdi, D. Grützmacher, D. Buca, Impact of tensile strain on low Sn content GeSn lasing, *Sci. Rep.* 9 (2019) 259, <https://doi.org/10.1038/s41598-018-36837-8>.
- [15] J. Sau, M.L. Cohen, Possibility of increased mobility in Ge-Sn alloy system, *Phys. Rev. B* 75 (2007), 045208, <https://doi.org/10.1103/PhysRevB.75.045208>.
- [16] J.A. Van Vechten, J.C. Phillips, New set of tetrahedral covalent radii, *Phys. Rev. B* 2 (1970) 2160, <https://doi.org/10.1103/PhysRevB.2.2160>.
- [17] R.W. Olesinski, G. Abbaschian, The Ge-Sn (germanium-tin) system, *Bull. Alloy Phase Diagrams* 5 (1984) 265, <https://doi.org/10.1007/BF02868550>.
- [18] P. Zaumseil, Y. Hou, M.A. Schubert, N. von den Driesch, D. Stange, D. Rainko, M. Virgilio, D. Buca, G. Capellini, The thermal stability of epitaxial GeSn layers, *APL Mater.* 6 (2018), 076108, <https://doi.org/10.1063/1.5036728>.
- [19] J. Aubin, J.M. Hartmann, A. Gassenq, J.L. Rouviere, E. Robin, V. Delaye, D. Cooper, N. Mollard, V. Reboud, V. Calvo, Growth and structural properties of step-graded, high Sn content GeSn layers on Ge, *Semicond. Sci. Technol.* 32 (2017), 094006, <https://doi.org/10.1088/1361-6641/aa8084>.
- [20] S. Assali, J. Nicolas, S. Mukherjee, A. Dijkstra, O. Moutanabbir, Atomically uniform Sn-rich GeSn semiconductors with 3.0–3.5  $\mu\text{m}$  room-temperature optical emission, *Appl. Phys. Lett.* 112 (25) (2018) 251903, <https://doi.org/10.1063/1.5038644>.
- [21] V.A. Timofeev, A.I. Nikiforov, A.R. Tuktamyshev, V.I. Mashanov, I.D. Loshkarev, A. A. Bloshkin, A.K. Gutakovskii, Pseudomorphic GeSiSn, SiSn and Ge layers in strained heterostructures, *Nanotechnology* 29 (2018), 154002, <https://doi.org/10.1088/1361-6528/aaac45>.
- [22] D. Stange, N. von den Driesch, T. Zabel, F. Armand-Pilon, D. Rainko, B. Marzban, P. Zaumseil, J.-M. Hartmann, Z. Ikonik, G. Capellini, S. Mantl, H. Sigg, J. Witzens, D. Grützmacher, D. Buca, GeSn/SiGeSn heterostructure and multi quantum well lasers, *ACS Photonics* 5 (2018) 4628, <https://doi.org/10.1021/acsp Photonics.8b01116>.
- [23] F. Oliveira, I.A. Fischer, A. Benedetti, P. Zaumseil, M.F. Cerqueira, M.I. Vasilevskiy, S. Stefanov, S.S. Chiussi, J. Schulze, Fabrication of GeSn-multiple quantum wells by

- overgrowth of Sn on Ge by using molecular beam epitaxy, *Appl. Phys. Lett.* 107 (2015) 1, <https://doi.org/10.1063/1.4938746>.
- [24] D. Stange, N. von den Driesch, D. Rainko, C. Schulte-Braucks, S. Wirths, G. Mussler, A.T. Tiedemann, T. Stoica, J.-M. Hartmann, Z. Ikonic, S. Mantl, D. Grützmacher, D. Buca, Study of GeSn based heterostructures: towards optimized group IV MQW LEDs, *Opt. Express* 24 (2016) 1358, <https://doi.org/10.1364/OE.24.001358>.
- [25] I.A. Fischer, C.J. Clausen, D. Schwarz, P. Zaumseil, G. Capellini, M. Virgilio, M. C. da Silva Figueira, S. Birner, S. Koelling, P.M. Koenraad, M.R.S. Huang, C. T. Koch, T. Wendav, K. Busch, J. Schulze, Composition analysis and transition energies of ultrathin Sn-rich GeSn quantum wells, *Phys. Rev. Mater.* 4 (2020), 024601, <https://doi.org/10.1103/PhysRevMaterials.4.024601>.
- [26] M. Yamazaki, S. Takeuchi, O. Nakatsuka, A. Sakai, M. Ogawa, S. Zaima, Scanning tunneling microscopy observation of initial growth of Sn and Ge1-xSnx layers on Ge(001) substrates, *Appl. Surf. Sci.* 254 (2008) 6048, <https://doi.org/10.1016/j.apsusc.2008.02.175>.
- [27] K. Tomatsu, K. Nakatsuji, T. Iimori, Y. Takagi, H. Kusunohara, A. Ishii, F. Komori, An atomic seesaw switch formed by tilted asymmetric Sn-Ge dimers on a Ge (001) surface, *Science* 315 (2007) 1696, <https://doi.org/10.1126/science.1137848>.
- [28] K. Tomatsu, K. Nakatsuji, T. Iimori, F. Komori, STM observation of initial growth of Sn atoms on Ge(001) surface, *Surf. Sci.* 601 (7) (2007) 1736–1746.
- [29] E.V.S. Hofmann, E. Scalise, F. Montalenti, T.J.Z. Stock, S.R. Schofield, G. Capellini, L. Miglio, N.J. Curson, W.M. Klesse, The formation of a Sn monolayer on Ge(100) studied at the atomic scale, *Appl. Surf. Sci.* 561 (2021), 149961, <https://doi.org/10.1016/j.apsusc.2021.149961>.
- [30] A. Tejada, R. Cortés, J. Lobo-Checa, C. Didiot, B. Kierren, D. Malterre, E.G. Michel, A. Mascaraque, Structural origin of the Sn 4d core level line shape in Sn/Ge(111)-(3x3), *Phys. Rev. Lett.* 100 (2008), 026103, <https://doi.org/10.1103/PhysRevLett.100.026103>.
- [31] Y.-T. Cheng, H.-W. Wan, C.-K. Cheng, C.-P. Cheng, J. Jueinai Kwo, M. Hong, T.-W. Pi, Surface electronic structure of Si1-xGex(001)-2x1: a synchrotron radiation photoemission study, *Appl. Phys. Express* 13 (2020), 095503, <https://doi.org/10.35848/1882-0786/abaf96>.
- [32] P. Ponath, A.K. Hamze, A.B. Posadas, S. Lu, W.H. Wei, D.J. Smith, A.A. Demkov, Surface structure analysis of Eu Zintl template on Ge(001), *Surf. Sci.* 674 (2018) 94, <https://doi.org/10.1016/j.susc.2018.04.003>.
- [33] A. Suzuki, S. Asaba, J. Yokoi, K. Kato, M. Kurosawa, M. Sakashita, N. Taoka, O. Nakatsuka, S. Zaima, Reduction of Schottky barrier height for n-type Ge contact by using Sn electrode, *Jpn. J. Appl. Phys.* 53 (2014) 04EA06, <https://doi.org/10.7567/JJAP.53.04EA06>.
- [34] T. Nishimura, K. Kita, A. Toriumi, Evidence for strong Fermi-level pinning due to metal-induced gap states at metal/germanium interface, *Appl. Phys. Lett.* 91 (2007), 123123, <https://doi.org/10.1063/1.2789701>.
- [35] P. Tsipas, A. Dimoulas, Modeling of negatively charged states at the Ge surface and interfaces, *Appl. Phys. Lett.* 94 (2009), 012114, <https://doi.org/10.1063/1.3068497>.
- [36] A. Dimoulas, P. Tsipas, A. Sotiropoulos, Fermi-level pinning and charge neutrality level in germanium, 89 (2006) 252110.
- [37] H. Seo, R.C. Hatch, P. Ponath, M. Choi, A.B. Posadas, A.A. Demkov, Critical differences in the surface electronic structure of Ge(001) and Si(001): Ab initio theory and angle-resolved photoemission spectroscopy, *Phys. Rev. B* 89 (2014), 115318, <https://doi.org/10.1103/PhysRevB.89.115318>.
- [38] M. Kuzmin, P. Laukkanen, J. Mäkelä, M. Tuominen, M. Yasir, J. Dahl, M.P. J. Punkkinen, K. Kokko, Origin of Fermi-level pinning and its control on the n-type Ge(100) surface, *Phys. Rev. B* 94 (2016), 035421, <https://doi.org/10.1103/PhysRevB.94.035421>.
- [39] F. Reichmann, E. Scalise, A.P. Becker, E.V.S. Hofmann, J. Dabrowski, F. Montalenti, L. Miglio, M. Mulazzi, W.M. Klesse, G. Capellini, New insights into the electronic states of the Ge(001) surface by joint angle-resolved photoelectron spectroscopy and first-principle calculation investigation, *Appl. Surf. Sci.* 571 (2022), 151264, <https://doi.org/10.1016/j.apsusc.2021.151264>.
- [40] H.J.W. Zandvliet, The Ge(001) surface, *Phys. Rep.* 388 (2003) 1–40, <https://doi.org/10.1016/j.physrep.2003.09.001>.
- [41] H.J.W. Zandvliet, B.S. Swartzentruber, W. Wulfhekel, B.J. Hattnik, B. Poelsema, Spontaneous formation of an ordered c(4x2)-(2x1) domain pattern on Ge(001), *Phys. Rev. B* 57 (1998) R6803, <https://doi.org/10.1103/PhysRevB.57.R6803>.
- [42] W.M. Klesse, G. Scappucci, G. Capellini, M.Y. Simmons, Preparation of the Ge(001) surface towards fabrication of atomic-scale germanium devices, *Nanotechnology* 22 (2011), 145604, <https://doi.org/10.1088/0957-4484/22/14/145604>.
- [43] V. Timofeev, A. Nikiforov, A. Tuktamyshev, V. Mashanov, M. Yesin, A. Bloshkin, Morphology, structure, and optical properties of semiconductor films with GeSiSn nanoislands and strained layers, *Nanoscale Res. Lett.* 13 (2018) 65, <https://doi.org/10.1186/s11671-017-2429-6>.
- [44] A.S. Kilian, A. Pancotti, R. Landers, A. de Siervoc, J. Morais, Probing the surface atomic structure of Au/Cr2O3/Pd(111) by photoelectron diffraction, *CrystEngComm* 16 (2014) 9291, <https://doi.org/10.1039/C4CE01389A>.
- [45] Y.-T. Cheng, Y.-H. Lin, W.-S. Chen, K.-Y. Lin, H.-W. Wan, C.-P. Cheng, H.-H. Cheng, J. Kwo, M. Hong, T.-W. Pi, Surface electronic structure of epi germanium (001)-2x1, *Appl. Phys. Express*, 10 (2017) 075701, doi: 10.7567/APEX.10.075701.
- [46] T. Miller, E. Rosenwinkel, T.-C. Chiang, Surface core-level shifts for Ge(100)-(2x1), *Solid State Commun.* 47 (1983) 935, [https://doi.org/10.1016/0038-1098\(83\)90125-4](https://doi.org/10.1016/0038-1098(83)90125-4).
- [47] G. Margaritondo, J.E. Rowe, C.S. B., Photoionization cross section of d-core levels in solids A: a synchrotron radiation study of the spin-orbit branching ratio, *Phys. Rev. B* 19 (1979) 2850, <https://doi.org/10.1103/PhysRevB.19.2850>.
- [48] T.-W. Pi, J.-F. Wen, C.-P. Ouyang, R.-T. Wu, Surface core-level shifts of Ge(100)-2x1, *Phys. Rev. B* 63 (2001), 153310, <https://doi.org/10.1103/PhysRevB.63.153310>.
- [49] E. Pehlke, M. Scheffler, Evidence for site-sensitive screening of core holes at the Si and Ge (001) surface, *Phys. Rev. Lett.* 71 (1993) 2338, <https://doi.org/10.1103/PhysRevLett.71.2338>.
- [50] K. Noatschk, E.V.S. Hofmann, J. Dabrowski, N.J. Curson, T. Schroeder, W. M. Klesse, G. Seibold, Ge(001) surface reconstruction with Sn impurities, *Surf. Sci.* 713 (2021), 121912, <https://doi.org/10.1016/j.susc.2021.121912>.
- [51] A.L. Allred, E. Rochow, A scale of electronegativity based on electrostatic force, *J. Inorg. Nucl. Chem.* 5 (1958) 264, [https://doi.org/10.1016/0022-1902\(58\)80003-2](https://doi.org/10.1016/0022-1902(58)80003-2).
- [52] K. Nakatsuji, Y. Takagi, F. Komori, H. Kusunohara, A. Ishii, Electronic states of the clean Ge(001) surface near Fermi energy, *Phys. Rev. B* 72 (2005), 241308, <https://doi.org/10.1103/PhysRevB.72.241308>.
- [53] T. Sakata, S.N. Takeda, K. Kitagawa, H. Daimon, Interband interaction between bulk and surface resonance bands of a Pb-adsorbed Ge(001) surface, *Semicond. Sci. Technol.* 31 (2016), 085012, <https://doi.org/10.1088/0268-1242/31/8/085012>.





## Chapter 7

# The electronic structure of $\epsilon$ -Ga<sub>2</sub>O<sub>3</sub>

Transparent semi-conducting oxides (TSOs) combine transparency in the visible to ultra-violet range of the light spectrum and semi-conducting properties. Because of this unique combination of properties, they can be found in various applications such as flat panel displays [70, 71], transparent electronics [72, 73], photovoltaics [74], solar-blind detectors [75], high-power electronics [76, 77], high-temperature gas sensors [78] and others [79, 80].

A prominent example of the ever increasing commercial and scientific interest in TSOs over the last decade has been Ga<sub>2</sub>O<sub>3</sub> [81, 82]. Ga<sub>2</sub>O<sub>3</sub> can exist in five different crystal structures, among which the  $\beta$ -phase is the thermodynamically most stable. This phase offers an ultra-wide band gap of 4.85 eV, making it a highly attractive material for deep-UV photonic and high-power electronic applications [83, 84].

The  $\epsilon$ -phase of Ga<sub>2</sub>O<sub>3</sub> is the thermodynamically second most stable, transitioning into the  $\beta$ -phase at about 900 °C [85]. It can be grown on commercially available *c*-oriented sapphire substrates at much lower thermal budget than the  $\beta$ -phase [86] and offers an orthorhombic (pseudo-hexagonal) crystallographic structure [87]. Furthermore, the band gap of 4.6 eV is of comparable width to the 4.85 eV band gap of  $\beta$ -Ga<sub>2</sub>O<sub>3</sub> [88].

In addition,  $\epsilon$ -Ga<sub>2</sub>O<sub>3</sub> offers ferroelectric behavior with a relatively large spontaneous polarization, which may allow to obtain a two-dimensional electron gas and thus high-mobility devices [89, 90].

Despite these interesting properties, a detailed investigation of the electronic structure has been missing. The goal of this chapter is to present an investigation of the  $\epsilon$ -Ga<sub>2</sub>O<sub>3</sub> electronic structure by ARPES and XPS on a sample, that was grown by metal-organic chemical vapor deposition on *c*-oriented sapphire.

## Chapter 7: Publication Contribution Statement

This Chapter has been published in APL Materials, 7 (2019) 022522, <https://doi.org/10.1063/1.5054395> [91]. All article content, except where otherwise noted, is licensed under a Creative Commons Attribution license (CC-BY).

The investigated sample was fabricated by the group of Prof. Dr. Roberto Fornari. Prior to the characterization by XPS and ARPES, I discussed with Dr. Mattia Mulazzi the surface preparation that should be applied.

Transferring the sample in the system and executing the cleaning was done by me, as well as the alignment of the sample for the XPS and ARPES characterization. Parameters such as pass energy, step size, dwell time and lens mode in the characterization by XPS and ARPES were chosen by me.

After obtaining the raw data, I discussed the results with Dr. Mattia Mulazzi, who then took care of creating the shown figures and writing the first draft. The results were then discussed with the theorists, which contributed the calculations that are also shown in the article.

Before the submission of the article by Dr. Mattia Mulazzi, I contributed to the corrections and improvements of the manuscript.



# The electronic structure of $\epsilon$ -Ga<sub>2</sub>O<sub>3</sub>

Cite as: APL Mater. **7**, 022522 (2019); <https://doi.org/10.1063/1.5054395>

Submitted: 31 August 2018 • Accepted: 17 December 2018 • Published Online: 22 January 2019

 M. Mulazzi, F. Reichmann, A. Becker, et al.

## COLLECTIONS

Paper published as part of the special topic on [Wide Bandgap Oxides](#)



View Online



Export Citation



CrossMark

## ARTICLES YOU MAY BE INTERESTED IN

[Recent progress on the electronic structure, defect, and doping properties of Ga<sub>2</sub>O<sub>3</sub>](#)

APL Materials **8**, 020906 (2020); <https://doi.org/10.1063/1.5142999>

[Crystal Structure of  \$\beta\$ -Ga<sub>2</sub>O<sub>3</sub>](#)

The Journal of Chemical Physics **33**, 676 (1960); <https://doi.org/10.1063/1.1731237>

[Tin-assisted heteroepitaxial PLD-growth of  \$\kappa\$ -Ga<sub>2</sub>O<sub>3</sub> thin films with high crystalline quality](#)

APL Materials **7**, 022516 (2019); <https://doi.org/10.1063/1.5054378>



Timing is everything.  
Now it's automatic.

A new synchronous source measure system for electrical measurements of materials and devices

 [Learn more](#)






# The electronic structure of $\varepsilon$ -Ga<sub>2</sub>O<sub>3</sub>

Cite as: APL Mater. 7, 022522 (2019); doi: 10.1063/1.5054395

Submitted: 31 August 2018 • Accepted: 17 December 2018 •

Published Online: 22 January 2019



M. Mulazzi,<sup>1,2</sup>  F. Reichmann,<sup>3</sup> A. Becker,<sup>3</sup> W. M. Klesse,<sup>3</sup> P. Alippi,<sup>4</sup>  V. Fiorentini,<sup>5,6</sup>  A. Parisini,<sup>7</sup>  
M. Bosi,<sup>8</sup>  and R. Fornari<sup>7,8</sup> 

## AFFILIATIONS

<sup>1</sup>Institut für Physik, Humboldt-Universität zu Berlin, Newtonstr. 15, D-12489 Berlin, Germany

<sup>2</sup>Leibniz-Institut für Kristallzüchtung, Max-Born-Str. 2, D-12489 Berlin, Germany

<sup>3</sup>IHP, Im Technologiepark 25, D-15236 Frankfurt (Oder), Germany

<sup>4</sup>CNR-ISM, Via Salaria km 29,300, I-00015 Monterotondo Stazione (Rome), Italy

<sup>5</sup>Department of Physics, Cagliari University, I-09042 Monserrato (CA), Italy

<sup>6</sup>CNR-IOM, UOS Cagliari University, I-09042 Monserrato (CA), Italy

<sup>7</sup>Department of Mathematical, Physical and Computer Sciences, Parma University, Viale delle Scienze 7/A, I-43124 Parma, Italy

<sup>8</sup>CNR, Institute of Electronic and Magnetic Materials, Viale delle Scienze 37/A, I-43124 Parma, Italy

## ABSTRACT

The electronic structure of  $\varepsilon$ -Ga<sub>2</sub>O<sub>3</sub> thin films has been investigated by *ab initio* calculations and photoemission spectroscopy with UV, soft, and hard X-rays to probe the surface and bulk properties. The latter measurements reveal a peculiar satellite structure in the Ga 2p core level spectrum, absent at the surface, and a core-level broadening that can be attributed to photoelectron recoil. The photoemission experiments indicate that the energy separation between the valence band and the Fermi level is about 4.4 eV, a valence band maximum at the  $\Gamma$  point and an effective mass of the highest lying bands of  $\sim 0.42$  free electron masses. The value of the bandgap compares well with that obtained by optical experiments and with that obtained by calculations performed using a hybrid density-functional, which also reproduce well the dispersion and density of states.

© 2019 Author(s). All article content, except where otherwise noted, is licensed under a Creative Commons Attribution (CC BY) license (<http://creativecommons.org/licenses/by/4.0/>). <https://doi.org/10.1063/1.5054395>

Gallium oxide (Ga<sub>2</sub>O<sub>3</sub>) is a wide bandgap transparent semiconducting oxide (TCO). Although known for decades, it is only in the last ten years that it received a lot of attention as a novel wide bandgap semiconductor for power electronic and deep-UV applications. Among five crystal structures of Ga<sub>2</sub>O<sub>3</sub>, the monoclinic  $\beta$  phase is the most thermodynamically stable and indeed the only one that can be grown from a Ga<sub>2</sub>O<sub>3</sub> melt, either by Czochralski<sup>1</sup> or Edge-defined Film-fed Growth (EFG).<sup>2</sup> Specific advantages of this material are the bandgap close to 5 eV, transparency up to the UV-C range, and very high breakdown voltage. Relatively high n-type conductivity can be achieved by doping with Si, Sn, or Ge, which makes  $\beta$ -Ga<sub>2</sub>O<sub>3</sub> suitable for fabrication of power transistors,<sup>3</sup> high-voltage diodes,<sup>4</sup> and UV photodetectors.<sup>5</sup>

The  $\varepsilon$  phase of Ga<sub>2</sub>O<sub>3</sub>, object of the present investigation, is the second most stable, after  $\beta$ , and was observed to be thermodynamically (meta)stable up to about 700 °C exhibiting

a complete transition to  $\beta$  around 900 °C.<sup>6</sup> This polymorph can easily be deposited on commercial c-oriented sapphire at temperatures much lower than those needed for  $\beta$ -Ga<sub>2</sub>O<sub>3</sub>.<sup>7</sup> In addition to having an orthorhombic (pseudo-hexagonal) crystallographic structure<sup>8</sup> and a wide bandgap of about 4.6 eV,<sup>9</sup>  $\varepsilon$ -Ga<sub>2</sub>O<sub>3</sub> presents unique properties such as ferroelectric behavior<sup>10</sup> with a relatively large spontaneous polarisation,<sup>11</sup> making this polymorph even more interesting, as it might be exploited to obtain a two-dimensional electron gas and thus high mobility devices.

Many angle-resolved photoemission spectroscopy (ARPES) studies have already been devoted to TCOs, ZnO,<sup>12-15</sup> CdO,<sup>16-18</sup> and In<sub>2</sub>O<sub>3</sub>,<sup>19-21</sup> and also to  $\beta$ -Ga<sub>2</sub>O<sub>3</sub>.<sup>22-25</sup> However, such an investigation is still lacking for  $\varepsilon$ -Ga<sub>2</sub>O<sub>3</sub>. The interesting properties of the  $\varepsilon$  phase, on the other hand, fully justify the investigation of its electronic structure and motivate our present ARPES investigation. In the following, we report on the

band structure of  $\epsilon$ -Ga<sub>2</sub>O<sub>3</sub> grown in the form of thin films of 250 nm thickness. ARPES excited with low- and high-energy photons was used to measure the core-levels as well as the valence band with high momentum resolution. The films are electrically conductive and stable against the sputtering and annealing procedure that we applied to clean the surface.

The  $\epsilon$ -Ga<sub>2</sub>O<sub>3</sub> thin films were grown by Metal-Organic Chemical Vapor Deposition (MOCVD) on 2-inches (0001) oriented sapphire by using the growth parameters reported in the literature.<sup>7</sup> The films were doped with diluted silane to get high conductivity (the resistivity of samples from the same wafer was 0.8–1  $\Omega$  cm and carrier concentration was  $2\text{--}3 \times 10^{18}$  cm<sup>-3</sup>), which prevented the charging effects that were previously observed in undoped  $\epsilon$ -Ga<sub>2</sub>O<sub>3</sub> epilayers.

The measurements were carried out at the surface cluster of the Institute for High-Performance Microelectronics (IHP), featuring a SPECS Phoibos 150 electron spectrometer. The photons used for the ARPES experiment are generated by a monochromatised He discharge lamp, while a monochromatised X-ray tube with aluminum and silver targets was used to obtain the Al K $\alpha$  and Ag L $\alpha$  emission lines at photon energies of  $h\nu_{\text{Al}} = 1468.7$  eV and  $h\nu_{\text{Ag}} = 2984.3$  eV, respectively. Prior to photoelectron spectroscopy, the surface of the films was prepared by repeated Ar ion sputtering and annealing cycles. While at the beginning an ion energy of 1 keV was used, at later stages, it was reduced to 500 eV to avoid excessive material removal. For the same reason, namely, the limited film thickness, the samples were sputtered 5 min per cycle. The films were heated at 500 °C for 30 min, a temperature at which no transition between the  $\epsilon$  and  $\beta$  phases occurs. All measurements were taken at room temperature, and the pressure in the chamber during the measurements was lower than  $2 \times 10^{-10}$  mbar and about  $5 \times 10^{-9}$  mbar during the annealing.

X-ray photoemission spectroscopy (XPS) is a refined and relatively easy technique that can be used to investigate the electronic structure of materials. While its main purpose is the identification of the chemical species in a compound, it has recently been applied to quantitatively determine the band bending in a semiconductor.<sup>26</sup> In comparison with this work in which UV radiation was used, X-rays were employed in the present study since they possess two advantages: measurements (1) of several core levels from either gallium or oxygen

and (2) of many values of the mean escape depth are possible. The bulk sensitivity is enhanced even more by the use of the higher photon energy  $h\nu_{\text{Ag}}$  imparting higher kinetic energy to the photoelectrons.

Figure 1 shows the spectrum of  $\epsilon$ -Ga<sub>2</sub>O<sub>3</sub> taken with the Al K $\alpha$  radiation,  $h\nu_{\text{Al}}$ .

All measured photoemission and Auger peaks of the spectrum of Fig. 1 could unambiguously be identified. These are the very first photoemission measurements on the  $\epsilon$  phase thin films. We stress that we observed no peaks from either aluminum or silicon, which has three implications: (i) the Ar sputtering cycles just removed a thin Ga<sub>2</sub>O<sub>3</sub> surface layer so that no substrate portions resulted exposed to X-rays and (ii) no Al migration from the substrate to epilayer occurred during the annealing. Moreover, (iii) the small amount of Si introduced via silane doping during growth must be well below the XPS detection limit ( $\approx 0.1\%$ ). In fact, the absence of any Si core-level peaks indicates that there is no Si surface segregation in the layers.

Next, we wish to discuss the Ga 2p core levels (the strongest lines measured) and the O 1s. With the intention of detecting differences between the surface and the bulk, we used the two photon energies mentioned above. Furthermore, for the Al K $\alpha$  case, we repeated measurements at two emission angles, namely, normal emission (labeled as 0°) and at 70° from normal emission, i.e., at a grazing emission angle of 20°.

The reason for the use of a grazing angle is to increase the surface sensitivity by effectively projecting the inelastic mean free path (IMFP) on the surface normal direction, reducing it by a factor  $\cos(\theta)$ . For  $\theta = 70^\circ$ , this equals  $\cos(70^\circ) \approx 0.342$ .

The first interesting feature observed in Fig. 2(a) is the appearance of two weak satellites when the photon energy is increased. Contrary to the spectra taken with  $h\nu_{\text{Al}}$ , the spectrum taken with  $h\nu_{\text{Ag}}$  shows a distinct peak at a binding energy of  $-110$  eV, lower than that of the Ga 2p<sub>3/2</sub> peak. Furthermore, at  $-1130$  eV binding energy, there is a second peak, also absent in the spectra taken with  $h\nu_{\text{Al}}$ . The importance of these two peaks lies in their energy difference relative to the Ga 2p<sub>3/2</sub> and Ga 2p<sub>1/2</sub> peaks. In fact, the Ga 2p is split in the final state by spin-orbit coupling by about 26.8 eV, and thus, every peak observed at an energy  $\Delta E$  from 3/2 peak should be replicated and located at a  $\Delta E$  energy from the 1/2 peak.

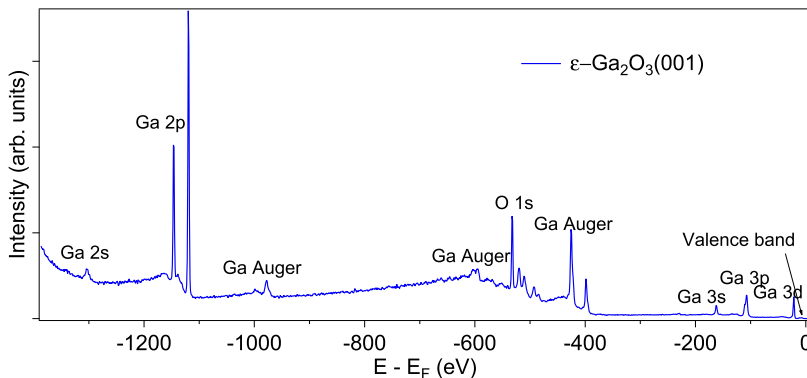


**FIG. 1.** XPS spectrum in a wide binding energy range measured at a photon energy  $h\nu_{\text{Ag}}$ . All core levels have been identified, as well as a number of Auger peaks located at about  $-950$  eV and in the  $-800$  eV to  $-400$  eV range. In this range, the Auger peaks overlap with the O 1s core level at  $-534$  eV. The black arrow indicates a very weak peak near zero binding energy, which is the valence band. The latter is hardly visible in XPS but is thoroughly investigated with the He I radiation.

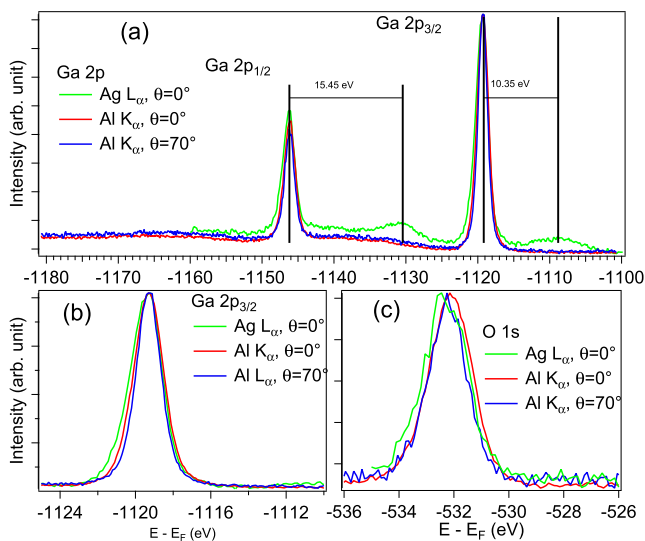


**FIG. 2.** Core-level measurements taken at different photon energies and emission angles, as indicated in the figure labels. (a) shows the spectrum of the 2p core level doublet split by spin-orbit coupling; (b) the  $2p_{3/2}$  component and (c) the O 1s core level.

Thus, the peak at  $-1110$  eV, located  $10.35$  eV above the Ga  $2p_{3/2}$ , should be replicated  $10.35$  eV above the  $1/2$  component. However, the peak positioned between the Ga  $2p_{3/2}$  and Ga  $2p_{1/2}$  lines is at  $15.45$  eV from the Ga  $2p_{1/2}$  component and therefore is not a replica but a further satellite.

While most of the photoemission satellites lie at the left of the main line, i.e., at lower kinetic energies and apparently higher binding energies, the peak at  $-1130$  eV lies on the right side, i.e., at higher kinetic energies. The attribution of this peak is not unambiguous as two possibilities are available, i.e., a non-local screening as it happens in manganites or a shake-down satellite, occurring when the photohole pulls electrons below the Fermi level in the final-state, leading to a more effective valence electron screening of the hole. However, in all previously studied systems,<sup>27–30</sup> the well-screened peaks appear only a few eV from the main line, but in our case, the difference is more than  $10$  eV, which is of the scale of the typical correlation energy in oxides. Therefore, we tend to believe that the satellite derives from a shake-down effect.

Figures 2(b) and 2(c) show zoomed-in images of the Ga  $2p_{3/2}$  and O 1s peaks in a narrow energy range. The qualitative behavior of the peaks upon photon energy and emission angle is the same. In fact, the binding energy of the peaks taken with  $h\nu_{Al}$  does not change upon a variation of the emission angle. However, the width of the peaks taken in the most surface sensitive conditions (the blue lines in Fig. 2) is slightly narrower than those measured at normal emission, which is more bulk sensitive. The measurements taken with  $h\nu_{Ag}$ , which are even more bulk sensitive, are broader and show an asymmetric tail on the left side. We attribute the left tail of the peaks taken at high energy at normal emission ( $\theta = 0^\circ$ ) to the recoil effect occurring in core-level peaks taken at high photon energy:<sup>30,31</sup> a hard X-ray can excite a photoelectron to

such high kinetic energies that, by momentum conservation, the ion left behind by the photoelectron is set in motion. The shift and asymmetric broadening of the photoemission peaks appears because the ion dissipates its energy to the lattice by phonon emission.

The electronic bands of  $\epsilon$ -Ga<sub>2</sub>O<sub>3</sub> have been calculated, after structural optimisation, within density-functional theory both in the generalized gradient approximation<sup>32</sup> (GGA) and the hybrid-functional<sup>33</sup> (HSE) approach, using the projector augmented wave method as implemented in the VASP code.<sup>34</sup> For Ga, we used the 13-electron “Ga-d” VASP PAW dataset with  $3d$  states in the valence and two projectors in the  $s$ ,  $p$ , and  $d$  channels and one  $f$  projector; for O, we used the 6-electron “O” VASP PAW dataset with two projectors in the  $s$  and  $p$  channels and one in the  $d$  channel. The energy cutoff is  $400$  eV, and the  $k$ -point mesh is  $4 \times 2 \times 2$  for self-consistency and optimization and  $8 \times 6 \times 6$  for the calculation of the density of states (DOS). The parameters  $\alpha = 0.25$  and  $\mu = 0.2$  are used in HSE.

$\epsilon$ -Ga<sub>2</sub>O<sub>3</sub> has a non-magnetic 40-atom unit cell. The valence manifold thus comprises 72 spin-degenerate bands that fall nicely in the experimental energy range. The total valence band width is  $6.96$  eV and  $7.26$  eV in GGA and HSE, respectively. The occupied bands are rather flat, while the first conduction band (CB) disperses strongly. The conduction band minimum (CBM) is at  $\Gamma$ , and the gap is, as expected, underestimated by GGA ( $2.32$  eV), whereas HSE yields  $4.26$  eV, comparable to the experiment. Previous calculations<sup>35</sup> using the B3LYP functional reported  $4.62$  eV, but any comparison of different beyond-local-DFT approaches carries uncertainties of order  $\pm 0.5$  eV, as shown, e.g., for  $\beta$ -Ga<sub>2</sub>O<sub>3</sub>.<sup>36</sup> The present ARPES experiments suggest (see below) a lower bound of  $4.41$  eV; photoconductivity and optical absorption indicate a value of about  $4.6$  eV.<sup>9</sup>

The experimental valence band dispersion is presented in Fig. 3(a) in a false-colour scale, as explained in the caption.

The data show that the valence band consists of a single rather broad band located  $6$  eV below the Fermi level (the zero of the  $y$ -scale in the left panel of Fig. 3) which reaches its minimum binding energy at the  $\Gamma$  point of the Brillouin zone. The binding energy of the band increases with the wave-vector, indicating a negative high effective mass. To obtain the latter, we extracted EDCs at  $0.05 \text{ \AA}^{-1}$  steps across the whole wave-vector range and fitted the spectra from  $-7$  eV to  $-3$  eV to obtain the binding energy of the maximum. Then we fitted the data with a parabola and obtained an effective mass  $m^* = -4.2$  electron masses. Thus, the effective mass is negative and large, and the bands are fairly flat. The resulting parabola is indicated by the red line superimposed to the band-structure calculations in the right panel of Fig. 3. As shown in Fig. 3, a large number of theoretical bands lie in the same energy range of the experimental signal, with a few dispersive bands overlapping with many flat ones, especially near the valence band maximum (VBM). The result of the calculations shown in Fig. 3 confirms that the GGA bandgap underestimates the experimental one, as mentioned.

The question of the characteristics of the bandgap cannot be addressed by ARPES, unless the CB is partially filled. Only

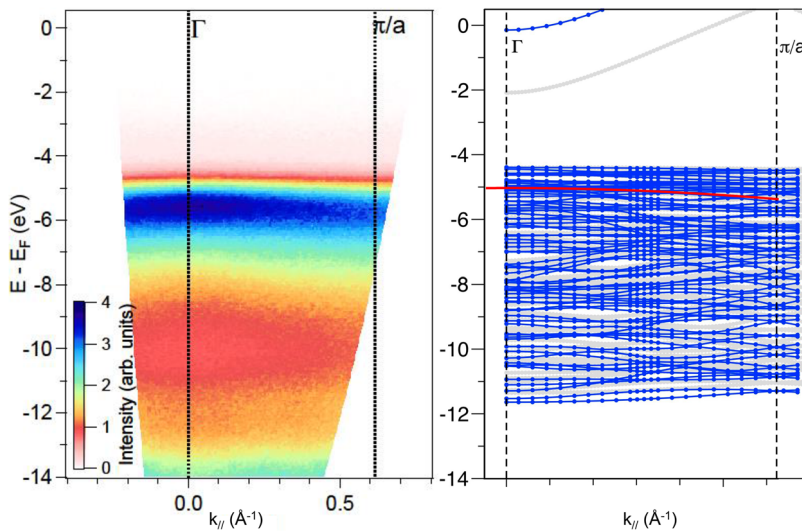


**FIG. 3.** (Left) ARPES map in false colours (as indicated by the linear colour scale) taken with the photon energy  $h\nu = 21.2$  eV. The strong intensity at about  $-6$  eV is due to the oxygen states dispersing to higher binding energies with momentum. (Right) Theoretical electronic bands within the GGA (gray continuous lines) and HSE (blue dotted lines) approximations, with the valence band top of both aligned with the experimental one at  $\Gamma$ . A parabolic band (red continuous line) is superimposed, with a mass of  $-4.2 m_0$  [as determined by fitting the experimental Energy Distribution Curves (EDCs)].

in this case, the position of the CBM in  $k$ -space can be directly observed. The experimental data show no intensity near the Fermi level [the zero for the energy scale in Fig. 3(a)], leading us to the conclusion that the CBM is not occupied. According to our calculations, as well as previous ones,<sup>35</sup> the CBM is at the  $\Gamma$  point. The experimental data suggest that the VBM is at or near (see Fig. 5) the zone centre, so  $\epsilon$ -Ga<sub>2</sub>O<sub>3</sub> is likely a direct-gap semiconductor.

Figure 4(a) shows the EDC taken at zero  $k_{\parallel}$  [vertical dashed line in Fig. 3(a)], which has been used to extract the size of the single-particle bandgap. The peak region and the right flank of the EDC have been fitted to obtain the inflexion point, from which a linear extrapolation to zero has been used to estimate the apparent bandgap, obtaining  $E_B = 4.41$  eV. This compares well with optical measurements on undoped as-grown films,<sup>9</sup> suggesting that (a) the Fermi level is pinned some 0.2 eV below the CBM and (b) correlation effects in optical experiments are small.

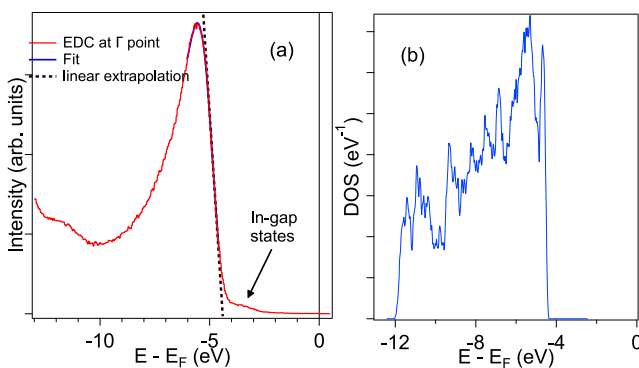


**FIG. 4.** (a) Experimental EDC taken at the  $\Gamma$  point superimposed to a fit of the spectrum used to do the linear extrapolation. (b) The theoretical calculation of the density of states, smoothed to better indicate the most prominent features, obtained with the hybrid functional.

Surprisingly, a weak shoulder peak is observed [Fig. 4(a)] inside the bandgap at about 3.5 eV below  $E_F$ . Its origin is unknown, but we associate it with localised native-defect states because of its almost vanishing dispersion and of similar observations made in other oxide systems.<sup>37–39</sup> The theoretical density of states in Fig. 4 finds no state in that region, supporting an extrinsic origin of this peak.

A direct comparison between theory and experiment is presented in Fig. 4, where the theoretical DOS and the experimental EDC at the  $\Gamma$  point are shown. Although the DOS is  $k$ -integrated, while the EDC is measured at a single  $k$ , the validity of the comparison is supported by the flatness of the bands. Indeed, the comparison relates fairly satisfactorily the computed occupations and observed intensities: in both cases, a dominant asymmetric peak is observed, topping at about  $-6$  eV and spanning a roughly 5 eV-wide interval, with a major dip around  $-10$  eV; the intensity then picks up again, peaking at  $-11$  eV. The theoretical DOS ends at  $-11.5$  eV, while the experimental one has a plateau at that energy, before increasing again toward higher binding energies. This latter intensity increase is due to the secondary electron background and not to primary photoelectrons. However, the peak at  $-11$  eV is a genuine feature, unrelated to the Ga 3d core levels. The binding energy of the Ga 3d is 21 eV from the Fermi level, in good agreement with the predictions of both GGA and HSE, i.e.,  $-20.2$  eV and  $-21.9$  eV below the same reference.

Concerning transport band masses and the characteristics of the gap, two points stand out upon a closer look (Fig. 5) at the highest valence bands. First, the gap is direct according to the more accurate HSE approach, which predicts a VBM at the  $\Gamma$  point (in accordance with the experiment). GGA would instead predict that the very flat top band has a local minimum at  $\Gamma$  and a maximum at  $k_{\parallel} = 0.35 \text{ \AA}^{-1}$ , hence a (barely) indirect band structure.

Second, although the main peak in the EDC centered around  $-5$  eV provides, as mentioned earlier, an average



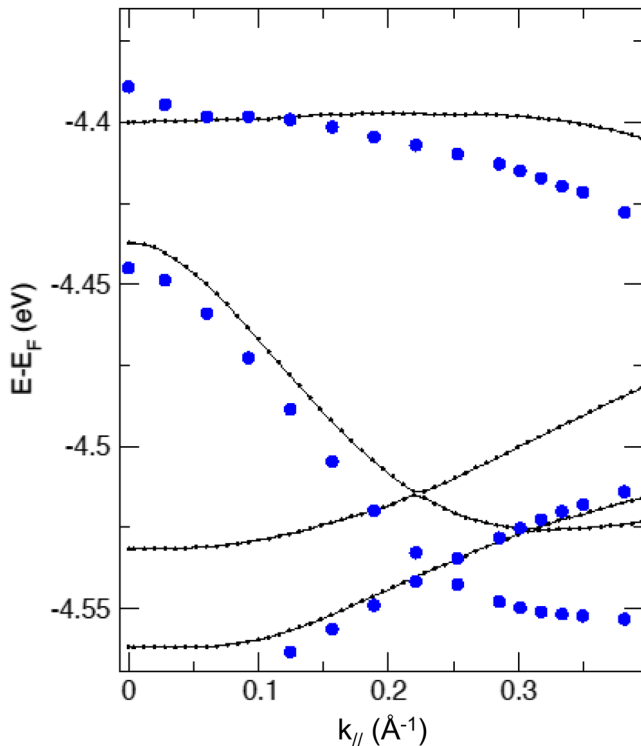


**FIG. 5.** Calculation of the bands near the VBM plotted from  $\Gamma$  along the experimentally explored direction with the GGA (black lines) and the HSE (blue dots).

valence mass of  $-4.2 m_e$ , the mass adopted by  $p$  carriers doped into the material will be that of the highest band (which, it is simple to estimate, is the only one that will be occupied for any reasonable carrier concentration, say below  $10^{21} \text{ cm}^{-3}$ ). Fitting a parabola to the highest computed HSE band in the experimentally explored direction, we find a very large effective mass of  $-15 m_e$ . Another likely occurrence we have not explored explicitly here is that the top valence band will probably be significantly anisotropic and will need to be described by more complex datasets such as Luttinger parameters.

The electronic structure of  $\varepsilon\text{-Ga}_2\text{O}_3$  films grown by MOCVD on  $c$ -oriented sapphire was investigated by XPS and ARPES. The main conclusions are that no band bending is observed, which excludes the presence of a large density of surface states. However, a careful check of the ARPES map shows an accumulation of states at about 3.5 eV from the Fermi level. These states are possibly related to intrinsic defects, but more comparative studies (for instance, on samples grown with different O-to-Ga ratios in the vapour phase) are necessary to clarify this question.

Our ARPES investigations indicate a weak maximum of the valence band at the  $\Gamma$  point, therefore strongly hinting that the  $\varepsilon$ -phase is indeed a direct bandgap semiconductor, although ARPES alone cannot supply a full confirmation since it cannot measure the CBM position. The effective mass for holes in the top of the VB was estimated to be about  $-4.2 m_0$ .

Theory reproduces rather well the experimental intensities and predicts the CBM as well as (in its arguably most accurate version) the VBM at  $\Gamma$ , with a gap not far from the experiment.

The authors wish to thank Professor A. Bosio, Dr. V. Montedoro, G. Garulli, A. Gorreri, and S. Vantaggio for their support in making ohmic contacts and electrical measurements of doped  $\text{Ga}_2\text{O}_3$  epilayers and Professor Dr. C. Wenger for allowing the use of the surface science cluster.

This work was supported in part by UniCA, Fondazione di Sardegna, Regione Sardegna via Progetto biennale di ateneo 2016 *Multiphysics approach to thermoelectricity*, and CINECA-ISCRA grants.

## REFERENCES

- Y. Tomm, P. Reiche, D. Klimm, and T. Fukuda, *J. Cryst. Growth* **220**, 510–514 (2000).
- A. Kuramata, K. Koshi, S. Watanabe, Y. Yu, T. Masui, and S. Yamakoshi, *Jpn. J. Appl. Phys., Part 1* **55**, 1202A2 (2016).
- M. Higashiwaki, K. Sasaki, H. Murakami, Y. Kumagai, A. Koukitu, A. Kuramata, T. Masui, and S. Yamakoshi, *Semicond. Sci. Technol.* **31**, 034001 (2016).
- M. A. Rozhkov, E. S. Kolodeznyi, A. M. Smirnov, V. E. Bougrov, and A. E. Romanov, *Mater. Phys. Mech.* **24**, 194–200 (2015).
- M. Zhong, Z. Wei, X. Meng, F. Wu, and J. Li, *J. Alloys Compd.* **619**, 572–575 (2015).
- R. Fornari, M. Pavesi, V. Montedoro, D. Klimm, F. Mezzadri, I. Cora, B. Péc, F. Boschi, A. Parisini, A. Baraldi, C. Ferrari, E. Gombia, and M. Bosi, *Acta Mater.* **140**, 411–416 (2017).
- F. Boschi, M. Bosi, T. Berzina, E. Buffagni, C. Ferrari, and R. Fornari, *J. Cryst. Growth* **443**, 25–30 (2016).
- I. Cora, F. Mezzadri, F. Boschi, M. Bosi, M. Caplovicova, G. Calestani, I. Dodony, B. Pecz, and R. Fornari, *CrystEngComm* **19**, 1509 (2017).
- M. Pavesi, F. Fabbri, F. Boschi, G. Piacentini, A. Baraldi, M. Bosi, E. Gombia, A. Parisini, and R. Fornari, *Mater. Chem. Phys.* **205**, 502–507 (2018).
- F. Mezzadri, G. Calestani, F. Boschi, D. Delmonte, M. Bosi, and R. Fornari, *Inorg. Chem.* **55**, 12079–12084 (2016).
- M. B. Maccioni and V. Fiorentini, *Appl. Phys. Express* **9**, 041102 (2016).
- R. A. Powell, W. E. Spicer, and J. C. McMenamin, *Phys. Rev. B* **6**, 3056 (1972).
- K. Ozawa, Y. Oba, K. Edamoto, M. Higashiguchi, Y. Miura, K. Tanaka, K. Shimada, H. Namatame, and M. Taniguchi, *Phys. Rev. B* **79**, 075314 (2009).
- L. F. J. Piper, A. R. H. Preston, A. Fedorov, S. W. Cho, A. DeMasi, and K. E. Smith, *Phys. Rev. B* **81**, 233305 (2010).
- R. Yukawa, K. Ozawa, S. Yamamoto, H. Iwasawa, K. Shimada, E. F. Schwier, K. Yoshimatsu, H. Kumigashira, H. Namatame, M. Taniguchi, and I. Matsuda, *Phys. Rev. B* **94**, 165313 (2016).
- P. D. C. King, T. D. Veal, C. F. McConville, J. Zuniga-Pérez, V. Munoz-Sanjosé, M. Hopkinson, E. D. L. Rienks, M. F. Jensen, and Ph. Hofmann, *Phys. Rev. Lett.* **104**, 256803 (2010).
- J. J. Mudd, T.-L. Lee, V. Munoz-Sanjosé, J. Zuniga-Pérez, D. Hesp, J. M. Kakh, D. J. Payne, R. G. Egdell, and C. F. McConville, *Phys. Rev. B* **89**, 035203 (2014).
- J. J. Mudd, T.-L. Lee, V. Munoz-Sanjosé, J. Zuniga-Pérez, D. J. Payne, R. G. Egdell, and C. F. McConville, *Phys. Rev. B* **89**, 165305 (2014).
- K. H. L. Zhang, R. G. Egdell, F. Offi, S. Iacobucci, L. Petaccia, S. Gorovikov, and P. D. C. King, *Phys. Rev. Lett.* **110**, 056803 (2013).
- C. Körber, V. Krishnakumar, A. Klein, G. Panaccione, P. Torelli, A. Walsh, J. L. F. Da Silva, S.-H. Wei, R. G. Egdell, and D. J. Payne, *Phys. Rev. B* **81**, 165207 (2010).

- <sup>21</sup>V. Scherer, C. Janowitz, A. Krapf, H. Dwelk, D. Braun, and R. Manzke, *Appl. Phys. Lett.* **100**(21), 212108 (2012).
- <sup>22</sup>M. Mohamed, C. Janowitz, I. Unger, R. Manzke, Z. Galazka, R. Uecker, R. Fornari, J. R. Weber, J. B. Varley, and C. G. Van de Walle, *Appl. Phys. Lett.* **97**, 211903 (2010).
- <sup>23</sup>M. Mohamed, I. Unger, C. Janowitz, R. Manzke, Z. Galazka, R. Uecker, and R. Fornari, *J. Phys.: Conf. Ser.* **286**(1), 012027 (2011).
- <sup>24</sup>C. Janowitz, V. Scherer, M. Mohamed, A. Krapf, H. Dwelk, R. Manzke, Z. Galazka, R. Uecker, K. Irmscher, R. Fornari, M. Michling, D. Schmeier, J. R. Weber, J. B. Varley, and C. G. Van de Walle, *New J. Phys.* **13**, 085014 (2011).
- <sup>25</sup>M. Mohamed, K. Irmscher, C. Janowitz, Z. Galazka, R. Manzke, and R. Fornari, *Appl. Phys. Lett.* **101**(13), 132106 (2012).
- <sup>26</sup>B. Thielert, C. Janowitz, Z. Galazka, and M. Mulazzi, *Phys. Rev. B* **97**, 235309 (2018).
- <sup>27</sup>K. Horiba, M. Taguchi, A. Chainani, Y. Takata, E. Ikenaga, D. Miwa, Y. Nishino, K. Tamasaku, M. Awaji, A. Takeuchi, M. Yabashi, H. Namatame, M. Taniguchi, H. Kumigashira, M. Oshima, M. Lippmaa, M. Kawasaki, H. Koinuma, K. Kobayashi, T. Ishikawa, and S. Shin, *Phys. Rev. Lett.* **93**, 236401 (2004).
- <sup>28</sup>M. Sperlich, C. König, G. Güntherodt, A. Sekiyama, G. Funabashi, M. Tsunekawa, S. Imada, A. Shigemoto, K. Okada, A. Higashiya, M. Yabashi, K. Tamasaku, T. Ishikawa, V. Renken, T. Allmers, M. Donath, and S. Suga, *Phys. Rev. B* **87**, 235138 (2013).
- <sup>29</sup>M. Taguchi, A. Chainani, N. Kamakura, K. Horiba, Y. Takata, M. Yabashi, K. Tamasaku, Y. Nishino, D. Miwa, T. Ishikawa, S. Shin, E. Ikenaga, T. Yokoya, K. Kobayashi, T. Mochiku, K. Hirata, and K. Motoya, *Phys. Rev. B* **71**, 155102 (2005).
- <sup>30</sup>*Hard X-Ray Photoelectron Spectroscopy (HAXPES)*, edited by J. Woicik (Springer, Heidelberg, 2016).
- <sup>31</sup>Y. Takata, Y. Kayanuma, M. Yabashi, K. Tamasaku, Y. Nishino, D. Miwa, Y. Harada, K. Horiba, S. Shin, S. Tanaka, E. Ikenaga, K. Kobayashi, Y. Senba, H. Ohashi, and T. Ishikawa, *Phys. Rev. B* **75**, 233404 (2007).
- <sup>32</sup>J. P. Perdew, M. Ernzerhof, and K. Burke, *J. Chem. Phys.* **105**, 9982 (1996).
- <sup>33</sup>J. Heyd, G. E. Scuseria, and M. Ernzerhof, *J. Chem. Phys.* **118**, 8207 (2003).
- <sup>34</sup>G. Kresse and J. Furthmüller, *Phys. Rev. B* **54**, 11169 (1996); G. Kresse and D. Joubert, *ibid.* **59**, 1758 (1999).
- <sup>35</sup>J. Kim, D. Tahara, Y. Miura, and B. G. Kim, *Appl. Phys. Express* **11**, 061101 (2018).
- <sup>36</sup>F. Ricci, F. Boschi, A. Baraldi, A. Filippetti, M. Higashiwaki, A. Kuramata, V. Fiorentini, and R. Fornari, *J. Phys.: Condens. Matter* **28**, 224005 (2016).
- <sup>37</sup>Y. Aiura, I. Hase, H. Bando, T. Yasue, T. Saitoh, and D. S. Dessau, *Surf. Sci.* **515**, 61 (2002).
- <sup>38</sup>A. F. Santander-Syro, C. Bareille, F. Fortuna, O. Copie, M. Gabay, F. Bertran, A. Taleb-Ibrahimi, P. Le Fèvre, G. Herranz, N. Reyren, M. Bibes, A. Barthlmy, P. Lecoeur, J. Guevara, and M. J. Rozenberg, *Phys. Rev. B* **86**, 121107(R) (2012).
- <sup>39</sup>S. Backes, T. C. Rödel, F. Fortuna, E. Frantzeskakis, P. Le Fèvre, F. Bertran, M. Kobayashi, R. Yukawa, T. Mitsuhashi, M. Kitamura, K. Horiba, H. Kumigashira, R. Saint-Martin, A. Fouchet, B. Berini, Y. Dumont, A. J. Kim, F. Lechermann, H. O. Jeschke, M. J. Rozenberg, R. Valentí, and A. F. Santander-Syro, *Phys. Rev. B* **94**, 241110(R) (2016).

## Chapter 8

# Experimental and Theoretical Investigation of the Surface Electronic Structure of $\text{ZnGa}_2\text{O}_4(100)$ Single-Crystals

A high thermal stability and ultra-wide bandgap make  $\beta\text{-Ga}_2\text{O}_3$  attractive for future high-power electronic and deep-UV optoelectronic applications, leading to an upsurge of scientific investigations in the last decade [92, 93, 94, 95]. The research activities have been focused on the growth and integration of the material, as well as understanding its fundamental properties [96, 97, 98].

However, the monoclinic crystal structure results in mechanical, electrical and thermal anisotropies, making the heteroepitaxy, substrate and device fabrication rather challenging [99]. Therefore, a material with a similar band gap width and isotropic properties is highly desirable.  $\text{ZnGa}_2\text{O}_4$  (ZGO) is a TSO that has isotropic thermal, mechanical and electrical properties thanks to its cubic spinel structure. Recently, high quality ZGO single-crystals were grown from melt at the Leibniz-institute of crystal growth (IKZ) [100]. The conductivity of these crystals is tunable by the choice of growth conditions and an optical band gap of 4.6 eV was reported.

While these promising characteristics have already led to the first ZGO based devices [101, 102, 103, 104] and sparked research activities on the fundamental physical properties of the material [105, 106], a detailed investigation of the electronic structure of the ZGO(100) surface has been missing. Such an investigation could allow a direct measurement of the band gap (in case of degenerate doping) and the localization of the valence band maximum in k-space, improving theoretical modelling of the band structure and providing a deeper understanding of the material. However, the investigation by PES requires the preparation of a clean surface, which has not been demonstrated by the standards of surface science. Furthermore, the preparation of a clean surface is potentially challenging, due to the materials complexity.

Therefore, the first goal of my study was the preparation of a clean surface by the standard surface science preparation techniques sputtering and annealing. The second goal was to investigate the electronic structure of a surface with sufficient quality to provide the first fundamental insights into the electronic structure.

## Chapter 8: Publication Contribution Statement

This Chapter has been published in *Physica Status Solidi B: Basic Solid State Physics*, 259 (2021) 2100452, <https://doi.org/10.1002/pssb.202100452> [107]. The article is licensed under the terms of the Creative Commons Attribution-NonCommercialNoDerivs License (CC-BY-NC-ND), which permits use and distribution in any medium, provided the original work is properly cited, the use is non-commercial and no modifications or adaptations are made.

The two samples that were investigated in this chapter were fabricated at the IKZ by Dr. Zbigniew Galazka.

I discussed with Dr. Zbigniew Galazka and Dr. Mattia Mulazzi the overall strategy of the sample preparation, while executing it by myself. This included the choice of sputtering parameters, annealing conditions and the annealing temperatures.

The sample transfer in the system was done me, as well as the alignment of the sample in the characterization by LEED, ARPES and XPS. All measurement parameters in these characterization methods were chosen by me.


The raw data was analyzed by me and I prepared a first draft of the experimental results, which I then discussed with Dr. Jaroslaw Dabrowski and Dr. Mattia Mulazzi. Dr. Jaroslaw Dabrowski then performed the calculations and I discussed with him the outcome. He then provided me with bullet points to include these calculations in the manuscript.

Based on the experimental results and the calculations by Dr. Jaroslaw Dabrowski, I prepared a first draft of the manuscript, which was then given to each co-author for corrections and remarks. I handled the communication and included all remarks in the manuscript.

During the submission of the article, I was in charge to communicate with editor and reviewers. Furthermore, I led the revision of the article based on the reviewer's comments and took care of the re-submission.



**Future 3D Additive Manufacturing**  
**The 3DMM20 Conference**



**3D Nano- and  
Micro-Manufacturing:  
Technology and  
Technical Application**

**REGISTER  
NOW!**

**April 3 – 8, 2022 | Schöntal Monastery, Germany**

# Experimental and Theoretical Investigation of the Surface Electronic Structure of $\text{ZnGa}_2\text{O}_4(100)$ Single-Crystals

Felix Reichmann,\* Jaroslaw Dabrowski,\* Andreas Paul Becker,  
Wolfgang Matthias Klesse, Klaus Irmscher, Robert Schewski, Zbigniew Galazka,  
and Mattia Mulazzi\*

Herein, a detailed experimental and theoretical investigation on the surface electronic structure of  $\text{ZnGa}_2\text{O}_4(100)$  bulk single-crystals, with a special emphasis on the surface preparation, is presented. The surface crystallizes in the bulk-derived structure, even at low annealing temperatures. Thermal treatments in ultra-high vacuum have detrimental effects, as they cannot remove the carbon contamination and induce substantial zinc losses, further exacerbated by sputtering. A short sputtering duration and annealing in oxygen atmosphere dramatically reduce the zinc and oxygen losses in the crystal surface, leading to a contamination-free, crystalline surface of nearly stoichiometric composition. The investigation of the valence states along the high symmetry directions of the Brillouin zone compares favorably with *ab initio* pseudopotential calculations, indicating a good surface quality and overall agreement with theory. An in-depth analysis of the measured and simulated valence band peak intensities reveals difficulties associated with the precise description of the metal-oxygen hybridization. This study provides a first fundamental understanding of the electronic structure of  $\text{ZnGa}_2\text{O}_4$ , while also indicating that the surface thermal instability is a challenging task that should be taken into account for the fabrication of heterostructures based on  $\text{ZnGa}_2\text{O}_4$ .

## 1. Introduction

Among the ultra-wide band gap transparent semiconducting oxides (TSOs),  $\beta\text{-Ga}_2\text{O}_3$  has attracted a lot of interest because its pseudo-direct band gap of 4.85 eV yields a high breakdown voltage and provides transparency in the UV-range.<sup>[1–5]</sup> These properties are accompanied by a good thermal stability, allowing the growth of bulk  $\beta\text{-Ga}_2\text{O}_3$  single crystals from the melt.<sup>[6,7]</sup> Accordingly,  $\beta\text{-Ga}_2\text{O}_3$  is seen as a potential candidate for high-power electronic devices and deep-UV optoelectronic devices.<sup>[8,9]</sup> The drawbacks are its mechanical, optical, and thermal anisotropies, due to the monoclinic crystal structure, which make the fabrication of substrates and devices a challenging task.<sup>[10]</sup>

For applications, a material with a band gap as wide as that of  $\beta\text{-Ga}_2\text{O}_3$ , but of higher symmetry, would therefore be highly desirable. Recently, Galazka et al. reported bulk, melt-grown  $\text{ZnGa}_2\text{O}_4$  (ZGO) single-crystals of high structural quality,


from which differently oriented insulating and semiconducting wafers could be prepared.<sup>[11,12]</sup> ZGO crystallizes in a cubic spinel structure ( $Fd\bar{3}m$  space group), as illustrated with a ball and stick model in **Figure 1**. Spinel refers to a class of compounds with a chemical formula  $\text{AB}_2\text{X}_4$ , in which A is a divalent cation like Zn, B is a trivalent cation like Ga, and X is a divalent anion like O. In the normal spinel structure of ZGO, Zn occupies the tetrahedral sites, while Ga occupies the octahedral sites. During growth from the melt, at high temperatures, the occupation of octahedral, and tetrahedral sites is random.<sup>[11]</sup> A long cool down stabilizes the normal spinel structure, while antisite defects are introduced by shorter cool down times. Antisite defects lead to n-type conductivity with free electron concentrations in the order of  $10^{18}\text{--}10^{19}\text{ cm}^{-3}$ . Upon post-growth annealing at 800–1400 °C for 10 h or 700 °C for 40 h in oxidizing atmosphere ZGO crystals can turn into an insulating state.<sup>[11–13]</sup> Thanks to its cubic spinel structure, ZGO has isotropic thermal and optical properties. The optical band gap of ZGO was found to be 4.6 eV wide, close to that of  $\beta\text{-Ga}_2\text{O}_3$  and no preferred cleavage plane was observed.<sup>[11,12]</sup>

These promising characteristics resulted in extensive research activities on the fundamental physical properties of the

F. Reichmann, J. Dabrowski, A. P. Becker, W. M. Klesse  
IHP – Leibniz-Institut für innovative Mikroelektronik  
Im Technologiepark 25, 15236 Frankfurt (Oder), Germany  
E-mail: reichmann@ihp-microelectronics.com;  
dabrowski@ihp-microelectronics.com

K. Irmscher, R. Schewski, Z. Galazka  
Leibniz-Institut für Kristallzüchtung  
Max-Born-Str. 2, 12489 Berlin, Germany

M. Mulazzi  
Institut für Physik  
Humboldt-Universität zu Berlin  
Newtonstr. 14, 12489 Berlin, Germany  
E-mail: mmulazzi@physik.hu-berlin.de

 The ORCID identification number(s) for the author(s) of this article can be found under <https://doi.org/10.1002/pssb.202100452>.

© 2021 The Authors. *physica status solidi (b) basic solid state physics* published by Wiley-VCH GmbH. This is an open access article under the terms of the Creative Commons Attribution-NonCommercial-NoDerivs License, which permits use and distribution in any medium, provided the original work is properly cited, the use is non-commercial and no modifications or adaptations are made.

DOI: 10.1002/pssb.202100452

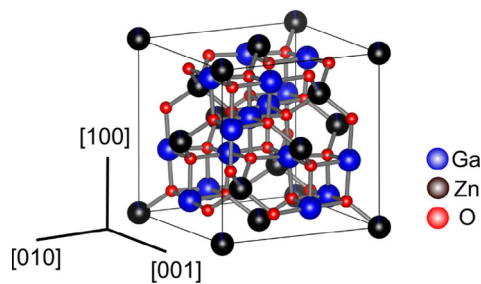


**Figure 1.** Ball and stick model of the  $\text{ZnGa}_2\text{O}_4$  unit cell with Ga in blue, Zn in black, and O in red.

material,<sup>[14–16]</sup> as well as the fabrication of ZGO based devices such as thin film transistors (TFTs),<sup>[17]</sup> metal-oxide field-effect transistors (MOSFETs),<sup>[18]</sup> thin-film phototransistors, and self-powered solar-blind UV photodetectors<sup>[19,20]</sup> However, a detailed investigation of the electronic structure of ZGO by photoelectron spectroscopy is still lacking, probably owed to the fact that no bulk crystals were available until recently.

Angle-resolved photoelectron spectroscopy (ARPES) offers a direct way of probing the electronic structure of surfaces and interfaces and was already used to detail the electronic structure of other TSOs such as:  $\text{ZnO}$ ,<sup>[21,22]</sup>  $\text{CdO}$ ,<sup>[23,24]</sup>  $\text{In}_2\text{O}_3$ ,<sup>[25,26]</sup>  $\beta\text{-Ga}_2\text{O}_3$ ,<sup>[27–29]</sup> and  $\epsilon\text{-Ga}_2\text{O}_3$ .<sup>[30]</sup> However, ARPES requires a contamination-free surface of single-crystalline quality, which can generally be achieved by in situ growth of thin films or careful in situ surface treatment of substrates. In any case, one needs to evaluate if the measured electronic structure is truly originating from ZGO or from a defective surface. Therefore, we present an investigation of the electronic structure of a ZGO(100) bulk single-crystal prepared by in situ sputtering and annealing, while also delving deep into the effects of the surface preparation.

In the first section, we address the effectiveness of the cleaning procedure and changes to the chemical composition by employing X-ray photoelectron spectroscopy (XPS). In particular, we compare surfaces resulting from annealing in ultra-high vacuum (UHV), annealing in oxygen atmosphere and sputtering. Low-energy sputtering and low temperature annealing in oxygen atmosphere is sufficient to prepare a near stoichiometric surface. We demonstrate, by using low-energy electron diffraction (LEED), that low temperature annealing is sufficient to obtain a crystalline surface, albeit no reconstruction is present.

In the second section, we focus on the electronic structure of the near stoichiometric surface, prepared in oxidizing conditions, utilizing XPS again. We present a detailed analysis of the core-level spectra observing that the surface preparation induces changes to the sample doping, evident by a repositioning of the Fermi-level. Peak fitting of the core-level is used to explain changes in the surface stoichiometry during the surface preparation, while angle-dependent measurements show no signs of a band bending.

In the third section, we show the valence band structure resolved by APRES along the high symmetry directions of the surface Brillouin zone, finding clear dispersion of the O 2p states and the valence band maximum.

In the fourth and fifth sections, ab initio calculations of the band structure are presented. Starting with the calculated bulk

band structure we observe a good agreement with the experiment if we take into account the projection of bulk bands to the surface. However, since the experimental surface is only near stoichiometric, we refine the results by discussing possible surface structures and comparing them to the experimentally obtained data.

## 2. Results

### 2.1. Comparison of the Surface Preparation in UHV Versus Oxygen Atmosphere

To evaluate the effectiveness of the surface preparation, we first examine the chemical composition and the removal of adventitious carbon by using XPS. For details on different steps of the surface preparation, see the Experimental Section. **Figure 2** shows the C 1s core-level regions for each applied surface treatment step in a) UHV and b) oxygen atmosphere. In the spectra of the as loaded samples, we observe a small shoulder in the C 1s core-level on the high binding energy side of the main peak (C–H, C–C), whose origin is the C–O binding states of carbon. These C 1s spectra are very similar to those of adventitious carbon, which adsorbed when the samples were in contact with air.<sup>[31,32]</sup>

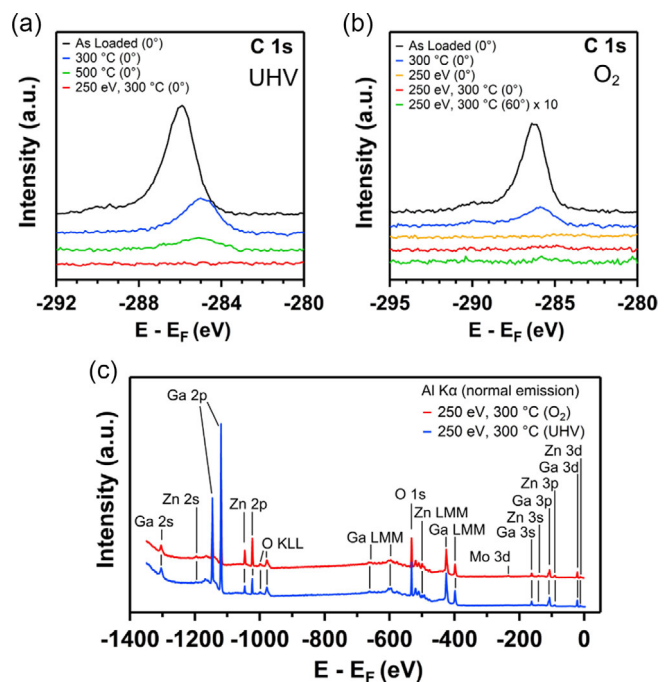


**Figure 2.** The C 1s core-level region is shown in dependence of the cleaning steps a) in ultra-high vacuum (UHV) conditions and b) when the sample is annealed in oxygen atmosphere ( $\text{O}_2$ ). Spectra were acquired with an excitation energy of 1486.7 eV in normal emission ( $0^\circ$ ), while in (b) an additional scan in grazing emission ( $60^\circ$ ) after sputtering and annealing is shown. The intensity was multiplied by a factor of 10 to account for the overall lower intensity in grazing emission. c) Normal emission survey scan after sputtering and annealing, comparing annealing in UHV conditions and oxygen atmosphere. The Mo 3d peak observed is due to the sample holder and has not influenced the chemical analysis.



Annealing the first sample in UHV at 300 °C for 30 min and afterward 500 °C for 30 min reduced the amount of carbon present on the first sample, but was not able to reduce it to below the detection limit (Figure 2a). After a single sputtering step of 250 eV for 10 min and annealing at 300 °C for 15 min it was possible to completely remove the carbon contamination. The normal emission scan in Figure 2c (blue line) shows the absence of any other contamination-related features. For details on the potential impurity species and their expected concentrations see the Supporting Information. However, the chemical composition analysis summarized in Table 1 reveals changes in the surface stoichiometry. The sensitivity factors of Wagner were used to normalize the fitted peak areas<sup>[33]</sup> While absolute values may suffer from inaccuracies, the relative trend is correct within a few percent. The stoichiometric composition of the crystal was checked prior to our experimental investigations.<sup>[11]</sup>

With increasing annealing temperature, the amount of Zn in the subsurface was gradually reduced. Annealing at 300 °C decreased the oxygen amount compared to the as loaded sample, but increasing the temperature to 500 °C caused no further reduction. After sputtering and annealing (250 eV, 300 °C (UHV)), around 66 % of the Zn and around 20% of the oxygen was lost. Continued sputtering of the sample with higher energy ions (500 eV, 20 min) revealed an increase of the Zn content and no further change can be observed with increased sputtering duration (500 eV, 40 min). This indicates a preferential sputtering of oxygen and gallium with respect to Zn, leading to a relative increase of Zn. However, annealing the sample again at 300 °C for 15 min (500 eV, 300 °C (UHV)) restores the composition to the previous one before the prolonged sputtering.

We conclude from these observations that the reducing conditions of UHV annealing lead to a significant reduction of Zn in the surface, already at low annealing temperatures. Sputtering was shown to be necessary to remove carbon. While Ga and O are preferentially sputtered with respect to Zn, the necessary follow up annealing (to achieve crystallinity) favors Zn deficiency, leading to a non-stoichiometric surface with about 66% of Zn missing.

To obtain a clean and ordered surface with approximately bulk stoichiometry, we treated a new sample in oxidizing conditions. To avoid excessive Zn loss, the annealing temperature was limited to 300 °C and the sputtering time was reduced to 5 min.

While the initial annealing at 300 °C for 30 min resulted in a reduction of the C 1s intensity (Figure 2b), sputtering was also in

**Table 1.** Chemical composition analysis by XPS of ZGO(100) prepared in UHV.

	Zn [%]	Ga [%]	O [%]
Nominal ZGO composition	14.3	28.6	57.1
As loaded	15	23.4	61.6
300 °C	12.7	31.3	56
500 °C	6.8	37.9	55.3
250 eV, 300 °C	5	42	53
500 eV, 20 min	9.6	40.6	49.8
500 eV, 40 min	9.6	41.2	49.2
500 eV, 300 °C	5	42.8	52.2

**Table 2.** Chemical composition analysis by XPS of ZGO(100) prepared in oxygen atmosphere.

	Zn [%]	Ga [%]	O [%]
Nominal ZGO composition	14.3	28.6	57.1
As loaded	15.6	24	60.4
300 °C	15.5	27.8	56.7
250 eV, 300 °C	13	31.5	55.5

this case necessary to achieve a contamination-free surface. After sputtering and a follow up annealing at 300 °C for 15 min, the carbon signal was reduced below the detection limit, even when the surface sensitivity was enhanced by grazing emission. The survey scan after sputtering and oxygen annealing shown in Figure 2c also indicates the absence of other contaminations. The Mo 3d peak associated with the sample holder has no influence on the subsequent analysis.

The annealing in oxygen atmosphere successfully reduced the Zn loss, as shown in Table 2. A further beneficial effect of the oxygen annealing is the reduction of the sputtering time necessary to clean the surface, which led to a reduction of the Zn and O amounts lost due to selective sputtering. The follow-up annealing in oxygen atmosphere minimally changed the composition, thus yielding a surface with nearly stoichiometric composition.

To evaluate the surface crystallinity, we show in Figure 3 the LEED diffraction pattern of the ZGO surface treated in oxygen atmosphere. No diffraction pattern is observable for the as loaded sample in Figure 3a, while annealing at 300 °C for 30 min in oxygen atmosphere results in sharp diffraction spots, shown in Figure 3b. Sputtering and subsequent annealing resulted in no qualitative change of the diffraction pattern in Figure 3c. The diffraction pattern has a fourfold symmetry, with the distances from the (11) to (01) and from the (11) to (10) spots being the same. Yellow arrows in Figure 3d indicate the directions of the reciprocal lattice vectors  $\mathbf{b}_1^*$  and  $\mathbf{b}_2^*$  and the arrow length corresponds to the distance between the diffraction spots. By measuring the distance, we obtain a length of  $1.1 \text{ \AA}^{-1}$  for  $\mathbf{b}_1^*$  and  $\mathbf{b}_2^*$ . Furthermore, the reciprocal vectors are rotated by  $45^\circ$  from the [10 10] directions. The real space vectors  $\mathbf{b}_1$  and  $\mathbf{b}_2$  in Figure 3e each have a length of  $\frac{\sqrt{2} \cdot a}{2}$ , hence the reciprocal vectors  $\mathbf{b}_1^*$  and  $\mathbf{b}_2^*$  each have a length of  $\frac{4\pi}{\sqrt{2}a} = 1.07 \text{ \AA}^{-1}$ , using a value of  $a = 8.336 \text{ \AA}$  for the lattice parameter.<sup>[11]</sup> The magnitude of the reciprocal lattice vectors is in good agreement with the measured value of  $1.1 \text{ \AA}^{-1}$  obtained by LEED. Additionally, the absence of any  $1/N$ -order spots ( $N = 2, 3, 4, \dots$ ) means that no reconstruction is observed.

While LEED is generally referred to as a surface sensitive technique, it was recently shown on SrTiO<sub>3</sub> surfaces that a  $(1 \times 1)$  pattern cannot warrant a pristine surface with a bulk-truncated  $(1 \times 1)$  termination.<sup>[34]</sup> In fact, LEED also probes the subsurface region about three monolayers deep. While smaller imperfections at the very surface may not necessarily be detected, a  $(1 \times 1)$  LEED pattern fitting to ZGO indicates that the low annealing temperatures are sufficient to achieve crystallinity in the same information depth that is probed by ARPES.

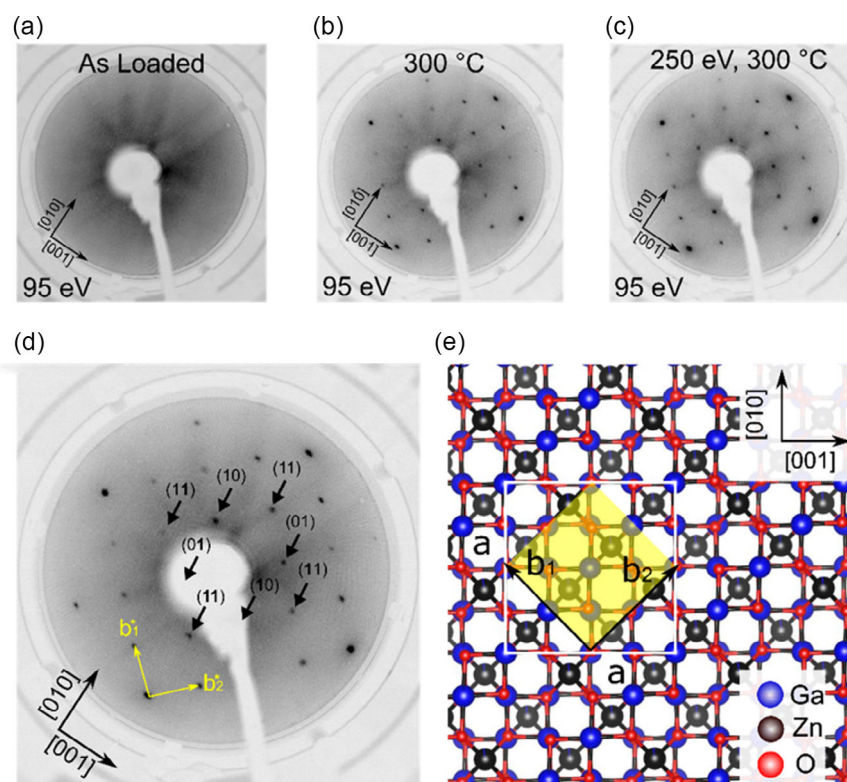


**Figure 3.** LEED diffraction pattern of the ZGO(100) surface obtained with electron kinetic energies of 95 eV a) for the as loaded sample, b) after annealing in oxygen atmosphere at 300 °C, and c) argon sputtering with 250 eV ion energy followed by annealing in oxygen atmosphere at 300 °C. An enlarged version of (b) is shown in (d), in which the first-order diffraction spots are marked by black arrows and labels. The yellow arrows mark the directions of the reciprocal lattice vectors  $b_1^*$  and  $b_2^*$ . In panels (a) to (d), the crystallographic directions of the bulk are specified on the left side. The real space surface of ZGO(100) is shown as a ball and stick model in (e) with the in-plane crystallographic directions in the top right corner. The surface of the bulk unit cell is marked by a white square with the side length  $a$ , while the surface unit cell is marked by a yellow square with the side length  $b_1$  and  $b_2$ .

## 2.2. Electronic Structure of the ZGO(100) Surface After Preparation in Oxygen Atmosphere

Since the preparation in oxidizing conditions yielded a nearly stoichiometric composition and sufficient crystalline structure, we focus now on the electronic structure of the surface, starting with a detailed analysis of the core-level measured by XPS. Figure 4a–c shows the Ga 2p<sub>3/2</sub>, Zn 2p<sub>3/2</sub> and O 1s core-level after each preparation step in oxygen atmosphere. After the initial annealing to 300 °C, a rigid shift toward lower binding energy by about 0.3 eV of all peaks is observed. Since all core-level shift by the same value, we attribute this observation to a Fermi-level ( $E_F$ ) shift relative to the valence band maximum and not to a chemical shift induced by the appearance of new chemical species.

After sputtering and annealing, the Ga 2p<sub>3/2</sub> and O 1s peaks shift by about 0.4 eV to higher binding energy, while the Zn 2p<sub>3/2</sub> peak only shifts by about 0.1 eV to higher binding energy. At the same time, a broadening of the Zn 2p<sub>3/2</sub> peak is observed, while the Ga 2p<sub>3/2</sub> peak has constant line shape, indicating that the cleaning procedure does not change the chemical state of Ga, while it does for Zn. Similarly, the O 1s core-level line shape changes depending on the cleaning step: a high-binding energy tail is present for the as loaded sample, which decreases in

intensity after annealing and vanishes after the sputtering and annealing step. An additional, shoulder on the low-binding energy side appears at about 0.9 eV from the main peak after sputtering and annealing. The peak fitting of the O 1s core-level with pseudo-Voigt model functions after subtraction of a Shirley background is reported in Figure 4d–f. The as loaded O 1s peak features a tail at the high binding energy side due to C–O bonding, which is consistent with previous studies for untreated ZGO and  $\beta$ -Ga<sub>2</sub>O<sub>3</sub> surfaces.<sup>[31,32]</sup> Fitting the O 1s peak of the as loaded sample with two components, one for the oxygen bond in ZGO and one for C–O, is sufficient. After annealing, the contribution of the carbon-related component is reduced, consistent with the observation on the carbon core-level in Section 2.1. In contrast, sputtering and annealing results in a complete removal of the C–O component and at the same time in the appearance of an additional peak on the low binding energy side of the peak, contributing about 7% to the total intensity. This component is separated by about 0.9 eV from the ZGO main line, a value that is consistent with that of ZnO in the report by Chikoidze et al.<sup>[32]</sup> The shoulder occurs together with the broadening a smaller shift of the Zn 2p<sub>3/2</sub> core-level, which indicates that a new chemical bond is formed between Zn and O. Therefore, we conclude, that sputtering and annealing in oxygen atmosphere induce the formation of ZnO.

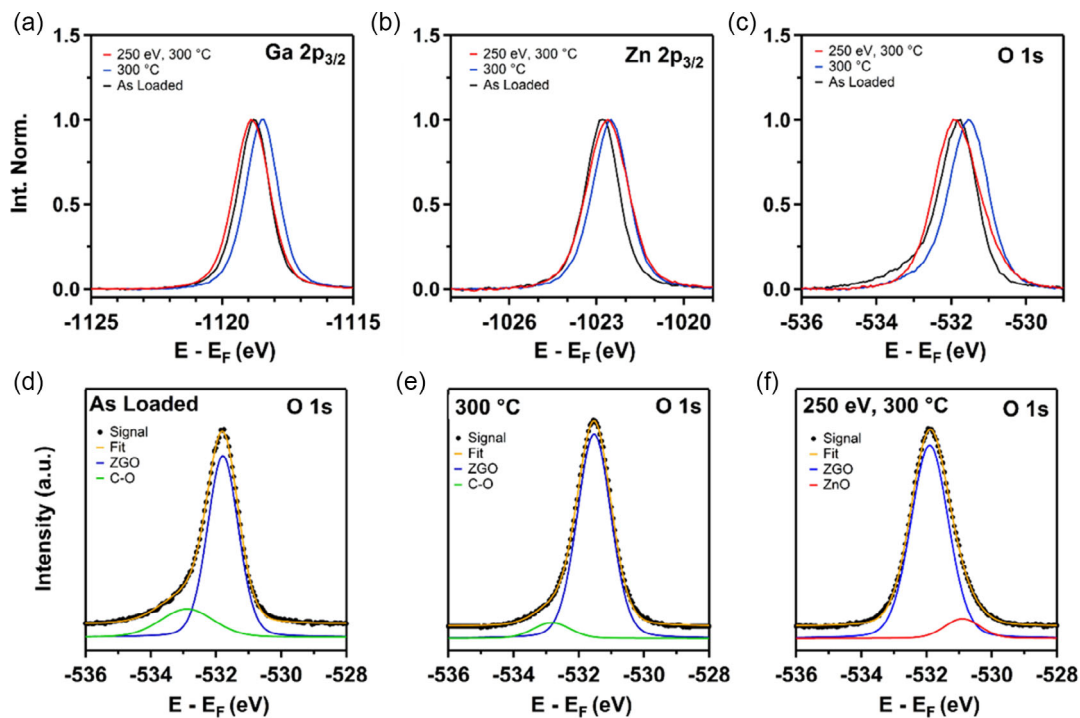


**Figure 4.** Intensity normalized XPS spectra (1486.7 eV) of a) Ga  $2p_{3/2}$ , b) Zn  $2p_{3/2}$ , and c) O  $1s$  for the as loaded ZGO(100) surface (“As Loaded”), after annealing in oxygen atmosphere (“300 °C”) and after sputtering and annealing in oxygen atmosphere (“250 eV, 300 °C”). d)–f) Fit of the O  $1s$  core-level region after each cleaning step measured at normal emission. Dotted lines indicate the measured signal, while solid lines of different colors indicate the fitted components.

Whether the ZnO is present as an overlayer or phase separated in the subsurface region can be answered by a non-destructive depth-profiling, for example, by angle-dependent XPS measurements, which, at the same time, provide information on the presence of a band bending.<sup>[35]</sup> We compare in **Figure 5a–d** the Ga  $2p_{3/2}$ , Zn  $2p_{3/2}$ , O  $1s$ , and Ga  $3d$  core-level spectra taken at normal emission ( $0^\circ$ ) with spectra taken at grazing emission ( $60^\circ$ ). Spectra in grazing emission have their information depth reduced by about 50% with respect to normal emission spectra. A band bending would result in a shift of all core-level peaks and/or a narrowing of the peaks upon reduction of the information depth.<sup>[36]</sup>

Such changes to the spectra could not be observed, indicating a band bending is either absent or too small to be detected, that is, smaller than 50 meV.

While the Ga  $2p_{3/2}$  core-level and the Zn  $2p_{3/2}$  core-level are angle-independent, the component related to ZnO in the O  $1s$  spectrum broadens. This can be explained by an increase in intensity of the ZnO-related component relative to the ZGO main line and thus, may be associated with an increase of the ZnO component at the surface. In contrast, the angle-independence of the Zn  $2p_{3/2}$  hints to uniform depth distribution of the ZnO within the information depth. This apparent contradiction is explained considering the differences in the information depth of O  $1s$  and Zn  $2p_{3/2}$ . If the ZnO is homogeneously distributed in a subsurface region of similar depth as the information depth of Zn  $2p_{3/2}$ , no angle-dependence will be noticeable. In contrast, since the O  $1s$  core-level has a much larger information depth,

it probes deeper below the surface. Halving the information depth with grazing emission ( $60^\circ$ ) probes the surface in a condition similar to that of the measurement of the Zn core-levels. From this, we conclude that the distribution of ZnO is uniform in the first nanometer of the subsurface region.

In grazing emission, one may also notice a small increase in intensity around the high binding energy side of the O  $1s$  peak. As stated earlier, such a shoulder can be associated with C–O bonds. Since we have shown in **Figure 2b** the absence of carbon after the cleaning, the observation of this shoulder indicates the adsorption of small amounts of C–O from the residual gas of the chamber during the final measurements in grazing emission.

At last, the intensity of the low-binding energy shoulder of the Ga  $3d$  core-level under the valence band is reduced in grazing emission with respect to normal emission. Furthermore, the Zn  $3d$  semi-core-level intensity is reduced with respect to that of Ga  $3d$ , indicating that a lower amount of Zn at the surface. As we will outline in the final section of this article, these observations could be related to the intrinsic stabilization of the surface by the termination with gallium oxide.

### 2.3. Valence Band Structure of the ZGO(100) Surface After Preparation in Oxygen Atmosphere

Our investigation of the surface by ARPES serves two purposes: First, it allows a direct probing of the  $k$ -space resolved valence band structure, enabling us to identify electronic states and the position of the valence band maximum of the probed sample.

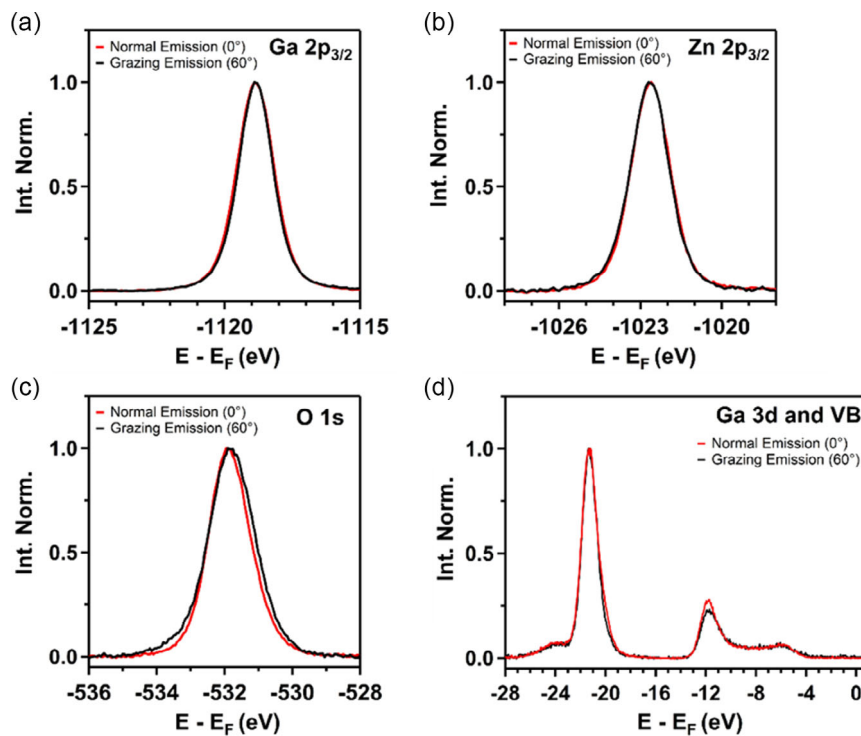


**Figure 5.** Angle-dependent XPS (1486.7 eV) scans after sputtering and annealing in oxygen atmosphere, shown for the a) Ga 2p<sub>3/2</sub>, b) Zn 2p<sub>3/2</sub>, c) O 1s, and d) the Ga 3d core-level regions. Two angles are compared with respect to the surface normal: Normal emission (0°) and grazing emission (60°).

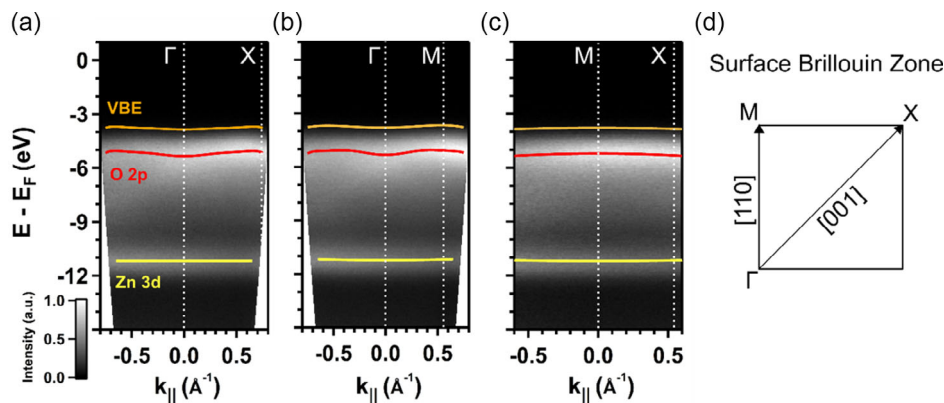


**Figure 6.** ARPES intensity maps along the a)  $\Gamma$ -X, b)  $\Gamma$ -M, and c) M-X high symmetry directions, measured with an excitation energy of 40.8 eV. Dispersion of the valence band leading edge (VBE) (orange), O 2p states (red), and Zn 3d semi-core-level (yellow) are indicated by lines. d) A schematic of the surface Brillouin zone, labeled with the in-plane crystallographic directions and the high symmetry points.

Second, the extremely high surface sensitivity will provide further information on the surface quality, especially when compared to calculations in the following sections.

ARPES intensity maps are reported in **Figure 6** for the three high symmetry directions in a-c, as described by the schematic of the surface Brillouin zone of **Figure 6d**. The first notable feature we observe is the Zn 3d semi-core-level located at a binding energy of -11.2 eV, indicated by the yellow lines. Due to its core-level character, the feature shows no dispersion in k-space. The most intense feature in the valence band is constituted by the

O 2p states and is located between -5 and -6 eV. A sizeable dispersion is present along each of the three high symmetry directions, as indicated by red lines in the graphs. The O 2p band reaches its highest binding energy around  $\Gamma$ , while it reaches the lowest binding energies at the M- and X-points. A similar trend is also observable for the valence band leading edge, indicated by orange lines between -3 and -4 eV. Looking at the dispersion along the M-X direction, we find that the electron bands reach a binding energy of -3.65 eV at the M-point, while they lie 100 and 150 meV higher in binding energy at the X- and  $\Gamma$ -point

respectively. This means that the valence band maximum (VBM) is located at the M-point.

A value of  $3.65 \text{ eV} \pm 0.05 \text{ eV}$  for  $E_F$ -VBM is significantly smaller than the optical band gap of  $4.6 \text{ eV}$ . In fact, the intrinsically high  $n$ -doping of  $6.1 \times 10^{18} \text{ cm}^{-3}$  due to antisite defects should result in a position of  $E_F$  at the conduction band minimum, that is, to a larger  $E_F$ -VBM value to be consistent with the optical gap, similar to investigations on other TSOs.<sup>[28]</sup> However, annealing in oxygen atmosphere is known to cause the formation of semi-insulating layers (which have the effect of shifting the Fermi-level toward the middle of the bandgap) on TSOs. It appears plausible that we observe a similar effect, as we also observed a shift of all core-level in XPS toward lower binding energy after annealing in oxygen atmosphere.

A flat dispersion of the valence states is expected due to the high effective masses of electrons in the valence band, as shown by our calculations for the ZGO bulk electronic structure in the following section. The presence of dispersion and intensity modulation indicates a good quality of the probed subsurface region, supported by the LEED measurements. However, the observed features in ARPES appear to be broadened, which can be explained by a large number of overlapping bands originating from the large number of atoms in the ZGO unit cell, albeit changes in the stoichiometry cannot be excluded as another possible source for the observed smearing of bands. We are now going to address this matter with the support of first-principles calculations in the following sections.

#### 2.4. Calculated ZGO Bulk Band Structure

In **Figure 7a** we show the calculated bulk band structure of ZGO, in a) the full band structure and in b) and c) the spectral density in a narrow range around the VBM. Although the details depend to a certain extent on the computational method (see the Supporting Information), this does not affect the discussion in

this paragraph. The theoretical VBM lies slightly above the highest occupied band at  $\Gamma$  and is located close to the M-point on the Brillouin zone edge, which is highlighted in **Figure 7b**. The location of the VBM around M is in excellent agreement with our experimental results obtained by ARPES. Furthermore, the large number of bands and for oxides usual broadening may explain the small number of resolvable features in the ARPES experiments. A point of disagreement between the calculated and experimental bulk band structures lies in the highest position of bands at X and M, whose energy difference between is too large. This is however not a true discrepancy, as the calculations are for the bulk, while the ARPES measurements show surface-projected bands. In fact, the surface-projected theoretical bulk band structure shown in **Figure 7c** is in good agreement with our ARPES experiments. Following these results, we are now going to discuss possible surface structures that may have influenced the obtained ARPES data.

#### 2.5. Surface Electronic Structure—Comparison of Theory and Experiment

The influence of the surface is visible in the comparison of experimental and calculated energy distribution curves (EDC) in **Figure 8**. Major features of the calculated EDC such as the O 2p peak at the VBM and the Zn 3d states together with its hybridized O 2p counterpart are recognizable already for the bulk. However, the O 2p peak is clearly too narrow, and some of its intensity moves to a shoulder that is missing from the experimental EDC. The relative height ratio of both peaks appears to be correct, but this may be due to fortunate cancellation of errors, as explained in Supporting Information.

To infer the surface composition in our calculations, we made use of experimentally acquired information on the periodicity and the electronic states. This way, the discussion of possible surface structures is not solely based on total energies. According to

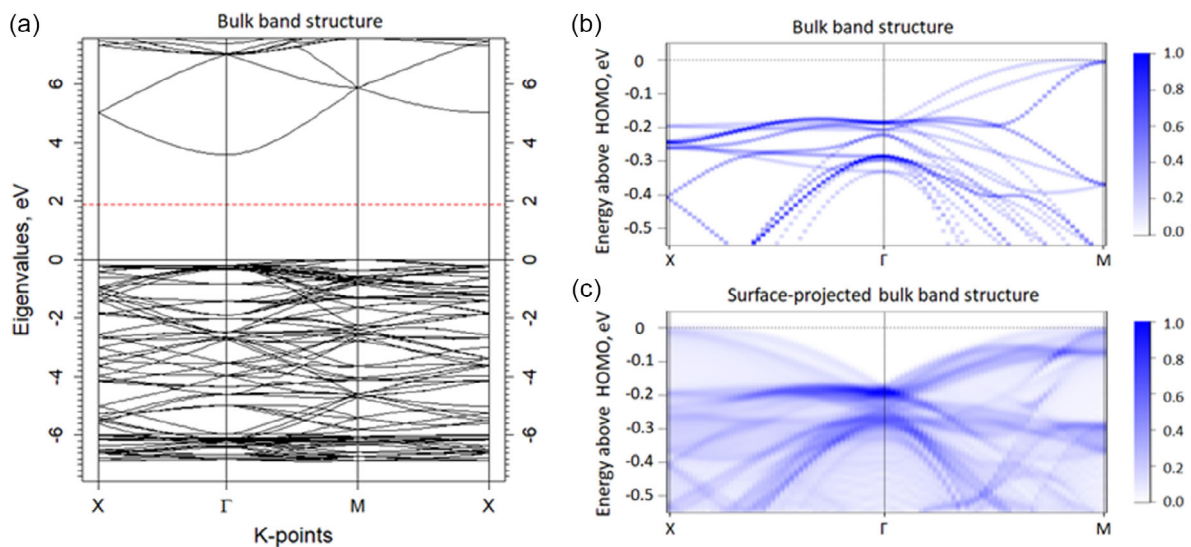


**Figure 7.** a) Calculated bulk band structure of ZGO (QExa/PBE, see Supporting Information). b) Enlarged valence band structure to highlight the maximum of the valence band around the valence band maximum at the M-point. c) Surface-projected bulk band structure of ZGO. The intensity scale in (b) and (c) reflects the expected photoemission intensity for excitation with He II radiation.

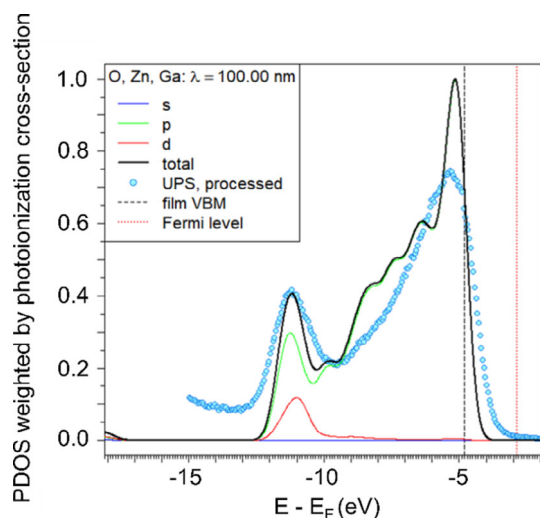


**Figure 8.** Comparison between the experimental energy distribution curve (EDC) (blue, dotted) and the calculated bulk component EDC, simulated for He II and normal emission (black, solid). The simulated EDC is broadened by 0.4 eV and normalized to the experimental curve area in the range between  $-3$  and  $-12.5$  eV.

LEED, we can sort out surface structures that will not result in a  $(1 \times 1)$  diffraction pattern. From the absence of a detectable band bending, we infer that there are no surface states able to trap the Fermi level in n-type samples at energies deeper than about 50 meV below the minimum of the conduction band. Excluded are also structures producing a strong photoemission signal from states within the band-gap and/or near the VBM.

The bulk of ZGO is composed of alternating (100)-oriented, one atom thick layers of two types: positively charged metal layers, Zn, and negatively charged oxide layers,  $\text{Ga}_2\text{O}_4$ . Because of the bilayer structuring of the bulk, there are two classes of ZGO(100): Zn-terminated and  $\text{Ga}_2\text{O}_4$ -terminated (see Figure 9a,b). The  $(1 \times 1)$  surface unit cell obtained by truncating the bulk at a (100) plane contains either two Zn atoms or two  $\text{Ga}_2\text{O}_4$  units. Zn-terminated stoichiometric ZGO(100)  $(1 \times 1)$  is n-type metallic, which would fit to the experiment. In attempt to account for the surface preparation induced loss of Zn revealed by XPS, we removed half of surface Zn; this renders the surface semiconducting without introducing new photoemission states. The Zn loss suggested by XPS (Table 2) is however higher: given that there are four layers of Zn per ZGO unit cell and an information depth of three-unit cells for the Zn  $2p_{3/2}$  core-level, up to two Zn monolayers disappear on sputtering and annealing in oxygen atmosphere. This means that the surface obtained after the sample preparation can only be Zn-terminated, if there was a Zn surplus on the surface of the as loaded sample. If the as loaded sample had a nearly stoichiometric surface, the surface preparation would not result in Zn termination.

Being p-type metallic, unreconstructed  $\text{Ga}_2\text{O}_4$ -terminated ZGO is incompatible with measurements. Dimerization of two O atoms in each  $1 \times 1$  cell reduces the energy by 1.5 eV per cell and turns the surface semiconducting. However, for any ZGO(100) surface with marked Zn deficiency, the VBM O 2p peak simulated for He II (40.8 eV) is too strong.

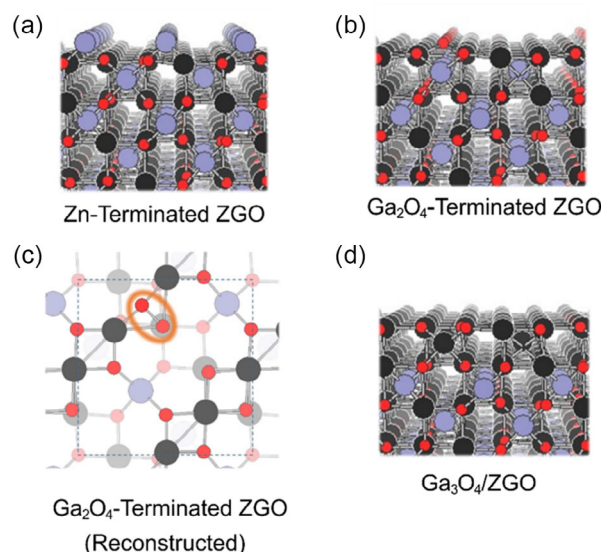


**Figure 9.** a,b) Side-views of Zn- and  $\text{Ga}_2\text{O}_4$ -terminated surfaces, respectively. Zn is blue, Ga is black, O is red. c)  $\text{Ga}_2\text{O}_4$ -terminated, reconstructed ZGO(100)  $1 \times 1$  (top view). The O dimer is indicated. d) Side-view model of ZGO(100) with a monolayer  $\text{Ga}_3\text{O}_4$ .

On  $\text{Ga}_2\text{O}_4$ -terminated ZGO, one O vacancy per  $(1 \times 1)$  cell (Figure 9c) reduces the O 2p peak only slightly, though the surface remains semiconducting, with occupied vacancy states within 1 eV to bulk VBM. Additional oxygen vacancies produce surface states, absent from the measured band structure. To explain the experiment, one must a) calibrate the inelastic mean free path (IMFP), b) refer to inaccuracy in the computed degree of Zn–O hybridization (see Supporting Information), or c) allow for a mixture of the two effects.

Further difficulty arises from the relative increase of Ga with respect to Zn at the surface, as detected by XPS. One may explain this increase by assuming that Ga atoms substitute Zn in the topmost bilayer of ZGO, leading to a monolayer of  $\text{Ga}_3\text{O}_4$  on top of a  $\text{Ga}_2\text{O}_4$ -terminated ZGO (Figure 9d), or Zn-terminated ZGO with two layers of cubic  $\text{Ga}_2\text{O}_3$  with O-rich stoichiometry ( $\text{Ga}_2\text{O}_{3.2}$ , or 7% O surplus). Such a surface remains semiconducting, with an occupied surface band extending over about 1 eV above VBM. However, the simulated photoemission O 2p peak is too high in intensity. Surface oxygen vacancies do not help, as they introduce prominent band gap states. Adjusting the IMFP  $\lambda$  improves the ratios between the peaks, but does not lead to satisfactory spectra, even if an infinite IMFP is assumed. We have therefore considered the possibility that the oxygen peak experiences additional broadening by surface-induced shifts due to atomic configuration dependence of Hubbard  $U$  (see Supporting Information). This reduces the relative height of the O 2p VBM peak, broadening its maximum, so that also the troublesome shoulder visible in Figure 8 is less pronounced. Nevertheless, the area of the oxygen peak remains too large and the peak maximum remains too high. The presence of surface defects will contribute to the broadening, but it is not immediately clear that it would significantly improve the relative area under the two peaks. However, the observed discrepancy

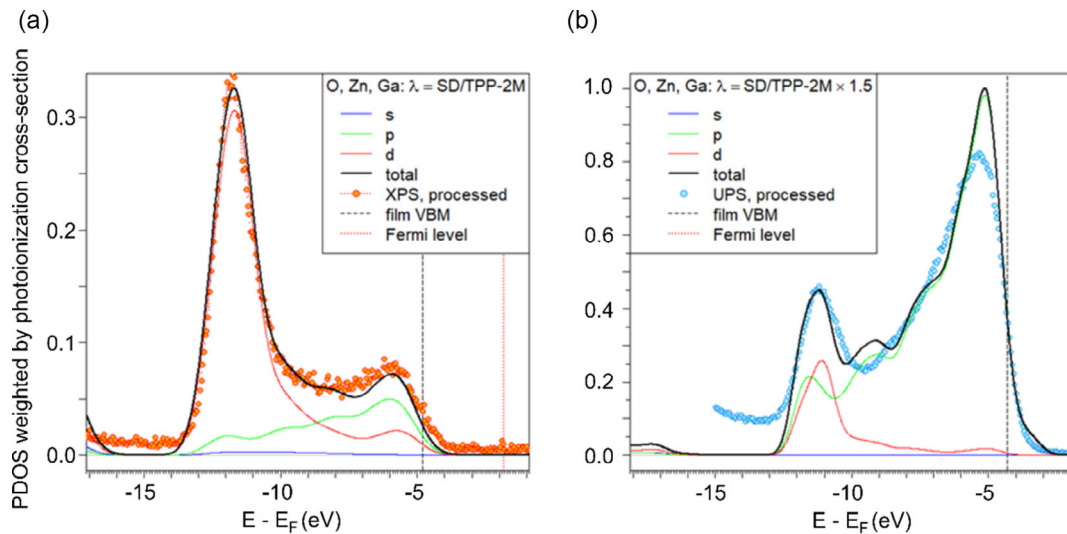


**Figure 10.** a) QEpaw/PBE calibration of photoemission cross-sections, with broadening by 0.65 eV and area normalization in the range from  $-3$  to  $-14$  eV. b) He II EDC simulated for  $\text{Ga}_3\text{O}_4/\text{ZGO}$ , with site-dependent Hubbard  $U(\text{O})$  and inelastic mean free path increased by 50%. The curve area is normalized to the experimental data in the range from  $-3$  to  $-12.5$  eV, broadening 0.4 eV.

may be associated with the fact that it is not always straightforward to obtain the correct amount of hybridization between oxygen and metal atoms;<sup>[37,38]</sup> indeed, even a computed Hubbard  $U$  is in practice a constrained quantity and may require renormalization.<sup>[39]</sup> For ZGO computed in the GGA +  $U$  framework, this amount does indeed depend on the pseudopotentials used (see Supporting Information). Because photoemission cross-sections depend strongly on the photon energy, this inaccuracy limits the transferability of the calibration made at Al  $K\alpha$  (1486.7 eV) shown in Figure 10a, to the simulations performed for He II (40.8 eV) shown in Figure 10b. This is not alleviated by a pseudopotential calculation with a hybrid functional (HSE). We obtained the best results with PBE exchange and correlation, with the QEpaw pseudopotential set, with oxygen Hubbard  $U$  for ZGO bulk determined by optimization of the ZGO bulk lattice constant, with site-dependent corrections to this bulk value computed self-consistently and with Zn and Ga Hubbard  $U$  adjusted to match the positions of the corresponding photoemission peaks. This ambiguity caused by the dependence of the hybridization degree on the pseudopotential might in general be resolved by introducing an intersite  $V$  term into the Hubbard functional.<sup>[40,41]</sup> However, this solution is unfortunately not practical in this particular case, because it implies the use of computed Hubbard parameters and the values of Hubbard  $U$  for the closed-shell atoms (Zn and Ga in ZGO) cannot be obtained in this way.

### 3. Conclusions

Our comparison of in situ surface preparation methods by sputtering and annealing revealed that annealing in UHV leads to significant Zn loss in the subsurface region, which we were able to suppress by the annealing in oxygen. While a high temperature stability of samples was reported by Galazka et al.,<sup>[11]</sup> our results indicate that the surface composition is unstable already

at much lower temperatures. After low temperature annealing, a  $(1 \times 1)$  LEED pattern with sharp spots was observed, indicating sufficient crystallinity in the probed subsurface region. This finding was crucial to justify the subsequent analysis by ARPES for comparison with theory. A noncrystalline subsurface region would hold less valuable information due to the lack of band dispersion. A sizeable Zn-loss of at least 17% from the first nanometer indicates stabilization of the surface in a  $\text{Ga}_2\text{O}_3$  phase. We found this hypothesis to be compatible with ab initio DFT simulations if this oxide is two monolayer thick, although this compatibility requires adjustments to some theoretical parameters (as energy-independent calibration of photoemission cross-sections and 50% increase of the IMFP of photoelectrons).

Reduced sputtering time and annealing in oxidizing conditions are crucial to obtain near-stoichiometric surfaces, albeit measurable quantities of gallium oxide and phase separated ZGO are present in the subsurface region. The optimization of the surface preparation should be investigated in the future by also exploring wet chemical etching in combination with low temperature annealing in oxygen atmosphere.

ARPES revealed dispersion of the O 2p states along the high symmetry directions and the results are compatible with the calculated bulk band structure, both methods finding the VBM located at the M-point. The result obtained by experiment and DFT are mutually supportive, indicating a good quality of the surface after preparation.

Overall, these results present important insights on the fundamental surface electronic structure of ZGO and the thermal instability of the surface, leading to Zn loss. The latter is especially important to consider for heterostructures in devices based on ZGO.

From the analysis of the relative peak height in measured and simulated EDCs we conclude that the Yeh-Lindau photoionization cross-sections need calibration for use with pseudopotential wave functions,<sup>[42]</sup> and inaccurate description of metal-oxygen

hybridization by DFT calculations with Hubbard U results in non-negligible calibration errors. This inaccuracy is not alleviated by pseudopotential calculations with Hartree–Fock admixture (hybrid). We also noticed that the site-dependency of Hubbard U has a visible influence on the width of simulated photoemission peaks.

#### 4. Experimental Section

**Experimental Details:** Two samples were cut from a high-quality melt-grown bulk ZGO single-crystal with one surface aligned parallel to the (100) crystal planes.<sup>[11]</sup> For details on the purity of the crystals see the Supporting Information.

The first sample showed n-type conductivity with an electron concentration of  $n = 7.49 \times 10^{19} \text{ cm}^{-3}$  and was treated in UHV (reducing) conditions. The intrinsically high doping stems from Ga/Zn antisite defects that have formed during the growth and were not compensated during cool down or by post-growth annealing.<sup>[11–13]</sup> The first step of the surface treatment procedure consisted in annealing at 300 °C for 30 min, followed by annealing to 500 °C for 30 min to study the influence of the annealing temperature on the chemical composition and the removal of carbon contamination. The sample temperature was monitored through a thermocouple and the ramping rate was  $\approx 0.7 \text{ K s}^{-1}$ . Subsequently, sputtering for 10 min by  $\text{Ar}^+$  ions with an energy of 250 eV followed by annealing at 300 °C for 15 min was employed to remove the remaining carbon contamination. For sputtering, Ar gas was inserted until a partial pressure of  $1 \times 10^{-5} \text{ mbar}$  was reached and the sputter current at the sample was 17  $\mu\text{A}$ . Following the initial sputtering and annealing, the sample was again sputtered by  $\text{Ar}^+$  ions, but this time with an energy of 500 eV for 20 min and afterward for an additional 20 min, to alter the composition and detect preferential sputtering. Finally, the sample was annealed at 300 °C for 15 min to investigate the chemical composition after this procedure.

The second sample showed, similar to the first sample, an intrinsic n-type conductivity with an electron concentration of  $n = 6.1 \times 10^{18} \text{ cm}^{-3}$  and was annealed in oxidizing conditions with an oxygen partial pressure of 10 mbar. The preparations steps include an initial annealing at 300 °C for 30 min after the sample was loaded into the system. Afterward, the sample was sputtered for 5 min by  $\text{Ar}^+$  ions with an energy of 250 eV, followed by annealing at 300 °C for 15 min. For annealing, the temperature was monitored with a thermocouple, the ramping rate was  $\approx 0.7 \text{ K s}^{-1}$  and the ramping was also done in an oxygen atmosphere of 10 mbar. Sputtering used an Ar partial pressure of  $1 \times 10^{-5} \text{ mbar}$  and the sputter current was 17  $\mu\text{A}$ .

The ARPES measurements were done with a Phoibos 150 analyzer and a monochromated Helium discharge lamp allowing the use of He II (40.8 eV) for the excitation of photoelectrons and delivering a beam of 0.7 mm diameter spot size. For ARPES, the angular resolution was better than  $0.2^\circ$  and the energy resolution was better than 120 meV, dominated by the thermal broadening at room temperature (as measured on the Fermi edge width of a Mo plate in electrical contact with the sample). For XPS, a monochromated Al  $K_{\alpha}$  X-ray source exhibiting a spot size of  $3.5 \times 1 \text{ mm}^2$  has been employed, showing an energy resolution better than 600 meV, corresponding to a full-width half maximum of  $\approx 700 \text{ meV}$  on the referenced Ag  $3d_{5/2}$  peak at  $(368.21 \pm 0.02) \text{ eV}$ . The angular acceptance of the analyzer was set to be  $\pm 2^\circ$ , enabling angle-dependent XPS measurements. LEED data was acquired with an ErLEED 150 optics and a CCD camera mounted on the backside of the fluorescent screen.

**Theoretical Approach:** We applied the ab initio plane wave density functional theory with Hubbard U correction (DFT + U),<sup>[43,44]</sup> ultrasoft and norm-conserving scalar-relativistic pseudopotentials of PBE type.<sup>[45]</sup> The calculations were conducted on the JUWELS cluster,<sup>[46]</sup> using the Quantum Espresso (QE) package.<sup>[47]</sup> The valence configuration was 3d 4s 4p for Zn, 3d 4s 4p for Ga, and 2s 2p for O; in tests, we used also 4s 4p for Ga and 3s 3p 3d 4s 4p for Zn. The cutoff energy was 40 Ry for ultrasoft and 80 to 260 Ry for norm-conserving pseudopotentials. The Brillouin zone was sampled with the  $2 \times 2$  Monkhorst-Pack grid with

offset. The slabs contained about 100 up to 300 atoms (but about 160 atoms for most of the simulations). Because in ZGO(100) the bulk dipole moment cannot be cancelled externally, we used slabs that are symmetric with respect to the middle plane. The slabs were separated by about 1.5 nm of vacuum. The Hubbard U correction was applied to the 3d and 2p states. Because self-consistent calculation of Hubbard U<sup>[44]</sup> is challenging for atoms with closed shells,<sup>[48,49]</sup> such as Zn and Ga, we first estimated U(O) by fitting the ZGO lattice constant and we adjusted the differences U(Ga)-U(O) and U(Zn)-U(O) to reproduce the positions of the measured XPS peaks. To judge on the site-dependence of Hubbard U, we then obtained self-consistent U(O) for each O atom. We assessed the degree of uncertainty due to the freedom in the pseudopotential construction and in the selection of Hubbard U by adapting various pseudopotential sets and by performing hybrid functional (HSE<sup>[50]</sup>) calculations for ZGO bulk and for the surface structures of most interest.

Photoemission was simulated from the projection of single-particle Bloch wave functions onto the atomic states. We adapted the photon energy dependence of photoionization cross-sections  $\sigma$  from the Hartree–Fock calculations by Yeh and Lindau for single atoms,<sup>[42]</sup> calibrating their relative magnitude to reproduce the VBM peak area ratio measured with Al  $K_{\alpha}$  radiation. The inelastic mean free paths (IMFP)  $\lambda_{\text{TPP2M}}$  for XPS and UPS were approximated as TPP2M,<sup>[51,52]</sup> roughly corrected at low energies  $E$  by a  $1/E^2$  term.<sup>[53]</sup> For detailed technical information, including accuracy analysis, see Supporting Information.

#### Supporting Information

Supporting Information is available from the Wiley Online Library or from the author.

#### Acknowledgements

The authors gratefully acknowledge the Gauss Centre for Supercomputing e.V. (www.gauss-centre.eu) for funding this project by providing computing time through the John von Neumann Institute for Computing (NIC) on the GCS Supercomputer JUWELS at Jülich Supercomputing Centre (JSC). Open access funding enabled and organized by Projekt DEAL.

#### Conflict of Interest

The authors declare no conflict of interest.

#### Data Availability Statement

The data that support the findings of this study are available from the corresponding author upon reasonable request.

#### Keywords

density functional theory (DFT), photoemission spectroscopy (PES), spinels, surface instabilities, transparent semiconducting oxides (TSOs)

Received: September 3, 2021

Revised: November 29, 2021

Published online:

- [1] S. J. Pearton, J. Yang, P. H. Cary, F. Ren, J. Kim, M. J. Tadjer, M. A. Mastro, *Appl. Phys. Rev.* **2018**, *5*, 011301.
- [2] Z. Galazka, *Semicond. Sci. Technol.* **2018**, *33*, 113001.
- [3] M. Orita, H. Ohta, M. Hirano, H. Hosono, *Appl. Phys. Lett.* **2000**, *77*, 4166.



- [4] J. B. Varley, J. R. Weber, A. Janotti, C. G. Van de Walle, *Appl. Phys. Lett.* **2010**, *97*, 142106.
- [5] H. Peelaers, C. G. Van de Walle, *Phys. Status Solidi B* **2015**, *252*, 828.
- [6] Z. Galazka, R. Uecker, D. Klimm, K. Irmscher, M. Naumann, M. Pietsch, A. Kwasniewski, R. Bertram, S. Ganschow, M. Bickermann, *ECS J. Solid State Sci. Technol.* **2017**, *6*, Q3007.
- [7] Z. Galazka, K. Irmscher, R. Uecker, R. Bertram, M. Pietsch, A. Kwasniewski, M. Naumann, T. Schulz, R. Schewski, D. Klimm, M. Bickermann, *J. Cryst. Growth* **2014**, *404*, 184.
- [8] M. Higashiwaki, K. Sasaki, A. Kuramata, T. Masui, S. Yamakoshi, *Appl. Phys. Lett.* **2021**, *100*, 013504.
- [9] M. Higashiwaki, K. Sasaki, H. Murakami, Y. Kumagai, A. Koukitu, A. Kuramata, T. Masui, S. Yamakoshi, *Semicond. Sci. Technol.* **2016**, *31*, 034001.
- [10] M. Baldini, Z. Galazka, G. Wagner, *Mater. Sci. Semicond. Process.* **2017**, *78*, 132.
- [11] Z. Galazka, S. Ganschow, R. Schewski, K. Irmscher, D. Klimm, A. Kwasniewski, M. Pietsch, A. Fiedler, I. Schulze-Jonack, M. Albrecht, T. Schröder, M. Bickermann, *APL Mater.* **2019**, *7*, 022512.
- [12] Z. Galazka, S. Ganschow, K. Irmscher, D. Klimm, M. Albrecht, R. Schewski, M. Pietsch, T. Schulz, A. Dittmar, A. Kwasniewski, R. Grueneberg, S. Bin Anooz, A. Popp, U. Juda, I. M. Hanke, T. Schroeder, M. Bickermann, *Prog. Cryst. Growth Character. Mater.* **2021**, *67*, 100511.
- [13] Z. Galazka, K. Irmscher, M. Pietsch, S. Ganschow, D. Schulz, D. Klimm, I. M. Hanke, T. Schröder, M. Bickermann, *J. Mater. Res.* **2021**, <https://link.springer.com/article/10.1557/s43578-021-00353-9>.
- [14] J. Boy, M. Handweg, R. Mitdank, Z. Galazka, S. F. Fischer, *AIP Adv.* **2020**, *10*, 055005.
- [15] M. Hilfiker, M. Stokey, R. Korlacki, U. Kilic, Z. Galazka, K. Irmscher, S. Zollner, M. Schubert, *Appl. Phys. Lett.* **2021**, *118*, 132102.
- [16] M. Stokey, R. Korlacki, S. Knight, M. Hilfiker, Z. Galazka, K. Irmscher, V. Darakchieva, M. Schubert, *Appl. Phys. Lett.* **2020**, *117*, 052104.
- [17] Y. Jang, S. Hong, J. Seo, H. Cho, K. Char, Z. Galazka, *Appl. Phys. Lett.* **2020**, *116*, 202104.
- [18] L.-C. Cheng, C.-Y. Huang, R.-H. Horng, *IEEE J. Electron Devices Soc.* **2018**, *6*, 432.
- [19] Y.-C. Shen, C.-Y. Tung, C.-Y. Huang, Y.-C. Lin, Y.-G. Lin, R.-H. Horng, *ACS Appl. Electron. Mater.* **2019**, *1*, 783.
- [20] D. Han, K. Liu, X. Chen, B. Li, T. Zhai, L. Liu, D. Shen, *Appl. Phys. Lett.* **2021**, *118*, 251101.
- [21] R. A. Powell, W. E. Spicer, J. C. McMenamin, *Phys. Rev. B* **1972**, *6*, 3056.
- [22] L. F. J. Piper, A. R. H. Preston, A. Fedorov, S. W. Cho, A. DeMasi, K. E. Smith, *Phys. Rev. B* **2010**, *81*, 23305.
- [23] P. D. C. King, T. D. Veal, C. F. McConville, J. Zuniga-Pérez, V. Munoz-Sanjosé, M. Hopkinson, E. D. L. Rienks, M. F. Jensen, P. Hofmann, *Phys. Rev. Lett.* **2010**, *104*, 256803.
- [24] J. J. Mudd, T.-L. Lee, V. Munoz-Sanjosé, J. Zuniga-Pérez, D. Hesp, J. M. Kahk, D. J. Payne, R. G. Egdell, C. F. McConville, *Phys. Rev. B* **2014**, *89*, 035203.
- [25] K. H. L. Zhang, R. G. Egdell, F. Offi, S. Iacobucci, L. Petaccia, S. Gorovikov, P. D. C. King, *Phys. Rev. Lett.* **2013**, *110*, 056803.
- [26] V. Scherer, C. Janowitz, A. Krapf, H. Dwell, D. Braun, R. Manzke, *Appl. Phys. Lett.* **2012**, *100*, 212108.
- [27] M. Mohamed, C. Janowitz, I. Unger, R. Manzke, Z. Galazka, R. Uecker, R. Fornari, J. R. Weber, J. B. Varley, C. G. Van de Walle, *Appl. Phys. Lett.* **2010**, *97*, 211903.
- [28] C. Janowitz, V. Scherer, M. Mohamed, A. Krapf, H. Dwell, R. Manzke, Z. Galazka, R. Uecker, K. Irmscher, R. Fornari, M. Michling, D. Schmeißer, J. R. Weber, J. B. Varley, C. G. Van de Walle, *New J. Phys.* **2011**, *13*, 085014.
- [29] M. Mohamed, K. Irmscher, C. Janowitz, Z. Galazka, R. Manzke, R. Fornari, *Appl. Phys. Lett.* **2012**, *101*, 132106.
- [30] M. Mulazzi, F. Reichmann, A. P. Becker, W. M. Klesse, P. Alippi, V. Fiorentini, A. Parisini, M. Bosi, R. Fornari, *APL Mater.* **2019**, *7*, 022522.
- [31] A. Navarro-Quezada, S. Alamé, N. Esser, J. Furthmüller, F. Bechstedt, Z. Galazka, D. Skuridina, P. Vogt, *Phys. Rev. B* **2015**, *92*, 195306.
- [32] E. Chikoidze, C. Sartet, I. Madaci, H. Mohamed, C. Vilar, B. Ballesteros, F. Belarre, E. del Corro, P. Vales-Castro, G. Sauthier, L. Li, M. Jennings, V. Sallet, Y. Dumont, A. Pérez-Tomás, *Cryst. Growth Des.* **2020**, *20*, 2535.
- [33] C. D. Wagner, *J. Electron Spectrosc. Relat. Phenom.* **1983**, *32*, 99.
- [34] I. Sokolović, G. Franceschi, Z. Wang, J. Xu, J. Pavelec, M. Riva, M. Schmid, U. Diebold, M. Setvín, *Phys. Rev. B* **2021**, *103*, L241406.
- [35] T. Ogama, *J. Appl. Phys.* **1988**, *64*, 753.
- [36] K. Kakushima, K. Okamoto, K. Tachi, J. Song, S. Sato, T. Kawanago, K. Tsutsui, N. Sugii, P. Ahmet, T. Hattori, H. Iwai, *J. Appl. Phys.* **2008**, *104*, 104908.
- [37] E. B. Linscott, D. J. Cole, M. C. Payne, D. D. O'Regan, *Phys. Rev. B* **2018**, *98*, 235157.
- [38] H. J. Kulik, N. Marzari, *J. Chem. Phys.* **2011**, *135*, 194105.
- [39] V. I. Anisimov, O. Gunnarsson, *Phys. Rev. B* **1991**, *43*, 7570.
- [40] H. J. Kulik, N. Marzari, *J. Chem. Phys.* **2011**, *134*, 094103.
- [41] V. L. Campo Jr, M. Cococcioni, *J. Phys.: Condens. Matter* **2010**, *22*, 055602.
- [42] J. J. Yeh, I. Lindau, *Atom. Data Nucl. Data Tables* **1985**, *32*, 1.
- [43] V. I. Anisimov, J. Zaanen, O. K. Andersen, *Phys. Rev. B* **1991**, *44*, 943.
- [44] M. Cococcioni, S. de Gironcoli, *Phys. Rev. B* **2005**, *71*, 035105.
- [45] J. P. Perdew, K. Burke, M. Ernzerhof, *Phys. Rev. Lett.* **1996**, *77*, 3685.
- [46] Forschungszentrum Jülich; Jülich Supercomputing Centre, *J. Large-Scale Res. Facilities* **2019**, *5*, A171.
- [47] P. Gianozzi, S. Baroni, N. Bonini, M. Calandra, R. Car, C. Cavazzoni, *J. Phys.: Condens. Matter* **2009**, *21*, 395502.
- [48] S.-J. Hu, S.-S. Yan, M.-W. Zhao, L.-M. Mei, *Phys. Rev. B* **2006**, *73*, 245205.
- [49] K. Yu, E. A. Carter, *J. Chem. Phys.* **2014**, *140*, 121105.
- [50] J. Heyd, G. E. Scuseria, M. Ernzerhof, *J. Chem. Phys.* **2003**, *118*, 8207.
- [51] D. R. Penn, *Phys. Rev. B* **1987**, *35*, 482.
- [52] S. Tanuma, C. J. Powell, D. R. Penn, *Surf. Interface Anal.* **1994**, *21*, 165.
- [53] A. Jablonski, S. Tanuma, C. J. Powell, *J. Appl. Phys.* **2008**, *103*, 063708.

# Thesis Conclusion

In my Thesis, I studied the surface electronic structure of Ge(001), Sn/Ge(001),  $\epsilon$ -Ga<sub>2</sub>O<sub>3</sub> and ZnGa<sub>2</sub>O<sub>4</sub> mainly by photoemission techniques. In the following, I am going to summarize the most important results and estimate the impact of this work.

Starting with the pristine Ge(001) surface, I have demonstrated that it is of conducting nature at room temperature. Based on my experiments, it was possible to identify the physical origin of this: at room temperature, thermally excited electrons occupy the surface conduction band minimum formed by the c(4×2) reconstruction. The predominant attribution of a semi-conducting nature in the existing literature may therefore be incorrect. Clearly, this could change our fundamental understanding of the surface and may be important to determine the role of the Ge(001) surface in advanced micro- and optoelectronics, leading to the publication in Applied Surface Science [32].

My investigation of the Ge(001) surface after adsorption of Sn provided new insights into the electronic and surface structure of the interface. A detailed analysis of surface core-level shifts allowed to reveal changes in the subsurface structure that were previously concealed, extending the known growth model of Sn on Ge(001). Valence states of Ge(001) appear to interact with a certain Sn ad-dimer configuration, leading to a new, Sn-related surface state. Notably, the conducting nature of the Ge(001) surface is lost after Sn adsorption. As a matter of fact, the Fermi-level remained pinned after Sn adsorption and/or incorporation, indicating that the Ge(001) surface states are not responsible for the strong Fermi-level pinning close to the valence band maximum. Overall, these results will be important for the applied and fundamental research activities on Sn(Ge) nanostructures and led to the publication in Applied Surface Science [69].

Following my investigation of the Sn/Ge(001) surface, I studied the electronic structure of TSOs that may serve as an alternative to  $\beta$ -Ga<sub>2</sub>O<sub>3</sub> in future (opto)electronic applications. The first TSO I investigated was a  $\epsilon$ -Ga<sub>2</sub>O<sub>3</sub> sample, grown on c-oriented sapphire by metal-organic chemical vapor and the surface was prepared by sputtering and annealing. The combination of XPS and hard-XPS allowed the detailed investigation of deep core-level electrons and revealed the impact of photoelectron recoil. The absence of a band bending based on angle- and energy-dependent XPS-measurements excludes a large density of surface states at the surface. Valence state dispersions measured by ARPES compared favourably with *ab initio* calculations, allowing to detail the effective mass the highest lying valence band. An overall good agreement between the optically and ARPES determined band gap width was observed and the evidence gathered by ARPES and calculations hints towards a direct band gap. These insights are important to define the role of  $\epsilon$ -Ga<sub>2</sub>O<sub>3</sub> in future optoelectronic devices, leading to the publication in APL Materials, 7 (2019) 022522 [91].

Finally I studied the surface electronic structure of ZnGa<sub>2</sub>O<sub>4</sub> single crystals with a (100) surface orientation. An unpredicted instability of the surface was observed, leading to Zn deficiency when such surfaces were annealed in ultra-high vacuum conditions, further exacerbated by sputtering.

I was able to demonstrate that the annealing in oxygen atmosphere can circumvent the surface instability, providing a first recipe for the preparation of nearly stoichiometric surfaces. In fact, I was able to show that the surface electronic structure of such surfaces compares favorably with calculated band structures, indicating a good quality. However, the annealing in oxygen atmosphere presumably lowers the concentration of free carriers at the surface, which may influence devices based on  $\text{ZnGa}_2\text{O}_4$ . This work provides important information for the fundamental research activities on the material, leading to the publication in *Physica Status Solidi B: Basic Solid State Physics* [107].



# References

- [1] P. Hofmann. *Surface Physics: An introduction*. Philip Hofmann, 2016. ISBN: 978-87-996090-1-7.
- [2] H. Ibach and H. Lüth. *Solid-State Physics: An Introduction to Principles of Materials Science*. Berlin: Springer, 2009. DOI: <https://doi.org/10.1007/978-3-540-93804-0>.
- [3] S. Hüfner. *Photoelectron Spectroscopy: Principles and Applications*. Berlin: Springer, 2003. DOI: <https://doi.org/10.1007/978-3-662-09280-4>.
- [4] A. Damascelli, Z. Hussain, and Z.-X. Shen. “Angle-resolved photoemission studies of the cuprate superconductors”. In: *Reviews of Modern Physics* 74 (2003), p. 473. DOI: <https://doi.org/10.1103/RevModPhys.75.473>.
- [5] J. C. Vickermann and I. S. Gilmore. *Surface Analysis – The Principal Techniques*. John Wiley and Sons Ltd, 2009. DOI: <https://doi.org/10.1002/9780470721582>.
- [6] M. P. Seah and W. A. Dench. “Quantitative electron spectroscopy of surfaces: A standard data base for electron inelastic mean free paths in solids”. In: *Surface and Interface Analysis* 1 (1979), p. 2. DOI: <https://doi.org/10.1002/sia.740010103>.
- [7] C. J. Powell und D. R. Penn S. Tanuma. “Calculations of electron inelastic free path data for 14 organic-compounds over the 50-2000 eV range”. In: *Surface and Interface Analysis* 21 (1994), p. 165. DOI: <https://doi.org/10.1002/sia.740210302>.
- [8] J. F. Watts and J. Wolstenholme. *An Introduction To Surface Analysis by XPS and AES*. JohnWiley and Sons Ltd, 2003. DOI: <https://doi.org/10.1002/9780470867930>.
- [9] A. Damascelli. “Probing the Electronic Structure of Complex Systems by ARPES”. In: *Physica Scripta* 109 (2003), p. 61. DOI: <https://doi.org/10.1238/Physica.Topical.109a00061>.
- [10] SPECS GmbH. *SPECS User Manual PHOIBOS 100/150—Hemispherical Energy Analyzer*. 2012.
- [11] ISO 19318:2004. *Surface chemical analysis – reporting of methods used for charge control and charge correction*.
- [12] G. Greczynski and L. Hultman. “X-ray photoelectron spectroscopy: Towards reliable binding energy referencing”. In: *Progress in Materials Science* 107 (2020), p. 100591. DOI: <https://doi.org/10.1016/j.pmatsci.2019.100591>.
- [13] G. H. Major et al. “Practical guide for curve fitting in x-ray photoelectron spectroscopy”. In: *Journal of Vacuum Science and Technology A* 38 (2020), p. 061203. DOI: <https://doi.org/10.1116/6.0000377>.
- [14] M. Engelhard et al. “Introductory guide to backgrounds in XPS spectra and their impact on determining peak intensities”. In: *Journal of Vacuum Science and Technology A* 38 (2020), p. 063203. DOI: <https://doi.org/10.1116/6.0000359>.

- [15] S. Tougaard. “Universality Classes of Inelastic Electron Scattering Cross-sections”. In: *Surface and Interface Analysis* 25 (1997), p. 137. DOI: [https://doi.org/10.1002/\(SICI\)1096-9918\(199703\)25:3<137::AID-SIA230>3.0.CO;2-L](https://doi.org/10.1002/(SICI)1096-9918(199703)25:3<137::AID-SIA230>3.0.CO;2-L).
- [16] R. J. Culbertson, Y. Kuk, and L. C. Feldman. “Subsurface strain in the Ge(001) and Ge(111) surfaces and comparison to Silicon”. In: *Surface Science* 167 (1986), p. 127. DOI: [https://doi.org/10.1016/0039-6028\(86\)90789-2](https://doi.org/10.1016/0039-6028(86)90789-2).
- [17] S. D. Kevan and N. G. Stoffel. “Metal-insulator transition on the Ge(001) surface”. In: *Physical Review Letters* 53 (1984), p. 702. DOI: <https://doi.org/10.1103/PhysRevLett.53.702>.
- [18] H. J. W. Zandvliet. “The Ge(001) surface”. In: *Physics Reports* 388 (2003), p. 1. DOI: <https://doi.org/10.1016/j.physrep.2003.09.001>.
- [19] J. Tersoff and D. R. Hamann. “Theory of the scanning tunneling microscope”. In: *Physical Review B* 31 (1985), p. 80. DOI: <https://doi.org/10.1103/PhysRevB.31.805>.
- [20] A. A. Stekolnikov, J. Furthmuller, and F. Bechstedt. “Absolute surface energies of group-IV semiconductors: Dependence on orientation and reconstruction”. In: *Physical Review B - Condensed Matter and Materials Physics* 65 (2002), p. 115318. DOI: <https://doi.org/10.1103/PhysRevB.65.115318>.
- [21] M. Needels, M. C. Payne, and J. D. Joannopoulos. “Ab initio molecular dynamics on the Ge(100) surface”. In: *Physical Review Letter* 58 (1987), p. 1765. DOI: <https://doi.org/10.1103/PhysRevLett.58.1765>.
- [22] L. Kipp, R. Manzke, and M. Skibowski. “The surface band gaps of Ge(001)  $2 \times 1$ ”. In: *Surface Science* 269 (1992), p. 854. DOI: [https://doi.org/10.1016/0039-6028\(92\)91361-E](https://doi.org/10.1016/0039-6028(92)91361-E).
- [23] L. Kipp, R. Manzke, and M. Skibowski. “An intrinsic metallic surface state on Ge(001)  $2 \times 1$ ”. In: *Solid State Communications* 93 (1995), p. 603. DOI: [https://doi.org/10.1016/0038-1098\(94\)00598-7](https://doi.org/10.1016/0038-1098(94)00598-7).
- [24] P. E. J. Eriksson et al. “Origin of a surface state above the Fermi level on Ge(001) and Si(001) studied by temperature-dependent ARPES and LEED”. In: *Physical Review B* 77 (2008), p. 085406. DOI: <https://doi.org/10.1103/PhysRevB.77.085406>.
- [25] K. Nakatsuji et al. “Electronic states of the clean Ge(001) surface near Fermi energy”. In: *Physical Review B* 72 (2005), p. 241308. DOI: <https://doi.org/10.1103/PhysRevB.72.241308>.
- [26] H. Seo et al. “Critical differences in the surface electronic structure of Ge(001) and Si(001): ab initio theory and angle-resolved photoemission”. In: *Physical Review B* 89 (2014), p. 115318. DOI: <https://doi.org/10.1103/PhysRevB.89.115318>.
- [27] O. Gurlu, H. J. W. Zandvliet, and B. Poelsema. “Electronic properties of  $(2 \times 1)$  and  $c(4 \times 2)$  domains on Ge(001) studied by scanning tunneling spectroscopy”. In: *Physical Review Letters* 63 (2004), p. 066101. DOI: <https://doi.org/10.1103/PhysRevLett.93.066101>.
- [28] S. D. Kevan. “Surface states and reconstruction on Ge(001)”. In: *Physical Review B* 32 (1985), p. 2344. DOI: <https://doi.org/10.1103/PhysRevB.32.2344>.
- [29] E. Landemark et al. “Electronic structure of clean and hydrogen-chemisorbed Ge(001) surfaces studied by photoelectron spectroscopy”. In: *Physical Review B* 49 (1994), p. 16523. DOI: <https://doi.org/10.1103/PhysRevB.49.16523>.

- [30] C. Jeon et al. “Evidence from ARPES that the Ge(001) surface is semiconducting at room temperature”. In: *Physical Review B* 74 (2006), p. 125407. DOI: <https://doi.org/10.1103/PhysRevB.74.125407>.
- [31] J. Azuma J. Kanasaki I. Yamamoto and S. Fukatsu. “Electronic structure of the surface unoccupied band of Ge(001)- c(4×2): direct imaging of surface electron relaxation pathways”. In: *Physical Review B* 96 (2017), p. 115301. DOI: <https://doi.org/10.1103/PhysRevB.96.115301>.
- [32] F. Reichmann et al. “New insights into the electronic states of the Ge(001) surface by joint angle-resolved photoelectron spectroscopy and first-principle calculation investigation”. In: *Applied Surface Science* 571 (2022), p. 151264. DOI: <https://doi.org/10.1016/j.apsusc.2021.151264>.
- [33] R. Pillarisetty. “Academic and industry research progress in germanium nanodevices”. In: *Nature* 479 (2011), p. 324. DOI: <https://doi.org/10.1038/nature10678>.
- [34] S. Wirths, D. Buca, and S. Mantl. “Si–Ge–Sn alloys: From growth to applications”. In: *Progress in Crystal Growth and Characterization of Materials* 62 (2016), p. 1. DOI: <https://doi.org/10.1016/j.pcrysgrow.2015.11.001>.
- [35] R. Cheng et al. “Mobility enhancement techniques for Ge and GeSn MOSFETs”. In: *Journal of Semiconductors* 42 (2021), p. 023101. DOI: <https://doi.org/10.1088/1674-4926/42/2/023101>.
- [36] S. Wirths et al. “Lasing in direct-bandgap GeSn alloy grown on Si”. In: *Nature Photonics* 9 (2015), p. 88. DOI: <https://doi.org/10.1038/nphoton.2014.321>.
- [37] S. Gupta et al. “Hole mobility enhancement in compressively strained Ge<sub>0.93</sub>Sn<sub>0.07</sub> pMOSFETs”. In: *IEEE Electron Device Letters* 34 (2013), p. 831. DOI: <https://doi.org/10.1109/LED.2013.2259573>.
- [38] O. Moutanabbir et al. “Monolithic infrared silicon photonics: The rise of (Si)GeSn semiconductors”. In: *Applied Physics Letters* 118 (2021), p. 110502. DOI: <https://doi.org/10.1063/5.0043511>.
- [39] J. Mathews et al. “Near IR photodiodes with tunable absorption edge based on Ge<sub>1-y</sub>Sn<sub>y</sub> alloys integrated on silicon”. In: *Applied Physics Letters* 33 (2010), p. 765. DOI: <https://doi.org/10.1149/1.3487607>.
- [40] M. Oehme et al. “Room-temperature electroluminescence from GeSn light-emitting pin diodes on Si”. In: *IEEE Photonics Technology Letters* 23 (2011), p. 1751. DOI: <https://doi.org/10.1109/LPT.2011.2169052>.
- [41] R. T. Beeler et al. “Compositional dependence of the absorption edge and dark currents in Ge<sub>1-x-y</sub>Si<sub>x</sub>Sn<sub>y</sub>/Ge(100) photodetectors grown via ultra-low-temperature epitaxy of Ge<sub>4</sub>H<sub>10</sub>, Si<sub>4</sub>H<sub>10</sub>, and SnD<sub>4</sub>”. In: *Applied Physics Letters* 101 (2012), p. 221111. DOI: <https://doi.org/10.1063/1.4768217>.
- [42] A. Gassenq et al. “GeSn/Ge heterostructure short-wave infrared photodetectors on silicon”. In: *Optics Express* 20 (2012), p. 27297. DOI: <https://doi.org/10.1364/OE.20.027297>.
- [43] D. Lei et al. “Germanium-tin (GeSn) p-channel fin field-effect transistor fabricated on a novel GeSn-on-insulator Substrate”. In: *IEEE Transactions on Electron Devices* 65 (2018), p. 3754. DOI: <https://doi.org/10.1109/TED.2018.2856738>.

- [44] J. Chrétien et al. “GeSn lasers covering a wide wavelength range thanks to uniaxial tensile strain”. In: *ACS Photonics* 6 (2019), p. 2462. DOI: <https://doi.org/10.1021/acsp Photonics.9b00712>.
- [45] Y. Zhou et al. “Optically pumped GeSn lasers operating at 270 K with broad waveguide structures on Si”. In: *ACS Photonics* 6 (2019), p. 1434. DOI: <https://doi.org/10.1021/acsp Photonics.9b00030>.
- [46] A. Elbaz et al. “Ultra-low-threshold continuous-wave and pulsed lasing in tensile-strained GeSn alloys”. In: *Nature Photonics* 14 (2020), p. 375. DOI: <https://doi.org/10.1038/s41566-020-0601-5>.
- [47] D. Rainko et al. “Impact of tensile strain on low Sn content GeSn lasing”. In: *Scientific Reports* 9 (2019), p. 259. DOI: <https://doi.org/10.1038/s41598-018-36837-8>.
- [48] J. Sau and M. L. Cohen. “Possibility of increased mobility in Ge-Sn alloy system”. In: *Physical Review B* 75 (2007), p. 045208. DOI: <https://doi.org/10.1103/PhysRevB.75.045208>.
- [49] R. W. Olesinski and G. Abbaschian. “The GeSn (germaniumtin) system”. In: *Bulletin of Alloy Phase Diagrams* 5 (1984), p. 265. DOI: <https://doi.org/10.1007/BF02868550>.
- [50] J. A. van Vechten and J. C. Phillips. “New Set of Tetrahedral Covalent Radii”. In: *Physical Review B* 2 (1970), p. 2160. DOI: <https://doi.org/10.1103/PhysRevB.2.2160>.
- [51] P. Zaumseil et al. “The thermal stability of epitaxial GeSn layers”. In: *APL Materials* 6 (2018), p. 076108. DOI: <https://doi.org/10.1063/1.5036728>.
- [52] J. Aubin et al. “Growth and structural properties of step-graded, high Sn content GeSn layers on Ge”. In: *Semiconductor Science and Technology* 32 (2017), p. 094006. DOI: <https://doi.org/10.1088/1361-6641/aa8084>.
- [53] D. Stange et al. “GeSn/SiGeSn heterostructure and multi quantum well lasers”. In: *ACS Photonics* 5 (2018), p. 4628. DOI: <https://doi.org/10.1021/acsp Photonics.8b01116>.
- [54] F. Oliveira et al. “Fabrication of GeSn-multiple quantum wells by overgrowth of Sn on Ge by using molecular beam epitaxy”. In: *Applied Physics Letters* 107 (2015), p. 1. DOI: <https://doi.org/10.1063/1.4938746>.
- [55] D. Stange et al. “Study of GeSn based heterostructures: towards optimized group IV MQW LEDs”. In: *Optics Express* 24 (2016), p. 1358. DOI: <https://doi.org/10.1364/OE.24.001358>.
- [56] I. A. Fischer et al. “Composition analysis and transition energies of ultrathin Sn-rich GeSn quantum wells”. In: *Physical Review Materials* 4 (2020), p. 024601. DOI: <https://doi.org/10.1103/PhysRevMaterials.4.024601>.
- [57] M. Yamazaki et al. “Scanning tunneling microscopy observation of initial growth of Sn and Ge<sub>1-x</sub>Sn<sub>x</sub> layers on Ge(001) substrates”. In: *Applied Surface Science* 254 (2008), p. 6048. DOI: <https://doi.org/10.1016/j.apsusc.2008.02.175>.
- [58] K. Tomatsu et al. “An atomic seesaw switch formed by tilted asymmetric Sn-Ge dimers on a Ge (001) surface”. In: *Science* 315 (2007), p. 1696. DOI: <https://doi.org/10.1126/science.1137848>.
- [59] K. Tomatsu et al. “STM observation of initial growth of Sn atoms on Ge(001) surface”. In: *Surface Science* 601 (2007), p. 1736. DOI: <https://doi.org/10.1016/j.susc.2007.01.049>.



- [60] E. V. S. Hofmann et al. “The formation of a Sn monolayer on Ge(100) studied at the atomic scale”. In: *Applied Surface Science* 561 (2021), p. 149961. DOI: <https://doi.org/10.1016/j.apsusc.2021.149961>.
- [61] A. Tejada et al. “Structural Origin of the Sn 4d Core Level Line Shape in Sn/Ge(111)-(3x3)”. In: *Physical Review Letters* 100 (2008), p. 026103. DOI: <https://doi.org/10.1103/PhysRevLett.100.026103>.
- [62] Y.-T. Cheng et al. “Surface electronic structure of Si<sub>1-x</sub>Ge<sub>x</sub>(001)-2×1: a synchrotron radiation photoemission study”. In: *Applied Physics Express* 13 (2020), p. 095503. DOI: <https://doi.org/10.35848/1882-0786/abaf96>.
- [63] P. Ponath et al. “Surface structure analysis of Eu Zintl template on Ge(001)”. In: *Surface Science* 674 (2018), p. 94. DOI: <https://doi.org/10.1016/j.susc.2018.04.003>.
- [64] A. Suzuki et al. “Reduction of Schottky barrier height for n-type Ge contact by using Sn electrode”. In: *Japanese Journal of Applied Physics* 53 (2014), 04EA06. DOI: <https://doi.org/10.7567/JJAP.53.04EA06>.
- [65] A. Dimoulasa, P. Tsipas, and A. Sotiropoulos. “Fermi level pinning and charge neutrality level in germanium”. In: *Applied Physics Letters* 89 (2006), p. 252110. DOI: <https://doi.org/10.1063/1.2410241>.
- [66] T. Nishimura, K. Kita, and A. Toriumi. “Evidence for strong Fermi level pinning due to metal-induced gap states at metal/germanium interface”. In: *Applied Physics Letters* 91 (2007), p. 123123. DOI: <https://doi.org/10.1063/1.2789701>.
- [67] P. Tsipas and A. Dimoulas. “Modeling of negatively charged states at the Ge surface and interfaces”. In: *Applied Physics Letters* 94 (2009), p. 012114. DOI: <https://doi.org/10.1063/1.3068497>.
- [68] M. Kuzmin et al. “Origin of Fermi level pinning and its control on the n-type Ge(100) surface”. In: *Physical Review B* 94 (2016), p. 035421. DOI: <https://doi.org/10.1103/PhysRevB.94.035421>.
- [69] F. Reichmann et al. “Modifications of the Ge(001) Subsurface Electronic Structure after Adsorption of Sn”. In: *Applied Surface Science* 599 (2022), p. 153884. DOI: <https://doi.org/10.1016/j.apsusc.2022.153884>.
- [70] H. Tolner et al. “Transparent conductive oxides for display applications”. In: *Information Display* 24 (2008), p. 28.
- [71] J. Souk et al. *Flat Panel Display Manufacturing*. John Wiley and Sons Ltd, 2018. ISBN: 978-1-119-16136-3.
- [72] P. Barquinha et al. *Transparent Oxide Electronics: From Materials to Devices*. John Wiley and Sons Ltd, 2012. ISBN: 978-0-470-68373-6.
- [73] M. Grundmann et al. “Transparent semiconducting oxides: materials and devices”. In: *Physica Status Solidi A: Applications and Materials Science* 207 (2014), p. 1437. DOI: <https://doi.org/10.1002/pssa.200983771>.
- [74] A. Klein et al. “Transparent Conducting Oxides for Photovoltaics: Manipulation of Fermi Level, Work Function and Energy Band Alignment”. In: *Materials* 3 (2010), p. 4892. DOI: <https://doi.org/10.3390/ma3114892>.
- [75] Z. Zhang et al. “Visible-blind and solar-blind ultraviolet photodiodes based on (In<sub>x</sub>Ga<sub>1-x</sub>)<sub>2</sub>O<sub>3</sub>”. In: *Applied Physics Letters* 108 (2016), p. 123503. DOI: <https://doi.org/10.1063/1.4944860>.

- [76] M. Higashiwaki et al. “Current status of Ga<sub>2</sub>O<sub>3</sub> power devices”. In: *Japanese Journal of Applied Physics* 55 (2016), 1202A1. DOI: <https://doi.org/10.7567/JJAP.55.1202A1>.
- [77] M. Higashiwaki and G. H. Jessen. “The dawn of gallium oxide microelectronics”. In: *Applied Physics Letters* 112 (2018), p. 060401. DOI: <https://doi.org/10.1063/1.5017845>.
- [78] T. Berthold et al. “Towards Understanding the Cross-Sensitivity of In<sub>2</sub>O<sub>3</sub> Based Ozone Sensors: Effects of O<sub>3</sub>, O<sub>2</sub> and H<sub>2</sub>O Adsorption at In<sub>2</sub>O<sub>3</sub>(111) Surfaces”. In: *Physica Status Solidi B: Basic Solid State Physics* 255 (2018), p. 1700324. DOI: <https://doi.org/10.1002/pssb.201700324>.
- [79] H. Ohta and H. Hosono. “Transparent oxide optoelectronics”. In: *Materials Today* 7 (2004), p. 42. DOI: [https://doi.org/10.1016/S1369-7021\(04\)00288-3](https://doi.org/10.1016/S1369-7021(04)00288-3).
- [80] U. Kim et al. “LaInO<sub>3</sub>/BaSnO<sub>3</sub> polar interface on MgO substrates”. In: *APL Materials* 4 (2016), p. 071102. DOI: <https://doi.org/10.1063/1.5046368>.
- [81] S. J. Pearton et al. “A review of Ga<sub>2</sub>O<sub>3</sub> materials, processing, and devices”. In: *Applied Physics Reviews* 5 (2018), p. 011301. DOI: <https://doi.org/10.1063/1.5006941>.
- [82] Z. Galazka. “ $\beta$ -Ga<sub>2</sub>O<sub>3</sub> for wide-bandgap electronics and optoelectronics”. In: *Semiconductor Science and Technology* 33 (2018), p. 113001. DOI: <https://doi.org/10.1088/1361-6641/aadf78>.
- [83] M. A. Rozhkov et al. “Comparison of characteristics of schottky diodes based on  $\beta$ -Ga<sub>2</sub>O<sub>3</sub> and other wide bandgap semiconductors”. In: *Materials Physics and Mechanics* 24 (2015), p. 194.
- [84] M. Zhong et al. “High-performance single crystalline UV photodetectors of  $\beta$ -Ga<sub>2</sub>O<sub>3</sub>”. In: *Journal of Alloys and Compounds* 619 (2019), p. 572. DOI: <https://doi.org/10.1016/j.jallcom.2014.09.070>.
- [85] R. Fornari et al. “Thermal stability of  $\epsilon$ -Ga<sub>2</sub>O<sub>3</sub> polymorph”. In: *Acta Materialia* 411 (2017), p. 140. DOI: <https://doi.org/10.1016/j.actamat.2017.08.062>.
- [86] F. Boschi et al. “Hetero-epitaxy of  $\epsilon$ -Ga<sub>2</sub>O<sub>3</sub> layers by MOCVD and ALD”. In: *Journal of Crystal Growth* 443 (2016), p. 25. DOI: <https://doi.org/10.1016/j.jcrysgro.2016.03.013>.
- [87] I. Cora et al. “The real structure of  $\epsilon$ -Ga<sub>2</sub>O<sub>3</sub> and its relation to  $\kappa$ -phase”. In: *CrystEngComm* 19 (2017), p. 1509. DOI: <https://doi.org/10.1039/C7CE00123A>.
- [88] M. Pavesi et al. “ $\epsilon$ -Ga<sub>2</sub>O<sub>3</sub>epilayers as a material for solar-blind UV photodetectors”. In: *Materials Chemistry and Physics* 205 (2018), p. 502. DOI: <https://doi.org/10.1016/j.matchemphys.2017.11.023>.
- [89] F. Mezzadri et al. “ $\epsilon$ -Ga<sub>2</sub>O<sub>3</sub>epilayers as a material for solar-blind UV photodetectors”. In: *Materials Chemistry and Physics* 55 (2016), p. 12079. DOI: <https://doi.org/10.1016/j.matchemphys.2017.11.023>.
- [90] M. B. Maccioni and V. Fiorentini. “Phase diagram and polarization of stable phases of (Ga<sub>1-x</sub>In<sub>x</sub>)<sub>2</sub>O<sub>3</sub>”. In: *Applied Physics Express* 9 (2016), p. 041102. DOI: <https://doi.org/10.7567/APEX.9.041102>.
- [91] M. Mulazzi et al. “The electronic structure of  $\epsilon$ -Ga<sub>2</sub>O<sub>3</sub>”. In: *APL Materials* 7 (2019), p. 022522. DOI: <https://doi.org/10.1063/1.5054395>.

- [92] Z. Galazka et al. “Scaling-Up of Bulk  $\beta$ -Ga<sub>2</sub>O<sub>3</sub> Single Crystals by the Czochralski Method”. In: *ECS Journal of Solid State Science and Technology* 6 (2017), Q3007. DOI: <https://doi.org/10.1149/2.0021702jss>.
- [93] Z. Galazka et al. “On the bulk  $\beta$ -Ga<sub>2</sub>O<sub>3</sub> single crystals grown by the Czochralski method”. In: *Journal of Crystal Growth* 404 (2014), p. 184. DOI: <https://doi.org/10.1016/j.jcrysgro.2014.07.021>.
- [94] M. Higashiwaki et al. “Recent progress in Ga<sub>2</sub>O<sub>3</sub> power devices”. In: *Semiconductor Science and Technology* 31 (2016), p. 034001. DOI: <https://doi.org/10.1088/0268-1242/31/3/034001>.
- [95] M. Higashiwaki et al. “Gallium oxide (Ga<sub>2</sub>O<sub>3</sub>) metal-semiconductor field-effect transistors on single-crystal  $\beta$ -Ga<sub>2</sub>O<sub>3</sub> (010) substrates”. In: *Applied Physics Letters* 100 (2021), p. 013504. DOI: <https://doi.org/10.1063/1.3674287>.
- [96] M. Orita et al. “Deep-ultraviolet transparent conductive  $\beta$ -Ga<sub>2</sub>O<sub>3</sub> thin films”. In: *Applied Physics Letters* 77 (2000), p. 4166. DOI: <https://doi.org/10.1063/1.1330559>.
- [97] J. B. Varley et al. “Oxygen vacancies and donor impurities in  $\beta$ -Ga<sub>2</sub>O<sub>3</sub>”. In: *Applied Physics Letters* 97 (2010), p. 142106. DOI: <https://doi.org/10.1063/1.3499306>.
- [98] H. Peelaers and C. G. Van de Walle. “Brillouin zone and band structure of  $\beta$ -Ga<sub>2</sub>O<sub>3</sub>”. In: *Physica Status Solidi B: Basic Solid State Physics* 252 (2015), p. 828. DOI: <https://doi.org/10.1002/pssb.201451551>.
- [99] M. Baldini, Z. Galazka, and G. Wagner. “Recent progress in the growth of  $\beta$ -Ga<sub>2</sub>O<sub>3</sub> for power electronics applications”. In: *Materials Science in Semiconductor Processing* 78 (2017), p. 132. DOI: <https://doi.org/10.1016/j.mssp.2017.10.040>.
- [100] Z. Galazka et al. “Ultra-wide bandgap, conductive, high mobility, and high quality melt-grown bulk ZnGa<sub>2</sub>O<sub>4</sub> single crystals”. In: *APL Materials* 7 (2019), p. 022512. DOI: <https://doi.org/10.1063/1.5053867>.
- [101] Y. Jang et al. “Thin film transistors based on ultra-wide bandgap spinel ZnGa<sub>2</sub>O<sub>4</sub>”. In: *Applied Physics Letters* 116 (2020), p. 202104. DOI: <https://doi.org/10.1063/5.0007716>.
- [102] L.-C. Cheng, C.-Y. Huang, and R.-H. Horng. “Thickness Effect on Operational Modes of ZnGa<sub>2</sub>O<sub>4</sub> MOSFETs”. In: *IEEE Journal of the Electron Devices Society* 6 (2018), p. 432. DOI: <https://doi.org/10.1109/JEDS.2018.2803078>.
- [103] D. Han et al. “Performance enhancement of a self-powered solar-blind UV photodetector based on ZnGa<sub>2</sub>O<sub>4</sub>/Si heterojunction via interface pyroelectric effect”. In: *Applied Physics Letters* 118 (2021), p. 251101. DOI: <https://doi.org/10.1063/5.0049747>.
- [104] Y.-C. Shen et al. “Study on Optoelectronic Characteristics of ZnGa<sub>2</sub>O<sub>4</sub> Thin-Film Phototransistors”. In: *ACS Applied Electronic Materials* 1 (2019), p. 783. DOI: <https://doi.org/10.1021/acsaem.9b00128>.
- [105] M. Hilfiker et al. “Zinc gallate spinel dielectric function, band-to-band transitions, and  $\gamma$ -point effective mass parameters”. In: *Applied Physics Letters* 118 (2021), p. 132102. DOI: <https://doi.org/10.1063/5.0043686>.
- [106] M. Stokey et al. “Brillouin zone center phonon modes in ZnGa<sub>2</sub>O<sub>4</sub>”. In: *Applied Physics Letters* 117 (2020), p. 052104. DOI: <https://doi.org/10.1063/5.0012526>.
- [107] F. Reichmann et al. “Experimental and Theoretical Investigation of the Surface Electronic Structure of ZnGa<sub>2</sub>O<sub>4</sub>(100) Single-Crystals”. In: *Physica Status Solidi B: Basic Solid State Physics* 259 (2021), p. 2100452. DOI: <https://doi.org/10.1002/pssb.202100452>.